

THE UNIVERSITY OF MICHIGAN
COLLEGE OF LITERATURE, SCIENCE, AND THE ARTS
Department of Physics

Technical Report

MESONS AND SPECTATOR PROTONS IN $\pi^+ d \rightarrow \pi^+ \pi^- \pi^0 pp$ AT 3.65 BeV/c

George C. Benson

ORA Project 04938

under contract with:

U. S. ATOMIC ENERGY COMMISSION
CHICAGO OPERATIONS OFFICE
CONTRACT NO. AT(11-1)-1112
ARGONNE, ILLINOIS

administered through:

OFFICE OF RESEARCH ADMINISTRATION

ANN ARBOR

November 1966

UMR 0315

his report was also a dissertation submitted in
partial fulfillment of the requirements for the de-
gree of Doctor of Philosophy in The University of
Michigan, 1966.

TABLE OF CONTENTS

	Page
LIST OF TABLES	vi
LIST OF FIGURES	vii
ABSTRACT	xi
CHAPTER	
I. INTRODUCTION	1
II. THE DEUTERON TARGET	7
A. The Deuteron	7
B. Angular Tests of the Spectator Model	9
C. The Moving Target	13
D. The Spectator Momentum Distribution	17
E. Spectators in Other Channels	18
F. Constraint of the Spectator Momentum	23
G. Meson-Spectator Scattering	28
H. Summary	29
I. Independence of the Meson Vertex	30
J. Glauber Screening	32
K. Pauli Exclusion	33
III. EVENT IDENTIFICATION	39
A. Validity Tests for $\pi^+\pi^-\pi^0_{pp}$	39
A.1 Missing mass distribution	39
A.2 Chi-squared and probability distribution	43
A.3 Other tests	47
B. Validity Tests for $\pi^+\pi^+\pi^-\pi^0_{pn}$	50
C. Ambiguities	52
C.1 Missing mass tests	55
IV. GENERAL MASS AND MOMENTUM TRANSFER DISTRIBUTIONS	61
V. RESONANCE PRODUCTION IN $\pi^+d \rightarrow \pi^+\pi^-\pi^0_{pp}$	73
A. $\pi^+d \rightarrow \eta^0_{pp}$	73
A.1 Mass and width	73
A.2 Total and differential cross section	74
A.3 Dalitz plot density	78

TABLE OF CONTENTS (Continued)

CHAPTER	Page
B. $\pi^+ d \rightarrow \omega^0 pp$	80
B.1 Mass and width	80
B.2 Total and differential cross section	85
B.3 Predictions of absorption and Regge model	88
B.4 Density matrix elements	90
B.5 Dalitz plot density	98
C. $\pi^+ d \rightarrow H^0 pp$	101
C.1 Mass distribution	102
C.2 Isotopic spin	106
C.3 Momentum transfer distributions	109
C.4 Spin-parity test	114
C.5 Density matrix elements	122
D. $\pi^+ d \rightarrow A_2^0 pp$	126
D.1 Three-pion and $\rho\pi$ mass spectra	127
D.2 Branching ratios of the A_2^0	133
D.3 Spin-parity of the A_2^0	134
D.4 A_2^0 Production mechanism	139
D.5 Aside on A_1^0 Production	141
D.6 Momentum transfer distributions	141
D.7 Density matrix elements	143
E. $\pi^+ d \rightarrow \rho\pi pp$	152
E.1 Cross sections, masses, and widths	152
E.2 Pion exchange	153
E.3 Nucleon exchange	157
E.4 Pion-pion scattering angles	160
VI. THREE-PRONG EVENTS	163
A. Fitting Odd-Prong Events	163
B. Three-Prong Event Cross Sections	166
C. Mass Spectra	167
D. Momentum of the Missing Spectator	170
VII. SUMMARY OF RESULTS AND CONCLUSIONS	177
APPENDIX	
A. EXPOSURE DETAILS	181
B. SCAN DETAILS	185
C. EVENT MEASUREMENT	189
D. GEOMETRIC RECONSTRUCTION	192

TABLE OF CONTENTS (Concluded)

	Page
E. BUBBLE DENSITY	194
F. KINEMATIC ANALYSIS	196
G. EVENT ANALYSIS	202
H. CROSS SECTION DETERMINATION	203
I. TOTAL DEUTERIUM CROSS SECTION DETERMINATION	215
J. THE LUBATTI-ROSENFELD CORRECTION TO PHASE SPACE	217
K. NOTES ON THE DENSITY MATRIX	221
L. ANGULAR DISTRIBUTIONS FOR THE H MESON	232
REFERENCES	234
ACKNOWLEDGMENTS	242

LIST OF TABLES

Table	Page
I. Spectator Fractions for π^0 , f^0 , ρ^0 , and ω^0 Mesons	28
II. Comparison of Deuterium Cross Sections with Charge Symmetric Hydrogen Data	31
III. Values Used to Predict the Effect of Pauli Exclusion on the Deuterium Cross Section	38
IV. Uncorrected Resolution in Missing Mass Squared for Good (π^0), Ambiguous (π^0)-(pn), and Good (pn) Events	60
V. Density Matrix Elements for the ω^0 from Other Experiments	95
VI. Density Matrix Elements for the ω^0 from This Experiment	97
VII. Resolution of $M(3\pi)$	105
VIII. Results of Fitting the $\cos \theta_n$, $\cos \theta_m$, and $\cos \theta_d$ Distributions for Various J^P Assignments of the H Meson	119
IX. Density Matrix Elements for the H Meson and Background Events	122
X. Density Matrix Elements for the A_2^- and A_2^0 Mesons	147
XI. Three-Prong Cross Sections	167
XII. Comparison of Three-Prong and $\pi^- p$ Cross Sections	170
XIII. Results of Measuring Machine Tests	190
XIV. Factors Used in Evaluating the Cross Section	211
XV. Channel Cross Section Corrections	213
XVI. Cross Section by Topology	216
XVII. Multipole Moments Expressed as a Function of Density Matrix Elements	227

LIST OF FIGURES

Figure		Page
1.	Laboratory angular distributions of the protons $\pi^+\pi^-\pi^0$ pp.	10
2.	Laboratory angular distributions of the protons and neutrons from $\pi^+\pi^+\pi^-\text{pn}$.	12
3.	The $\Delta^2(d \rightarrow p_s)$ distribution.	14
4.	Distribution of center of mass energies.	16
5.	Momentum distribution of the slower proton.	19
6.	Fractions of spectators having a momentum greater than 250 MeV/c as a function of channel, mesons produced, and Δ^2 (mesons).	20
7.	Sample event of the type $\pi^+d \rightarrow \omega^0$ pp with high momentum protons.	25
8.	Sample event of the type $\pi^+d \rightarrow \omega^0$ pp with low momentum protons.	26
9.	The deuteron form factor and predictions for deuterium cross sections based on Pauli exclusion and hydrogen data.	35
10.	Missing mass squared distribution for unique (π^0) events.	41
11.	Comparison of the resolution curve with Gaussian and Breit-Wigner forms.	44
12.	Distribution of χ^2 for the unique (π^0) events.	45
13.	Probability distribution for (π^0) events.	48
14.	Comparison of the unfit π^0 momentum with the unfitted π^- momentum and the missing momentum of $\pi^+d \rightarrow \pi^+\pi^-\text{pp}$ events.	49
15.	Missing mass squared for the π^0 but calculated as if for a neutron.	51
16.	Missing mass squared for the unique (pn) events with the corrected neutron resolution function.	53

LIST OF FIGURES (Continued)

Figure	Page
17. Probability distribution for (pn) events.	54
18. Probability distributions for ambiguous (π^0)-(pn) events.	56
19. Missing mass squared for good (π^0) events and ambiguous events.	58
20. Missing mass squared for good (pn) events and ambiguous events.	59
21. $M(\pi^+\pi^-\pi^0)$ distribution for the $\pi^+\pi^-\pi^0$ pp final state.	62
22. Scatter plot of $\Delta^2(3\pi)$ as a function of $M(3\pi)$.	64
23. Histogram of $\Delta^2(3\pi)$ for all events.	65
24. Histogram of $\Delta^2(3\pi)$ less Δ_{\min}^2 .	66
25. Backward production angular distribution for the three-pion system.	68
26. Two-body effective mass distributions.	69
27. Masses of the pion-slower proton systems.	71
28. Masses of the pion-pion-faster proton systems.	72
29. Total cross section for η^0 production as a function of beam momentum and comparison with hydrogen data.	76
30. Differential cross section for η^0 production with the Regge prediction.	77
31. Radial Dalitz plot densities for η^0 , ω^0 , H^0 , and A_2^0 mass regions.	79
32. Invariant mass in the η^0 and ω^0 regions.	81
33. Fitted and unfitted mass squared in the η^0 and ω^0 regions.	84
34. Distribution of $\Delta^2(\omega^0)$.	87
35. Angular distributions of the ω^0 decay plane normal.	92

LIST OF FIGURES (Continued)

Figure	Page
36. Density matrix elements predicted by the absorption and Regge pole models.	96
37. Dalitz plot density for the ω^0 .	100
38. Invariant mass of $\pi^+\pi^-\pi^0$ with the requirement of ρ^+ , ρ^0 , or ρ^- showing the H meson.	103
39. The data of Fig. 38 with $\Delta^2(3\pi) < 0.85 \text{ (BeV/c)}^2$ imposed and ρN^* removed.	104
40. The $(\rho\pi)^0$ mass spectrum combined with data from $\pi^+p \rightarrow (\rho\pi)^0 N^{*++}$.	107
41. The $(\rho\pi)^0$ mass spectrum for single ρ events.	108
42. The $(\rho\pi)^0$ mass spectrum of Fig. 39 with all ρ^0 events removed.	110
43. Histogram of $\Delta^2(H)$.	111
44. Scatter plot of $\Delta^2(\rho^+)$, $\Delta^2(\rho^-)$, or $\Delta^2(\rho^0)$ versus $M(3\pi)$.	113
45. Angular distributions of the H decay plane normal, bachelor pions, and married pions.	115
46. Fitted curves for $J^P = 2^+$ or 2^- .	118
47. The bachelor and married pion distributions in each of the ρ bands.	121
48. Angular distributions in the H and control regions.	123
49. Predicted density matrix elements from the absorption model.	124
50. $M(\pi^+\pi^-\pi^0)$ for all events.	128
51. Dalitz plot for the A_2^0 .	129
52. $M(\pi^+\pi^-\pi^0)$ for single, double, and triple ρ events.	131
53. $M(\pi^+\pi^-\pi^0)$ for non- ρ events.	132

LIST OF FIGURES (CONCLUDED)

Figure		Page
54.	Comparison of A_2^0 and A_2^- production.	135
55.	Theoretical predictions of the A_2 Dalitz plot density.	137
56.	Experimental Dalitz plot densities.	138
57.	$\Delta^2(A_2^0)$ distribution.	142
58.	The decay plane normal distribution of A_2^- at 2.75 BeV/c.	145
59.	Absorption model predictions for the A_2 density matrix.	146
60.	Decay plane normal and bachelor pion distributions for the A_2^0 .	149
61.	Decay plane normal for central and edge A_2^0 events.	151
62.	Comparison of $\Delta^2(\rho^0)$ in $\pi^-p \rightarrow \rho^0 N^{*0}$ and $\Delta^2(\rho_0^+)$ in $\pi^+n \rightarrow \rho_0^+ N^{*0}$.	156
63.	Production angular distributions for ρ^+ , ρ^0 , and ρ^- .	158
64.	Pion-pion scattering angles in the ρ rest frames.	162
65.	Mass spectra from three-prong (missing spectator) events.	168
66.	Comparison of measuring error and fitted missing spectator momentum.	172
67.	Comparison of fitted missing spectator momentum with the Hulthen prediction.	173
68.	Plots of the cosine of the spectator dip angle as a function of spectator momentum.	175
69.	Missing mass squared for "no-fit" events which were re-measured.	200
70.	Sketch of the fiducial region.	206
71.	The correction factor used to peripheralize phase space.	219

ABSTRACT

We have taken 250,000 pictures in the 20-in. Brookhaven National Laboratory deuterium bubble chamber. The chamber was exposed to 3.65 BeV/c π^+ mesons. Cross sections for reactions in deuterium are compared with charge symmetric cross sections in hydrogen. The number of high momentum spectators is studied in two- and four-prong two proton final states. Galuber screening and Pauli exclusion are discussed.

The 2993 events (3.44 ± 0.31 mb), of the type $\pi^+\pi^-\pi^0pp$, are studied in detail. The χ^2 probability and missing mass distributions show evidence for some contaminating events with $2\pi^0$'s present. The number of π^0 events in π^0 -neutron ambiguous events is determined by comparing missing mass squared and resolution functions.

The differential cross sections are presented for η^0 , ω^0 , H^0 , A_2^0 , ρ^+ , ρ^0 , and ρ^- mesons. A spin test for the H^0 meson is made using the decay plane normal, bachelor, and married pions. A spin test for the A_2^0 is made using mass squared variables. The real part of the density matrix is determined for the ω^0 , H^0 , and A_2^0 mesons. For each density matrix a comparison is made with the prediction of the absorption model. Cross sections for A_2^0 and ρ^+N^* production in deuterium are compared with hydrogen data for A_2^- and ρ^0N^{*0} .

Results from the processing of a few odd-prong events are discussed.

In the Appendices details of our experimental methods are presented, including scan rules and the cross section determination. The general theory of the density matrix and the Lubatti-Rosenfeld method for peripheralizing phase space are discussed.

CHAPTER I

INTRODUCTION

The film analyzed in this experiment was exposed in the Brookhaven National Laboratory 20-inch bubble chamber. The proposal for the experiment was submitted to Brookhaven in December 1962, and an exposure of 80,000 frames was completed in November 1963. The early stages of the analysis showed interesting results (primarily $f^0 \rightarrow$ all neutrals), and also that more film would be needed for a detailed study. An additional exposure was requested and completed by December 1964, making a total film sample of 250,000 frames.

There are a number of π^+ in deuterium experiments currently in progress. We are aware of experiments at beam momenta of 0.82,¹ 1.23,² 1.7,³ 2.5,⁴ 3.25,⁵ 3.65 (this),⁶ 4.5,⁷ 5.1,⁸ and 6.0 BeV/c.⁹ Many short reports have been published, but only the experiment at 1.23 BeV/c has been published in final form.

The film has proven to be as interesting as our early results indicated. At present, studies are being made on the following channels:

$$\pi^+ d \rightarrow X^0 pp \quad (X^0)$$

(X^0 denotes one or more missing neutrals) where π^0 and $f^0 \rightarrow$ (all neutrals) production is being studied;

$$\pi^+ d \rightarrow \pi^+ \pi^- pp \quad (pp)$$

where $\rho^0 \rightarrow \pi^+\pi^-$ and $f^0 \rightarrow \pi^+\pi^-$ are observed;

$$\pi^+d \rightarrow \pi^+\pi^-\pi^0pp \quad (\pi^0)$$

which is the subject of this report, in which η^0 , ω^0 , H^0 , A_2^0 , ρ^+ , ρ^0 , and ρ^- mesons are observed;

$$\pi^+d \rightarrow \pi^+\pi^-(m\pi^0)pp ; m \geq 2 \quad (m\pi^0)$$

where η^* production has been observed;

$$\begin{aligned} \pi^+d &\rightarrow K^+K^-pp \\ &\rightarrow K_1^0K_1^0pp \\ &\rightarrow K_1^0K_2^0pp \end{aligned}$$

where some evidence for ϕ production has been observed;

$$\pi^+d \rightarrow (m\pi)K\Lambda p ; m \geq 0$$

in which a search is being made for resonant states in the Λp system;

$$\begin{aligned} \pi^+d &\rightarrow \pi^+d \\ &\rightarrow \pi^+\pi^0d \\ &\rightarrow \pi^+\pi^+\pi^-d \end{aligned}$$

in which elastic scattering, resonance production, and diffraction dissociation are being studied; and

$$\begin{aligned} \pi^+d &\rightarrow \pi^+\pi^+\pi^-\pi^-pp \\ &\rightarrow \pi^+\pi^+\pi^-\pi^-\pi^0pp \end{aligned}$$

where the η^* has been observed and other resonances are being sought.

We will refer to the first four reactions at times by the abbreviations in the parentheses and will also discuss the reaction

$$\pi^+ d \rightarrow \pi^+ \pi^+ \pi^- pn \quad (pn).$$

We have identified by ionization and by fitting the following numbers of events:

(X^0)	1392
(pp)	1983
(π^0)	2993
$(\pi\pi^0)$	2075
(pn)	2000

Events which were kinematically consistent with either (pp) or (π^0) were assumed to be (pp) as discussed further in Appendix F. Events which could be either (π^0) or (pn) have been kept separate (called ambiguous) and are discussed in Chapter III.

We give here the reason for doing this experiment in deuterium rather than in hydrogen. The reaction in hydrogen

$$\pi^- p \rightarrow \pi^+ \pi^- \pi^0 n$$

has two neutral particles missing. Neither of these neutral particles leaves a track in the bubble chamber, and one can do little more than study the $\pi^+ \pi^-$ system. Under charge symmetry ($\pi^- \rightarrow \pi^+$, $\pi^+ \rightarrow \pi^-$, $\pi^0 \rightarrow \pi^0$, and

$p \rightarrow n$), the reaction

$$\pi^+ n \rightarrow \pi^- \pi^+ \pi^0 p$$

should be identical to the reaction $\pi^- p \rightarrow \pi^+ \pi^- \pi^0 n$. Since free neutron targets cannot be made, the next best target is the neutron in the deuteron, so we study

$$\pi^+ d \rightarrow \pi^- \pi^+ \pi^0 p(p) \quad .$$

Here the momentum of the single missing neutral can be inferred from conservation of momentum, and all of the combinations of the final state particles can now be studied.

In the study of these events, we have found evidence for the following unstable particles and decay modes:

$$\eta^0 \rightarrow \pi^+ \pi^- \pi^0$$

$$\omega^0 \rightarrow \pi^+ \pi^- \pi^0$$

$$H^0 \rightarrow \rho^+ \pi^-, \rho^0 \pi^0, \text{ or } \rho^- \pi^+$$

$$A_2^0 \rightarrow \rho^+ \pi^- \text{ or } \rho^- \pi^+$$

$$\rho^+ \rightarrow \pi^+ \pi^0$$

$$\rho^0 \rightarrow \pi^+ \pi^- \quad \text{and}$$

$$\rho^- \rightarrow \pi^0 \pi^- \quad .$$

The ω^0 has been well studied previously at 3.25 BeV/c, and the η^0 well studied in spark chamber experiments. Very few details on the other processes have been published to date for this channel. These details

form the chief part of this report.

At the present, studies of cross sections and ρ^0 -meson production indicate that the bound neutron is acting like a free neutron for π^+ at 1.7 BeV/c and 3.65 BeV/c. We present in this report a study of the spectator protons from this reaction and from others. The results are not entirely understood. When properly understood, they may shed some light on the importance of double scattering in the deuteron.

The notation we use throughout this report is

E	energy
\vec{P}, P	momentum
M	mass = $\sqrt{(\sum E)^2 - (\sum P)^2}$
t, T	four-momentum transfer squared $(\Delta E)^2 - (\Delta P)^2$
Δ^2	four-momentum transfer squared $(\Delta P)^2 - (\Delta E)^2$
$\Delta^2(\text{mesons})$	Δ^2 calculated between the beam and the mesons
T	kinetic energy
θ	polar angle in a spherical coordinate system
ϕ	azimuthal angle in a spherical coordinate system.

The cross sections per event which are used in this report are for

$$\Delta^2(\text{mesons}) < 1.9 \pm 0.3 (\text{BeV/c})^2$$

$$1.06 \pm 0.09 \text{ } \mu\text{b/event} \quad (\text{all events})$$

$$1.20 \pm 0.10 \text{ } \mu\text{b/event} \quad (\text{above background}) ,$$

$$\text{and for } \Delta^2(\text{mesons}) > 1.9 \pm 0.3 (\text{BeV/c})^2$$

$1.60 \pm 0.24 \text{ } \mu\text{b/event}$ (all events)

$1.74 \pm 0.26 \text{ } \mu\text{b/event}$ (above background) .

The average value is

$1.15 \pm 0.10 \text{ } \mu\text{b/event}$.

We have placed standard technical details in the Appendices and have included only novel or crucial details and experimental results in the text which follows. The hurried reader should consult the Table of Contents and Chapter VII for a further summary of this investigation.

CHAPTER II

THE DEUTERON TARGET

The target particle in this experiment is the deuteron, so that, strictly speaking, our results are for a π^+ meson colliding with a deuteron. Because the binding energy of the neutron and proton is so small (2.23 MeV) compared to the beam energy (3650 MeV), it is expected that most of the interactions will take place as though the target were a single free nucleon. This point of view is called the spectator model. It has been the subject of considerable theoretical and experimental work.

In this chapter we discuss some of the properties of the deuteron and then show to what extent the slower protons in this experiment can be interpreted as non-participants in the interaction (i.e., as spectators). Many other properties of the deuteron may be found in the literature.¹⁰

A. THE DEUTERON

The deuteron is a bound state of a neutron and a proton. The nucleons are held together by nuclear forces, presumably by the exchange of virtual pions. These forces can be described by a suitable potential, and the radial wave function can then be obtained from a solution of the Schrödinger equation. One such wave function is that of Hulthén¹¹

$$\psi(r) = N \left(\frac{e^{-\alpha r}}{r} - \frac{e^{-\beta r}}{r} \right),$$

where

$N^2 = 2\alpha\beta(\alpha + \beta)/(\alpha - \beta)^2$ is the normalization factor,

r is the separation of the two nucleons,

$\alpha = 45.5 \text{ MeV} = (1/4.13) F^{-1}$, and

$\beta = 5 \text{ to } 7\alpha$.

The constant α is fixed by the binding energy, E , of the deuteron and the reduced mass of the nucleon μ through the relation $\alpha^2 = 2\mu E$. One F is equal to 10^{-13} cm .

Two discrete values of β are currently prominent in the literature.^{12,13} The value due to Salpeter¹⁴ is $\beta = 7\alpha$. The other value is due to Moravcsik,¹⁵ who found $\beta = 5.18\alpha$ was the best value for his approximation of the Gartenhaus wave function.

To estimate the mean diameter of the deuteron, the average value of r can be found immediately from the Hulthen wave function

$$\begin{aligned}\bar{r} &= \int_0^{\infty} r \psi^2 r^2 dr \\ &= \frac{N^2}{4\alpha^2} \left(1 - \frac{8}{(1+k)^2} + \frac{1}{k^2} \right) \\ &= 3F .\end{aligned}$$

We have used $k = \beta/\alpha = 7$ for the numerical result. For comparison, the diameter of the nucleon is taken to be one or two F .^{16,17}

B. ANGULAR TESTS OF THE SPECTATOR MODEL

If our unpolarized deuteron target were to decay spontaneously into two nucleons, then this decay would be isotropic about any fixed axis in the laboratory (rest frame of the target). In the framework of the spectator model, the spectator proton acts just as though it were the result of a decay. The isotropy of the spectator is, therefore, a test of the model. In Fig. 1 (a) is shown the angular distribution of the spectator proton relative to the beam direction for all events with two observed protons and identified as $\pi^+\pi^-\pi^0$ pp. It is essentially isotropic in the backward direction (39% of the events have $\cos\theta < 0$) but shows some tendency for the spectator to be carried along with the beam. The shaded events have spectators with momenta less than 250 MeV/c. These are somewhat more isotropic with 46% having $\cos\theta < 0$.

The cause of the forward peaking is not known. Some peaking is to be expected in a bound target. For example, if the proton is considered a bound state of π^+ and neutron, and one studies $\pi^-p \rightarrow \pi^+\pi^-n$, none of the spectator neutrons will have $\cos\theta < 0$ because of conservation of energy. Alternatively one would also expect forward peaking if rescattering were taking place; for example, by the two step reaction

$$\pi^+d \rightarrow \rho^0 pp_s ; \rho^0 p_s \rightarrow \rho^0 \pi^0 p .$$

Calculations have not been made which would indicate the relative importance of these two effects.

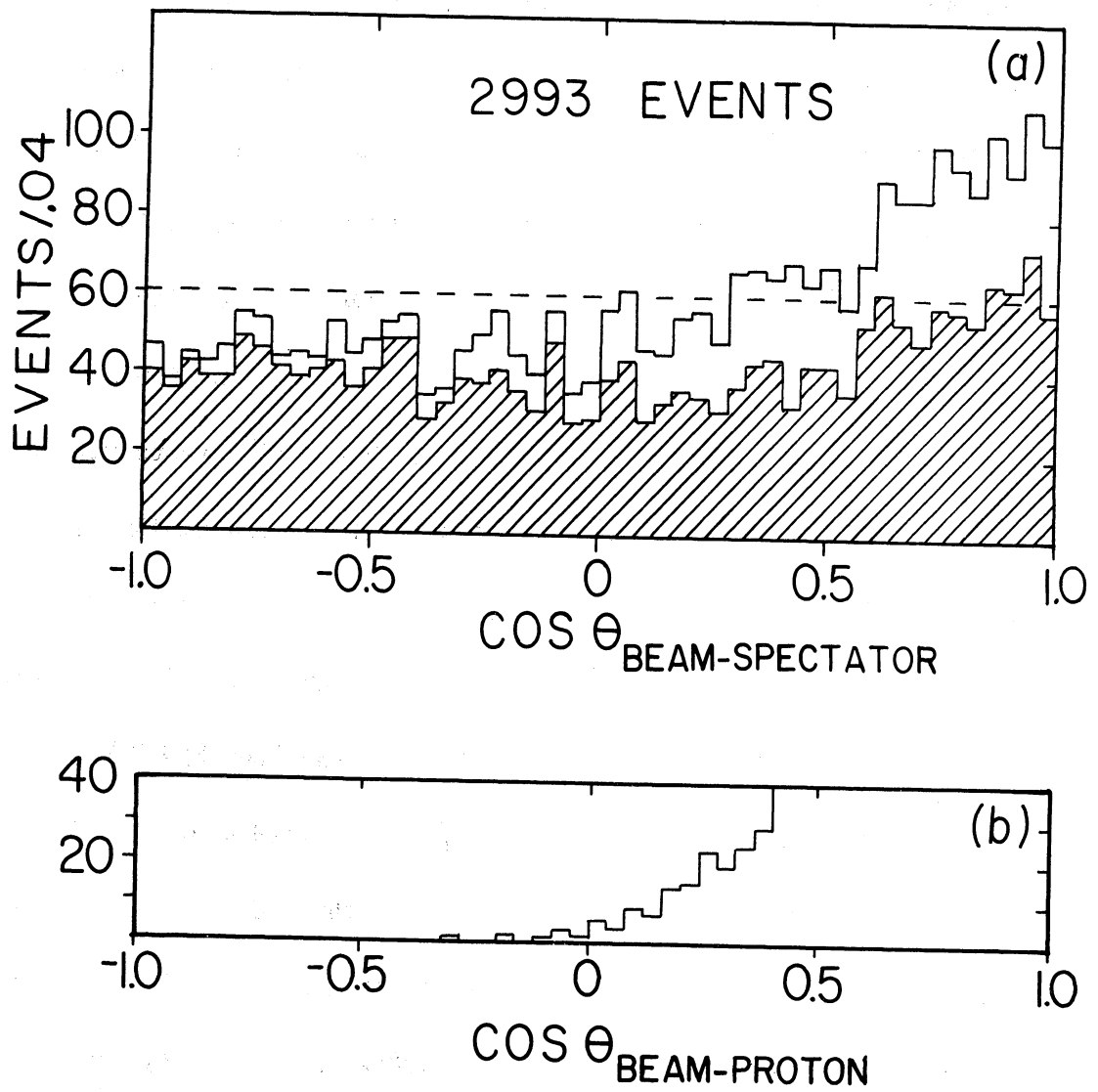


Figure 1. (a) Angular distribution of the slower proton relative to the beam direction. Shaded events have a proton with momentum less than 250 MeV/c. (b) Angular distribution of the faster proton.

We define the proton of lower momentum to be the spectator. The angular distribution of the faster proton is shown in Fig. 1 (b). As expected for the struck proton, very few have $\cos\theta < 0$.

In Figs. 2 (a, b, c, d) we show scatter plots of the cosine of the angle between the beam and the proton (x axis) and between the beam and the neutron (y axis) in the reaction $\pi^+d \rightarrow \pi^+\pi^+\pi^-pn$. The neutron angles in all four plots have been inferred from overall conservation of momentum and energy. The events ambiguous between (π^0) and (pn) have been included here since we conclude (later in the text) that 3/4 of them are the (pn) type. The 421 events with a deuteron in the final state, $\pi^+d \rightarrow \pi^+\pi^+\pi^-d$, are plotted in Fig. 2 (d) if $M(pn) = 1.8785 \pm 0.0015$ BeV. The mass interval is higher than the deuteron mass because we are approximating the charged track as a proton (rather than a deuteron) and performing a one-constraint fit to the missing neutron. This is also the reason that the events do not lie exactly on a 45° line.

The remaining events are selected by the momentum of the neutron. Our scan rules have preselected the proton to have a momentum of less than about 250 MeV/c. If the momentum of the neutron is less than 150 MeV/c (328 events), it is most likely a spectator neutron resulting from a $\pi^+p \rightarrow \pi^+\pi^+\pi^-p$ collision which is known to have a very large cross section for low momentum transfers.^{18,19} This is borne out by the isotropy of the neutron in Fig. 2 (b). If the momentum of the neutron is high (we require at least 300 MeV/c, which is satisfied by 1481 events), then the neutron was the target, and the protons should

$$\pi^+ d \rightarrow \pi^+ \pi^+ \pi^- p n$$

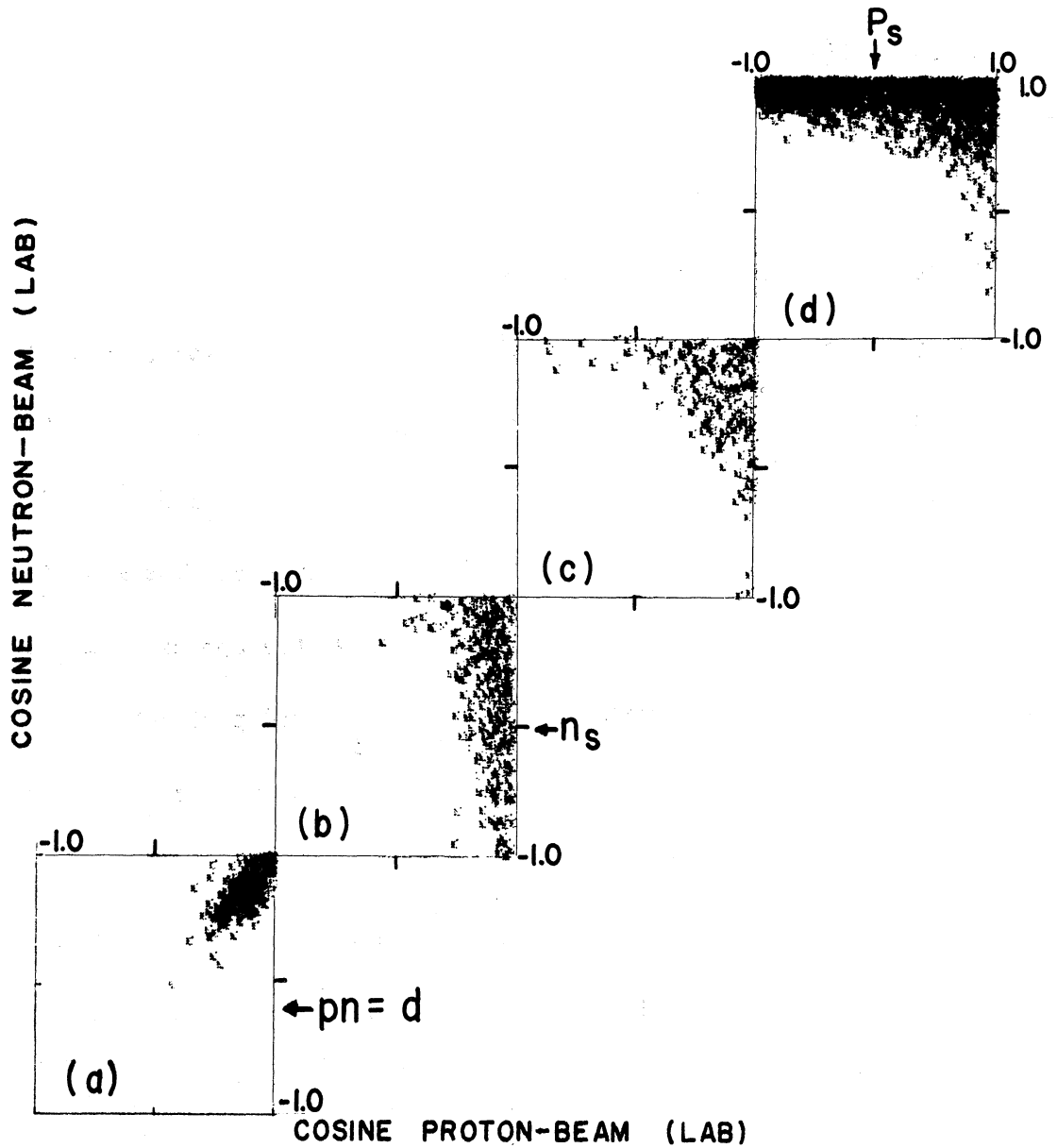


Figure 2. Scatter plot of the cosine of the angle between the beam and the proton (x axis) and the beam and the neutron (y axis) for events of the type $\pi^+ d \rightarrow \pi^+ \pi^+ \pi^- p n$, if (a) the pn invariant mass is that of a deuteron, and (b), (c), (d) the momentum of the neutron falls in the range < 150 , $150 - 300$, > 300 MeV/c.

be isotropic. Again this is the case as seen in Fig. 2 (d). For the intermediate case (227 events) with momenta between 150-300 MeV/c, one would expect to see some mixture of isotropic neutrons and protons, with the spectator model predicting exactly 50% of the events with either a neutron or a proton with $\cos\theta < 0$. Instead Fig. 2 (c) shows that very few events (about 10%) have either a proton or a neutron in the backward direction. It is difficult to interpret this effect as rescattering.

C. THE MOVING TARGET

In Fig. 3 is shown a typical diagram of the $\pi^+\pi^-\pi^0pp$ channel which illustrates the double-peripheral nature of the reaction. Diagrams of this type have been calculated where the exchanged particles were both mesons.²⁰ The lower neutron exchange diagram is equivalent to the reaction $\rho^+d \rightarrow pp$. Theoretical studies²¹ of the similar and time reversed reaction $pp \rightarrow \pi^+d$ have been made. The experimental results²¹ for $pp \rightarrow \pi^+d$ can be qualitatively understood with a neutron exchange model. The Chew-Low method²² was, of course, formulated to correct for the fact that the neutron is "off the mass shell." Both successful and unsuccessful extrapolations to the free nucleon pole have been reported.²³ The histogram of $\Delta^2(d \rightarrow p_s)$ in Fig. 3 can be interpreted as a histogram of minus the mass of the exchanged neutron by inserting conservation of energy at the dnp vertex:

$$\Delta^2(d \rightarrow p_s) = |\vec{P}_s|^2 - (M_d - E_s)^2$$

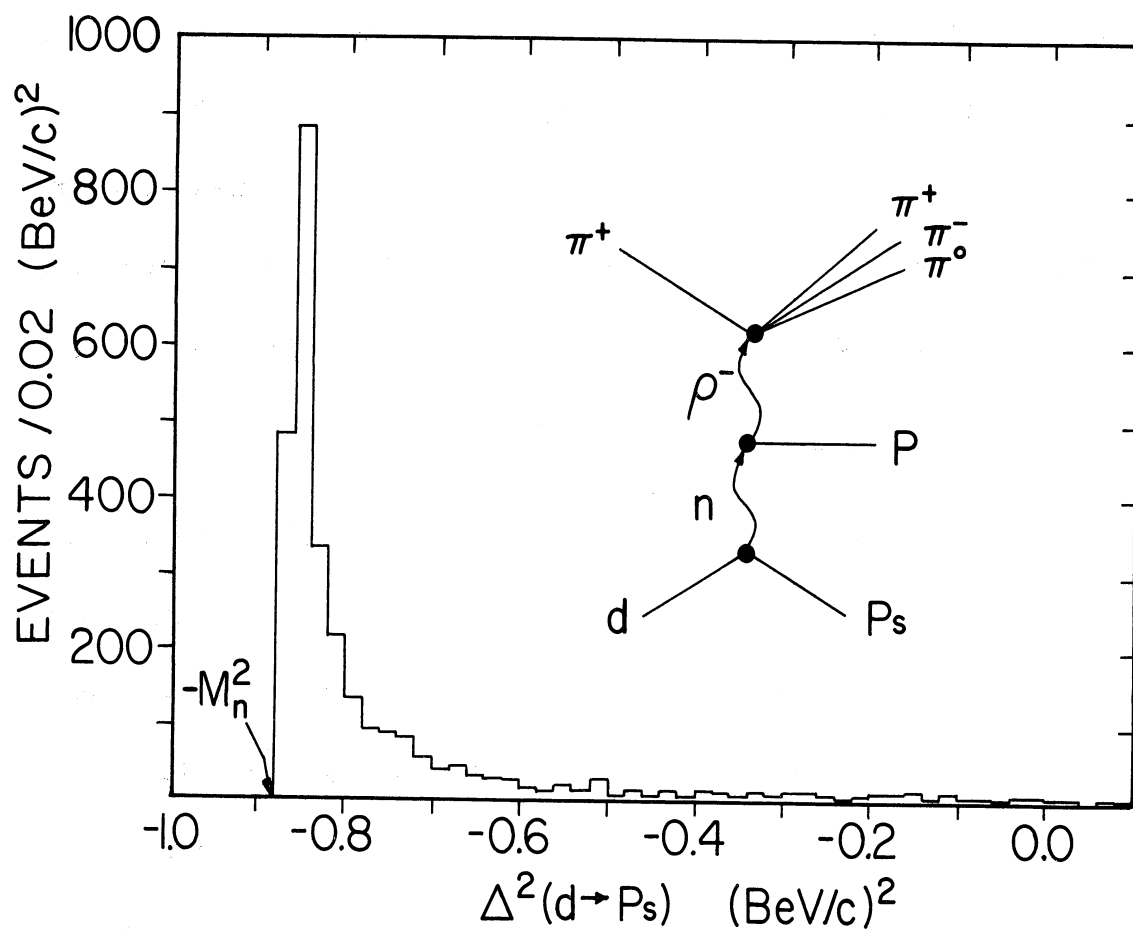


Figure 3. Momentum transfer distrib
slower proton. The diagram is a typ

$$\begin{aligned}
&= |\vec{P}_n|^2 - E_n^2 \\
&= -M_n^2.
\end{aligned}$$

This interpretation is somewhat difficult for $\Delta^2 > 0$ where the neutron has $\beta \geq 1$ and a Lorentz transformation to its rest frame would be impossible. (For the exchanged meson Δ^2 is always ≥ 0 .) The sharp rise of events near $\Delta^2 = -M_n^2$ is evidence for the nucleon exchange process. This also implies a preference for small values of $|\vec{P}_s|$ since the largest negative value of $\Delta^2(d \rightarrow p_s)$ is reached with $|\vec{P}_s| = 0$. The odd prong events (where the range of the spectator is too short to be measured) we have not included would thus fall into the bins nearest $\Delta^2 = -M_n^2$.

The incoming beam interacts with a moving neutron target. This means the center of mass system of the collision will vary depending on the momentum and angle of attack of the neutron. The range of center of mass energies found in the (π^0) reaction of this experiment is shown in Fig. 4. This is calculated from the invariant mass of all the outgoing particles except the spectator. The range of beam energies that would be needed to reach these same energies with a free nucleon target is shown above the drawing. The results of this experiment are thus an average over beam momenta from 3.0-4.5 BeV/c.

At this high energy most of the measured cross sections, density matrices, etc., should be sufficiently smoothly varying that our values averaged over center of mass energies will be approximately the value obtained with a stationary target and 3.65 BeV/c beam pion. There are two exceptions to this.

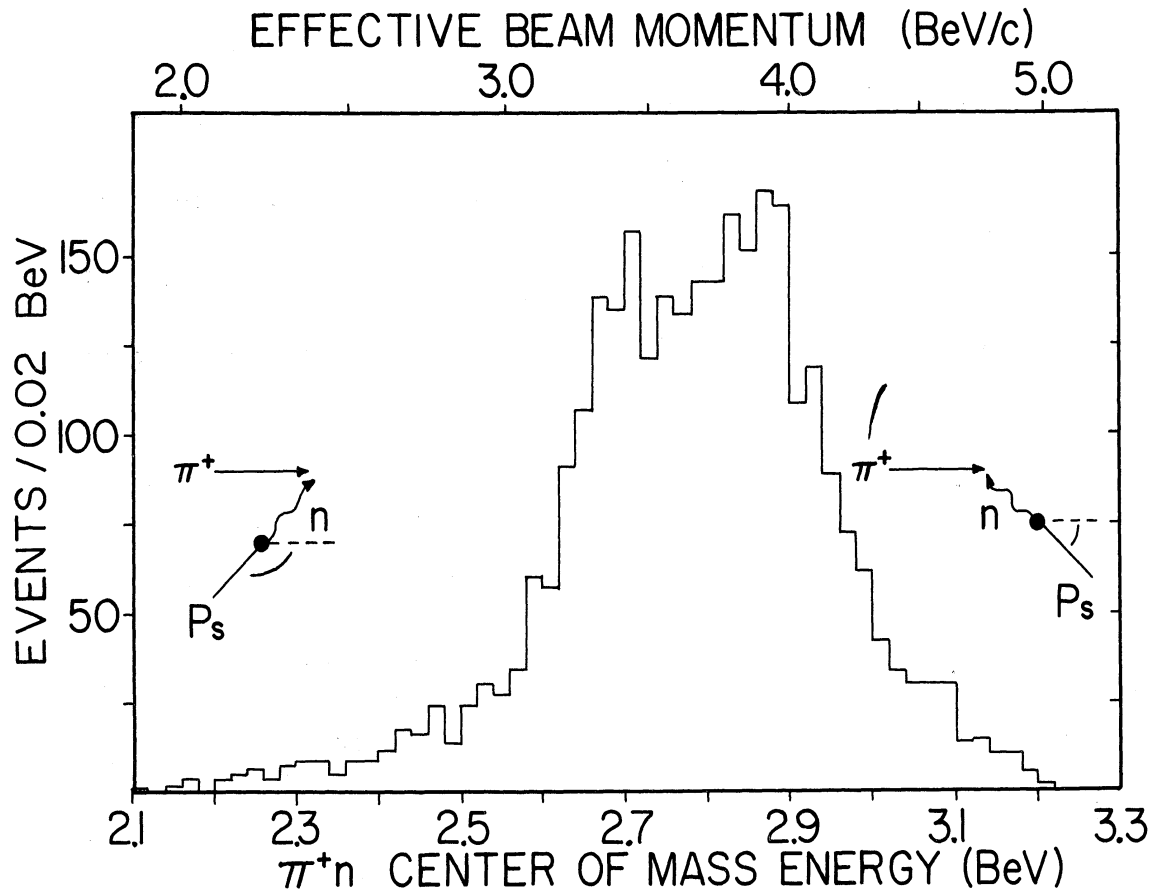


Figure 4. Distribution of center of mass energies found in this experiment. The upper scale shows the beam momentum needed to reach a given center of mass energy with a stationary target.

First, the phase space estimate for a fixed center of mass energy predicts that the invariant mass of any subgroup of particles will always be less than the center of mass energy less the sum of the masses of the remaining particles. A variable center of mass energy causes this kinematic limit to be variable and produces a high mass trail. To correct the phase space estimate we calculate a phase space for each of 14 equally spaced center of mass energies, weight each of these according to our observed center of mass energy distribution, and sum them. The result can be seen in Chapter IV.

The second variable that must be corrected is Δ^2 (beam-mesons). Again the highest value of Δ^2 at a given meson mass is limited by center of mass energy. If there were a backward peak (i.e., at a production angle of 180° and at Δ_{\max}^2) in the data at a given center of mass energy, it might not appear in a Δ^2 plot after the average over center of mass energies. To avoid this we plot instead the production angle in the center of mass ($\cos\theta^*$). The center of mass rest frame is defined to be that of all the outgoing particles except the spectator. Low values of Δ^2 are essentially independent of center of mass energy, and then either Δ^2 or $\cos\theta^*$ can be plotted.

D. THE SPECTATOR MOMENTUM DISTRIBUTION

In the spectator model, the momentum of the spectator is supposed to be unchanged by the collision. The spectator, therefore, emerges from the deuteron with the direction of motion and the Fermi momentum it had inside the deuteron. This momentum spectrum is given by the

Fourier transform of the radial wave function of the deuteron. For the Hulthen wave function the expected distribution (with arbitrary normalization) is

$$\frac{dW}{dP_s} = \left[\frac{1}{(\alpha^2 + P_s^2)} - \frac{1}{(\beta^2 + P_s^2)} \right] P_s^2.$$

In Fig. 5 the theoretical curves with $\beta = 7\alpha$ and $\beta = 5.18\alpha$ are shown with the data. The curves are normalized to the data at 125 MeV/c. We will discuss problems associated with this normalization in Chapter VI. The excess of spectators with momentum greater than 250 MeV/c over the Hulthen prediction has also been observed in $K^+d \rightarrow K^0pp$.²⁴ The authors attributed the discrepancy to double scattering in the deuteron.

E. SPECTATORS IN OTHER CHANNELS

To attempt to understand the spectator distribution of this channel we now compare it with other data from the two and four prong, two proton, channels of this experiment. In Fig. 6 we plot f , the fraction of observed spectators with momentum greater than 250 MeV/c less the estimated fraction from the Hulthen wave function of 0.09 (dashed line, Fig. 5). The particular value subtracted, which is uncertain because of uncertainty in the normalization and in the deuteron wave function, is not important as far as this study is concerned. It is only important that the spectator model predicts some value which is independent of the variables associated with meson production. The denominator of this fraction is all events with two observed protons. The points are plotted in the order of increasing numbers of pions in the final states for the

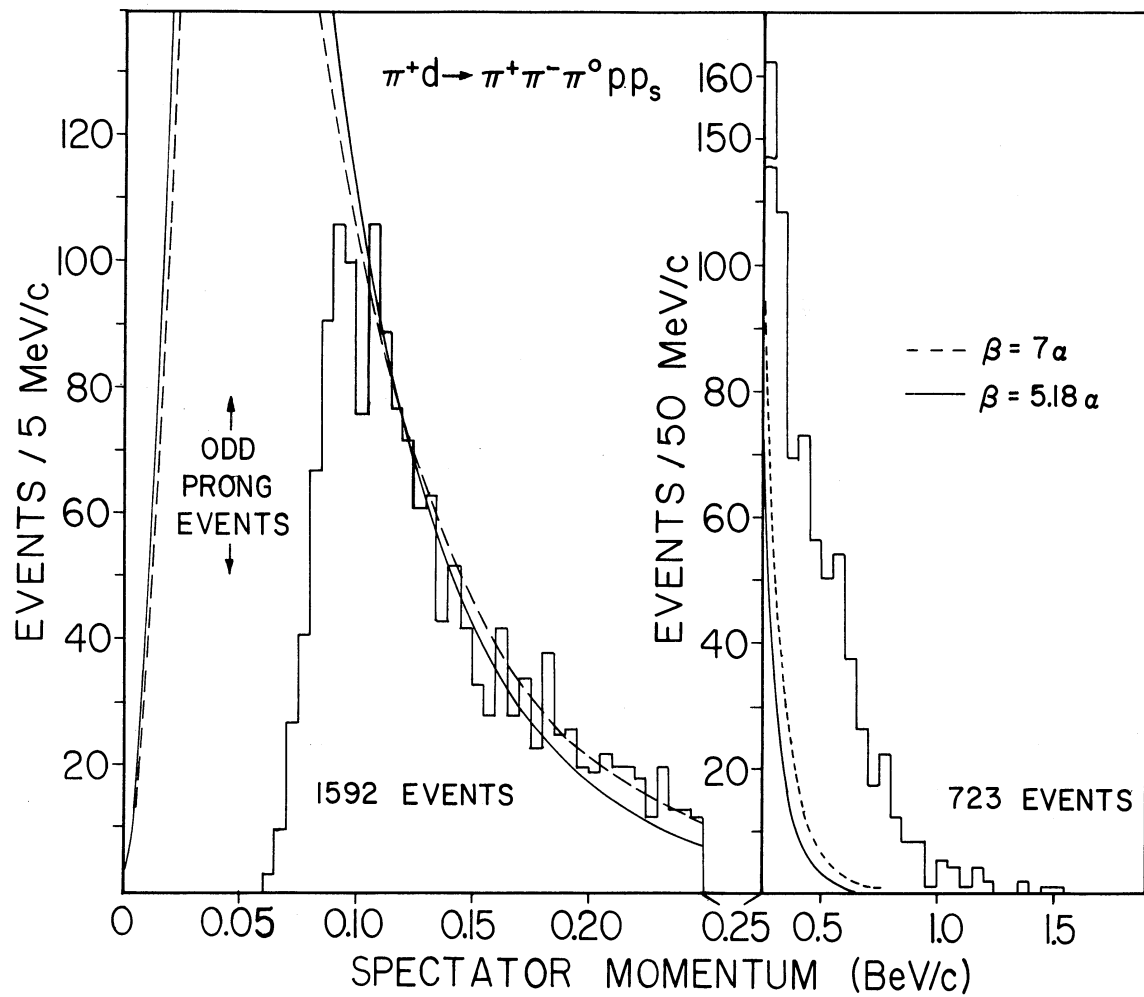


Figure 5. Momentum distribution of the slower proton. The theoretical curves are from the Hulthen wave function with values of $\beta = 5.18 \alpha$ (solid) and $\beta = 7 \alpha$ (dashed).

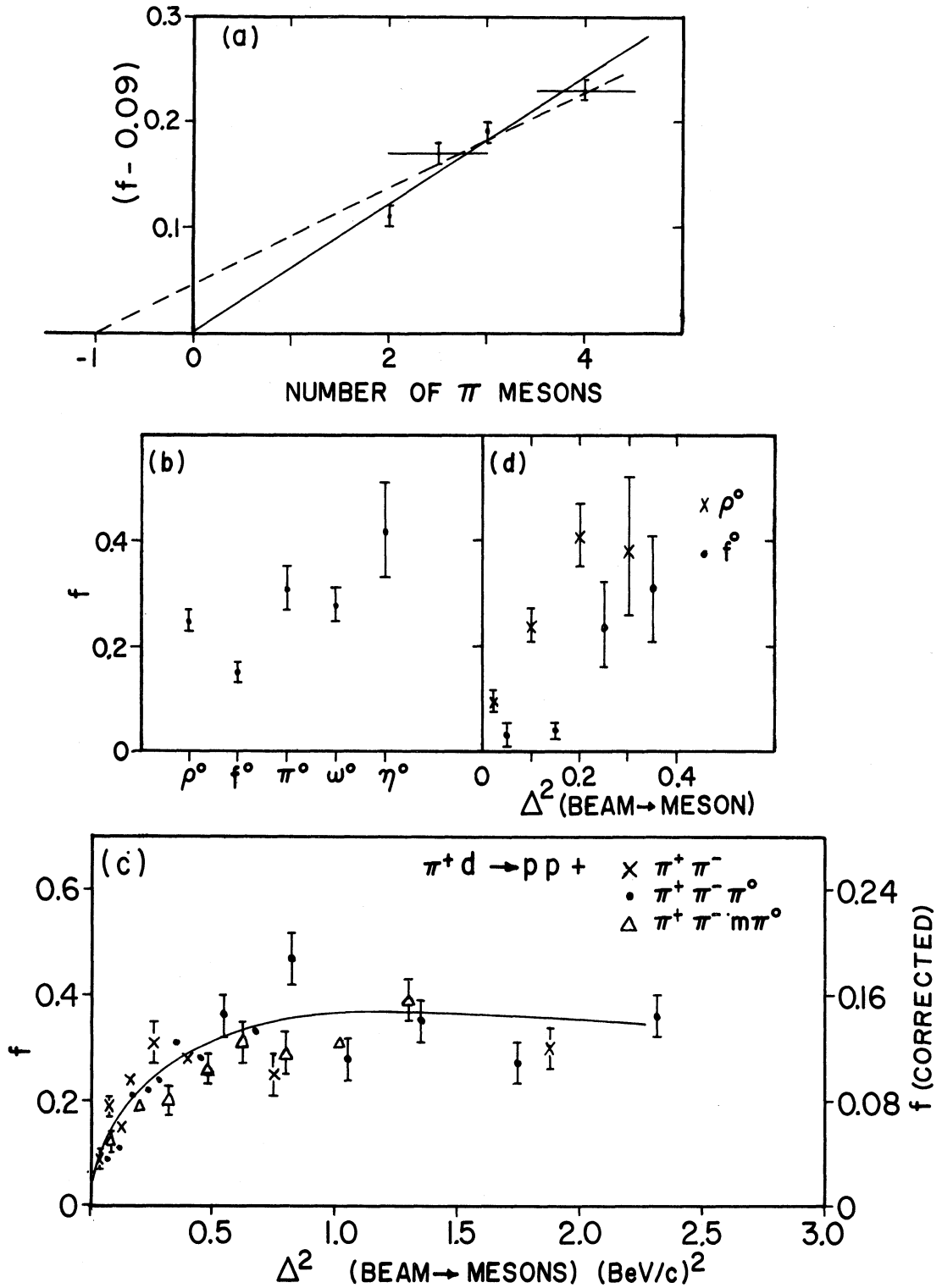
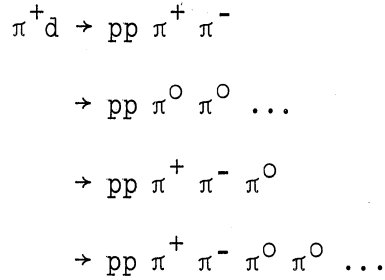


Figure 6. (a) The fraction of events with a spectator proton of momentum greater than 250 MeV/c, f , less the Hulthén prediction for $\pi^+ \pi^-$, $\pi \pi^0$, $\pi^+ \pi^- \pi^0$, and $\pi^+ \pi^- \pi \pi^0$ final states. (b) f for production of ρ^0 , f^0 , π^0 , ω^0 , and η^0 particles only. (c) f as a function of Δ^2 (beam \rightarrow mesons). (d) f as a function of Δ^2 (beam \rightarrow meson) for ρ^0 and f^0 production only. The smooth curve and lines are drawn arbitrarily.

reactions



The uncertainty in the average number of pions in the "no-fit" channels is indicated by the horizontal error bars. The fact that f depends on channel means that the upper vertex of the double exchange diagram (Fig. 3) cannot be neglected when the properties of the lower vertex are studied. As a consequence, the excess of high momentum spectators could not be fully understood even if the correct wave function for the deuteron were known. We emphasize that the scan was performed in the same way for the spectator protons for all these channels. The observed differences are a clear violation of the spectator model.

We therefore seek further properties of these high momentum spectators. Very naively, if these spectators were caused by a final state rescattering of the pions, then the spectator excess might be proportional to the number of pions in the channel. In this case a line through our data would intersect the x axis at zero pions if our subtraction of 0.09 were correct. Furthermore, if the struck proton also rescattered in the same manner as a pion, then the line would intersect at -1 pion. If the subtraction were based on the wrong deuteron wave function, then the intersection could be anywhere. It is remarkable that the results of Fig. 6(a)

can be extrapolated to zero pions. We show evidence below, however, that this result is probably an accident.

We now examine (see Fig. 6 (a)) the fraction of high momentum spectators for events of various channels in which a single meson is produced at the upper vertex: $\rho^0 \rightarrow \pi^+ \pi^-$, $f^0 \rightarrow \pi^+ \pi^-$, $\pi^0 \rightarrow \gamma\gamma$, $\omega^0 \rightarrow \pi^+ \pi^- \pi^0$, and $\eta^0 \rightarrow \pi^+ \pi^- \pi^0$ (or $\pi^+ \pi^- \gamma$). If each of these had a laboratory momentum of 3.5 BeV/c, then their mean laboratory decay lengths would be, in the same order: 7.3, 4.6, 1.4×10^9 , 73, and 3×10^8 F. Before traveling the mean deuteron diameter (3F), 48% of the f^0 , 34% of the ρ^0 , and 4% of the ω^0 mesons will decay. All of these reactions have negligible backgrounds.

If meson-proton final state scattering were the mechanism for producing the high momentum spectators, then the ρ^0 events should have more high momentum spectators than the π^0 events. This is partly because one fourth of the ρ^0 mesons will decay into two pions before reaching the spectator proton and partly because results from $\gamma p \rightarrow \rho^0 p$ seem to indicate that the ρ -p cross section is as much as three times as large as π -p cross sections.²⁵ We know the $\pi^0 p$ cross section from the relation based on charge independence,²⁶

$$\sigma_{el}(\pi^0 p) = \left[\sigma_{el}(\pi^+ p) + \sigma_{el}(\pi^- p) \right] / 2 - \sigma_{cex}(\pi^- p \rightarrow \pi^0 n) .$$

Since σ_{cex} is small at our energy, $\sigma_{el}(\pi^0 p)$ is nearly the same as $\sigma_{el}(\pi^+ p)$.

We see in Fig. 6 (b) that this is not the case. Further, if the conjecture of Biaľas²⁷ were correct, that the interaction radius of the

ω^0 and η^0 were smaller than π^0 , ρ^0 , etc., then ω^0 and η^0 production might be associated with fewer high momentum spectators. Again this is not the case.

All of these mesons have been produced and studied in hydrogen. This means that the properties of the upper two vertices alone are well known. The order shown in Fig. 6 (b) is in order of increasing average momentum transfer at the upper vertex. The ρ^0 and f^0 mesons are produced with differential cross sections that approximate elastic scattering. The lower kinematic limit for $\Delta^2(f^0)$ is slightly higher than that for $\Delta^2(\rho^0)$ so it ranks possibly higher in average momentum transfer. The π^0 and ω^0 mesons are produced with a differential cross section slope about half that of elastic scattering. The η^0 production slope is still flatter.

F. CONSTRAINT OF THE SPECTATOR MOMENTUM

The fact that the high momentum spectators are associated with mesons whose production mechanisms tend to deliver larger momentum transfers to the target suggests a simple kinematic explanation for the results of Figs. 6 (a,b). In hydrogen, if $\Delta^2(\text{beam} \rightarrow \text{meson})$ is known, the final momentum of the target proton $|\vec{P}|$ can be calculated from the expression

$$\Delta^2 \approx |\vec{P}|^2$$

which holds for small values of Δ^2 . It can be shown that the correspond-

ing relation in deuterium is*

$$\Delta^2 \approx |\vec{P}_1 + \vec{P}_2|^2$$

where \vec{P} is now replaced with the vector sum of the momenta of the two protons. If $\vec{P}_1 = -\vec{P}_2$, we see that $\Delta^2 = 0$, but there is no limit to the magnitude of P_1 and P_2 in this approximation. In Fig. 7 we show an event of this type ($\pi^+d \rightarrow \omega^0 pp$) with $\Delta^2(\text{beam} \rightarrow \omega^0) = 0.075 (\text{BeV}/c)^2$ and with protons of high momenta and oppositely directed. In Fig. 8 is another event with $\Delta^2(\omega^0) = 0.078 (\text{BeV}/c)^2$ again, but this time the protons are not in opposite directions and are thus kinematically limited. If $\vec{P}_1 = \vec{P}_2 = \vec{P}$, then the kinematic requirement

$$\frac{\Delta^2}{2} \approx |\vec{P}|^2$$

is even more severe than in hydrogen. The average limitation of the proton momentum may, therefore, be comparable to that in hydrogen. So we see that the $\pi^+\pi^-pp$ channel, which is nearly all low $\Delta^2(\text{beam} \rightarrow \pi^+\pi^-)$, may kinematically constrain its protons into fair agreement with the Hulthen curve.

We can make a prediction if the proton constraint explanation is correct. All of our channels should look the same if the spectator fraction, f , is plotted as a function of $\Delta^2(\text{beam} \rightarrow \text{mesons})$. Furthermore, other similar experiments in deuterium at any beam energy should lie on the

*The author is indebted to J. Vander Velde for pointing out this simple expression.

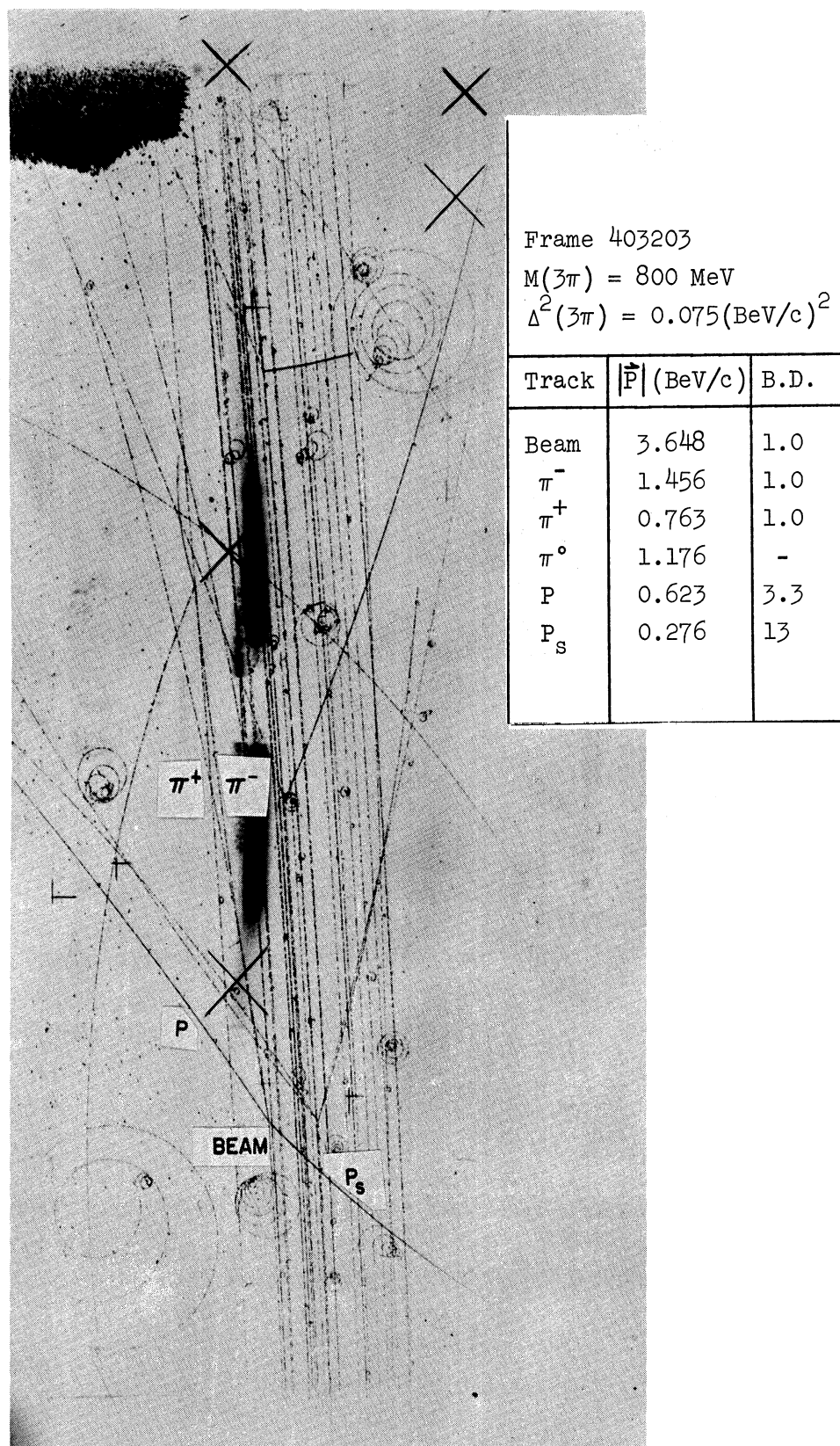


Figure 7. Sample event of the type $\pi^+d \rightarrow \omega^0 pp$ showing a high momentum pair of protons. The distance between the two vertical X marks on the center of the front glass window of the chamber is 4.7 in.

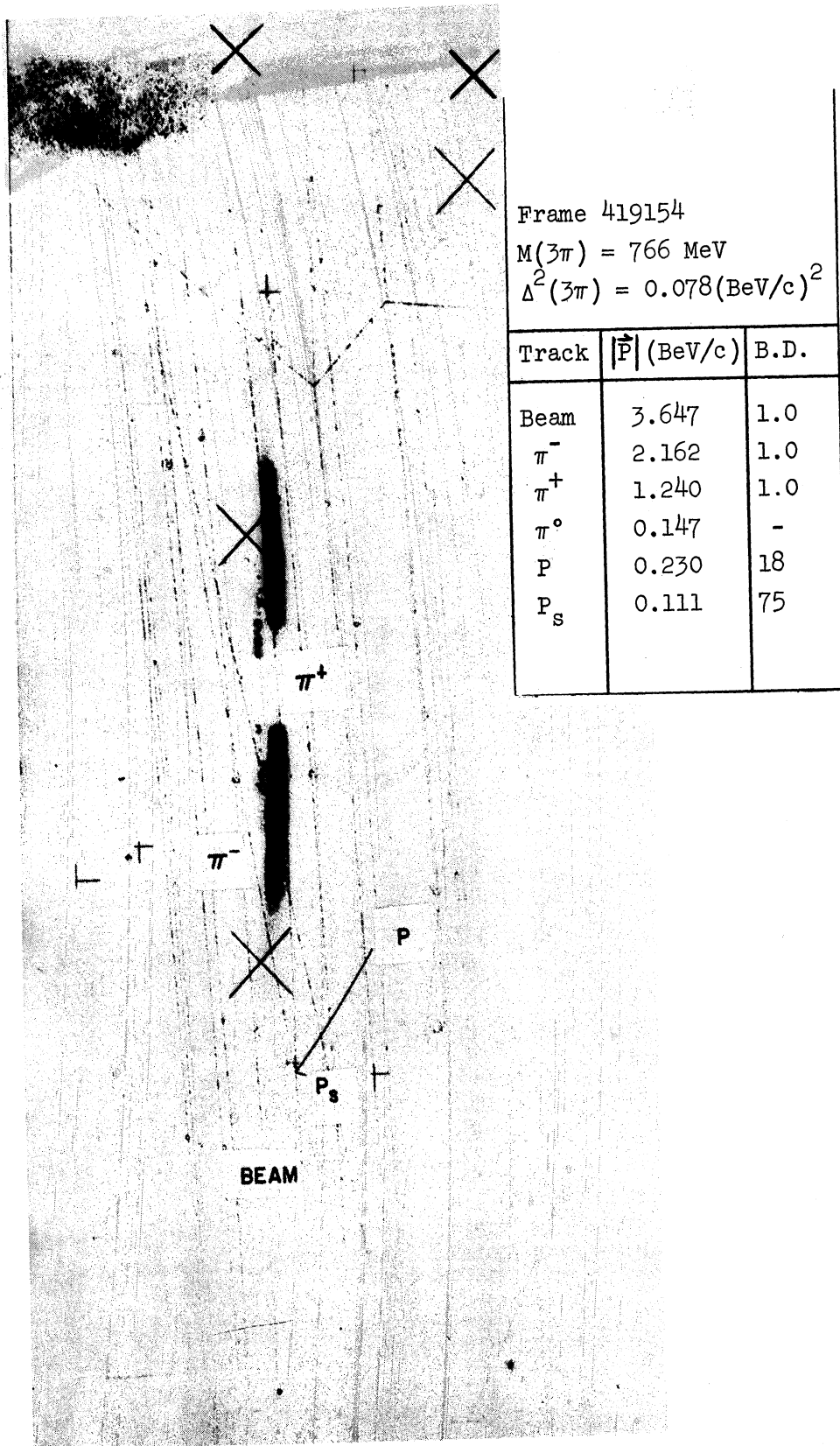


Figure 8. An event similar to Fig. 7 of the type $\pi^+d \rightarrow \omega^0 pp$ having the same Δ^2 (beam $\rightarrow \omega^0$) but having a low momentum pair of protons.

same curve. We see in Fig. 6 (c) that the $\pi^+\pi^-$, $\pi^+\pi^-\pi^0$, and $\pi^+\pi^-\pi\pi^0$ channels do indeed follow a single curve when plotted as a function of Δ^2 . The scale on the right side of the curve results from the application of two correction factors: one is for spectators with momentum above 250 MeV/c which were not scanned for in 17% of the film (1.17 ± 0.03), and the other is for the odd prong events which were not included $(2.89 \pm 0.17)^{-1}$. These factors would be important if one were to attempt any absolute prediction for f. The odd prong correction is discussed further in Chapter VI and in Appendix H.

We know of results from other experiments which also can be explained by proton constraint. Data from $K^+d \rightarrow K^0pp$ between 230 and 812 MeV/c showed excellent agreement with the Hulthen prediction for both even and odd prong events.²⁸ Since the maximum value of $\Delta^2(K^+ \rightarrow K^0)$ that was allowed at their highest beam momentum was $0.8 (\text{BeV}/c)^2$, the protons should be constrained.

The same channel at 2.3 BeV/c had many more high momentum spectators than predicted by the Hulthen curve, and those authors suggested that the excess might be evidence for double scattering.²⁴ The K^0 mesons cannot be produced by pion exchange; hence we expect a contribution from larger Δ^2 . Therefore, the spectators in this higher energy K^+ experiment should be similar to our events rather than following the Hulthen curve.

The reaction $\bar{p}d \rightarrow \bar{p}\pi^-pp$ had spectators which followed the Hulthen curve moderately well.²⁹ Since these events are produced presumably by

pion exchange, the protons should be constrained.

G. MESON-SPECTATOR SCATTERING

We have not yet fully explained the relative values of f for ρ^0 and f^0 production. We expected that f for the ρ^0 would be slightly lower than f for f^0 production if rescattering were unimportant, whereas in Fig. 6 (b) they are reversed. In Fig. 6 (d) we plot f for each meson as a function of $\Delta^2(\text{meson})$. We see that the values are very different at values of $\Delta^2 \cong 0.2 (\text{BeV/c})^2$.

The fact that f is small at low values of Δ^2 for each meson can be taken as evidence that the protons are somewhat constrained. We do not interpret the difference in the two curves as evidence for meson-proton final state scattering. The two reasons for this are based on Table I.

TABLE I

SPECTATOR FRACTIONS, $f(\%)$, FOR π^0, f^0, ρ^0 , AND ω^0 MESONS
(The data for " f^0 " is from a control region with $M(3\pi) = 1.15\text{-}1.35 \text{ BeV}$)

Δ^2 (BeV/c) ²	$\rightarrow X^0$		$\rightarrow \pi^+ \pi^-$		$\rightarrow \pi^+ \pi^- \pi^0$	
	π^0	f^0	ρ^0	f^0	ω^0	" f^0 "
0 - 0.1	31 \pm 10	3 \pm 3	17 \pm 3	3 \pm 3	19 \pm 6	3 \pm 7
0.1 - 0.2	30 \pm 10	9 \pm 3	32 \pm 4	4 \pm 2	28 \pm 7	10 \pm 3
0.2 - 0.3	33 \pm 11	17 \pm 5	37 \pm 8	24 \pm 8	31 \pm 7	26 \pm 5
0.3 - 0.4	25 \pm 15	28 \pm 9	36 \pm 13	31 \pm 10	46 \pm 12	26 \pm 6
0.4 - 0.5	33 \pm 19	31 \pm 15	25 \pm 12	25 \pm 12	27 \pm 9	32 \pm 7

First, contrary to our expectations, f for the π^0 meson is comparable to f for the ρ^0 meson. Second, examination of events in each of the three channels at either low mass or near the f^0 mass shows the same values of f and the same dependence of f on Δ^2 . It, therefore, appears that there is a single expression for all channels relating f to Δ^2 (mesons) and $M(\text{mesons})$. The strong mass dependence is a surprise to us and may hold the key to understanding the effects we have presented.

H. SUMMARY

While the above discussion has been speculative and will require further experimental and theoretical study, the results are interesting. We summarize the results as we interpret them.

- a) The tendency of some experiments and some channels to follow the Hulthen prediction can be understood if low values of Δ^2 (beam-mesons) kinematically limit the momentum of the outgoing protons. Agreement (or lack of agreement) with the Hulthen curve does not necessarily show that rescattering is negligible (or large).
- b) If rescattering effects are to be observed, studies must be made as a function of Δ^2 in order to subtract the effect of the kinematic limitation.
- c) The number of high momentum spectators depends only on Δ^2 (mesons) and $M(\text{mesons})$ and not on which mesons are produced.

- d) At low Δ^2 , the number of high momentum spectators decreases as the meson mass increases. We do not have an explanation for this behavior.

I. INDEPENDENCE OF THE MESON VERTEX

While we have shown conclusively that the upper vertex affects the deuteron vertex, we do not know to what extent the deuteron vertex affects the meson vertex. To partly answer this important question we cite experimental evidence from the channel $\pi^+d \rightarrow \pi^+\pi^-pp$ and its charge symmetric channel $\pi^-p \rightarrow \pi^+\pi^-n$ which has also been studied at 3.65 BeV/c by this laboratory.³⁰

In the present state of analysis, the effective masses and angular distributions, and the density matrix elements for the ρ^0 , are nearly identical (except for backgrounds) in these two channels.^{6,31} This suggests that the deuteron vertex has a negligible influence on meson production.

We also cite the fairly good agreement of our cross sections with charge symmetric data in Table II as further evidence. Similar agreement has been reported at 1.7 BeV/c.^{3,32} We note, however, that our result for $\pi^+d \rightarrow \pi^+\pi^-pp$ is more than two standard deviations below the π^-p data. If our cross section is correct, it shows either that the spectator proton does affect meson production, or that the one-constraint fit to the neutron allows more background than estimated by the experimenters in these hydrogen experiments.

TABLE II

COMPARISON OF CROSS SECTIONS FROM THIS EXPERIMENT
WITH CHARGE SYMMETRIC FREE NUCLEON DATA

Reference	Beam (BeV/c)	Reaction	Cross Section (mb)
a	3.0	$\pi^-p \rightarrow \pi^+\pi^-n$	3.2 ± 0.1
b	3.63	$\pi^-p \rightarrow \pi^+\pi^-n$	$4.33^{+0.22}_{-0.98}$
c	4.0	$\pi^-p \rightarrow \pi^+\pi^-n$	3.16 ± 0.13
This	3.65	$\pi^+d \rightarrow \pi^+\pi^-pp$	2.58 ± 0.21
a	3.0	$\pi^-p \rightarrow \pi^+\pi^-n(m\pi^0)$	6.8 ± 0.2
c	4.0	$\pi^-p \rightarrow \pi^+\pi^-n(m\pi^0)$	5.57 ± 0.17
This	3.65	$\pi^+d \rightarrow \pi^+\pi^-pp(m\pi^0)$	6.32 ± 0.47
d	3.65	$\pi^-p \rightarrow n(m\pi^0)$	1.97 ± 0.07
This, e	3.65	$\pi^+d \rightarrow pp(m\pi^0)$	1.95 ± 0.19

- a. V. Hagopian, dissertation (University of Pennsylvania, 1963); V. Hagopian (private communication, 1965).
- b. Y. Lee, W. Moebs, B. Roe, D. Sinclair, and J. Vander Velde (submitted to Phys. Rev., 1966).
- c. L. Bondar, et al., Aachen-Birmingham-Hamburg-London (I.C.)-München Collaboration, Nuovo Cimento 31, 731 (1964).
- d. P. Yamin (private communication, 1966) from the counter experiment of M. Feldman, et al., Phys. Rev. Letters 14, 869 (1965). The result has been reduced 10% to account for undetected strange V's. See T. Wangler, A. Erwin, and W. Walker, Phys. Rev. 137, B414 (1965) and J. Bartsch, et al., Aachen-Hamburg-London (I.C.)-München Collaboration (unpublished preprint).
- e. Our result has been increased by 20% to account for undetected high $\Delta^2(d \rightarrow pp)$ events and reduced by 4% to account for strange V's decaying to all neutrals and K^+ mesons mistaken for protons.

J. GLAUBER SCREENING

We do know of two corrections that should be made to deuterium data. We will show that they are small enough to be neglected. The first correction (Glauber screening) has been observed experimentally, while the second (Pauli exclusion) has not. We will show that the exclusion could be detected with present experimental techniques.

Glauber suggested in 1955 that the screening of one nucleon by the other in the deuteron could reduce the total deuterium cross section below the expected sum of cross sections on free nucleons.³³ Experimentally at our energy³⁴ (using π^-p for π^+n by charge symmetry)

$$\begin{aligned}\sigma(\pi^+d) &= 57.0 \pm 0.1 \\ \sigma(\pi^+p) + \sigma(\pi^-p) &= \underline{58.5 \pm 0.2} \\ \text{net} &= -1.5 \pm 0.3 \quad .\end{aligned}$$

The cross section defect is $2.6 \pm 0.5\%$ of the total π^+d cross section.

The theoretical expression of Glauber is

$$\sigma_d = \sigma_p + \sigma_n - \langle 1/r^2 \rangle (\sigma_p \sigma_n / 4\pi)$$

where $\langle 1/r^2 \rangle$ is the average value of r^{-2} in the deuteron (r is the distance between the centers of the two nucleons). This expression can be derived by considering the nucleons as black spheres with geometrical cross sections equal to one half the total cross section or derived from diffraction theory.

Very recently it has been shown that Glauber's expression was not charge invariant and therefore incorrect.³⁵ The corrected result (for $\pi^{\pm}d$) is

$$\sigma_d = \sigma_p + \sigma_n - \langle 1/r^2 \rangle \left[\sigma_p \sigma_n - \frac{1}{4} (\sigma_p - \sigma_n)^2 \right] / 4\pi .$$

At our energy, the correction term is small compared to $\sigma_p \sigma_n$, $(\sigma_p - \sigma_n)^2 / (4 \sigma_p \sigma_n) = 0.0026$. Also recently it has been suggested that experimental studies of total cross section defects might test whether or not high energy elastic scattering can be described by exchange of Regge trajectories.³⁶ These two examples show that there is contemporary interest in this problem.

It is not known at present exactly how this defect is to be apportioned to the various channels in the π^+d reaction. It is somewhat plausible that the correction to any one channel will be at most (plus or minus) twice the total defect, i.e., $\pm 5.2\%$, which we have neglected. Sitenko, for example, has suggested that the scattering part of the cross section (elastic plus break up) will be slightly enhanced while the absorption cross section will be reduced by slightly more than the total observed defect.³⁷

K. PAULI EXCLUSION

A Pauli exclusion correction should be applied to this channel to correct for Pauli exclusion of certain angular momentum final states between the two protons. While the effect makes a negligible difference in the total cross section, it greatly affects the events with

$$\Delta^2(d \rightarrow pp) < 0.1 \text{ (BeV/c)}^2.$$

As previously pointed out^{24,12} in the analysis of $K^+d \rightarrow K^0pp$, the differential cross section in deuterium including the Pauli effect is given by:

$$\begin{aligned} d\sigma/dt = & [1-H(t)] (d\sigma/dt)_{nf} \\ & + [1-(1/3) H(t)] (d\sigma/dt)_f, \end{aligned} \quad (1)$$

where $(d\sigma/dt)_{nf}$ and $(d\sigma/dt)_f$ are the free neutron cross sections for non-flip and spin flip respectively. The deuteron form factor, $H(t)$, is given by $H = \int \psi^*(\vec{r}) \exp(-i\vec{q} \cdot \vec{r}) \cdot \psi(\vec{r}) d\vec{r}$, where ψ is the deuteron spatial wave function, and \vec{q} is the difference between the initial and final meson momenta in the laboratory.

If the Hulthen wave function is used to calculate $H(t)$, then one obtains¹²

$$\begin{aligned} H(t) = & [u(2\alpha) - 2u(\alpha+\beta) + u(2\beta)] (\alpha+\beta) \\ & \cdot 2\alpha\beta(\alpha-\beta)^{-2} / \sqrt{-t}, \end{aligned}$$

$$\text{with } u(x) = \tan^{-1} (\sqrt{-t}/x)$$

$$\text{and } \alpha = 0.0455 \text{ BeV.}$$

The dependence of $H(t)$ on the choice of wave function is illustrated in Fig. 9 (a) where the upper curve has $\beta = 7\alpha$, the middle curve has $\beta = 5.18\alpha$, and the lower curve, G , is $H(t)$ calculated from the four parameter fit of the Gartenhaus wave function by Moravcsik.^{15,38}

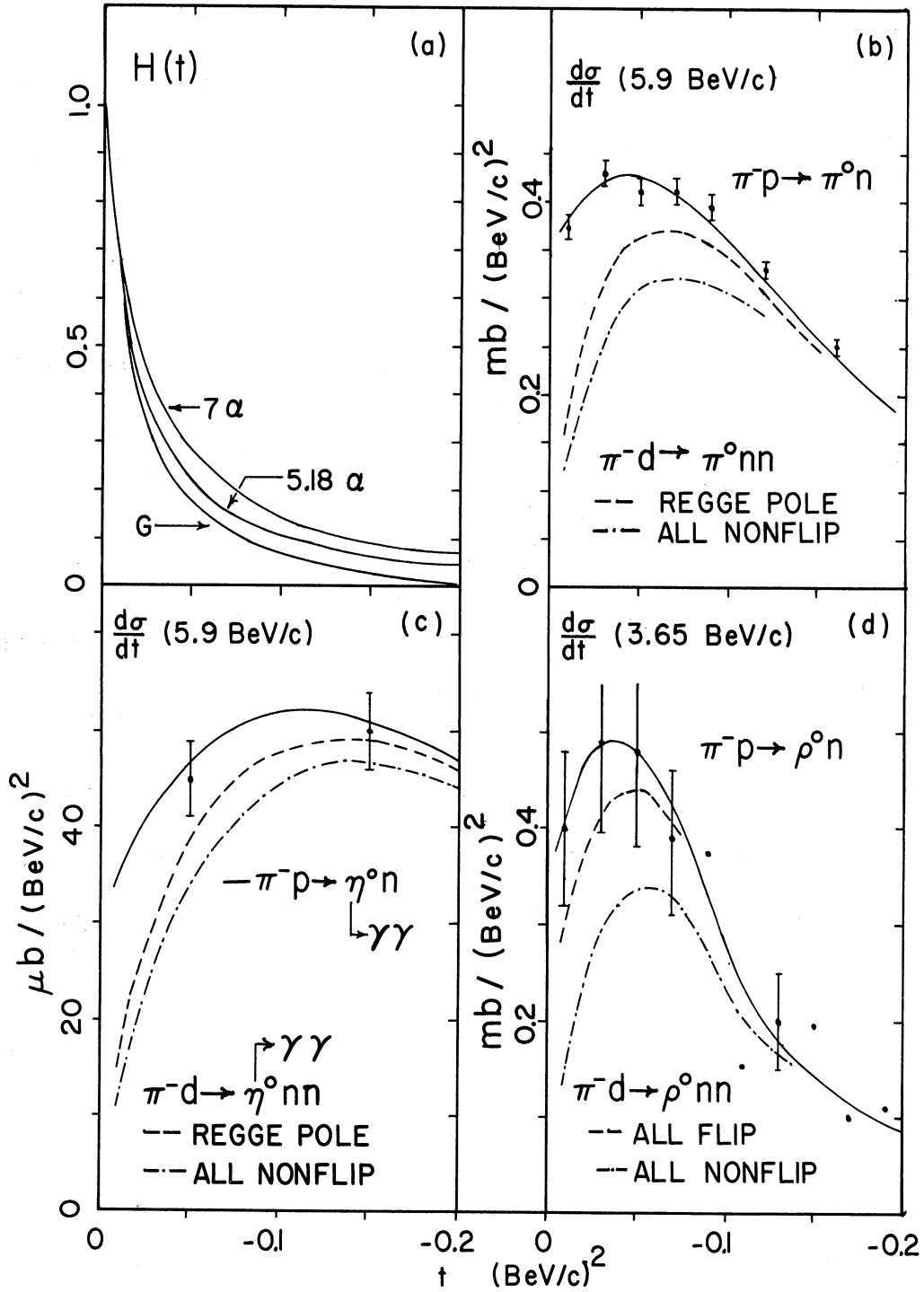


Figure 9. (a) plot of $H(t)$ as a function of the four-momentum transfer squared between the beam and the produced meson. curves 7α and 5.18α are calculated from the Hulthen wave function, and G is from the Gartenhaus wave function. (b), (c) Prediction for $\pi^-d \rightarrow \pi^0nn$ and $\pi^-d \rightarrow \eta^0nn$ based on the Regge pole model and the Hulthen wave function. The solid curves are the fits to the data by Phillips and Rarita. (d) Prediction for $\pi^-d \rightarrow \rho^0nn$ shown separately for all spin flip and all spin nonflip. The solid curve is arbitrary.

The derivation of (1)¹² uses the closure approximation to evaluate terms containing the final state two-proton wave functions. The effect of the Pauli exclusion principle is included, but final state interactions have been ignored. Expression (1) should apply to any charge exchange process, but to express (2) in terms of (t) , we have assumed a negligible difference in the free nucleon center of mass momenta before and after the collision. Studies of final state interactions and various other forms for $\psi(\vec{r})$ may be found in the literature.^{12,13,38}

Equation (1) can be understood intuitively at $t = 0$ where $H(t)=1$. There the final state protons will have the same orbital angular momentum they had before the collision ($L=0$ if we neglect d-wave). If there is no spin flip, the final state total spin of the two protons will still be $S=1$ (i.e., the spin of the deuteron is one). Pauli exclusion forbids this state entirely, which explains why there is no nonflip contribution at $t=0$.

The unpolarized deuteron can be described as three states of nucleon spin, up-up, down-down, and up-down plus down-up. If a spin is flipped in each of these states, only the third state must remain a state of $S=1$ and again forbidden. This gives the $1-1/3$ factor in equation (1). If, as is usually assumed, the entire spin flip contribution in hydrogen vanishes at $t = 0$, then our differential cross section must vanish at $t = 0$ in deuterium.

To aid in calculation we define the deuterium reduction factor, R , to be

$$R = (\mathrm{d}\sigma/\mathrm{d}t)_{\text{deuterium}} / (\mathrm{d}\sigma/\mathrm{d}t)_{\text{hydrogen}} ,$$

and the nonflip fraction to be

$$r = (\mathrm{d}\sigma/\mathrm{d}t)_{\text{nf}} / \left[(\mathrm{d}\sigma/\mathrm{d}t)_{\text{nf}} + (\mathrm{d}\sigma/\mathrm{d}t)_{\text{f}} \right] .$$

A rearrangement of (1) gives

$$R = 1 - H(t)[(1 + 2r)/3] .$$

In order to correct deuterium cross sections, one can either take the extreme values of $r(t)$ ($0 \leq r \leq 1$) or use model dependent values. The recent study of Phillips and Rarita of πN and KN data in terms of the Regge pole model provides model dependent values for reactions $(\pi^+ d \rightarrow \pi^0 pp)^{39}$ and $(\pi^+ d \rightarrow \eta^0 pp)^{40}$. They assume the production mechanisms are ρ exchange and A_2 exchange respectively. The values of r calculated from their formulae are shown in Table III.

It is interesting to note that the cross section reduction could be measured in deuterium with present experimental techniques. We show in Figs. 9(b,c,d) the expected results (dashed curves) for π^0 , η^0 , and ρ^0 production with $\beta = 7\alpha$ used for $H(t)$. The experimental data is from $\pi^- p$ experiments.^{41,42,30} For ρ^0 production by pion exchange, one expects all spin flip ($r = 0$). The dot-dashed curves show the all nonflip prediction of $r = 1$.

To estimate the cross section reduction for the (π^0) channel we use R_{pex} from Table III. We assume a flat differential cross section in hydrogen

TABLE III

VALUES USED TO PREDICT THE EFFECT OF PAULI EXCLUSION ON THE
DEUTERIUM CROSS SECTION. R IS THE REDUCTION AND r IS
THE FRACTION OF THE CROSS SECTION WHICH IS SPIN NONFLIP

Δ^2 (BeV/c) ²	$H(t)$ (5.18 α)	η^0 $r_{A_{2ex}}$	π^0 $r_{\rho_{ex}}$	$r = 1$ R_{nf}	$R_{A_{2ex}}$	$R_{\rho_{ex}}$	$r = 0$ $R_{\pi_{ex}}$
0	1	1	1	0	0	0	.667
.01	.608	.80	.71	.392	.472	.509	.797
.02	.434	.67	.55	.566	.661	.696	.855
.03	.333	.60	.41	.667	.756	.795	.889
.04	.267	.54	.32	.733	.815	.854	.911
.05	.220	.50	.26	.780	.854	.889	.927
.06	.185	.44	.21	.815	.883	.912	.938
.07	.159	.40	.16	.841	.905	.930	.947
.08	.138	.36	.13	.862	.921	.942	.954
.09	.117	.34	.10	.883	.934	.953	.961
.10	.104	.31	.08	.896	.943	.959	.965
.15	.062	.25	.01	.938	.969	.979	.979
.20	.041	.20	.00	.959	.980	.986	.986
.25	.030	.18	.01	.970	.986	.990	.990
.30	.022	.16	.06	.978	.991	.992	.993

for $\Delta^2 < 0.2$ (BeV/c)² which gives $\bar{R} = 0.8$ for $\Delta^2 < 0.1$ and $\bar{R} = 0.97$
for $0.1 < \Delta^2 < 0.2$ (BeV/c)². This amounts to about 47 events lost to
exclusion or a 1.6% reduction in total cross section for which we have
not corrected. Since the differential cross section probably drops in
hydrogen, due to the kinematic limits at low Δ^2 and due to the lack of
highly peripheral processes, the loss should be even less than this value.

CHAPTER III

EVENT IDENTIFICATION

A. VALIDITY TESTS FOR $\pi^+\pi^-\pi^0$ pp

A general description of the identification rules and the kinematic fitting process used in this experiment is given in the Appendix. In brief, we define a good (π^0) event as one having a χ^2 probability and the bubble density of all tracks consistent with the $\pi^+\pi^-\pi^0$ hypothesis. If the event is also consistent with the hypothesis $\pi^+\pi^-\pi^0$, we assume it has no π^0 . If a proton cannot be identified by bubble density (i.e., if its momentum is greater than 1.7 BeV/c or if it is highly dipped relative to the film plane), then the event is "good" if it does not fit the $\pi^+\pi^+\pi^-\pi^0$ reaction. If it also fits a missing neutron, it is called "ambiguous" and is dealt with specifically in Section C of this chapter.

The same rules were used to identify the (pn) reaction; however, we do not attempt a fit to $\pi^+\pi^+\pi^-\pi^0$ since the presence of two nucleons is guaranteed by baryon conservation. Because we require only that the χ^2 probability be greater than 2%, the distributions of χ^2 and the missing mass distributions can be compared to the theoretical distributions to test both our error estimates and our event selection procedure.

A.1 Missing Mass Distribution

The missing mass squared for the good (π^0) events is shown in Fig.

10 (a).^{*} Because most of the events were positively identified by bubble density (85%), the chief contaminating reaction is expected to be $\pi^+ d \rightarrow \pi^+ \pi^- pp \pi^0 \pi^0$. These events will tend to have a positive missing mass whereas the single π^0 events should be symmetric about $M(\pi^0)^2 = 0.0182 \text{ BeV}^2$. The events which remain after a subtraction of events with (missing mass squared) $MM^2 < 0.02 \text{ BeV}^2$ from those with $MM^2 \geq 0.02 \text{ BeV}^2$ is shown in Fig. 10 (b). There are in fact 336 more events with $MM^2 \geq 0.0182 \text{ BeV}^2$ than below. The fact that these contaminating events first appear near the $2\pi^0$ threshold (0.073 BeV^2) supports our conclusion that 11% of the events assumed (π^0) are really $\pi^+ \pi^- pp \pi^0 \pi^0$. (The sharpness of the rise at the $2\pi^0$ threshold must be regarded as a statistical accident in view of our measuring error estimates for missing mass squared.)

If these 336 events really have two rather than one π^0 , then the "no-fit" reaction $\pi^+ d \rightarrow \pi^+ \pi^- pp(m\pi^0)$, $m \geq 2$, must be lacking these events.

A comparison of the missing mass spectrum for the no-fit events with phase space shows that roughly this number of events is missing from the low mass end of the spectrum.

No effort has been made to remove these contaminating events from the events used in this study. Their distribution should be roughly the same as the distribution of the non-resonant events with a single π^0 missing. This is because

* The events used in this chapter are from a sample which is slightly reduced in size (2924 (π^0), 1754 (pn), and 504 ambiguous events). This happens because the χ^2 , missing mass, etc., information was not available on magnetic tape for some events due to difficulties in the initial stages of the event processing.

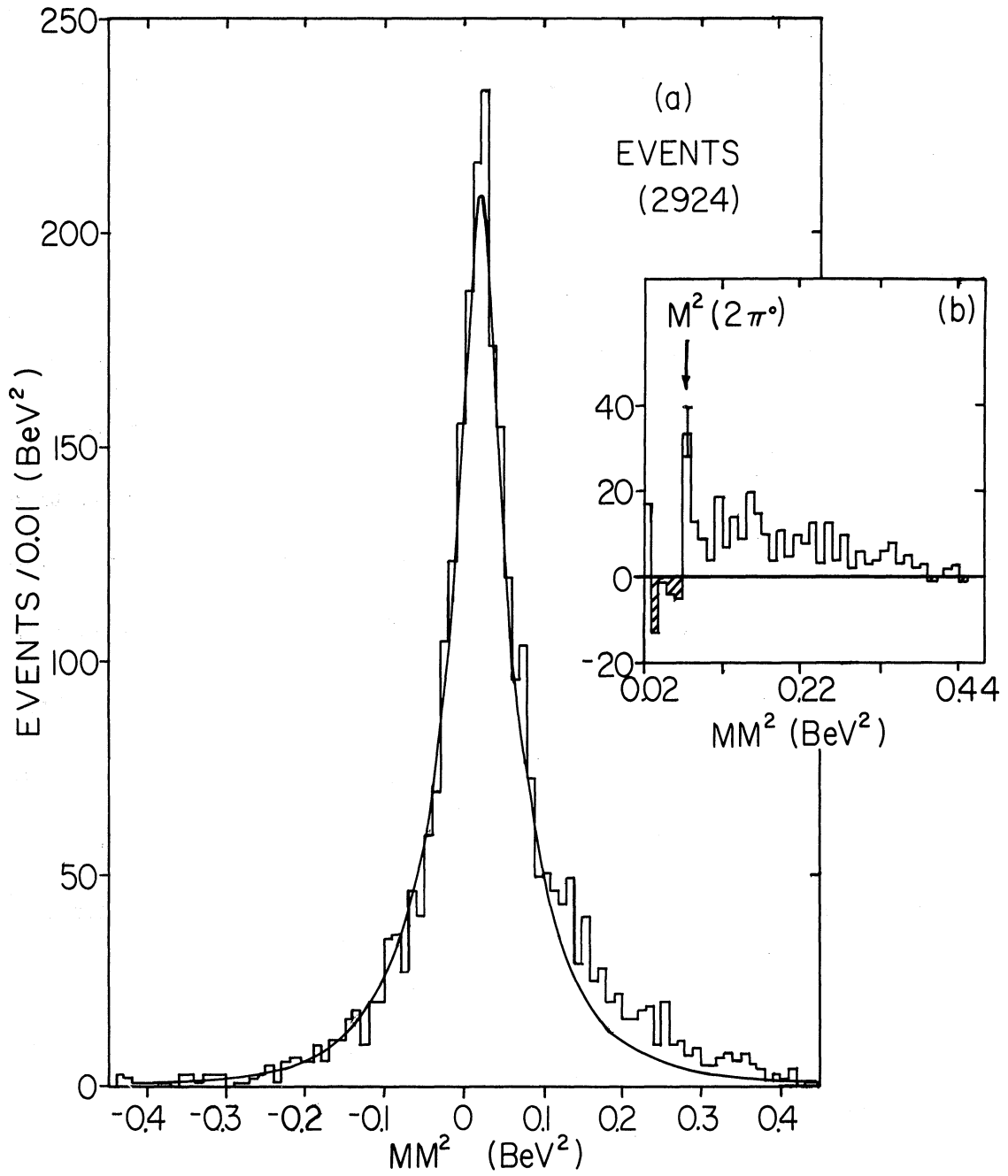


Figure 10. (a) The missing mass squared distribution for the events identified as (π^0) . The solid curve is the corrected resolution function. (b) The distribution resulting from a subtraction of the events with $MM^2 < 0.02 \text{ BeV}^2$ from those with $MM^2 \geq 0.02 \text{ BeV}^2$.

- a) the effective mass of the two π^0 mesons is limited to small values by the requirement that it fit a single π^0 hypothesis, and
- b) no strong resonant behavior has been observed in the no-fit events which do not fit the single π^0 hypothesis.

Assuming the remaining events are relatively free from badly identified events, we may compare our experimental distribution to a resolution function (Fig. 10 (a)). The resolution function is constructed in SUMX⁴⁴ by adding together Gaussians of unit area with standard deviation equal to the error in missing mass squared as calculated by GRIND⁴⁵ from the measurement errors as estimated by TRED.⁴⁶ Each Gaussian is centered at $M^2(\pi^0)$. The sum of these Gaussians should match the MM^2 distribution if the error in each event has been correctly assessed. The area of the resolution function in the figure is set equal to the estimated number of events with a single π^0 missing (2588) rather than the total number of events in the plot.

We find that the errors as estimated by our version of TRED are somewhat too large. The χ^2 probability that the uncorrected resolution function fits the data between $-0.2 \leq MM^2 \leq 0.0 \text{ BeV}^2$ is less than 0.01%. The curve shown in Fig. 10 (a) is the corrected resolution function which is produced when the estimated errors are all multiplied by $1/\alpha = 1/1.2$. The χ^2 probability for the corrected curve is 50% in the same mass squared interval. We have made plots with various values of α and from these conclude that we have overestimated our errors by $\alpha = 1.2 \pm 0.1$.

We wish to point out that although one might guess that the π^0 resolution function would be Gaussian in shape, it instead seems to be rather well reproduced by an s-wave Breit-Wigner curve.⁴⁷ A comparison of the π^0 resolution function and Gaussian and Breit-Wigner forms, all with the same full width at half maximum, is shown in Fig. 11.

A.2 Chi-Squared and Probability Distributions

The values of χ^2 resulting from the one-constraint fit to the mass of the π^0 are shown in Fig. 12. The distribution should follow the equation

$$N \Delta \rho'(\chi^2) = N \Delta \alpha^2 \rho(\alpha^2 \chi^2) \equiv \frac{N \Delta \alpha^2 e^{-(\alpha^2 \chi^2)/2}}{(2 \pi \alpha^2 \chi^2)^{1/2}} \quad (1)$$

for a one-constraint fit. This equation is obtained from the usual equation for the χ^2 distribution by replacing χ^2 with $\alpha^2 \chi^2$. Here N is the total number of events, Δ is the bin width on the graph, and α is the scale factor which takes into account malassignment of errors. The normalization factor α^2 is then chosen so that

$$\int_0^{\infty} \rho'(\chi^2) d\chi^2 = \int_0^{\infty} \rho(\chi^2) d\chi^2 = 1.$$

The factor $N \Delta$ then normalizes the distribution to the total area of our histogram. The curve shown in Fig. 12 is the expected distribution with errors properly estimated (i.e., $\alpha = 1$). It is in moderate agreement with the data. The theoretical average value of χ^2 calculated from ρ' is given by

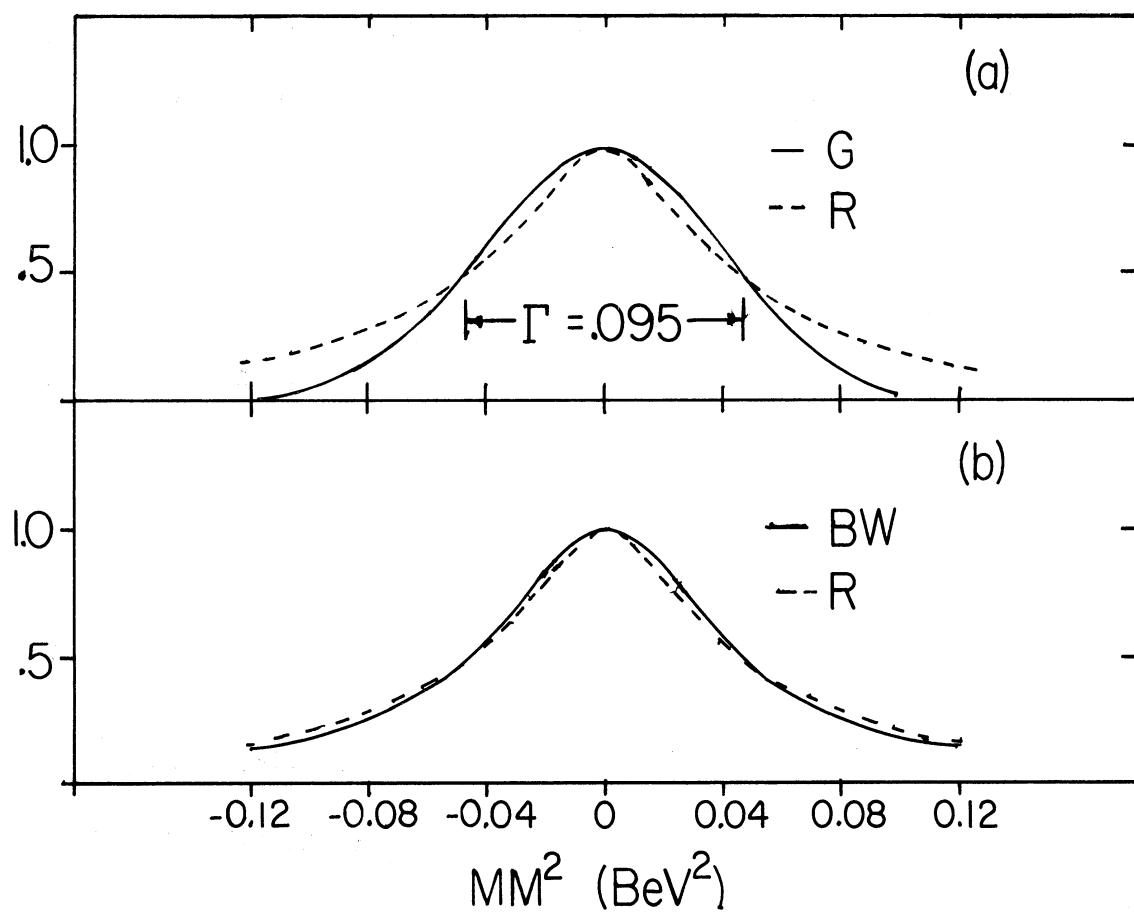


Figure 11. (a) Comparison of Gaussian (G) and r curves. (b) Comparison of Breit-Wigner (BW) and curves.

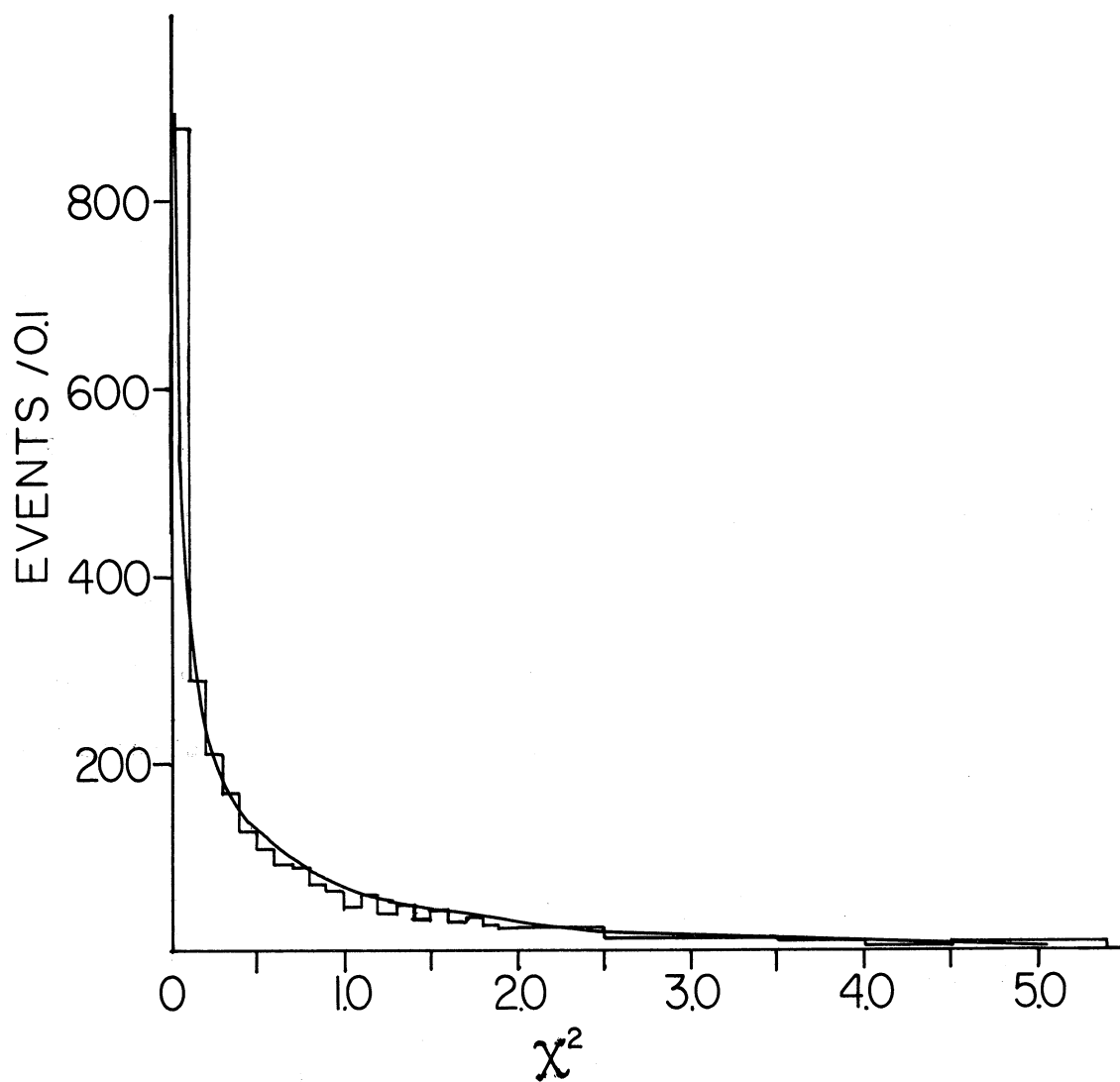


Figure 12. (a) Distribution of χ^2 for the unique (π^0) events. The solid curve is the theoretical curve for properly estimated errors.

$$\begin{aligned}
\int_0^{\infty} \chi^2 \rho'(\chi^2) d\chi^2 &= \frac{1}{\alpha^2} \int_0^{\infty} \alpha^2 \chi^2 \rho(\alpha^2 \chi^2) d\alpha^2 \chi^2 \\
&= \frac{1}{\alpha^2} \int_0^{\infty} y^2 \rho(y^2) dy^2 \\
&= \frac{n}{\alpha^2}
\end{aligned}$$

where n is the number of constraints in general, but is equal to one for our case as can be shown by explicitly integrating formula (1).

Using the histogram of χ^2 as a weighing factor, we obtain $\bar{\chi}^2$ (experimental) = 1.0. This implies $\alpha^2 = 1$, which contradicts our previous determination of α from the resolution curve. This discrepancy is caused by the $2\pi^0$ events which tend to give more weight to large values of χ^2 than the theoretical curve would. This can best be seen by plotting the probability for all events (Fig. 13 (a)) separately for the sample of events with $MM^2 \leq 0.0182 \text{ BeV}^2$ (Fig. 13 (b)). The expected distribution in probability is

$$N\Delta \rho(P) = N\Delta \alpha^2 \rho(\alpha^2 \chi^2) / \rho(\chi^2) = N\Delta \alpha^2 e^{-(\alpha^2-1)\chi^2/2} \quad (2)$$

where N is the total number of events and Δ is the bin size. This may be derived by equating $-\rho(P)dP = [\alpha^2 \rho(\alpha^2 \chi^2)] d\chi^2$ and calculating $dP/d\chi^2$ from the formula used by GRIND to convert χ^2 to probability:

$$P(\chi^2) = \int_{\chi^2}^{\infty} \rho(\chi'^2) d\chi'^2 .$$

For $\alpha = 1$ the distribution is a constant (i.e., a straight line).

The curves shown in Fig. 13(b) are calculated from equation (2) with $\alpha = 1.0$ and 1.2 . The agreement with the $\alpha = 1.2$ curve is reasonable. Comparing this histogram to the probability histogram for the events with $MM^2 \geq 0.0182 \text{ BeV}^2$ (Fig. 13 (c)) shows that the distributions are quite sensitive to the presence of events with $2\pi^0$'s.

A.3 Other Tests

Although the evidence for the presence of $2\pi^0$ events is convincing, it could be argued that there still are large amounts of contaminating events in the sample. We counter these arguments by counting the numbers of η^0 and ω^0 events (which are nearly background free) which have probabilities above and below 0.55 . This cut divides the overall data into two equal parts. Assuming the 11% contamination by $2\pi^0$ is contained entirely in the low probability half, we predict

$$\frac{\text{No. of events } (\eta^0 + \omega^0) \text{ high P}}{\text{No. of events } (\eta^0 + \omega^0) \text{ low P}} = 1.29 .$$

Our experimental result is 1.24 ± 0.09 . If the contamination had been larger than 11% and concentrated in the low probability half, then the experimental value would have been larger than the predicted value.

Contamination from the $\pi^+\pi^-pp$ channel is considered in Fig. 14. If our procedure of accepting all events which fit the (pp) reaction were faulty, or if the four-constraint (pp) fitting procedure were faulty, then the unfitted momentum of the π^0 should have respectively a hole or a peak below $150 \text{ MeV}/c$. In Fig. 14 the unfitted momentum of

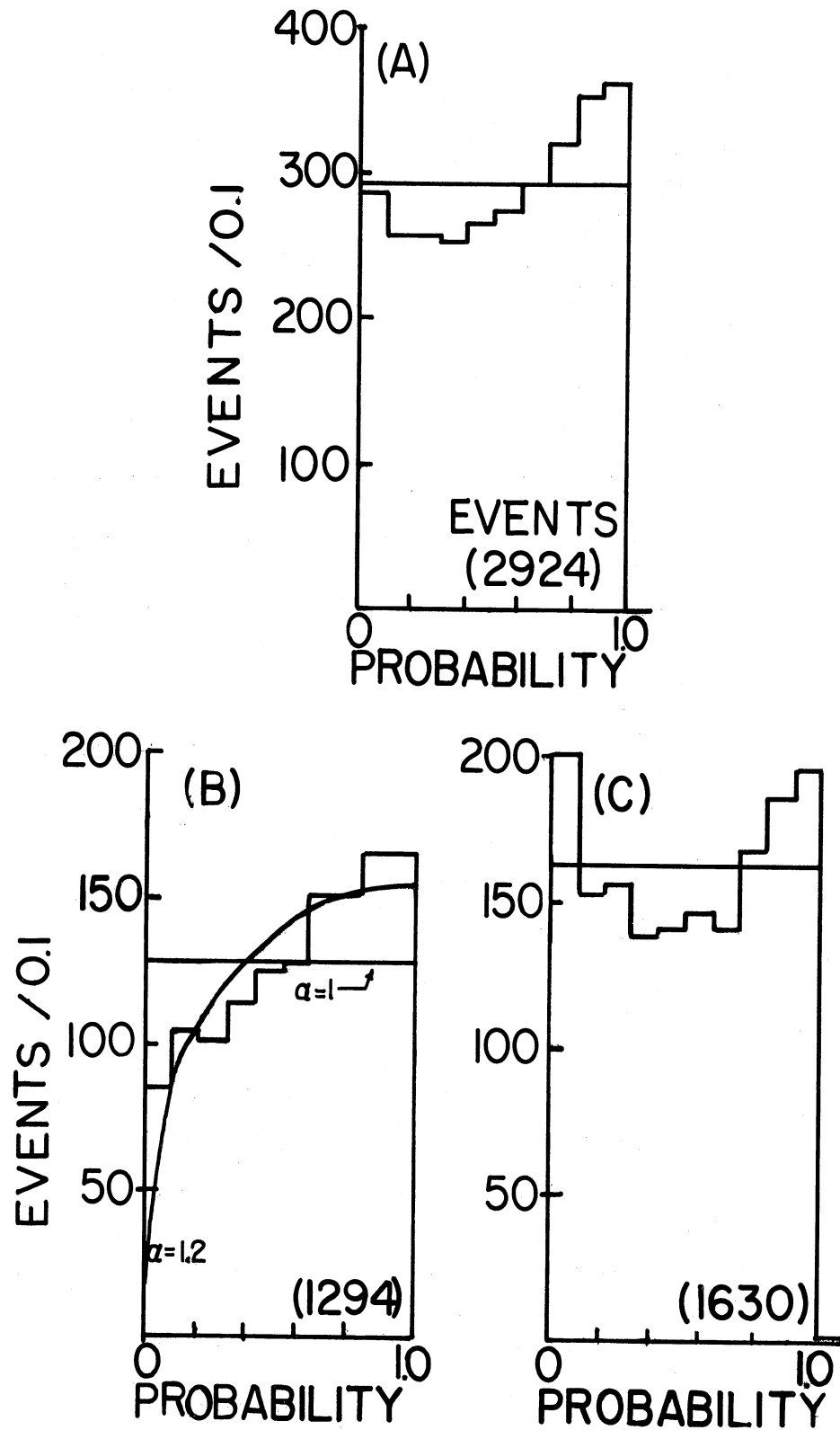


Figure 13. Probability distribution for all unique (π^0) events. (b) Probability distribution for events with $MM^2 < 0.0182 \text{ BeV}^2$. (c) Probability distribution for events with $MM^2 \geq 0.0182 \text{ BeV}^2$. The curves are discussed in the text.

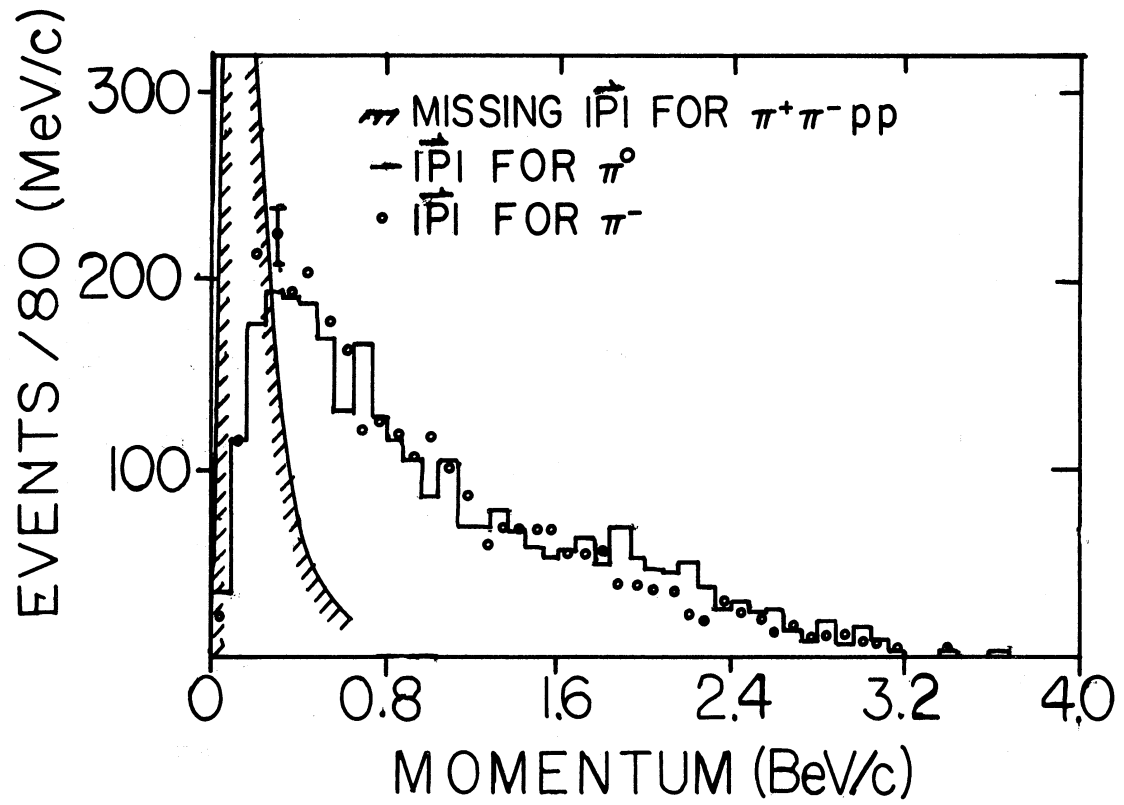


Figure 14. Unfitted momentum distributions for the π^0 and π^- from the (π^0) events compared to the missing momentum of the events which fit $\pi^+ d \rightarrow \pi^+ \pi^-$.

the π^- is shown for the same events. (The π^- track is a good track to compare with the π^0 since both pions can result from the decay of the $N^*(1238)$.) The generally good agreement between the two momenta indicates that the correct number of events has been assigned to the (π^0) reaction at low momentum.

Finally in Fig. 15 we show that there is no contamination from events of the type $\pi^+\pi^+\pi^-\text{pn } \pi^0$. If the MM^2 is calculated assuming the positive tracks are pions, the events do in fact extend into the $n \pi^0$ region (to the right of the smooth "neutron" curve).

All of the high mass events, however, have two protons identified by bubble density. The shaded events are those which were assigned by the unique fit rather than by bubble density. It is seen that most of these lie too low in mass squared to interpret them as $\pi^+\pi^+\pi^-\text{pn } \pi^0$. This graph points out the crucial role played by bubble density in the identification of these events.

From all the above we conclude that both the measuring errors and the contamination of the "good" $\pi^+\pi^-\pi^0\text{pp}$ events are well understood.

B. VALIDITY TESTS FOR $\pi^+\pi^+\pi^-\text{pn}$

Making a similar analysis of the $\pi^+\pi^+\pi^-\text{pn}$ events is more difficult for two reasons:

1. The missing mass can be contaminated above $M(n)^2$ by events with a neutron and a π^0 missing, and above and below $M(n)^2$ by events of the type $\pi^+\pi^-\pi^0\pi^0\text{pp}$ where one of the protons has a momentum greater than 1.7 BeV/c. (Above 1.7 BeV/c we cannot

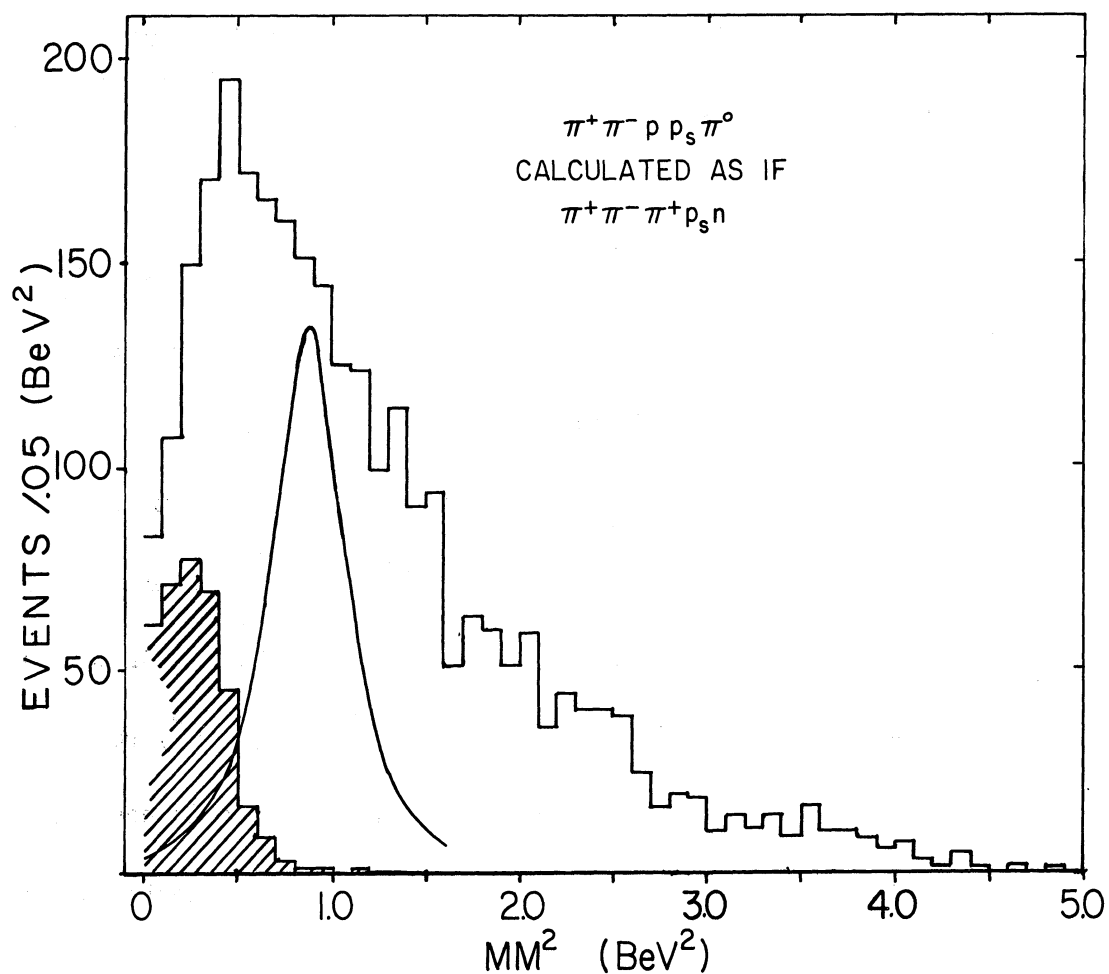


Figure 15. Unfitted missing mass squared distribution for the (π^0) events calculated assuming the proton were a π^+ . The curve represents the neutron mass squared spectrum for the good (pn) events plus ambiguous events. The shaded events have a proton of momentum greater than 1.7 BeV/c.

identify protons by bubble density.) The latter source of contamination is of concern since in only 9.5% of our biased* sample of (pn) events can both π^+ mesons be identified by bubble density.

2. The nature of the ambiguity problem distorts the neutron mass spectrum as discussed in the next Section. The missing mass squared of the neutron in Fig. 16 is in obvious disagreement with the resolution function.

The probability distribution for the "good" (pn) events is shown in Fig. 17. The fact that it is identical to the overall probability distribution for the (π^0) reaction suggests that the contamination and measuring errors conclusion will be the same as in the (π^0) reaction. As we have seen, however, the missing mass squared in this case is in poor agreement with the corrected ($\alpha = 1.2$) resolution function. The source of this disagreement is discussed below.

C. AMBIGUITIES

The two channels, $\pi^+\pi^-\pi^0$ pp and $\pi^+\pi^+\pi^--$ pn, are naturally ambiguous with one another because each has three pions and two nucleons in the final state, and because they are both one-constraint reactions. This can be seen by considering a case where a positive track has the same unfitted momentum as the neutral track within the measuring errors.

*We deliberately rejected events with two slow π^+ mesons in 80% of the film.

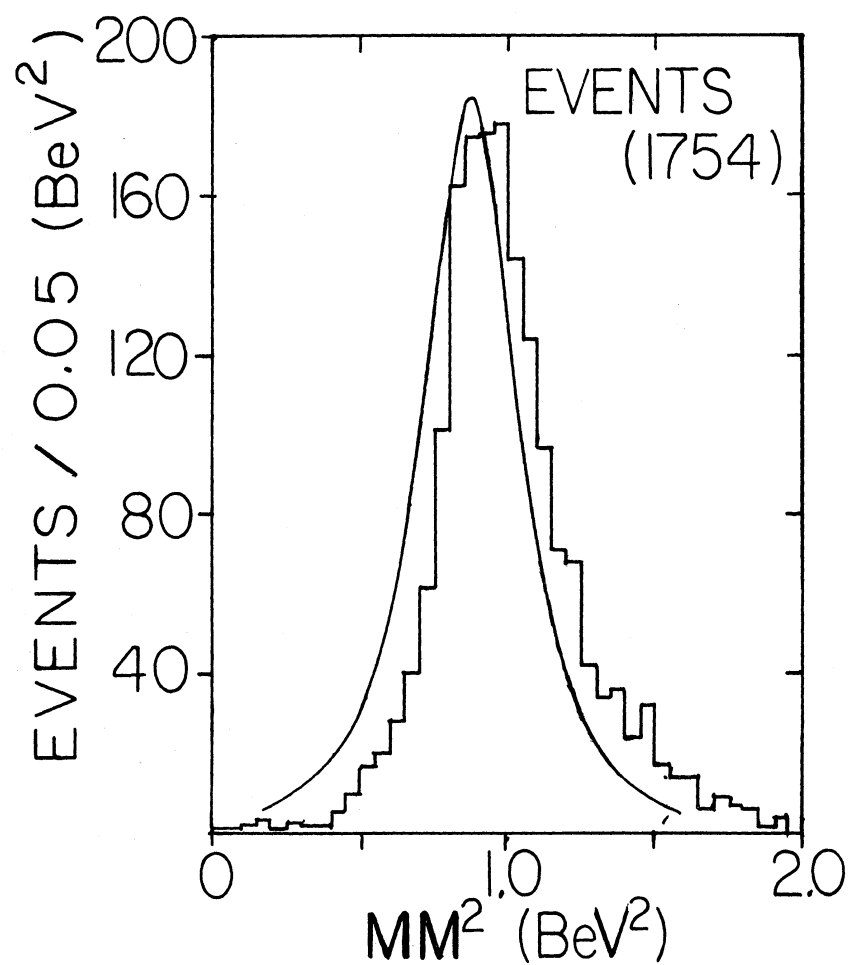


Figure 16. Missing mass squared distribution for the unique (pn) events with the corrected resolution function.

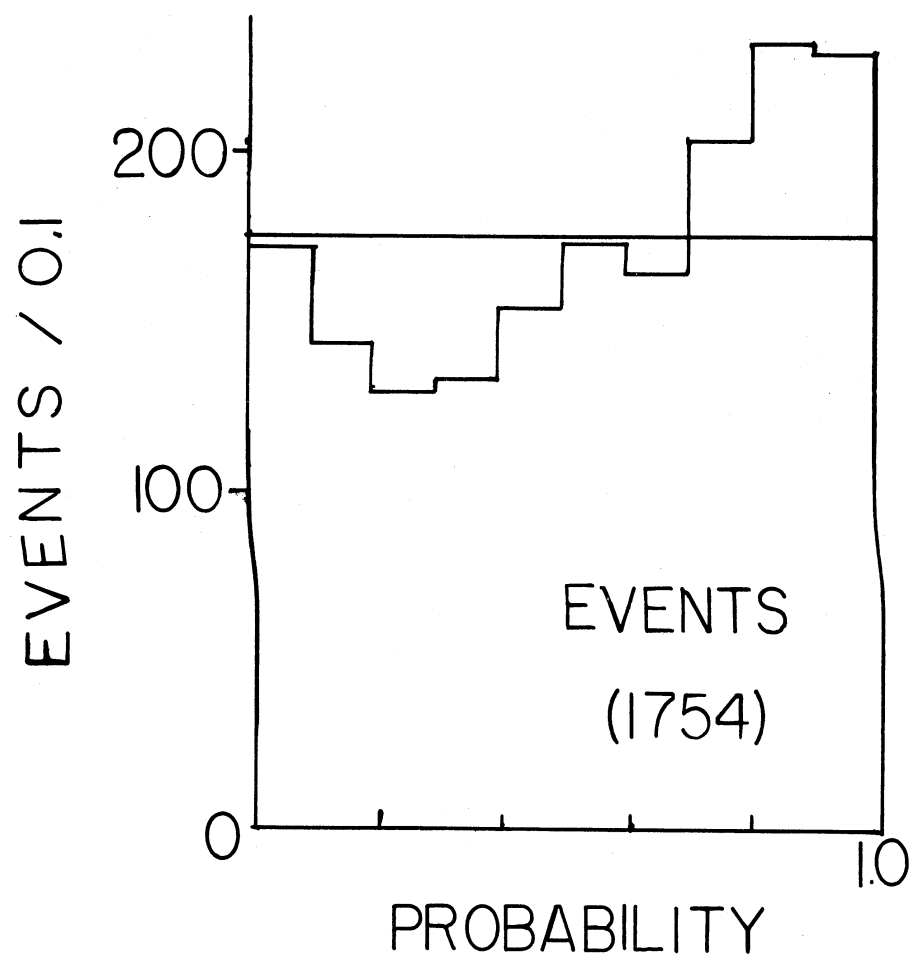


Figure 17. Probability for the (pn) events.

If the positive track is fast (as is the case in events which cannot be distinguished by bubble density), then the momentum of the track is primarily dependent on curvature and only slightly dependent on mass. Thus if energy is properly balanced for the (π^0) reaction, it will also balance for the (pn) reaction since $E_+ + E_0 = \sqrt{p_+^2 + m_+^2} + \sqrt{p_0^2 + m_0^2}$ is unchanged by switching m_+ and m_0 whenever the momenta are equal ($p_+ = p_0$). The larger the errors are in momentum, the more often will these channels overlap. Since our errors are large (due to the high beam momentum relative to the chamber size), we suffer from a large percentage of ambiguous events (good (π^0): ambiguous: good (pn) = 1.7: 0.29: 1), and we, therefore, must treat them carefully if our cross sections are to represent the entire channel. Previous experiments with this beam momentum and chamber have a) ignored the problem,⁴⁸ b) concluded the events were hopelessly ambiguous since they had identical χ^2 distributions,⁴⁶ or c) concluded from Δ^2 distributions that $\approx 80\%$ of the events ambiguous between $\pi^-p \rightarrow \pi^-p \pi^0$ and $\pi^-p \rightarrow \pi^+ \pi^-n$ were in fact the $\pi^+ \pi^-n$ final state.³⁰ Our probability distributions for the two hypotheses (Fig. 18) are seen to be identical as would be expected from the π^-p results.^{30,46}

C.1 Missing Mass Tests

In the following we reach essentially the same conclusion as (c), but we use a more powerful test; namely, the distributions of missing mass squared. The method is more powerful than the Δ^2 distributions because the $\Delta^2(\rightarrow \text{target})$ is very dependent on the momentum of the positive

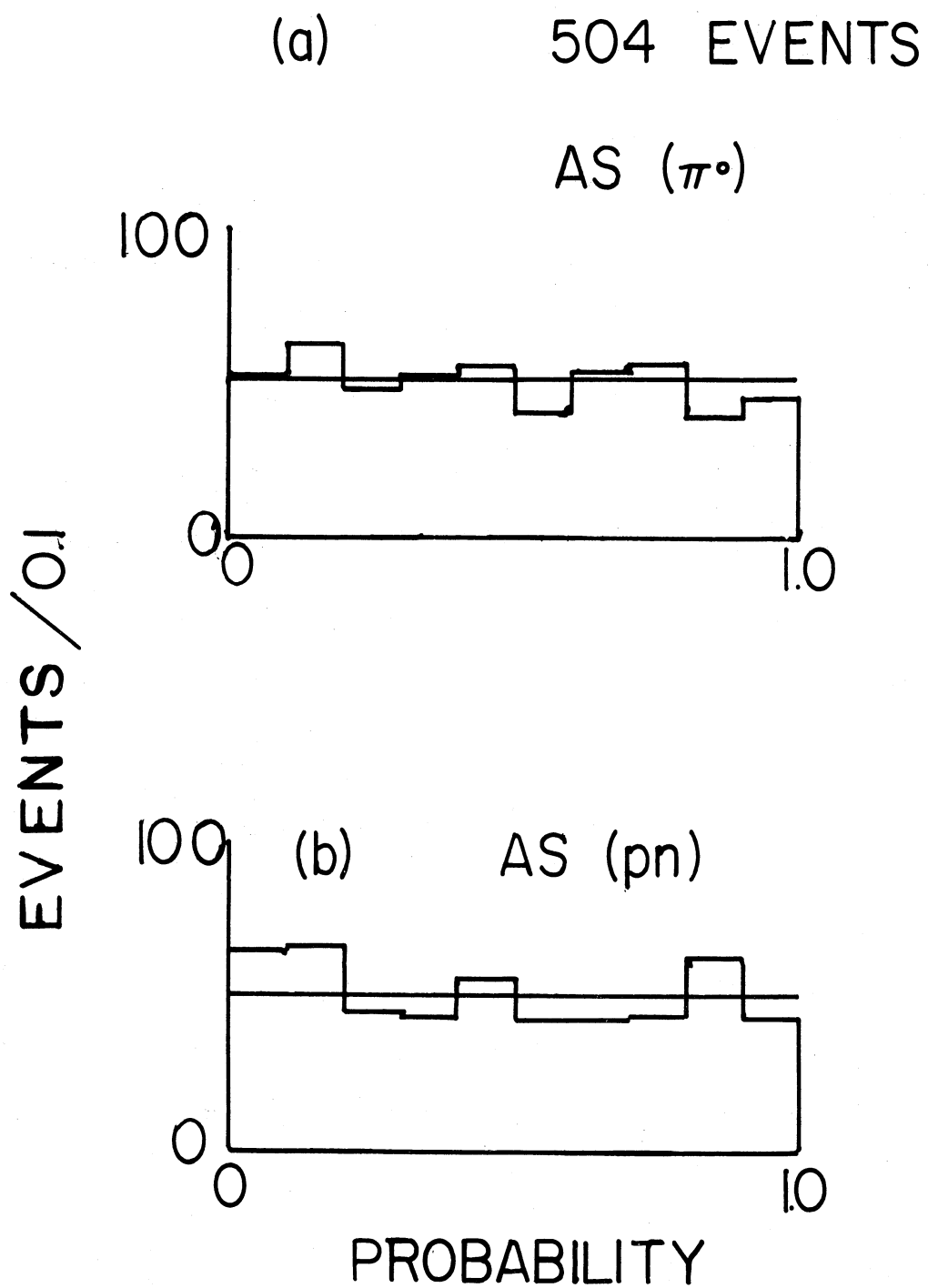


Figure 18. Probability distribution for the ambiguous events calculated for (a) the (π^0) hypothesis, and (b) the (pn) hypothesis.

track, whereas the missing mass is essentially independent of the momentum of the outgoing tracks if the events are correctly identified.

The unshaded events of Fig. 19 are the 442 unambiguous events with a proton of momentum greater than 1.7 BeV/c. The corrected resolution function normalized to 442 events is in general agreement with the data. It predicts 56 events with $MM^2 < -0.3$, and there are 50 events. All of the 504 ambiguous events (with missing mass squared calculated assuming the unidentified track is a proton) are shown shaded. The corrected resolution function for these events, but normalized to 255 events, is added to the previous resolution function to give the upper curve. This is an upper limit to the number of (π^0) events contained in the ambiguous events since the addition of more events would cause the peak of the overall resolution function to rise above the histogram. This curve estimates 44 ambiguous events with $MM^2 < -0.3$ whereas there are only 21. Thus about one half of these, 125 ± 80 events, is our estimate of the number of (π^0) events in the ambiguous events. This is 25% of the ambiguous events.

We now consider the missing mass squared calculated as a neutron shown in Fig. 20. There are 1035 good (pn) events where a positive pion could not be identified by bubble density. The corrected resolution function normalized to 1035 events does not fit well. This time the corrected resolution function for the ambiguous events is added but is now normalized to the 379 remaining ambiguous events. Because the data is now roughly consistent with the sum of the two resolution functions, we conclude that $(125 \pm 80)/(379 \pm 80)$ is the correct division of the ambiguous events.

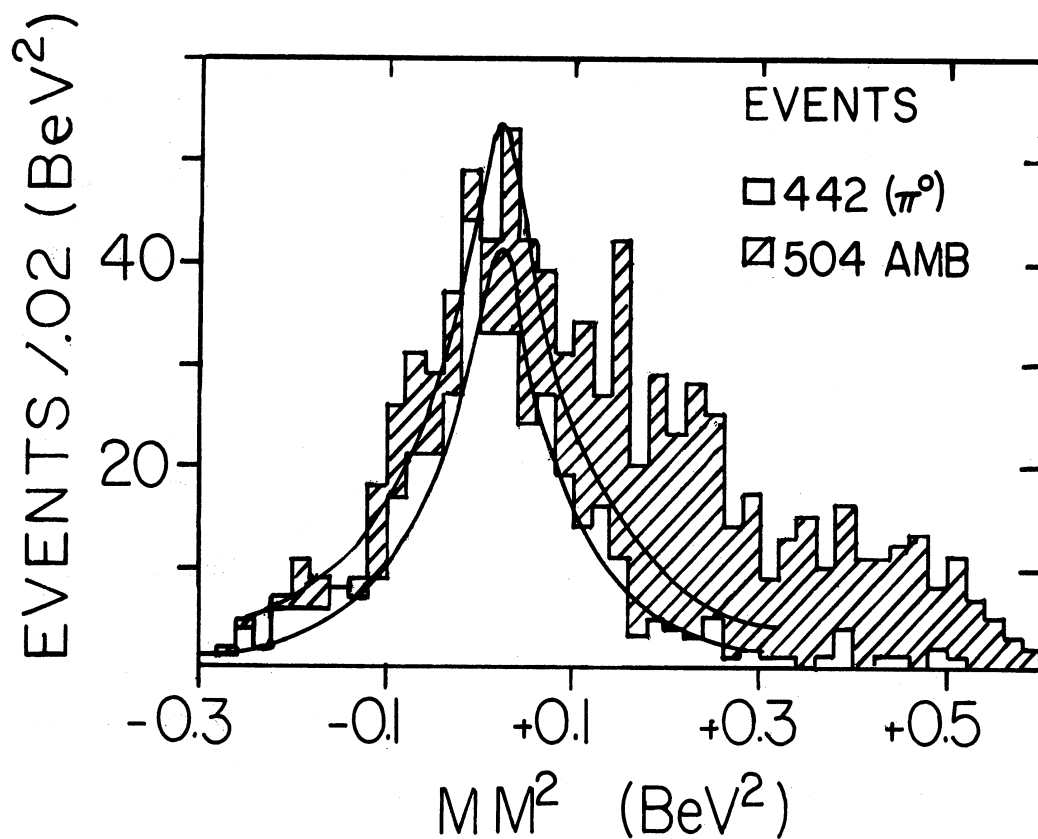


Figure 19. Missing mass squared for the good (π^0) events with a proton of momentum greater than 1.7 BeV/c and (shaded) for the ambiguous events.

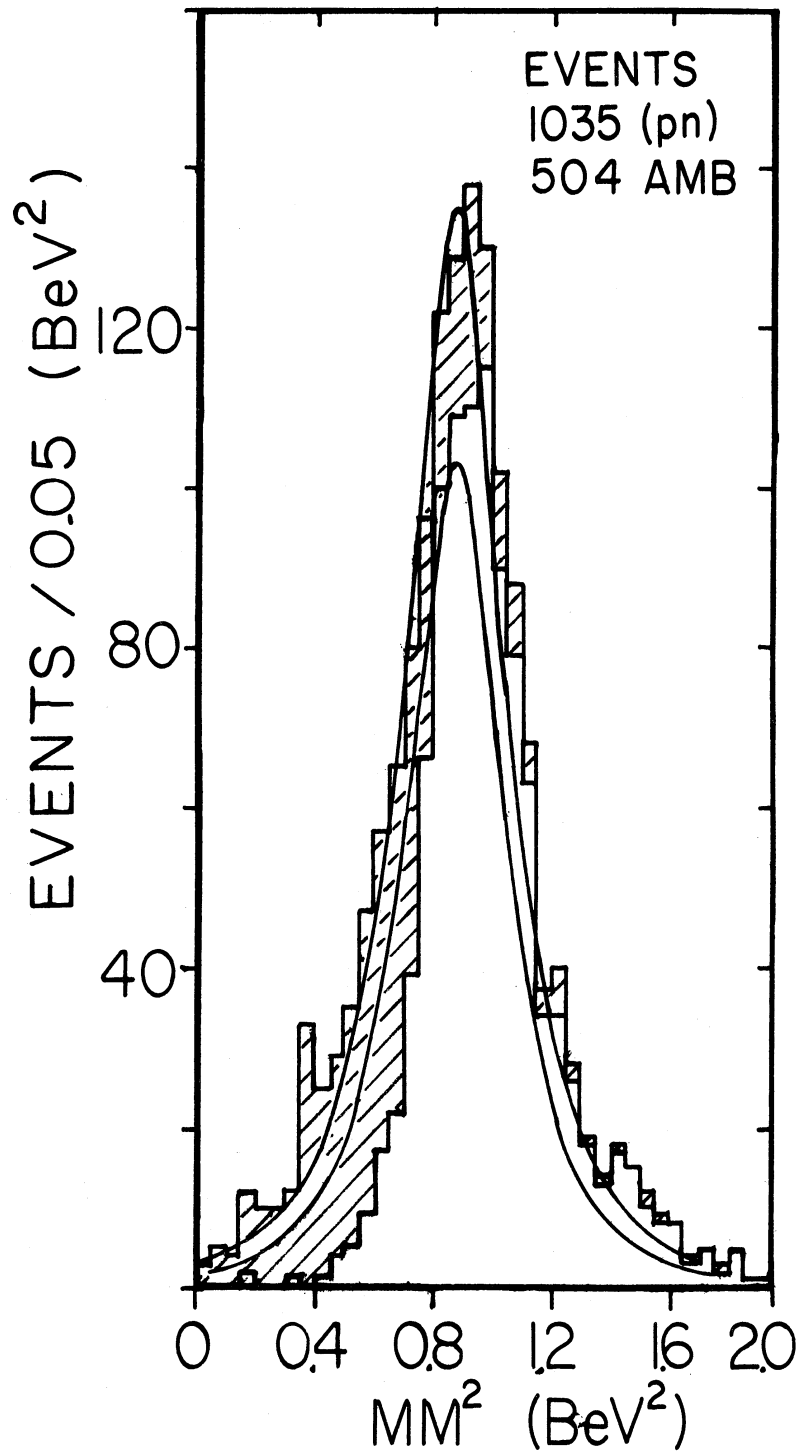


Figure 20. Missing mass squared distribution for the (pn) events having a π^+ track with momentum greater than 1.7 BeV/c and (shaded) for the ambiguous events.

The full widths at half maximum of the uncorrected resolution functions for the various events classes are summarized in Table IV. It is seen that events with positive tracks of high momentum have a larger than average error in missing mass squared. Also, the ambiguous events have a larger error in missing mass squared than the unique events of similar topology. The corrected full widths are 0.833 times the uncorrected widths in the

TABLE IV

RESOLUTION IN MISSING MASS SQUARED

(The uncorrected full widths at half maximum, Γ , are shown for all events and for only those events with a positive track of momentum greater than 1.7 BeV/c)

Γ in BeV ²	Good (π^0)		Ambiguous (π^0)-(pn)	Good (pn)	
	All	> 1.7 BeV/c		> 1.7 BeV/c	All
Γ as n	0.332	0.323	0.592	0.472	0.441
Γ as π^0	0.095	0.154	0.349	0.305	0.172
Events	2924	442	504	1035	1754

CHAPTER IV

GENERAL MASS AND MOMENTUM TRANSFER DISTRIBUTIONS

The invariant mass of the $\pi^+\pi^-\pi^0$ system is shown in Fig. 21. In addition to the η^0 and ω^0 meson peaks, a broad enhancement is seen around 1300 MeV. Our results indicate that the peak is the A_2^0 . There is no evidence for A_1^0 (1080) or A_3^0 (1600) production.⁴⁹ At $M(3\pi) = 1.0$ BeV is seen evidence for the H^0 meson. These resonances are discussed further in the sections following this one. For details from other experiments, the reader is referred to the compilation of references and data by Rosenfeld, et al.⁵⁰

The solid line of Fig. 21 is a phase space distribution calculated for the reaction $\pi^+ + n \rightarrow 3\pi + p$ and modified to take into account the Fermi motion of the neutron as discussed in Chapter II. The normalization is discussed in Section D of Chapter V. The curve does not fit the data well with any normalization. The dashed curve is the previous phase space multiplied by the correction factor of the type suggested by Lubatti and Rosenfeld.⁵¹ The fit to the data is considerably better. The background it estimates for the ω^0 agrees with an independent estimate obtained from curve fitting in the ω^0 region. This correction factor takes into account the preference of the data for low Δ^2 . The correction assumes that $(d\sigma/d\Delta^2) \propto e^{-A\Delta^2}$, with $A = 3.5 \text{ (BeV/c)}^2$ for our data. The correction formula and its derivation are given in Appendix J.

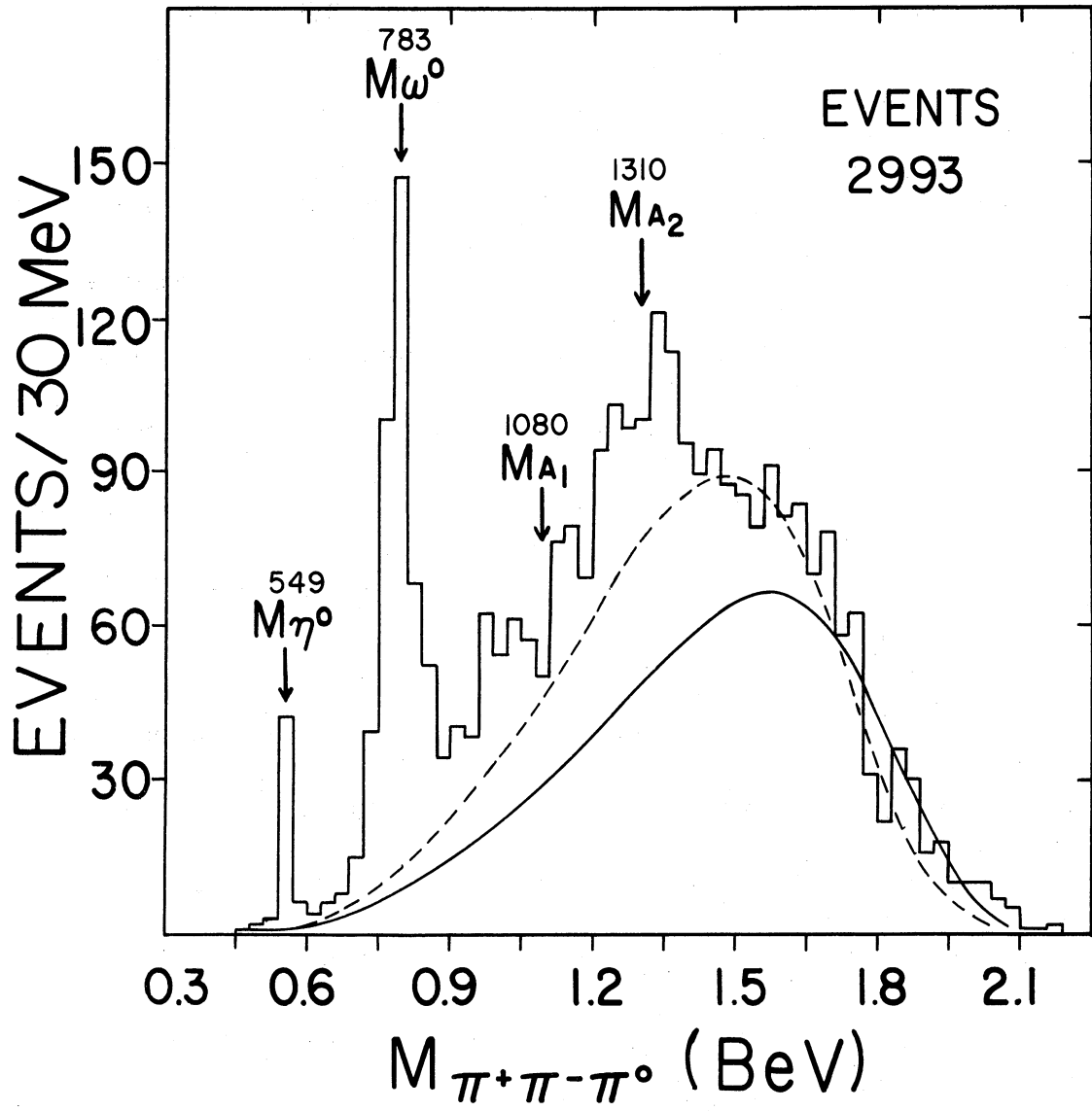


Figure 21. Invariant mass of $\pi^+\pi^-\pi^0$ for all events from $\pi^+d \rightarrow \pi^+\pi^-\pi^0pp$. The solid curve is a phase space estimate. The dashed curve is a peripherialized phase space estimate.

A scatter plot* in Fig. 22 of $M(\pi^+\pi^-\pi^0)$ against $\Delta^2(3\pi)$ shows that the η^0 and ω^0 events are produced at low values of $\Delta^2(3\pi)$ as, in fact, are most of the events of the channel. The lower solid curve shows the kinematic limits for π^+ hitting a stationary nucleon and producing a group of new particles with invariant mass M . Some events should fall outside this line because of the Fermi momentum of the target neutron. The outer curve is the kinematic limit for $\pi^+d \rightarrow M d$. This curve is the absolute limit for our reaction $\pi^+d \rightarrow \pi^+\pi^-\pi^0 pp$. The fact that the effective mass of the two protons is always greater than that of a deuteron means that events cannot quite reach this boundary.

The projection of this plot on the $\Delta^2(3\pi)$ axis is shown in Fig. 23. This plot does not give a meaningful picture of the average differential cross section, $d\sigma/d\Delta^2$, because kinematically allowed and excluded regions are lumped together when one averages over $M(3\pi)$. To rectify this we show in Fig. 24 a plot of $\Delta^2(3\pi) - \Delta_{\min}^2$, where $\Delta^2(3\pi)$ is the four-momentum transfer squared to the 3π system, and Δ_{\min}^2 is the minimum kinematically allowed value of Δ^2 for the given event. Both Δ_{\min}^2 and $\cos\theta^*$ (below) have been calculated for each event by defining the center of mass system to be that of all the outgoing particles except the spectator proton. We exclude η^0 and ω^0 events. Events with $M(3\pi) > 1.7$ BeV are also excluded to assure that the entire region of Δ^2 in the plot is kinematically allowed. A fit of the form $e^{-A\Delta^2}$ gives $A = 3.4 \pm 0.2$ (BeV/c) $^{-2}$. Elastic

*The author is indebted to L. Lovell and A. Loceff for the scatter plotting program.

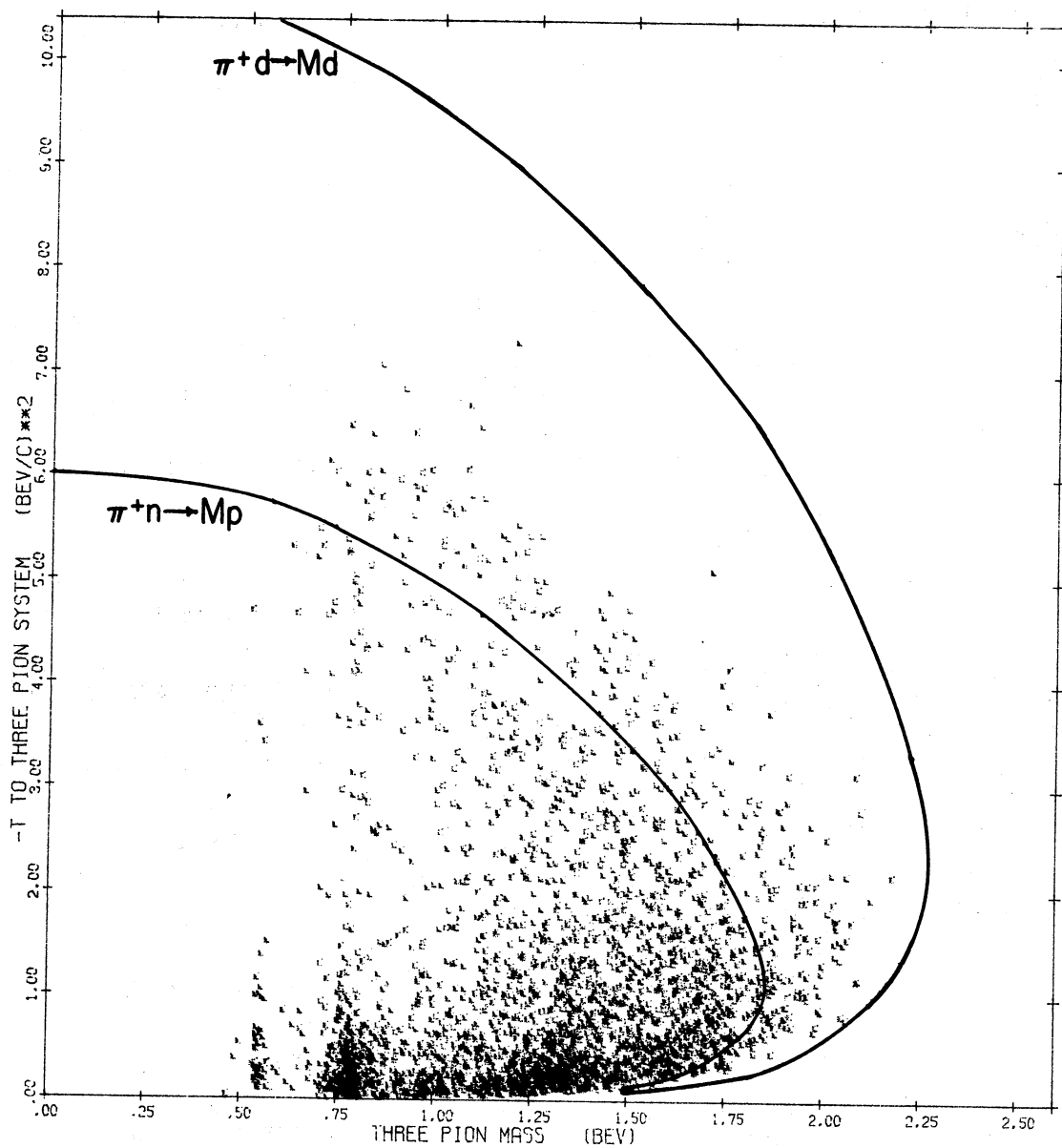


Figure 22. Scatter plot of $\Delta^2(3\pi)$ as a function of $M(3\pi)$. The curves show kinematically allowed regions for a stationary neutron or deuteron target respectively.

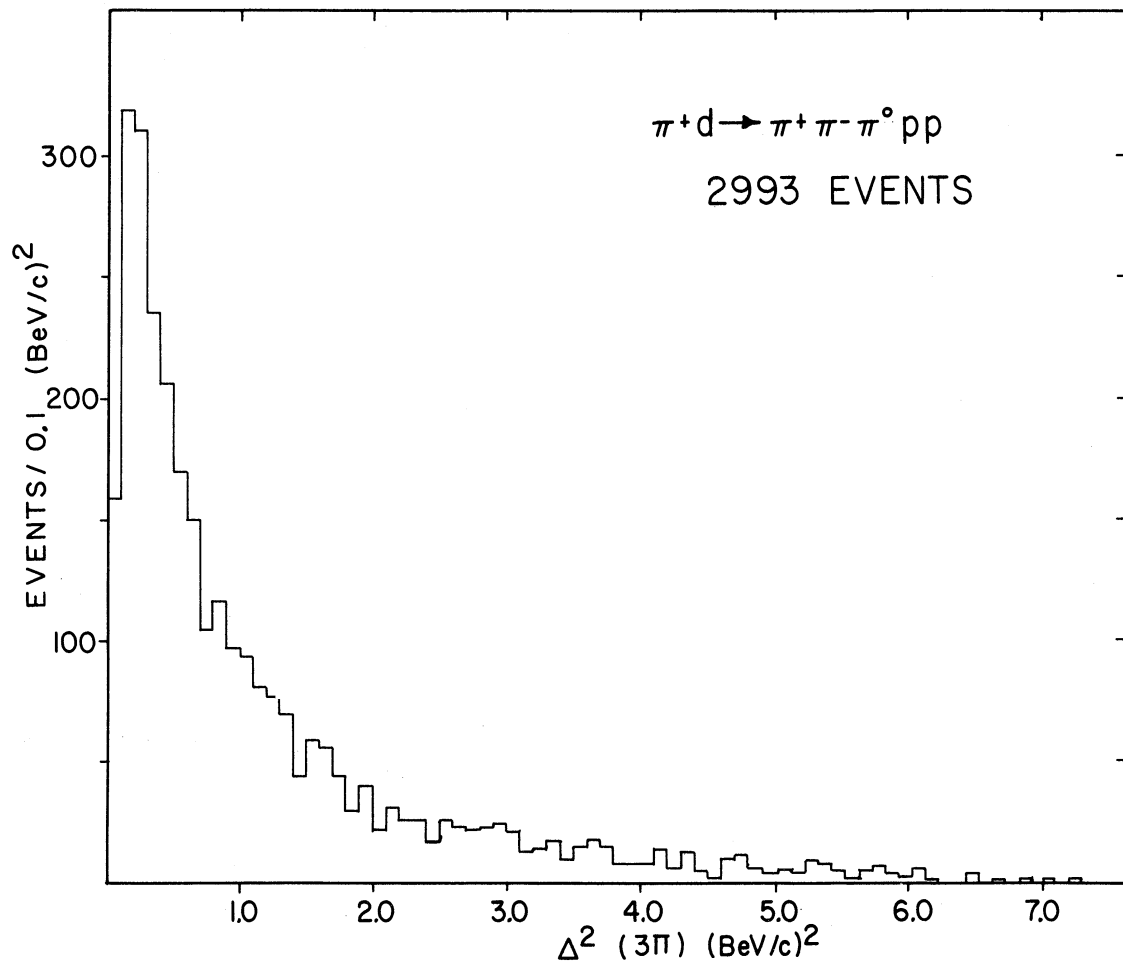


Figure 23. Histogram of $\Delta^2(3\pi)$ for all events.

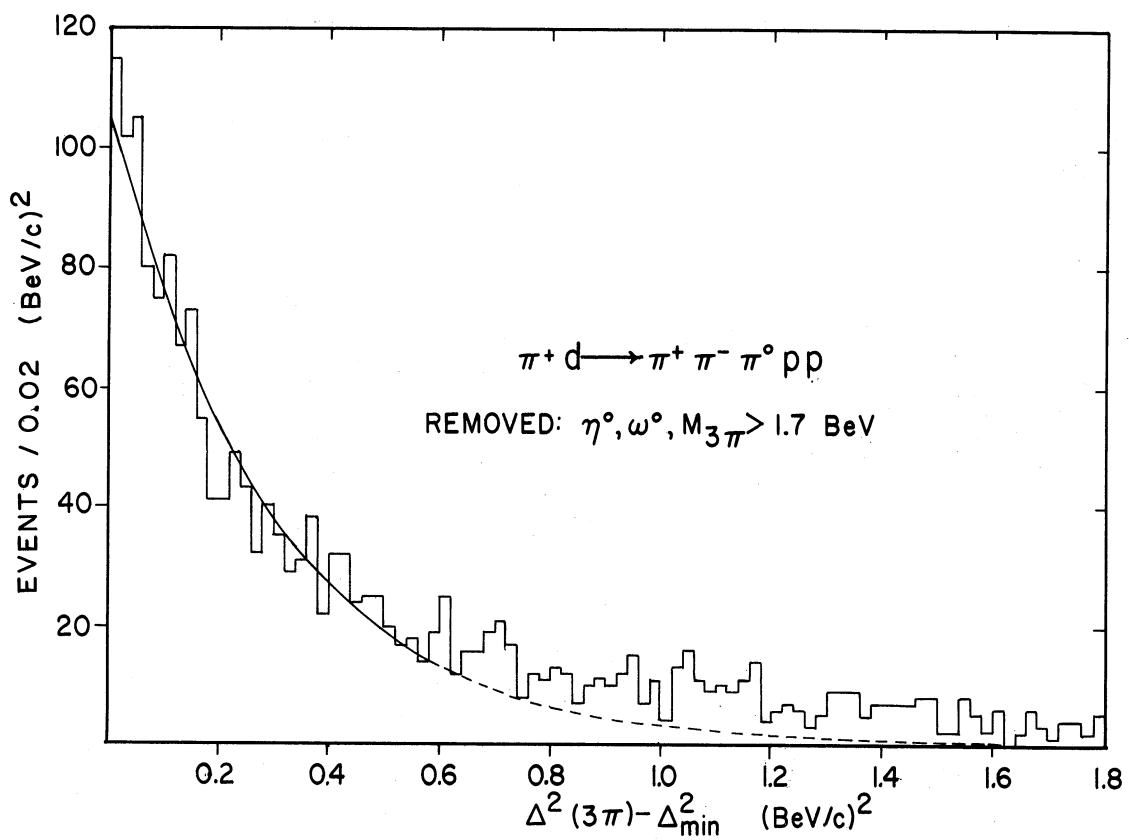


Figure 24. Histogram of $\Delta^2(3\pi)$ less Δ^2_{\min} , the minimum allowed value of $\Delta^2(3\pi)$ for the event.

(π^-p) scattering near our energy⁵² has a much larger slope of $A = 7.5 \pm 0.2$.

There recently has been experimental interest⁵³ in high momentum transfer events in elastic scattering ($\cos\theta^* = -1$). They have been interpreted theoretically⁵⁴ as nucleon exchange processes. We note in Fig. 25 that there is evidence for a small backward peak in this channel. It does not appear to be associated with any particular three-pion mass.

The two-body mass plots shown in Fig. 26 give evidence for ρ^+ , ρ^0 , and ρ^- production and for production of the two-body final states $\rho^+ + N^{*0}(1238)$ and $\rho^0 + N^{*+}(1238)$. Figures 26 (a,b,c) show the $\pi\pi$ invariant mass distributions. Figures 26 (d,e,f) show the invariant mass of the remaining pion and proton of higher momentum. The $\Delta^2(\rho)$ (i.e., from the beam to the ρ) distributions for the events having mass combinations simultaneously in the $\rho^+(\rho^0, \rho^-)$ and $N^{*0}(N^{*+}, N^{*++})$ regions are given in the inserts. The difference in the Δ^2 plots (see inserts) is perhaps explained by the fact that ρ^+ and ρ^0 can be produced in π^+n collisions by one-pion exchange but ρ^- cannot. The Δ^2 distribution shapes and total numbers of events in Fig. 26 (d') and 26 (e') are in excellent agreement with being identical, as predicted by the one-pion exchange diagrams drawn in Figs. 26 (a,b). The ρ region throughout this report is taken as 650-850 MeV, and the $N^*(1238)$ region is defined throughout as 1140-1340 MeV. The phase spaces are normalized arbitrarily to events in Fig. 26 (a) and Fig. 26 (d) and then copied onto the other histograms of Fig. 26.

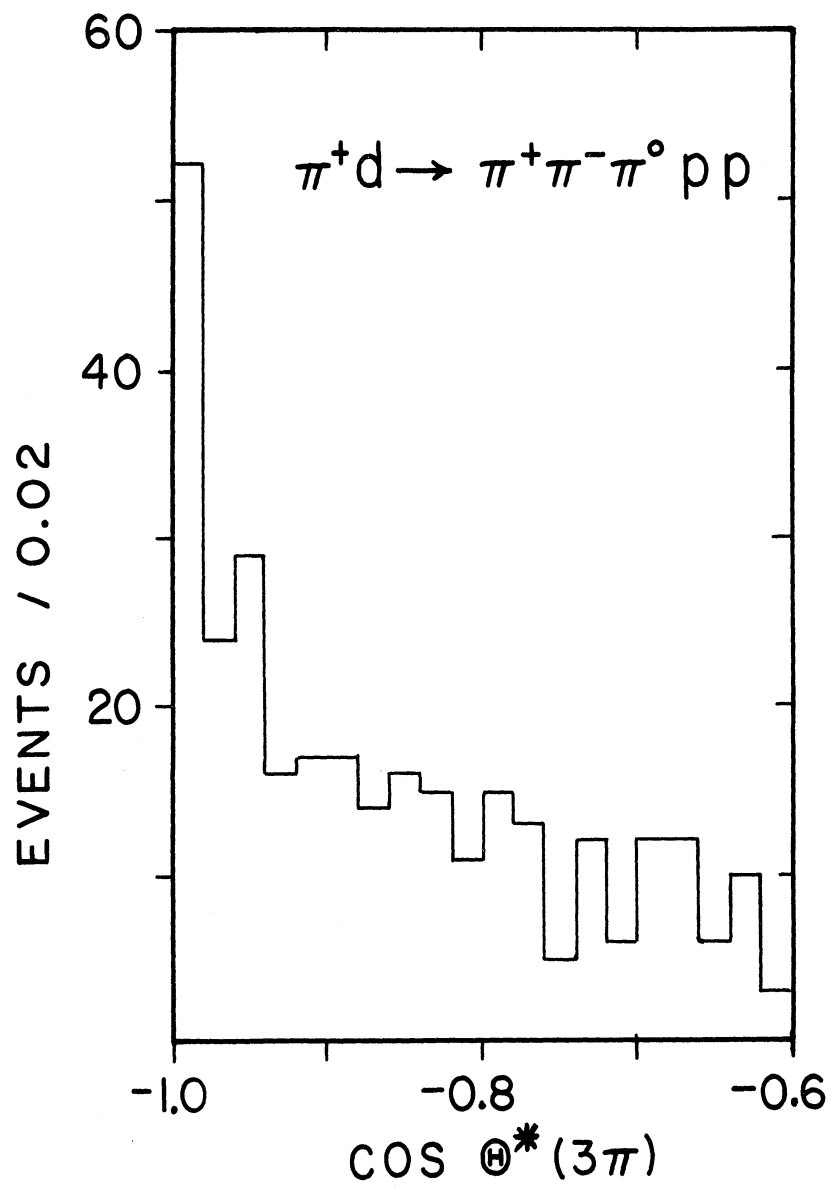


Figure 25. Production angular distribution for the three-pion system,

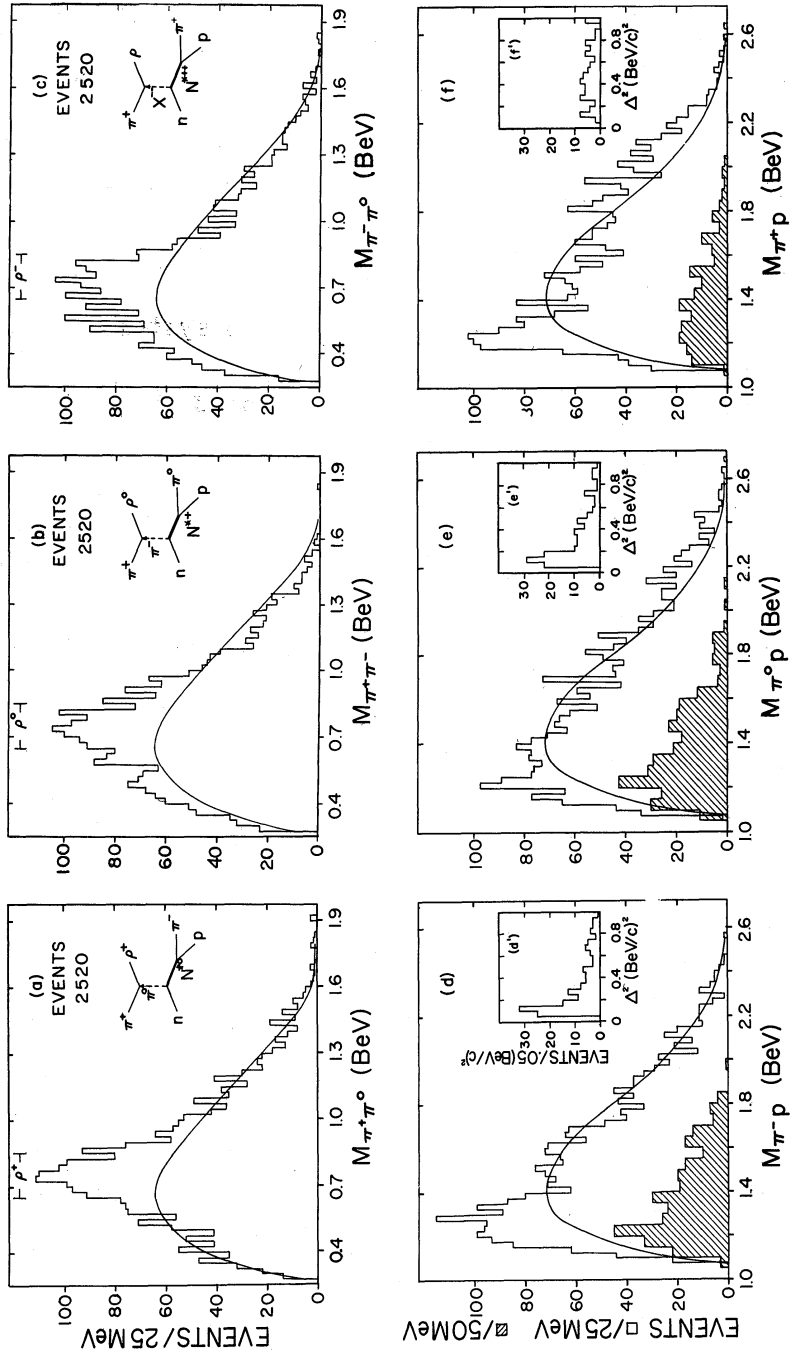


Figure 26. Two body effective masses after removal of $535 < \eta^0 < 575$ MeV and $705 < \omega < 875$ MeV. (a) $M(\pi^+\pi^0)$, (b) $M(\pi^+\pi^-)$, (c) $M(\pi^-p)$, (d) $M(\pi^0p)$, (e) $M(\pi^0\pi^0)$, and (f) $M(\pi^+\pi^+)$. Shaded πp effective masses have a mass associated with ρ^+ in (d), ρ^0 in (e), and ρ^+ in (f) and $\Delta^2(\rho) < 0.6$ (BeV/c) 2 . The $\Delta^2(\rho)$ is shown in (d') for ρ^+ and N^{*0} , in (e') for ρ^0 and N^{*+} , and in (f') for ρ^- and N^{*++} . The solid curves are two-body phase spaces.

Figure 27 shows the invariant mass of the pions combined with the spectator proton. At first sight it is a surprise to see how similar the π -p and π -spectator mass histograms are. Evidently the momentum differences of the two protons are not great enough to change the mass spectra. The curves are the same π p phase spaces as in Fig. 26. Note however, that the evidence for $N^{*++}(1238)$ seen in the π^+p plot is not seen in the π^+p (spectator) plot.

The invariant masses of the $\pi^-\pi^0p$, $\pi^+\pi^-p$, and $\pi^+\pi^0p$ systems are shown in Fig. 28 with a phase space estimate. One would expect to see some of the higher N^* resonances in these plots. The lack of evidence for them is evidently due to the large backgrounds. Events with $\eta^0(535-575$ MeV) or $\omega^0(705-875$ MeV) have been removed before making the plots of Figs. 26, 27 and 28.

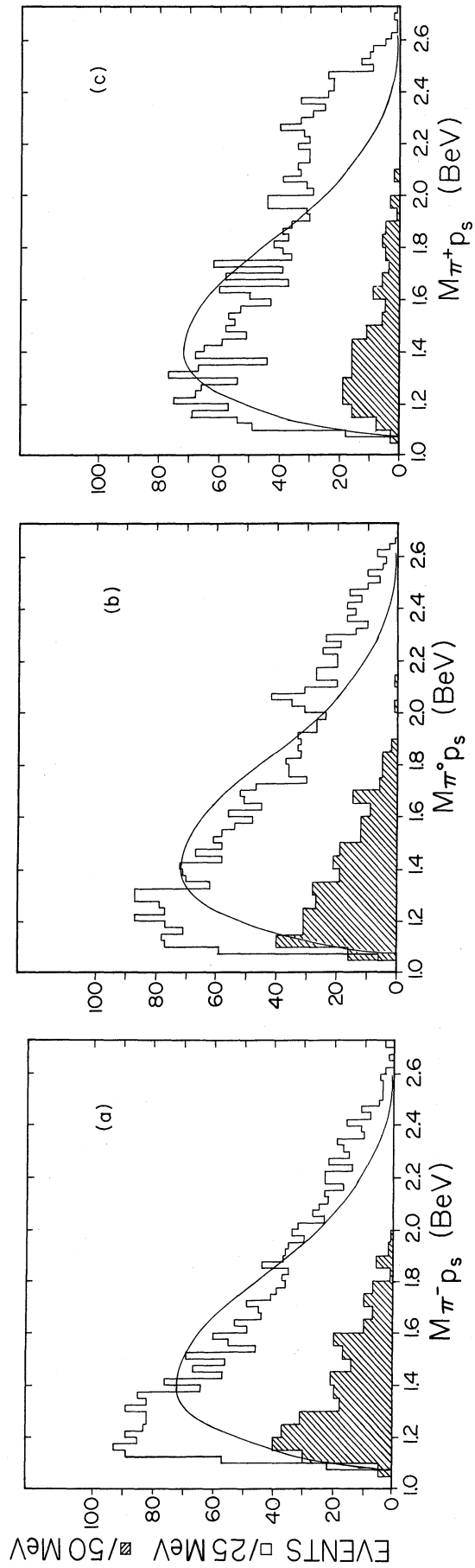


Figure 27. Invariant mass of the pion and the slower proton systems. The shaded events have a ρ meson associated with $\Lambda^2(\rho) < 0.6 \text{ (GeV/c)}^2$ as in Fig. 26.

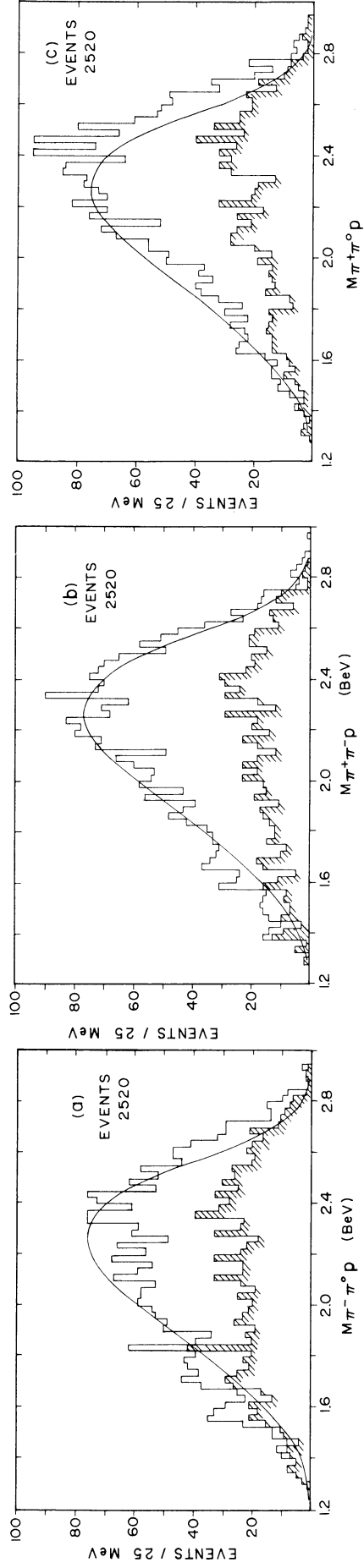


Figure 28. Invariant mass of the pion-pion-faster proton systems. The shaded events have (a) $\Delta^2(\pi^+)$, (b) $\Delta^2(\pi^0)$, and (c) $\Delta^2(\pi^-)$ less than 0.6 (BeV/c)^2 . The smooth curves are the phase space estimate.

CHAPTER V

RESONANCE PRODUCTION IN $\pi^+d \rightarrow \pi^+\pi^-\pi^0pp$

A. $\pi^+d \rightarrow \eta^0pp$

The η^0 meson, since its discovery⁵⁵ in 1961 in this reaction ($\pi^+d \rightarrow \pi^+\pi^-\pi^0pp$), has been well studied. A variety of decay modes have been found (a recent example being the rare mode,⁵⁶ $\eta^0 \rightarrow \pi^+\pi^-\pi^0$); charge-conjugation invariance, C, has been studied in the $\pi^+\pi^-\pi^0$ decay mode,^{1,57} and the production and differential cross sections have been measured in a recent high energy spark chamber experiment in the reaction $\pi^-p \rightarrow \eta^0n$; $\eta^0 \rightarrow \gamma\gamma$.⁴²

A.1 Mass and Width

The η^0 (whose quantum numbers are J^{PG} , Mass = 0^{-+} , 548.8 MeV) is seen in this experiment in Fig. 21. We define the η^0 region as 0.53 to 0.57 BeV. The average mass of these 44 η^0 events is

$$M(\eta^0) = 551 \pm 3 \text{ MeV}$$

in good agreement with the world average. The full width in mass is about 20 MeV which is a measure of our instrumental resolution. The events presumably include both the $\eta^0 \rightarrow \pi^+\pi^-\pi^0$ and $\eta^0 \rightarrow \pi^+\pi^-\gamma$ decay modes since our resolution of the missing neutral is poor (see Fig. 10). From phase space we estimate only one or two background events in this sample (2 - 5%). For comparison it is interesting to note that the re-

cent low energy study of the η^0 in this reaction (beam momentum of 820 MeV/c) found a slightly larger background of $7 \pm 1\%$.

A.2 Total and Differential Cross Section

Our cross section at 3.65 BeV/c for 43 η^0 events is

$$\sigma(\eta^0 \rightarrow \pi^+ \pi^- \pi^0 \text{ or } \pi^+ \pi^- \gamma) = 52 \pm 8 \text{ } \mu\text{b} .$$

This includes our 8% uncertainty in normalization. Assuming we are observing $30.5 \pm 2.0\%$ of the total cross section,⁵⁸ we get

$$\sigma_{\text{tot}}(\eta^0) = 160 \pm 30 \text{ } \mu\text{b} .$$

The comparison point of Guisan, et al.,⁴² in hydrogen and from the $\gamma\gamma$ decay mode at 3.72 BeV/c (see Fig. 29) is

$$\sigma_{\text{tot}}(\eta^0) = 111 \pm 15 \text{ } \mu\text{b} .$$

This error includes a 10% systematic uncertainty. These two measurements are in moderate agreement since the difference is expected statistically once in five experiments. This is a rough indication that our cross sections do approximate free neutron cross sections.

There are two experimental uncertainties which would bring these points into even closer agreement. First, the hydrogen point assumes $(\eta^0 \rightarrow \gamma\gamma) / (\eta^0 \rightarrow \text{all}) = 38.7 \pm 2.7\%$. If the value of this branching ratio were closer to 30%, as suggested by a recent preliminary result,⁵⁹ then the hydrogen cross section would become

$$\sigma_{\text{tot}}(\eta^0) = 143 \mu\text{b}.$$

Second, 40% of our η^0 events have slower protons with momenta greater than 250 MeV/c. If these are rejected as not having been produced on a free nucleon (as is sometimes done in π^+d experiments), then our value would become 140 μb .

Phillips and Rarita^{40,60} have fit the differential cross sections for η^0 production with a set of parameters based on the Regge pole model with A_2 -meson exchange. The data⁴² used in their fit were taken between 6 and 20 BeV/c from the reaction $\pi^-p \rightarrow \eta^0 n$; $\eta^0 \rightarrow \gamma\gamma$. It is interesting to see how low in energy their result can be extrapolated and how well their prediction fits our data. This is shown in Fig. 29. The low energy π^-p data is from Bulos, et al.,⁶¹ and the other π^+d datum is from Bacon, et al.³.

The solid curve is a numerical integration of their differential cross section formula from $\Delta^2 = 0$ to 1 (BeV/c)². Some appreciation for the success of the extrapolation (dashed line) can be gained by noting that a straight line will pass through the four fitted points, but will miss the 2.9 and 3.7 BeV/c points entirely.

Our differential cross section at 3.65 BeV/c is shown in Fig. 30. The solid curve is the prediction calculated from the work of Phillips and Rarita.⁴⁰ There is no adjusted parameter. The dashed curve is our estimate of the effect of Pauli exclusion (see Chapter II). From the π^-p data at 3.72 BeV/c⁴² and the established branching ratios,⁵⁸ we

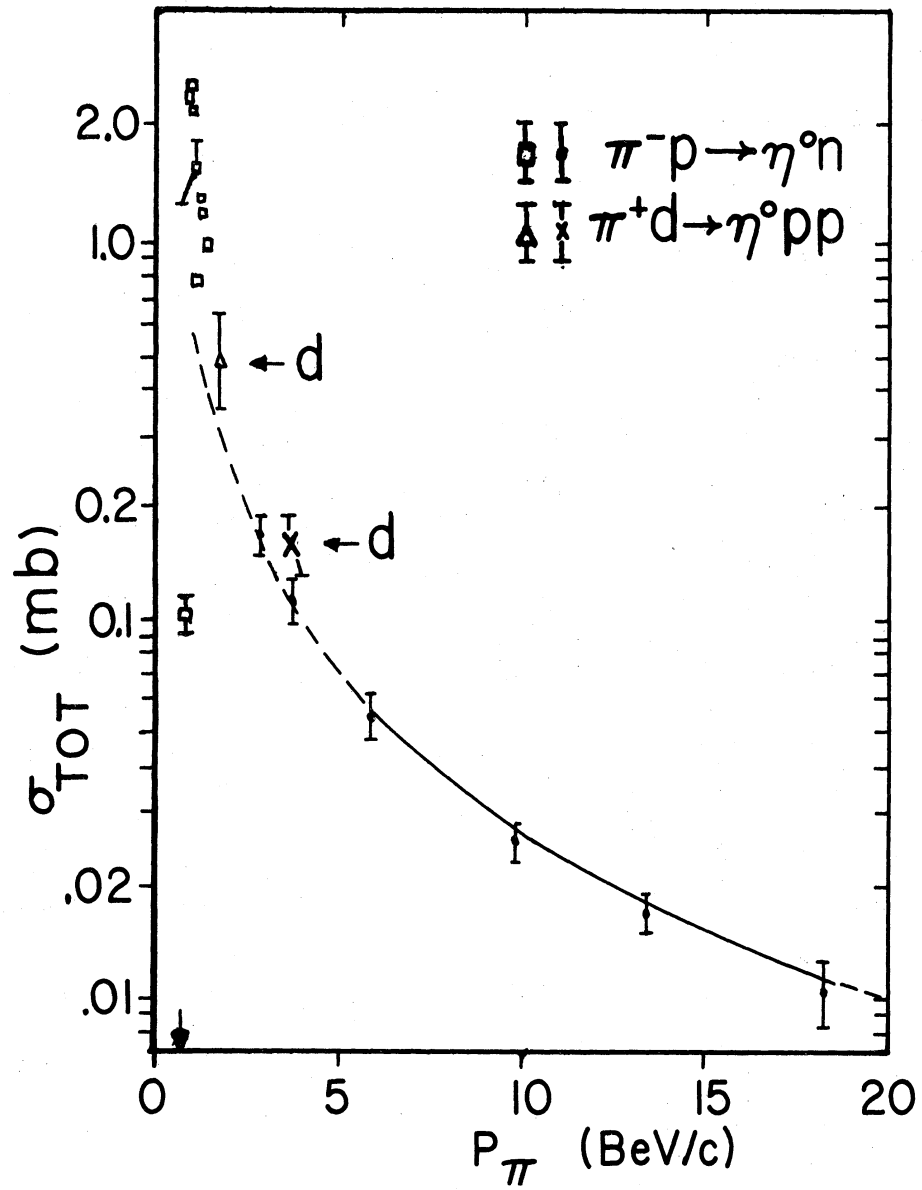


Figure 29. Total cross section for η^0 production. The solid curve is the Regge pole fit to the hydrogen data. The dashed curve is the extrapolation of the solid curve in the Regge formalism. The point (x) is from this experiment.

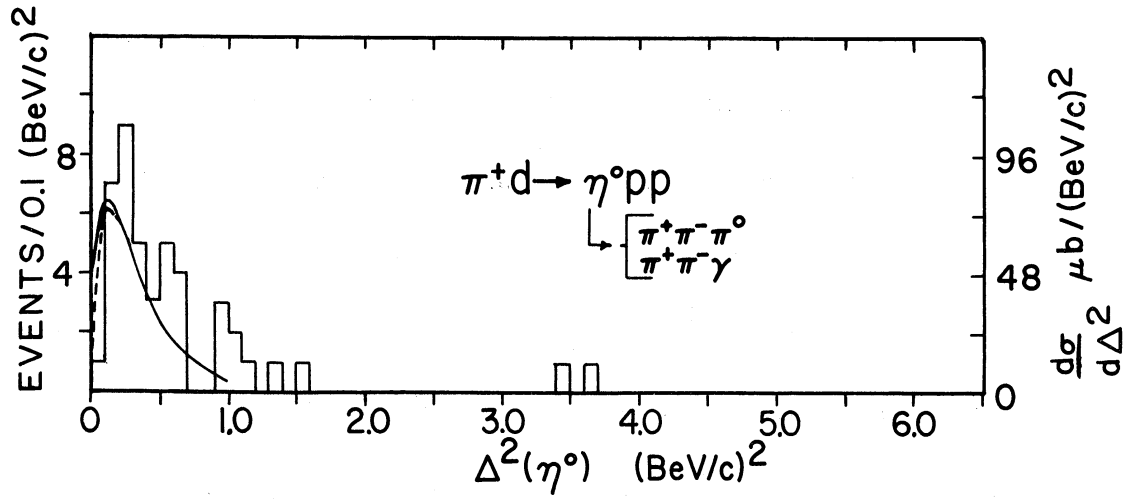


Figure 30. Differential cross section for the η^0 meson. The solid curve is the π^-p Regge prediction. The dashed curve is the π^+d prediction which takes Pauli exclusion into account.

estimate we should have 5.7 ± 1 events $(68 \pm 12 \mu\text{b}/(\text{BeV}/c)^2)$ with $\Delta^2(\eta^0) < 0.1 (\text{BeV}/c)^2$. We find we have only one event. Our result is even less than our theoretical estimate of 4 ± 1 (5 ± 1) events which assumes the production process is all nonflip (all flip). As seen in Fig. 8 and Fig. 9, we do not believe events at low Δ^2 suffer from serious scan bias because of the dramatic appearance of the two protons. We therefore consider our result interesting and worthy of further study in other experiments. We do note the remote possibility that the two missing events were thought to have Dalitz (e^+e^-) pairs (contrary to the rules of our scan) and were treated as two-prong events.

A fit to an exponential drop in Δ^2 for $\Delta^2 = 0.1 - 1.5 (\text{BeV}/c)^2$ gives a slope $A = 3.0 \pm 0.7 (\text{BeV}/c)^{-2}$. This is consistent with the π^-p result.⁴² This flatter than elastic slope can be interpreted as evidence for the exchange of a heavy, high spin meson (only the A_2 is presently known to satisfy the J^{PG} requirements). Bias²⁷ has shown that this may also be interpreted (in the framework of the Byers and Yang "Coherent Droplet" model) as evidence that the radius of the η^0 droplet is smaller than that of particles produced with steeper slopes.

A.3 Dalitz Plot Density

Since the η^0 meson is spin zero, it is expected that the matrix element for its decay is roughly independent of the position of the event on the Dalitz plot.⁶² For each event we calculate the distance of the event from the center of the Dalitz plot, R , and the maximum

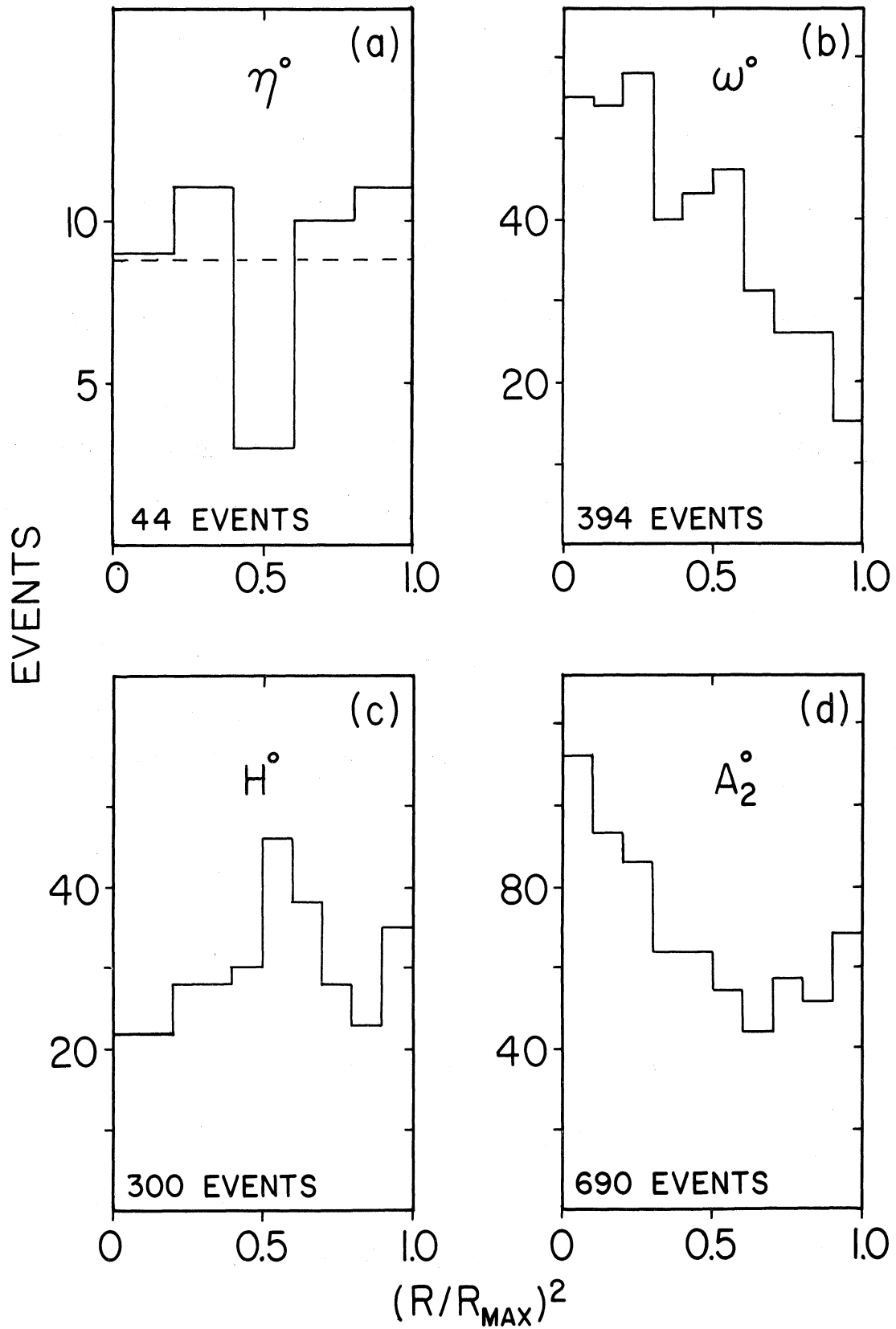


Figure 31. Radial Dalitz plot density for events in (a) the η^0 meson, (b) ω^0 meson, (c) H^0 meson, and (d) A_2^0 meson mass regions.

distance from the center of the Dalitz plot allowed by kinematics, R_{\max} .^{*} Because we want events per unit area, and area is proportional to R^2 , we show in Fig. 31 the distribution of events per unit $(R/R_{\max})^2$. The χ^2 probability that the distribution represents a constant matrix element is 30%.

The most precise measurement of the asymmetry of the Dalitz plot to date is $A = (N^+ - N^-)/(N^+ + N^-) = +0.003 \pm 0.010$.⁵⁷ Here, $N^+(N^-)$ is the number of events whose $\pi^+(\pi^-)$ has more kinetic energy than its $\pi^-(\pi^+)$. The kinetic energies are calculated in the η^0 rest frame. The value for our η^0 events is

$$A = -0.04 \pm 0.15 .$$

The result is consistent with no violation ($A = 0$). (The same number for our ω^0 events is $A = +0.05 \pm 0.05$.)

B. $\pi^+ d \rightarrow \omega^0 pp$

B.1 Mass and Width

The ω^0 meson was discovered in the reaction $\bar{p}p \rightarrow \pi^+ \pi^- \omega^0$; $\omega^0 \rightarrow \pi^+ \pi^- \pi^0$.⁶³

The peak was not as prominent as the one shown in Fig. 21. A detail of the η^0 and ω^0 mass region is shown in Fig. 32 with a least squares fit** to the ω^0 . The curve is the Breit-Wigner form added to phase space (PS), i.e.,

*The author is indebted to L. Lovell for the program which calculates R_{\max} .

**The author is indebted to W. Gibbs and L. Lovell for the use of their fitting program.

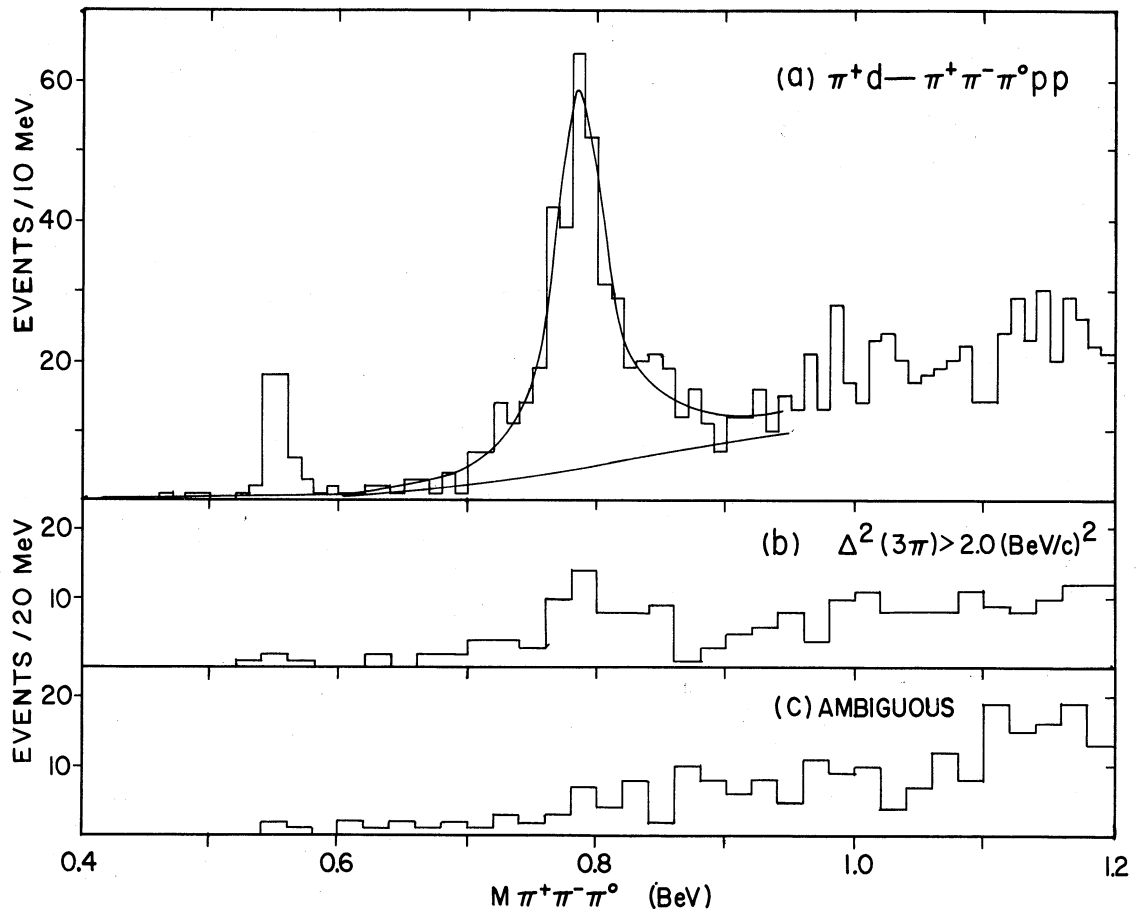


Figure 32. Invariant mass of $\pi^+\pi^-\pi^0$ (a) for all uniquely identified events, (b) for the subsample of (a) with $\Delta^2(3\pi) > 2.0 (\text{BeV}/c)^2$, and (c) for all events ambiguous with $\pi^+\pi^+\pi^-\text{pn}$.

$$N(M) = PS(M) \left[1 + \frac{\text{const.}}{(M - M_0)^2 + (\Gamma/2)^2} \right] .$$

Here, M is the three-pion mass, M_0 is the value of M at the peak, and Γ is the full width at half maximum of the resonance. The fitted values are

$$M_0 = 783 \pm 2 \text{ MeV}$$

$$\Gamma = 48 \pm 6 \text{ MeV} .$$

The presently accepted world average values are⁵⁸

$$M_0 = 782.8 \pm 0.5 \text{ MeV}$$

$$\Gamma_\omega = 12.0 \pm 1.7 \text{ MeV} .$$

We are in excellent agreement with M_0 . To compare Γ and Γ_ω we must subtract our estimated resolution in mass. Frazer, Fulco, and Halpern⁶⁴ have pointed out that the combination of two Breit-Wigner forms with widths Γ_ω and Γ_E gives a new Breit-Wigner form with width $\Gamma = \Gamma_\omega + \Gamma_E$. Since the curve fits our data nicely ($\chi^2 = 30$ for 47 degrees of freedom), and the ω^0 alone is probably Breit-Wigner in shape and in any case much narrower than our resolution, we conclude that our errors must be better represented by a Breit-Wigner curve rather than by a Gaussian curve.

Our resolution function (defined as a sum of Gaussian curves in Chapter III) calculated for 118 fitted ω^0 events has $\Gamma_E = 32 \text{ MeV}$. If we assume our overestimate of the π^0 mass (see Chapter III) calculated from unfitted variables will apply now to the fitted values of $M_{\pi^+\pi^-\pi^0}$,

this value of Γ_E must be divided by 1.2 ± 0.1 , giving $\Gamma_E = 27 \pm 2$ MeV.

Subtracting this from our fitted width gives

$$\Gamma_\omega = 21 \pm 6 \text{ MeV} .$$

This is in moderate agreement with the accepted value. We note that had we assumed $\Gamma^2 = \Gamma_\omega^2 + \Gamma_E^2$, as is appropriate for the addition of two Gaussians, we would be in disagreement with the accepted width.

We have examined the ω^0 peak in events with spectator momenta less than 150 MeV/c and greater than 150 MeV/c. This makes roughly two equal samples. If the ω^0 were interacting with the spectator proton, one might expect a broadening or (even less likely) a shifting of the peak. We find the two samples have the same peak position, and the ω^0 events with a slow spectator have a width about 14% broader than the total sample. Since this is just what we predict from our π^0 resolution functions for these two samples, we conclude we have no evidence for a final state ω^0 proton interaction.

The sharp ω^0 peak enables us to answer several questions about the one-constraint fitting process. The one-constraint fit is known to be rather "loose," and the question arises as to how much improvement in the three-pion mass resolution comes from the fitting process (i.e., from adjusting momentum components until the missing mass is that of a π^0). The answer from the mass squared plots of Figs. 33 (a) and (c) is that the fitting reduces the unfitted width by nearly 1/3, from $0.19 \pm 0.06 \text{ BeV}^2$ to $0.073 \pm 0.010 \text{ BeV}^2$. (Recall that $\Gamma(\text{BeV}^2) = 2M_0 \Gamma(\text{BeV}).$)

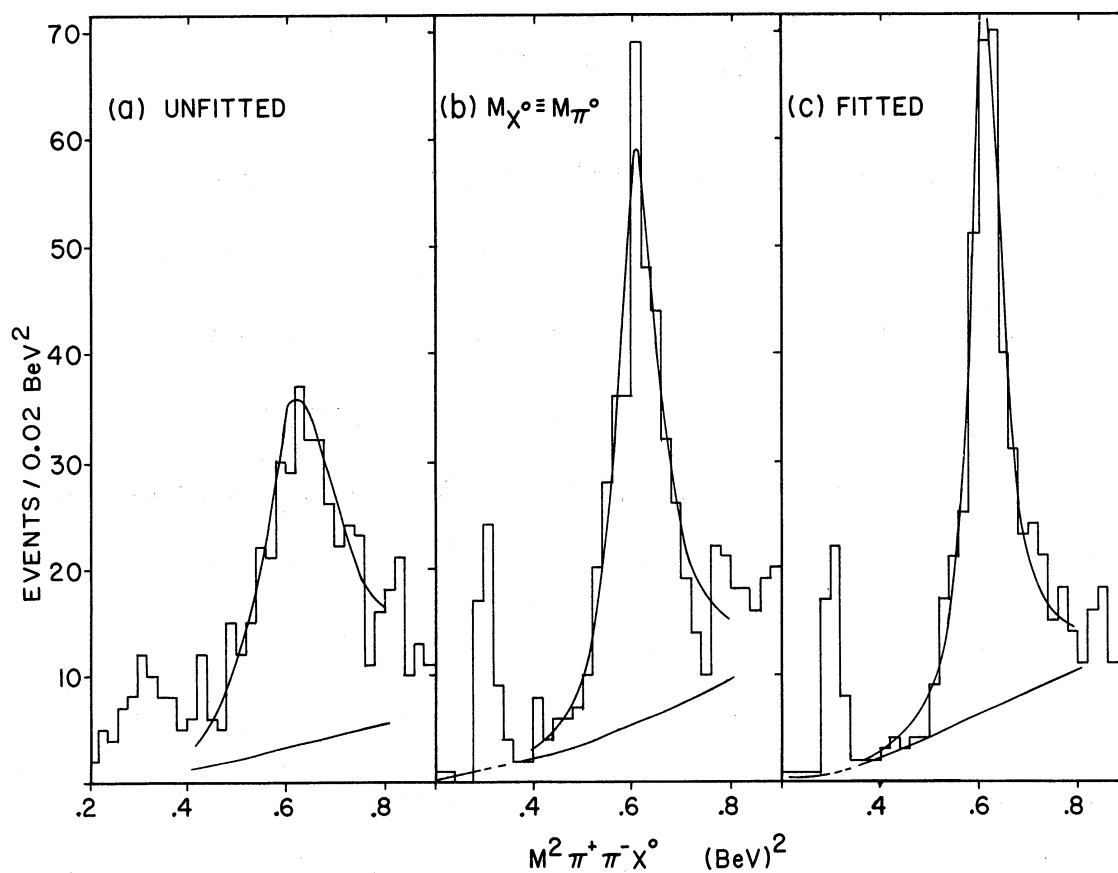


Figure 33. Invariant mass squared of the $\pi^+\pi^-\pi^0$ system (a) unfitted, (b) unfitted but with the mass of the neutral defined to be $M(\pi^0)$, and (c) fitted.

A second question is whether the same result will be obtained by calculating the momentum of the π^0 from momentum conservation and then calculating its energy from $E_{\pi^0}^2 = M_{\pi^0}^2 + P_{\pi^0}^2$ (i.e., ignoring the adjustments necessary to conserve energy). The answer is that the width is considerably reduced (by $\frac{1}{2}$) but not quite as much as by fitting. The width in Fig. 33 (b) is $0.102 \pm 0.016 \text{ BeV}^2$. This result is of practical importance. We used it in our search for $\eta^* \rightarrow \eta^0 \pi^+ \pi^-$; $\eta^0 \rightarrow$ all neutrals. These events originally did not fit any hypothesis. We defined all events of the type $\pi^+ \pi^- X^0$ pp to have $M(X^0) = M(\eta^0)$. After a calculation of the $\pi^+ \pi^- \eta^0$ invariant mass, the η^* was considerably sharper, thus confirming the presence of $\eta^* \rightarrow \pi^+ \pi^- \eta^0$ without a costly run through the programs needed for fitting.

B.2 Total and Differential Cross Section

To obtain the ω^0 cross section we count the events above the phase space curve of Fig. 32. We have some confidence in this background estimate since it nearly agrees with (is 10% higher than) the background predicted by the dashed curve of Fig. 21. Our cross section for 359 events above background is

$$\sigma(\omega^0 \rightarrow \pi^+ \pi^- \pi^0) = 0.46 \pm 0.05 \text{ mb} .$$

The quoted 11% error includes 9% normalization, 5% statistical, and 5% background uncertainties. Assuming $(\omega^0 \rightarrow \pi^+ \pi^- \pi^0)/(\omega^0 \rightarrow \text{all}) = 0.90 \pm 0.05$,⁵⁸ we get

$$\sigma_{\text{tot}}(\omega^0) = 0.50 \pm 0.06 \text{ mb} .$$

It is often useful to have cross sections with a Δ^2 cut, so we also give values for

$$\Delta^2(\omega^0) < 1.0(\text{BeV}/c)^2, \sigma(\omega^0 \rightarrow \pi^+\pi^-\pi^0) = 0.35 \pm 0.04 \text{ mb} ,$$

and for

$$\Delta^2(\omega^0) > 1.0(\text{BeV}/c)^2, \sigma(\omega^0 \rightarrow \pi^+\pi^-\pi^0) = 0.11 \pm 0.02 \text{ mb} .$$

This is essentially the same result as was reported previously⁶⁵ based on 76 ω^0 events, but the error has been reduced to 2/3 the previous value.

The $\Delta^2(\omega^0)$ distribution is given in Fig. 34. (For the rest of this section we define $M(\omega^0) = 0.72$ to 0.86 BeV. This leaves a sample of 394 events of which 18% (71 events) are non- ω^0 background events.) To estimate whether or not any ω^0 mesons are produced with high $\Delta^2(\omega^0)$, the mass plot for only those events with $\Delta^2(\omega^0) > 2.0 (\text{BeV}/c)^2$ is shown in Fig. 32 (b). There does seem to be an ω^0 peak. We expect a slightly broader ω^0 at high Δ^2 due to our decreasing resolution (see Table IV).

About 14% of the ω^0 mesons have $\Delta^2 > 2.0 (\text{BeV}/c)^2$. For comparison, about 6% of the η^0 events have $\Delta^2 > 2.0 (\text{BeV}/c)^2$, and for the whole $\pi^+\pi^-\pi^0$ channel about 17% have $\Delta^2 > 2.0 (\text{BeV}/c)^2$. The lack of any evidence for ω^0 in the ambiguous events (Fig. 32 (c)) is consistent with our estimate that 3/4 of these ambiguous events do not have a π^0 present.

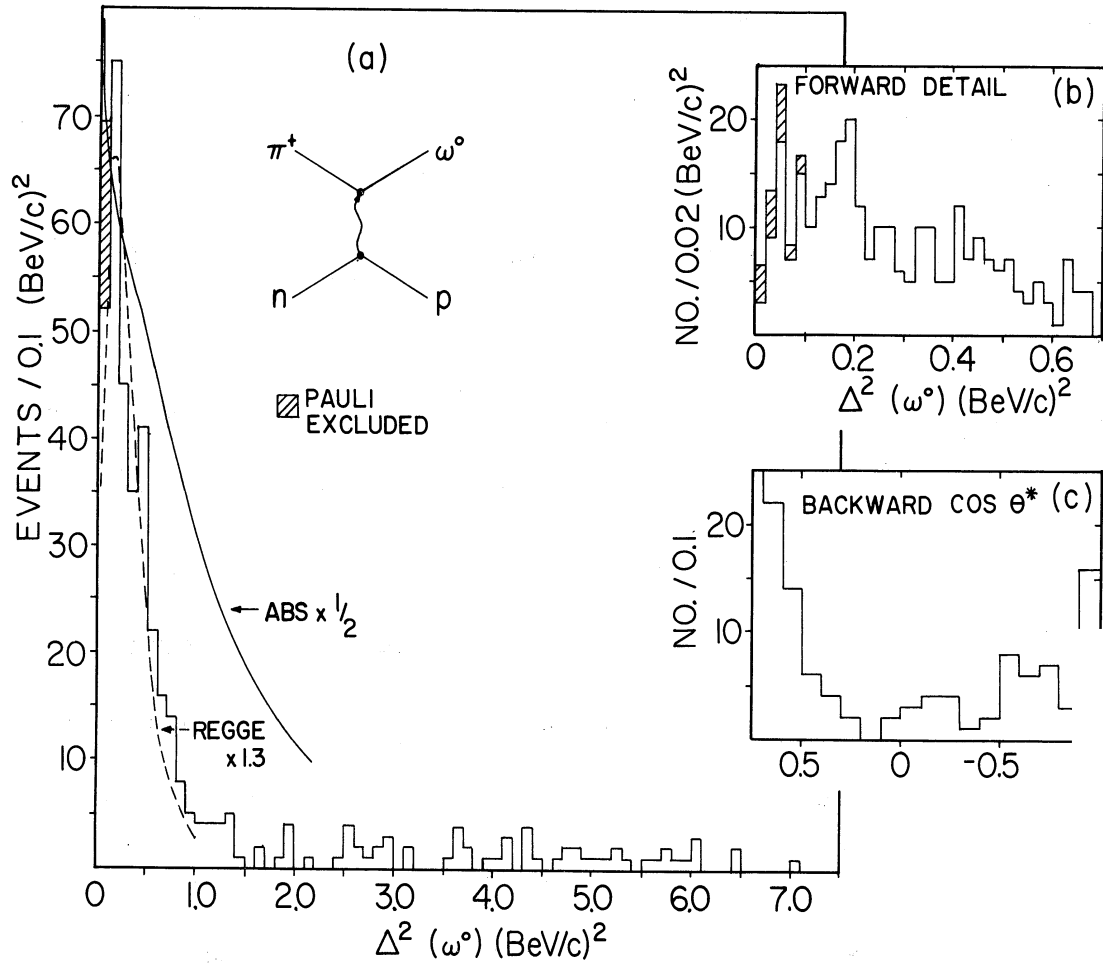


Figure 34. (a) Histogram of $\Delta^2(\omega^0)$ for $M(3\pi) = 0.72 - 0.86 \text{ BeV}$, (b) detail of the forward direction, and (c) the production angular distribution in the backward direction. The shaded events are added to compensate for the loss of events by Pauli exclusion. The theoretical curves are (solid) absorption model and (dashed) Regge pole model.

An exponential fit of the Δ^2 distribution for the ω^0 events gives a slope of $3.0 \pm 0.3 \text{ (BeV/c)}^{-2}$. This is similar to the average slope of $3.4 \pm 0.2 \text{ (BeV/c)}^{-2}$ which was determined from the events in this channel with $M(3\pi) > M(\omega^0)$. It is possible, therefore, that the ω^0 events and the background events under the ω^0 have roughly the same distribution in Δ^2 . The correct normalization for the events in Fig. 34 with $\Delta^2 < 1.9 \pm 0.3 \text{ (BeV/c)}^2$ is $1.1 \pm 0.1 \text{ } \mu\text{b/event}$. For events with $\Delta^2 > 1.9 \pm 0.3 \text{ (BeV/c)}^2$ the normalization is $1.6 \pm 0.3 \text{ } \mu\text{b/event}$. These values are chosen so that the sum over the unshaded events of the plot gives $\sigma(\omega^0 \rightarrow \pi^+\pi^-\pi^0) = 0.46 \pm 0.5$. It thus assumes that the background events have the same distribution as the resonant events. The theoretical effect of Pauli exclusion on the two final state protons (see Table III, ρ exchange, $\beta = 5.18\alpha$) is illustrated by the shaded events which have been added to the events we observe. The cross section should increase by this amount (a total of 4%) if the experiment were performed on a free nucleon. There are no hydrogen results available at present for $\pi^-p \rightarrow \omega^0n$.

B.3 Predictions of Absorption and Regge Models

The results of ω^0 production in this channel are very important for testing particle exchange models since the only known particles which can be exchanged in production are the ρ and B mesons. (The diagram is in Fig. 34.) If the B meson were "real," the fact that it decays mostly to $\omega^0\pi$ would make it a very likely contributor to ω^0 production in spite of the fact that it has a higher mass than the ρ meson. The

B meson has not been seen, however, in compilations of data,⁶⁶ and has been interpreted as a kinematical effect.⁶⁷ For this reason it is not generally included in theoretical predictions for our ω^0 . Recently the B meson has been revived by a sighting of it in the reaction $\bar{p}p \rightarrow \omega^0 + \pi^+ \pi^-$,⁶⁸ but we will include only the ρ meson in what follows until the density matrix of the ω^0 is discussed.

The dashed curve in Fig. 34 (a) is the prediction of the Regge pole model⁶⁹ with its magnitude increased by 1.3. The solid curve is a one-rho exchange prediction with absorption⁷⁰ but decreased in magnitude by $\frac{1}{2}$. The parameters used for the absorption model are $\gamma_1 = 0.04$, $C_1 = 0.75$, $\gamma_2 = 0.03$, $C_2 = 1.0$, and $G_T/G_V = 3.7$. These are discussed in detail in the review article by Jackson;⁷¹ however, we note here that these parameters control the initial and final state absorption respectively. The elastic amplitudes in the initial state are approximated by

$$e^{2i\delta_j(l)} = 1 - C_1 e^{-\gamma_1(x - \frac{1}{2})^2}.$$

Here, $x = j + \frac{1}{2}$ is the integration variable for j , the angular momentum of the partial wave,

$$C_1 = \frac{\sigma_T(l)}{4\pi A_1},$$

$$\gamma_1 = \frac{1}{2q^2 A_1},$$

$\sigma_T(l)$ is the total cross section for scattering in the initial state, q is the incident center of mass momentum, and A_1 is the elastic slope

parameter of $d\sigma_{el}/dt \propto e^{A_1 t}$. Similar relations hold for the final state. Looking at these one can see that the value of $C_2 = 1.0$ implies complete absorption of relative s-wave final states ($x = \frac{1}{2}$). The absorption in the initial $\pi^+ n$ system can be determined from $\pi^- p$ elastic scattering, but the $\omega^0 p$ final state parameters must be guessed. It has been pointed out⁷² in ω^0 production that anything less than $C_2 = 1.0$ is totally incompatible with the observed differential cross section.

The value of $G_T/G_V = 3.7$ used by Jackson is taken from the isovector magnetic moment of the nucleons. An alteration of G_T/G_V can radically change the shape of the solid curve of Fig. 34. These altered curves may be seen in the literature.^{72,73} The value $G_T/G_V = 2$ can cause the predicted curve to decrease rather than increase below $\Delta^2 = 0.1$ (BeV/c)² and considerably improve the fit. The value of G_T/G_V used by Barmawi⁶⁹ in the Regge calculation is 2.98. The magnitude of the cross section is governed by the $\pi\rho\omega$ and $n\rho p$ coupling constants. The choice $(f^2/4\pi) = 20$, was used in the absorption calculation while 26.7 was used in the Regge calculation.

The prediction dependence of the cross section for increasing beam energy is increasing (decreasing) with the absorption (Regge) model. Experimentally⁷² the cross section is decreasing and cannot, therefore, be described by the absorption model.

B.4 Density Matrix Elements

We now determine the spin state of the ω^0 . This is done in the density matrix formalism. (Properties of the density matrix are discussed

in Appendix K.) Recall that the density matrix diagonal elements ρ_{mm} give the percentage of states which have a spin component, m , along the z axis in the chosen coordinate system. This system is shown in Fig. 35 (a). We follow the coordinate prescription given by Gottfried and Jackson.⁷⁴ The z axis is along the beam as seen in the ω^0 rest frame. The y axis is the normal to the production plane with the direction $\hat{\text{beam}} \times \hat{\omega}^0$. (The opposite direction causes $\text{Re}\rho_{10} \rightarrow -\text{Re}\rho_{10}$.) The x axis is $\hat{y} \times \hat{z}$. The normal to the decay plane is calculated in the ω^0 rest frame with the direction $\hat{\pi}^- \times \hat{\pi}^+$ which is arbitrary as far as the theory is concerned.

The range of allowed values for ρ_{00} is $0 \leq \rho_{00} \leq 1$. If the ω^0 is produced completely at random then $\rho_{00} = 1/3$. The value of ρ_{11} is obtained from ρ_{00} by the usual normalization condition $\rho_{11} = (1-\rho_{00})/2$. Thus $0 \leq \rho_{11} \leq 0.5$ and $1/3$ is again the random value. The physical meaning of the other elements of the density matrix is less obvious. They can be interpreted as expectation values of sums of products of angular momentum operators (see Appendix K). A determination of the entire density matrix specifies all the physical information contained in the spin state.

Our value of $\rho_{00}(0.40 \pm 0.04)$ is determined by a least squares fit to the angular distributions of the decay plane normal relative to the beam direction (Fig. 35 (b)). The expression for any $J^P = 1^-$ particle decaying into three spinless particles is⁷⁵

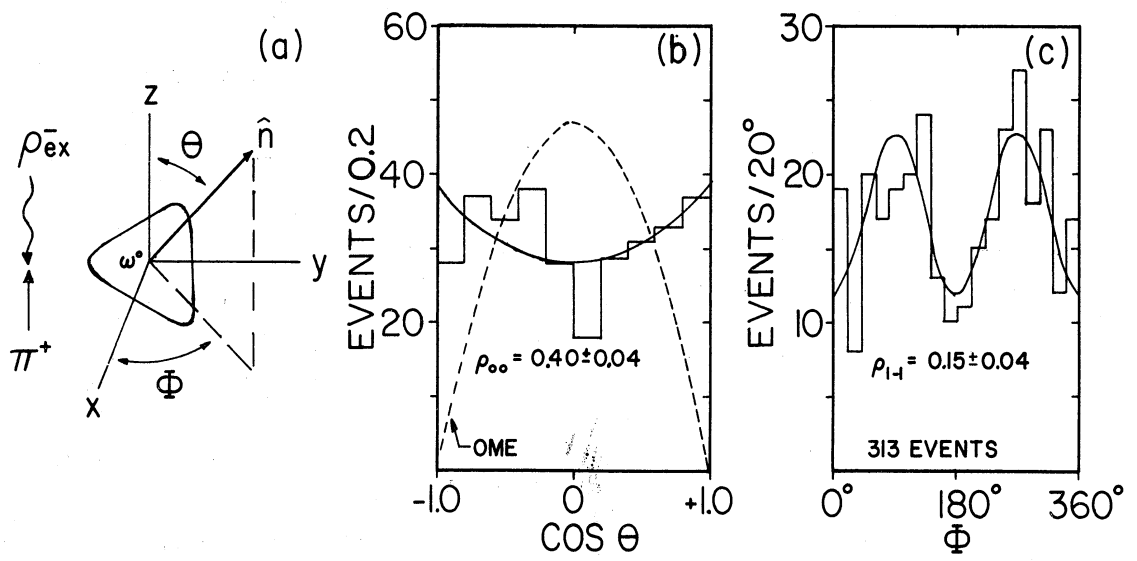


Figure 35. (a) Coordinate system in the rest frame of the ω^0 , (b) and (c) experimental distributions for the normal to the decay plane. The solid curves are fitted. The dashed curve is the prediction based on one-meson exchange.

$$\frac{dW}{d \cos \theta} = \frac{3}{2} \left[\frac{1}{2} (1 - \rho_{00}) \sin^2 \theta + \rho_{00} \cos^2 \theta \right] .$$

Our value of ρ_{1-1} (0.15 ± 0.04) is obtained from the azimuthal angle ϕ by fitting

$$\frac{dW}{d\phi} = \frac{1}{2\pi} (1 - 2\rho_{1-1} \cos 2\phi)$$

to the data of Fig. 35 (c). The histogram was folded at 180° and summed prior to fitting. Jackson has shown that ϕ is the same as the Treiman-Yang angle.⁷⁶

We use an averaging method to determine $\text{Re}\rho_{10}$, i.e.,

$$\text{Re}\rho_{10} = -\frac{5}{4\sqrt{2}} \langle \sin 2\theta \cos \phi \rangle = -0.08 \pm 0.03 .$$

These values are for all events with $\Delta^2 < 1.0 \text{ (BeV/c)}^2$ and $M(3\pi) = 0.72 - 0.86 \text{ BeV}$. As suggested by Minnaert,⁷⁷ and independently by Dalitz, an upper limit can be set on the only remaining undetermined element of the density matrix $\text{Im}\rho_{10}$ (see Property 7' of Appendix K). Our experimental limit is

$$|\text{Im}\rho_{10}| \leq 0.15 .$$

From this and the equation for δ^2 in Appendix K, we deduce that the degree of polarization, δ , ($0 \leq \delta \leq 1$) of these ω^0 events lies between

$$0.3 \leq \delta \leq 0.5 .$$

These last two results neglect the uncertainties in the measured values

of the density matrix elements.

We have determined ρ_{00} for the left and right halves of the ω^0 peak ($\Delta^2 < 1.0$) separately to see what influence unsubtracted background might have. The measuring errors in the two samples should be the same, but the background level is 50% greater in the right half. The near equality of these two values ($\rho_{00}(\text{left}) = 0.39 \pm 0.07$ and $\rho_{00}(\text{right}) = 0.42 \pm 0.05$) suggests that background effects are negligible. We have also determined ρ_{00} for the events with a spectator of momentum less than 0.150 BeV/c (0.42 ± 0.06) and greater than 0.150 BeV/c (0.41 ± 0.06) to see if there is any dependence. Again we find no dependence.

The density matrix for ω^0 production with a beam pion has been studied in other reactions, and in this reaction at other energies.^{48,78} A summary is shown in Table V. It is remarkable how similar all of the results are. It is possible that experimental problems (backgrounds, measuring errors, etc.) cause the differences in results rather than fundamental differences in the production process. Because the unmodified ρ -meson exchange model predicted $\rho_{00} = 0$, many of the early studies of ω^0 production concluded that ρ exchange was not the dominant production mechanism. The dashed curve of Fig. 35 (b) shows the angular prediction for ρ -meson exchange. (The prediction of $\rho_{00} = 0$, briefly, is made as follows. Because we use the beam as a quantization axis, all orbital angular momentum states, J , have $J_z = m = 0$. To make an ω^0 , $J^P = 1^-$, in a state $\psi_J^m(\omega^0) = \psi_1^0(\omega^0)$ we have, therefore, to couple an orbital state of $\psi_1^0(\text{orbital})$ to a ρ -meson spin state of $\psi_1^0(\rho)$.

TABLE V

DENSITY MATRIX ELEMENTS FOR THE ω^0 FROM OTHER EXPERIMENTS

Beam (BeV/c)	Reaction	Δ^2 (BeV/c ²)	ρ_{00}	ρ_{1-1}	Re ρ_{10}
2.75 ^a	$\pi^- p \rightarrow \omega_{N33}^{*0}$	all	0.44 ± 0.10	0.19 ± 0.07	0.05 ± 0.04
2.75 ^a	$\pi^+ p \rightarrow \omega_{N33}^{*++}$	< 0.8	0.56 ± 0.02	0.02 ± 0.02	-0.02 ± 0.02
3.65 ^b	$\pi^+ p \rightarrow \omega_{N33}^{*++}$	< 0.6	0.45 ± 0.06	-0.02 ± 0.05	-0.14 ± 0.03
4.0 ^a	$\pi^+ p \rightarrow \omega_{N33}^{*++}$	< 0.6	0.47 ± 0.05	0.13 ± 0.05	-0.10 ± 0.03
1.7 ^a	$\pi^+ n \rightarrow \omega_p^0$	< 0.4	0.56 ± 0.04	-0.05 ± 0.06	-0.06 ± 0.04
3.25 ^a	$\pi^+ n \rightarrow \omega_p^0$	all	$0.62^{+0.15}_{-0.04}$	0.19 ± 0.05	0.25
3.65 ^c	$\pi^+ n \rightarrow \omega_p^0$	< 1.0	0.40 ± 0.04	0.15 ± 0.04	-0.08 ± 0.03

a. Reference 78

b. Reference 48

c. This experiment

Because a $\psi_1^0(\text{orbital}) \times \psi_1^0(\rho)$ state will not couple to $\psi_1^0(\omega^0)$ (zero Clebsch-Gordan coefficient), the $\psi_1^0(\omega^0)$ state cannot be populated at all, and $\rho_{00} = 0$.) One of the most important contributions of the absorption model is that it shows that the ω^0 spin states are, after all, compatible with a ρ -exchange model.

The absorption predictions by Jackson are shown in Fig. 36. We have broken the data into three roughly equal parts, $\Delta^2(\omega^0) < 0.2$, $0.2-0.5$,

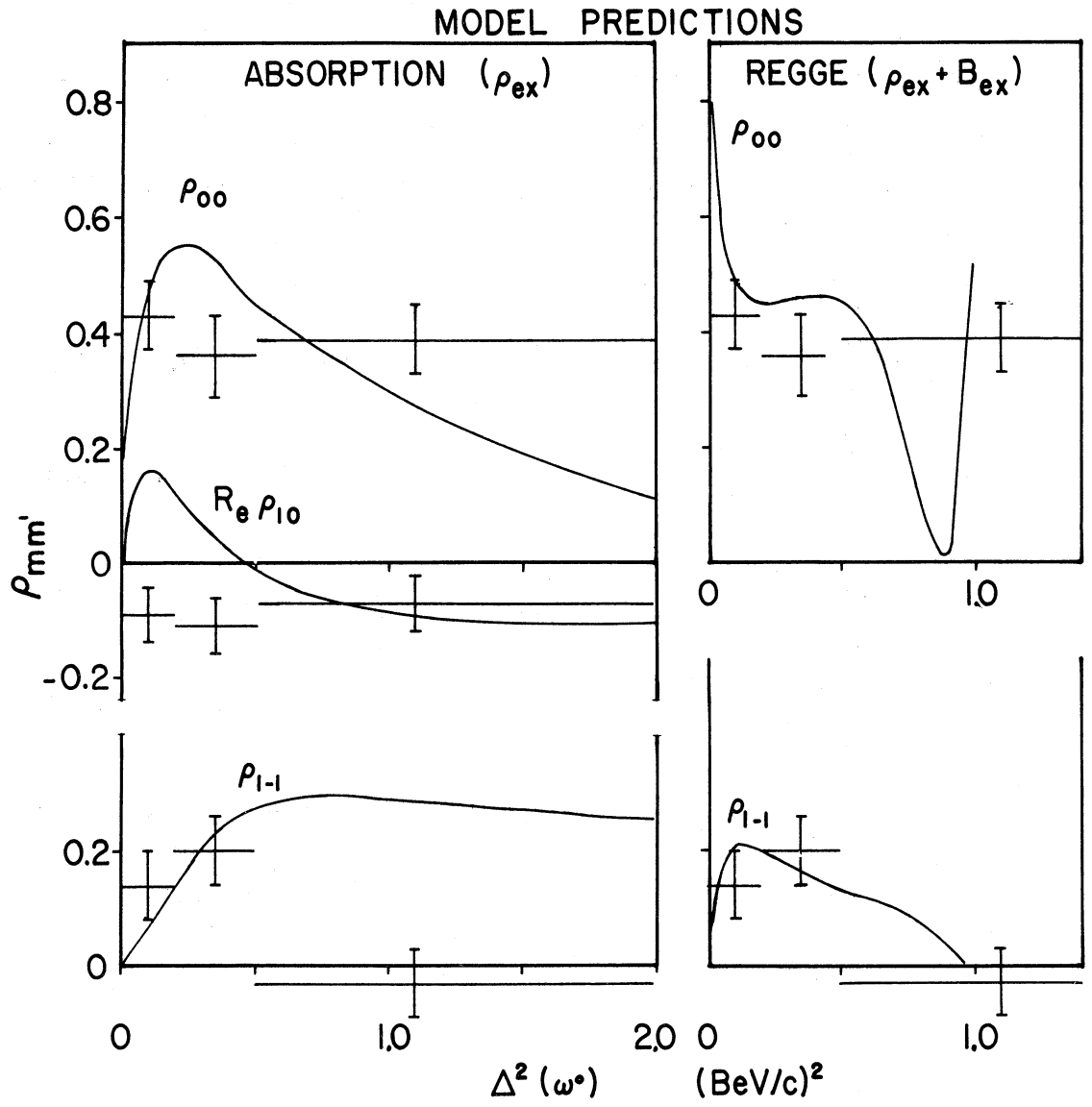


Figure 36. Density matrix predictions of the absorption model based on ρ -meson exchange and the Regge pole model based on ρ - and B-meson exchange.

and $> 0.05 \text{ (BeV/c)}^2$ (see Table VI), and determined the density matrix for each part. The parameters used in the theory were discussed with the momentum transfer discussion. The effect of variation of the parameters on the density matrix may be found in the work of Jackson, et al.⁷² We note that the predictions⁷⁰ shown in Fig. 36 differ slightly from older calculations in that they have been calculated with an exact partial wave sum for the helicity amplitudes rather than the Bessel function approximations used previously.⁷²

TABLE VI

DENSITY MATRIX ELEMENTS FOR THE ω^0 FROM THIS EXPERIMENT

$\Delta^2(\omega^0)$ (BeV/c) ²	ρ_{00}	χ^2 Prob.	ρ_{1-1}	χ^2 Prob.	Re ρ_{10}
< 1.0	0.40 ± 0.04	30%	0.15 ± 0.04	15%	-0.08 ± 0.03
< 0.2	0.43 ± 0.06	10%	0.14 ± 0.06	15%	-0.09 ± 0.05
$0.2-0.5$	0.36 ± 0.07	90%	0.20 ± 0.06	40%	-0.11 ± 0.05
> 0.5	0.39 ± 0.06	0.5%	-0.03 ± 0.06	15%	-0.07 ± 0.05

Also shown are the predictions for the density matrix calculated for 3.25 BeV/c by Barmawi.⁷⁹ These values are based on the Regge pole model with two contributing trajectories, $J^{PG} = 1^{-+}$ (assumed ρ meson) and $J^{PG} = 1^{++}$ (assumed B meson). As pointed out by Barmawi, if only ρ exchange is allowed, the Regge pole model would give the same predictions as the unmodified one-meson exchange model, i.e., $\rho_{00} = 0$ and $\rho_{10} = 0$ for all values of $\Delta^2(\omega^0)$.

We consider that our density matrix data is moderately compatible with either the absorption or the Regge pole calculation. The value of ρ_{1-1} at large Δ^2 is interesting, but because the average is taken over a very large range of Δ^2 values to gain statistics, it needs further study. In view of the possibly slow variation of $\rho_{mm'}$ with beam energy, it might be interesting and useful to compile data from different energies in order to get a better determination of the dependence of $\rho_{mm'}$ on $\Delta^2(\omega^0)$.

Concerning the models, if the B meson does not become a respectable member of an established nonet, ω^0 production will be left with the Regge model describing the differential and total cross sections and with the absorption model describing the density matrix. One would hope that a theoretical merger might take place. It is perhaps no surprise that such a merger has already been proposed.⁸⁰

B.5 Dalitz Plot Density

We now show that the Dalitz plot density for the ω^0 events is consistent with the simplest matrix element prediction⁶² for an $I, J^P = 0, 1^-$ particle, which is

$$\frac{dW}{dR^2} \propto 1 - (R/R_{\max})^2,$$

where R is the distance in MeV of the event from the center of the Dalitz plot, and R_{\max} is the maximum distance from the center that is kinematically allowed. Integrating this between R_1^2 and R_2^2 gives

$$\Delta W = \int_{R_1^2}^{R_2^2} dW \propto [R_2^2 - R_1^2] [1 - (R_1^2 + R_2^2)/(2R_{\max}^2)] .$$

Thus the prediction is a straight line of negative slope, provided constant intervals in $R_2^2 - R_1^2$ are chosen. Background events should be distributed uniformly since this is what we observe in the three-pion mass region just above the ω^0 .

Our results for the ω^0 events with $M(3\pi) = 0.72 - 0.86$ BeV are shown in Fig. 31 (b). The χ^2 probability is only 5% that the data fit the prediction (with 18% of the events being background).

Of the possible causes of this discrepancy, we rule out a poor estimate of the background-to-resonance ratio because of the high χ^2 of the fit in mass and the agreement with the phase space estimate extrapolated from the higher mass phase space. We also rule out the possibility that the simplest matrix element approach is incorrect since it agreed with the results from a large sample of 4600 events of $K^-p \rightarrow \omega^0 \Lambda^0$ at 1.2 - 1.8 BeV/c.⁸¹ Suspecting then that measuring errors might be more important than we previously thought, we plotted only the events in the center of the ω^0 mass peak as seen in Fig. 37. The predicted distribution shown with the events has a χ^2 probability of 95%.

To check the conjecture that measuring errors were at fault, the momentum of the most poorly measured track was changed in three events by plus and minus one standard deviation. This changed the mass by an average of ± 3 MeV and the position on the $(R/R_{\max})^2$ plot by an average of ± 0.03 . Thus the same measuring errors that give us ω^0 events as

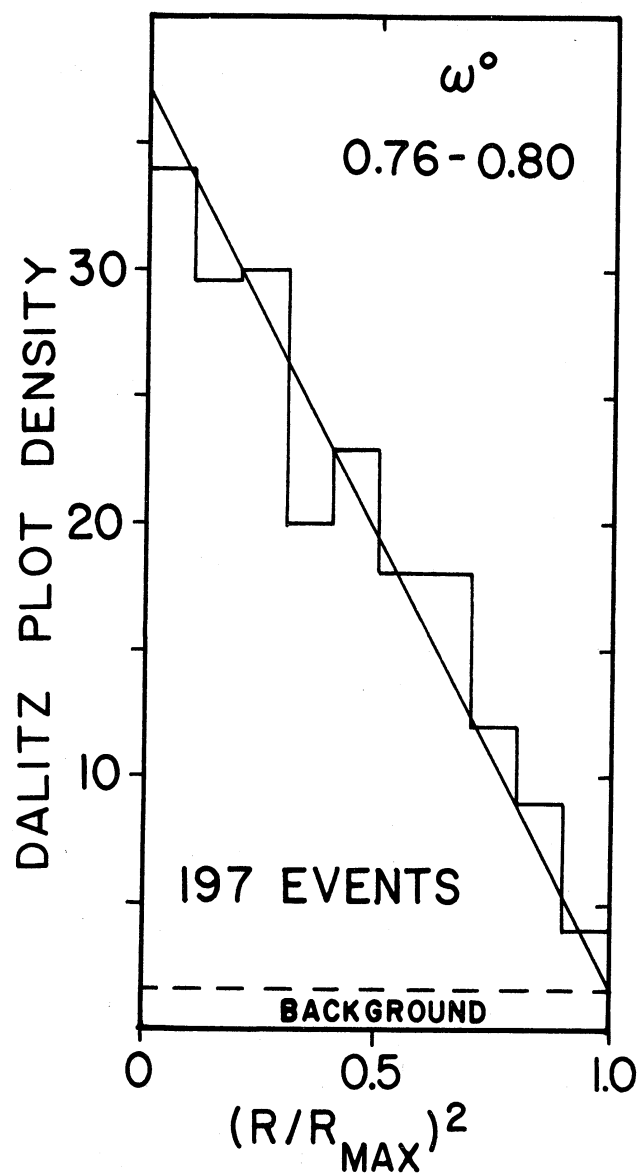


Figure 37. Dalitz plot density and theoretical curve for ω^0 decay.

much as 50 MeV from the central mass value can seriously distort the Dalitz plot density. The net shift in the events should be radially outward, of course, since the theoretical distribution is peaked in the center. We have not found any similar effect in the decay plane normal. It is more difficult to detect in this case, however, because theory does not predict any points in the plots where the data must vanish.

C. $\pi^+ d \rightarrow H^0 pp$

The H meson is the least well established of the mesons discussed in this report. The presence of the H meson has been reported in one previous experiment at 4.0 BeV/c in the reaction $\pi^+ p \rightarrow \pi^+ \pi^- \pi^0 N^{*++}$.⁸² Events from this channel, $\pi^+ d \rightarrow \pi^+ \pi^- \pi^0 pp$, but at 5.1 BeV/c, which showed no evidence for the H, were reported at the Berkeley Conference (1966). The J^P assignment is unsettled although it appears to be 1^+ . The H meson should therefore continue to be an interesting object of study.

Some of the following text and figures have been reported previously.⁸³ Most of the analysis and text on the isotopic spin and Dalitz plot variables is due to J. Vander Velde but is included here for completeness.

Many of the properties of the H meson are reminiscent of the A_1 (e.g., $\rho\pi$ decay, location near $\rho\pi$ threshold, and $\cos^2\theta$ distribution of the $\pi\pi$ scattering angle). This at first made us question the resonant nature of the H. There are two important differences. From the relative amounts of $H^0 \rightarrow \rho^+ \pi^-$: $\rho^0 \pi^0$: $\rho^- \pi^+$ (as observed in both experiments), a Deck production mechanism⁸⁴ can be ruled out. Because the H peak is

gone when the ρ band overlap is greatest (1100 MeV), it is doubtful that the effect is a triangle singularity.⁸⁵

C.1 Mass Distributions

Figure 38 shows the $\pi^+\pi^-\pi^0$ mass spectra for this experiment* with the previous evidence⁸² for the H superimposed and shaded. In both sets of data it is required that at least one of the dipion masses be in the rho region (650-850 MeV for our data, 640-860 for the others). A further requirement in the ABBBHLM data is that one of the $\pi^+\rho$ combinations is in the $N^*(1238)$ region. The curve illustrated, which applies only to our data, was calculated by multiplying that fraction of an isotropic Dalitz plot that contains at least one rho by a three-pion phase space. We have made a similar calculation using a Dalitz plot density appropriate for an $I = 0$, $J^P = 1^+$ three-pion state decaying into $\rho\pi$ via s-wave. This increases the $1 \text{ BeV}/c^2$ shoulder somewhat but still falls far short of explaining the bump in the data.

In an effort to remove some of the background from the H region we have made the following additional cuts on the data. (1) We require $\Delta^2(H) < 0.85 (\text{BeV}/c)^2$. (2) $\rho^0 N^{*+}(1238)$ and $\rho^+ N^{*0}(1238)$ events are removed if $\Delta^2(\rho) < 0.2 (\text{BeV}/c)^2$. The resulting mass distribution is shown in Fig. 39. This leaves 129 events in the H region (0.92 - 1.08 BeV). Fitting these events (a fitted curve is shown), with and without the $\Delta^2(H)$ cut, to a Breit-Wigner resonance form gives an average value

* The discovery of the H peak in this data was made by E. Marquit.

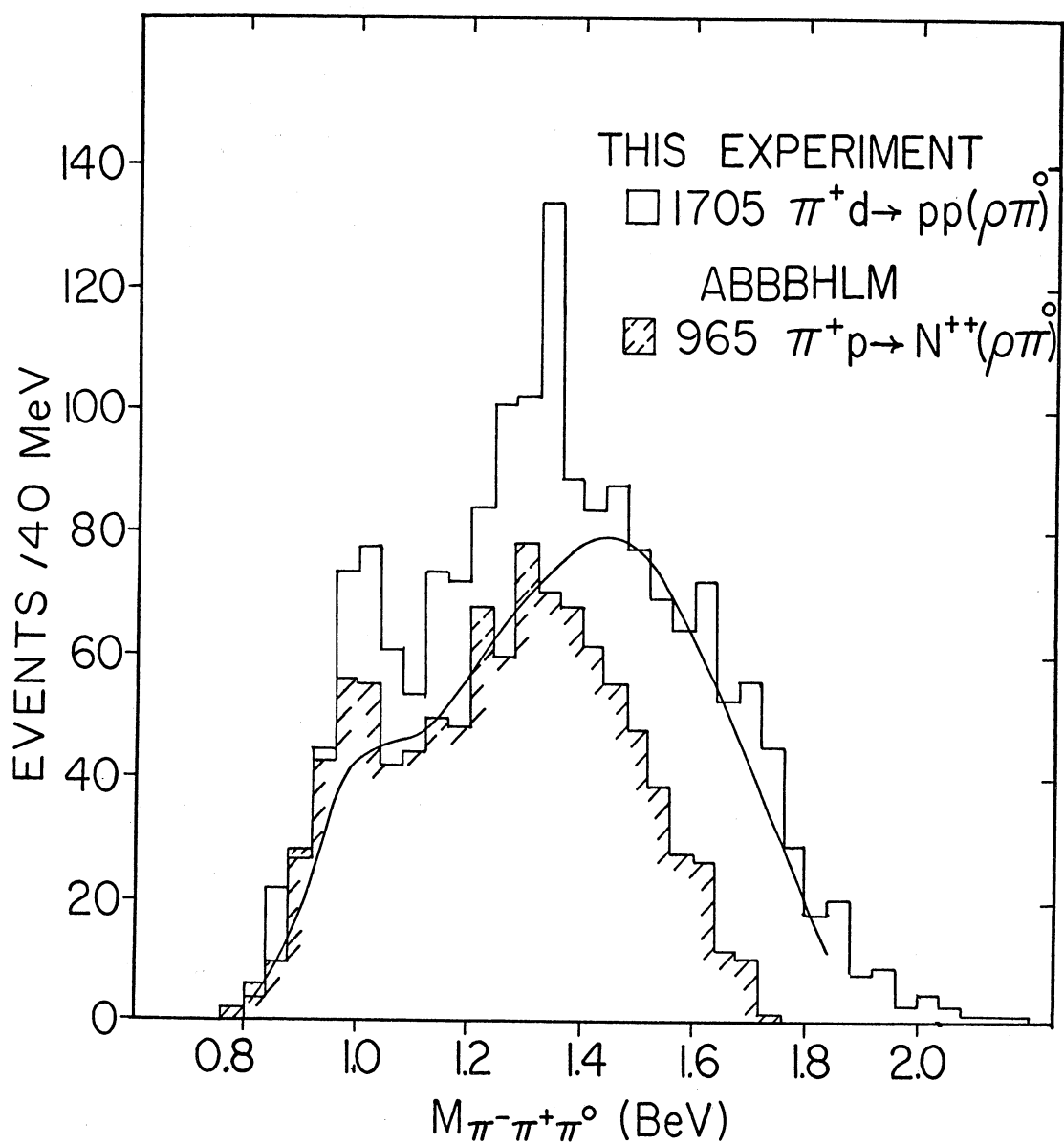


Figure 38. Invariant mass of the $\pi^+\pi^-\pi^0$ system for events with ρ^+ , ρ^- , or ρ^0 . The outer histogram is data from this experiment and the superimposed shaded histogram is from Ref. 82.

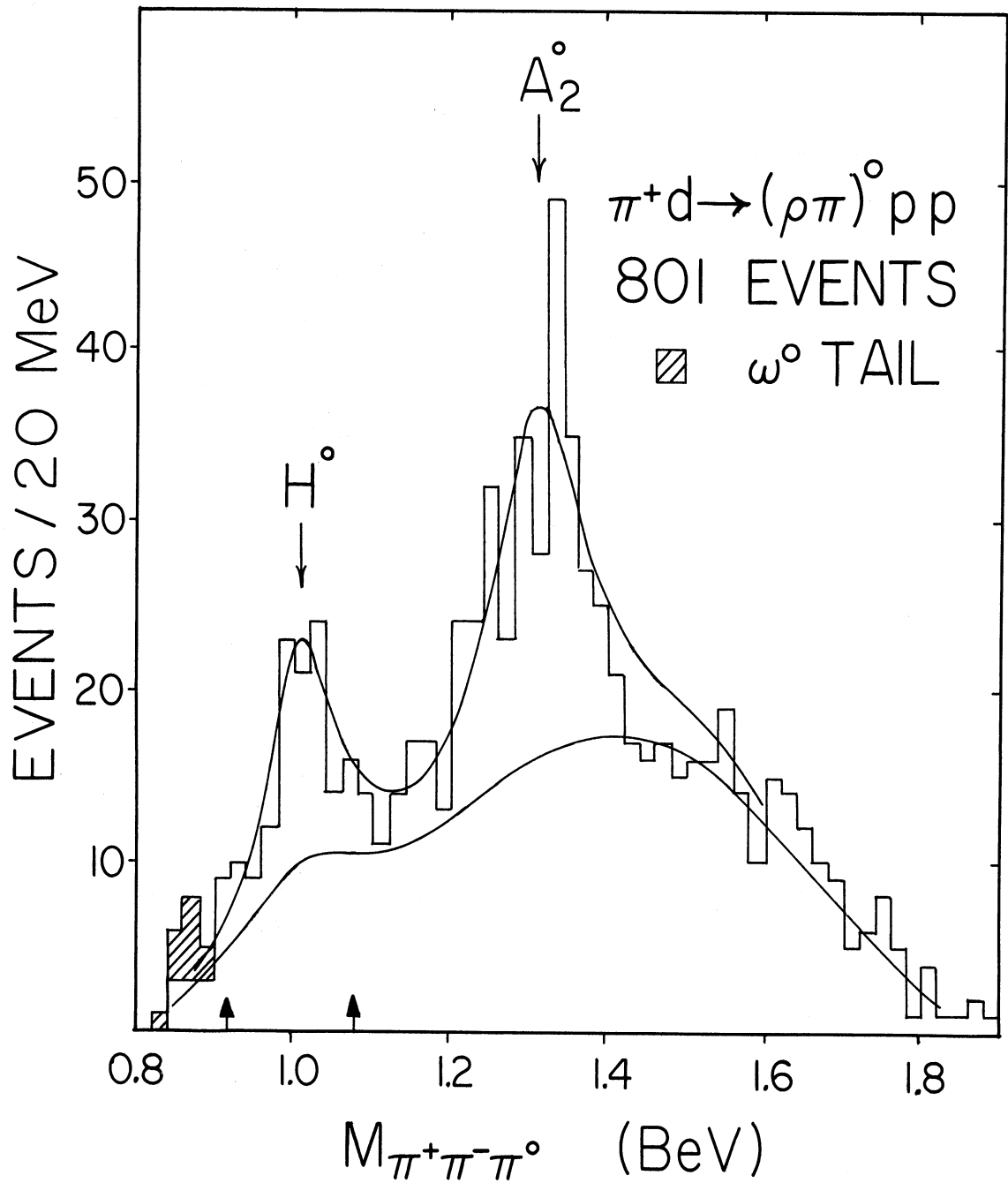


Figure 39. Invariant mass of $\pi^+\pi^-\pi^0$ after requiring ρ^+ , ρ^0 , or ρ^- and $\Delta^2(3\pi) < 0.85 \text{ (BeV/c)}^2$. The events with $\rho^+ N^{*0}(1238)$ or $\rho^0 N^{*+}(1238)$ have been removed if $\Delta^2(\rho) < 0.2 \text{ (BeV/c)}^2$. The fitted curve has $M(H) = 1007$, $\Gamma(H + \text{resolution}) = 84$, $M(A_2) = 1305$, and $\Gamma(A_2 + \text{resolution}) = 139 \text{ MeV}$. The phase space has been peripheralized as discussed in the Appendix.

$$M(H) = 998 \pm 10 \text{ MeV}$$

and $\Gamma(H + \text{resolution}) = 75 \pm 30 \text{ MeV}$. This is to be compared with the ABBBHL⁸² results of $M(H) = 975 \pm 15 \text{ MeV}$ and $\Gamma = 120 \text{ MeV}$. The differences are probably due to differences in the assumed form of phase space. Subtracting our resolution of 30 MeV from $\Gamma(H + \text{resolution})$ gives

$$\Gamma(H) = 45 \pm 30 \text{ MeV} .$$

This linear subtraction procedure gives reasonable widths for both the ω^0 and A_2^0 . It is suggested by the Breit-Wigner shapes of our π^0 and ω^0 mass distributions as discussed with the ω^0 data. Table VII summarizes our resolution as a function of three-pion mass. These uncorrected values must still be multiplied by 0.83 as discussed in Chapter III. Our production cross section for the H is $(75 \pm 15) \mu\text{b}$ above background after making the subtractions mentioned above.

TABLE VII

RESOLUTION OF THE $\pi^+ \pi^- \pi^0$ MASS (UNCORRECTED)

$M(3\pi)(\text{BeV})$	Resolution (MeV)
< 0.7	21
$0.7 - 0.9$	32
$0.9 - 1.2$	36
$1.2 - 1.4$	38
$1.4 - 1.8$	44

C.2 Isotopic Spin

Figure 40 shows the sum of our data and that of ABBBHLM. The lower histogram is a compilation⁸⁶ of data on $\pi^\pm p \rightarrow \rho^0 \pi^\pm p$ showing the $A_1^+(1080)$ enhancement. It is clear from this that the H is not the neutral member of an A_1 triplet. The lack of an H effect in the lower histogram is evidence that the H does not have $I = 1$ since charge independence requires $\sqrt{\sigma_+} + \sqrt{\sigma_-} \geq \sqrt{\sigma_0}$, where $\sigma_+ = \sigma(\pi^+ p \rightarrow H^+ p)$, $\sigma_- = \sigma(\pi^- p \rightarrow H^- p)$, $\sigma_0 = \sigma(\pi^+ n \rightarrow H^0 p)$. (We have left out a factor of 2 under the radical on the right hand side of the inequality because the $\rho^\pm \pi^0$ mode is not normally observed for H^\pm .) $I = 2$ for the H is ruled out since this would mean $\sigma_+ : \sigma_- : \sigma_0 = 3 : 3 : 4$. The observed A_1^\pm cross sections at these energies are about 100 μb .

The 129 events divide into 45 $\rho^+ \pi^-$, 42 $\rho^0 \pi^0$, and 42 $\rho^- \pi^+$, and include 17 double ρ events in which two of the three dipions fall in the ρ region. If the H has $I = 0$ (1 or 2), one expects the ratios of events in the above three categories to be 1 : 1 : 1 (1 : 0 : 1 or 1 : 4 : 1). The single ρ events are shown in Fig. 41. To make our treatment of background completely symmetric, three events of the 42 $\rho^- \pi^+$ events should be subtracted since they also fall in the $\rho^- N^{*++}$ region with $\Delta^2(\rho^-) < 0.2 \text{ (BeV/c)}^2$. Because this subtraction is small, we have not made it in histograms we present here. Our observed numbers, as they stand, clearly favor $I=0$; however, a subtraction of 6 ± 3 events should be made from the $\rho^0 \pi^0$ sample. We expect this number of $\pi^+ \pi^- \gamma$ decays of the $\eta^*(959)$ meson to fall in the H-mass interval, and we cannot distinguish $\pi^+ \pi^- \gamma$ from $\pi^+ \pi^- \pi^0$ in this

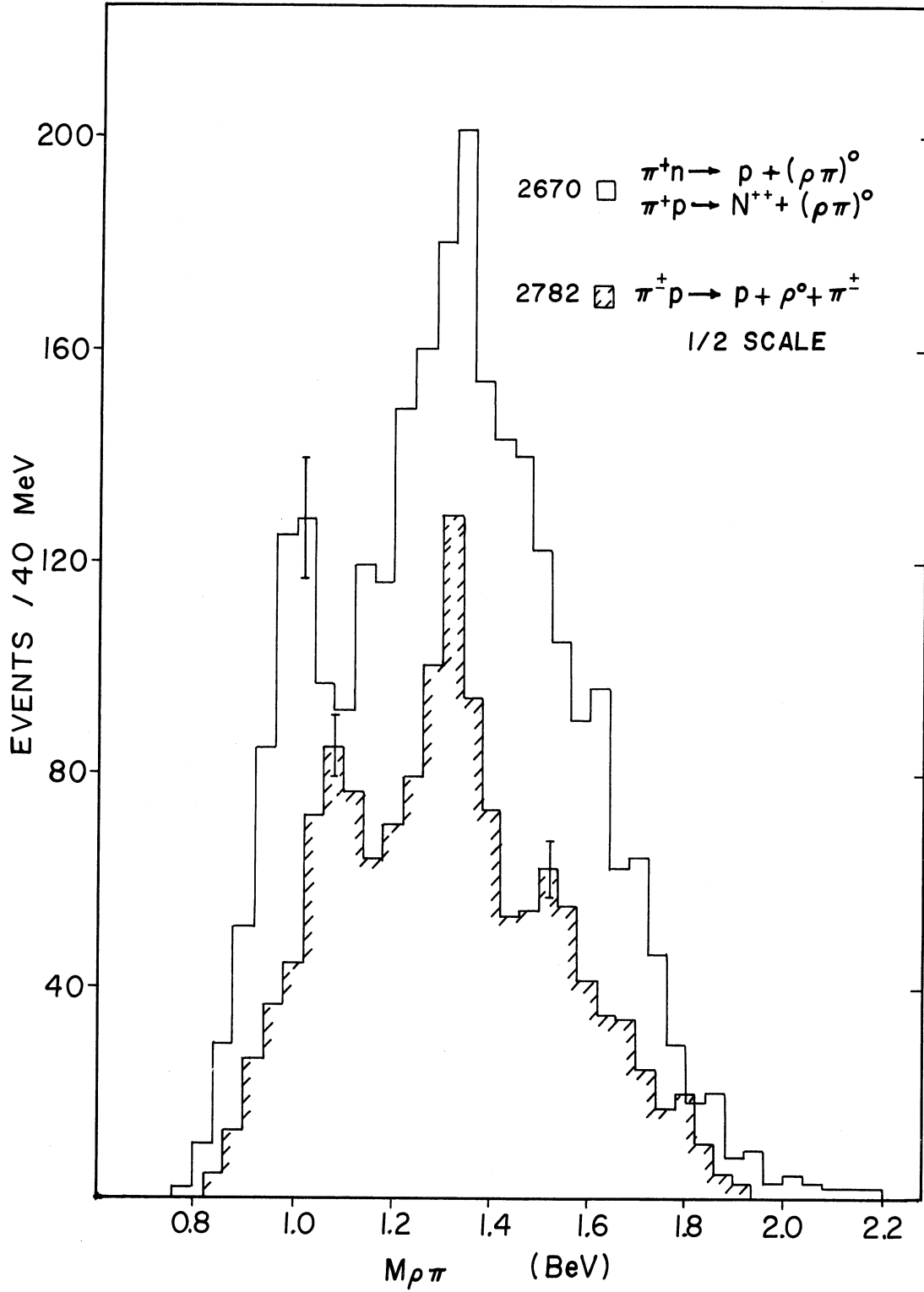


Figure 40. The combined data of this experiment and $\pi^+ p \rightarrow (\rho\pi)^0 N^{*++}$ at 4.0 BeV/c. For comparison, the shaded and superimposed histogram, drawn to one-half scale, is a compilation of $\pi^\pm p \rightarrow \rho^0 \pi^\pm p$ data.

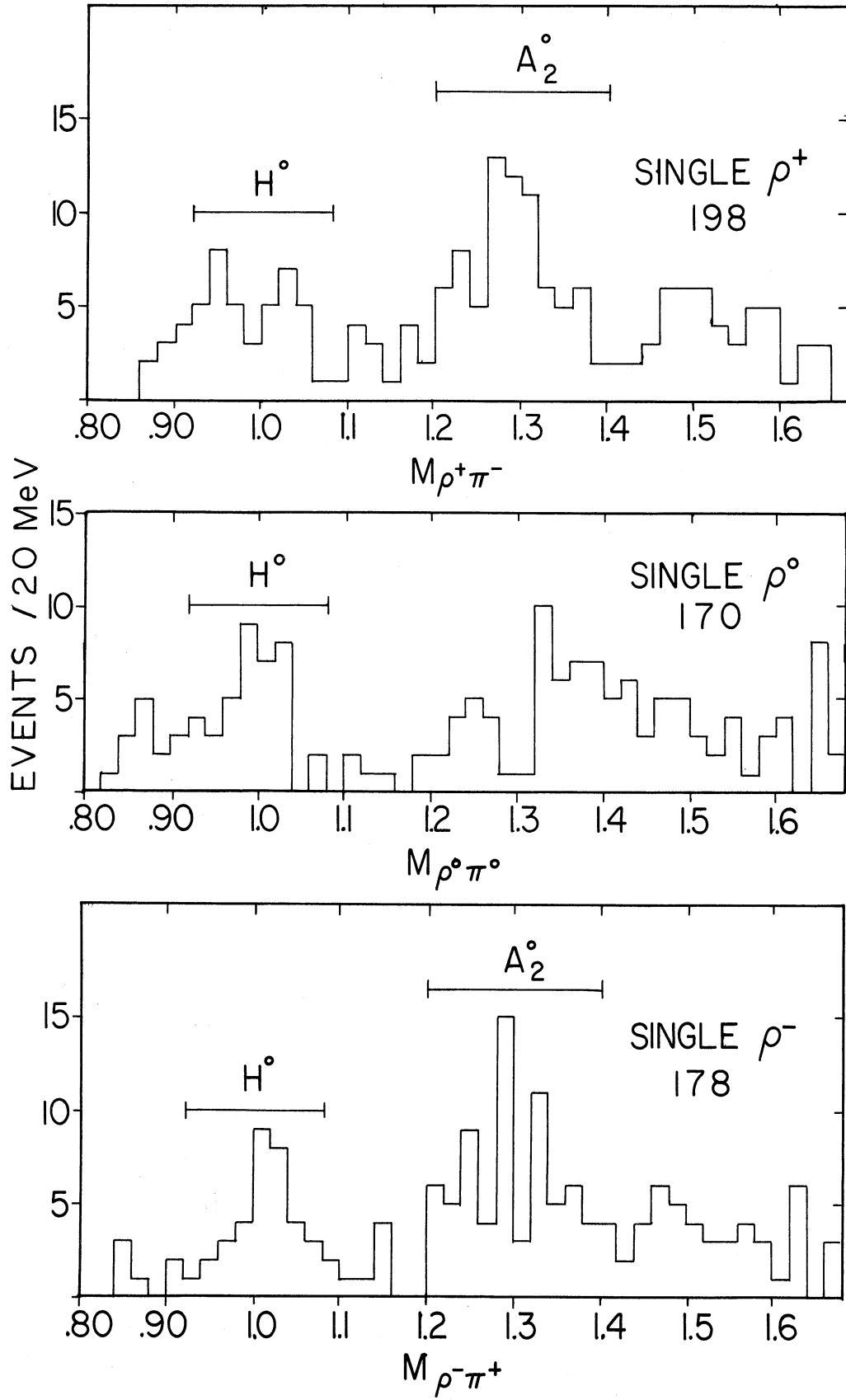


Figure 41. $M(\rho\pi)$ for those events of Fig. 39 which have a single ρ^+ , ρ^0 , or ρ^- in 20 MeV bins.

experiment. The number 6 ± 3 is based on our observed number (13 ± 5) ⁸⁷ of $\eta^* \rightarrow \pi^+ \pi^- (+ \geq 2\pi^0)$ events and the published branching ratios⁸⁸ for this mode and the $\pi^+ \pi^- \gamma$ mode of the η^* . We have included a correction factor of 0.82 which is based on our observed $\Delta^2(\eta^*)$ distribution and our imposed Δ^2 cutoff of $0.85 (\text{BeV}/c)^2$. The contamination is expected to fall mostly in the $\rho^0 \pi^0$ events since the $\pi^+ \pi^- \gamma$ mode of the η^* is mostly $\rho^0 \gamma$.⁸⁸ This somewhat weakens the argument for $I=0$ since it makes our observed mass spectrum for $\rho^0 \pi^0$ alone fall closer to our attempts at generating a phase space curve to account for the H effect. The η^* contribution does not account for the entire H peak since a peak is still seen when the mass plot is made with all $\rho^0 \pi^0$ events removed (See Fig. 42).

C.3 Momentum Transfer Distributions

The momentum transfer distribution, $\Delta^2(H)$, is shown in Fig. 43. The $\rho^0 N^*{}^+$ subtraction discussed above is shaded. The ρN^* subtraction is clearly important for a correct estimate of the differential cross section. We are indebted to Jackson and Donahue for calculating for us the expected differential cross section (smooth curve, Fig. 43) based on ρ -meson exchange with absorption.⁸⁹ Their calculation assumes $G_T/G_V = 3.7$, $\gamma_1 = 0.043$, $\gamma_2 = 0.032$, $C_1 = 0.78$, and $C_2 = 1.0$. (See Section B of this chapter for a discussion of these constants.) The smooth curve fits the data well after the ρN^* subtraction is made. The normalization is arbitrary.

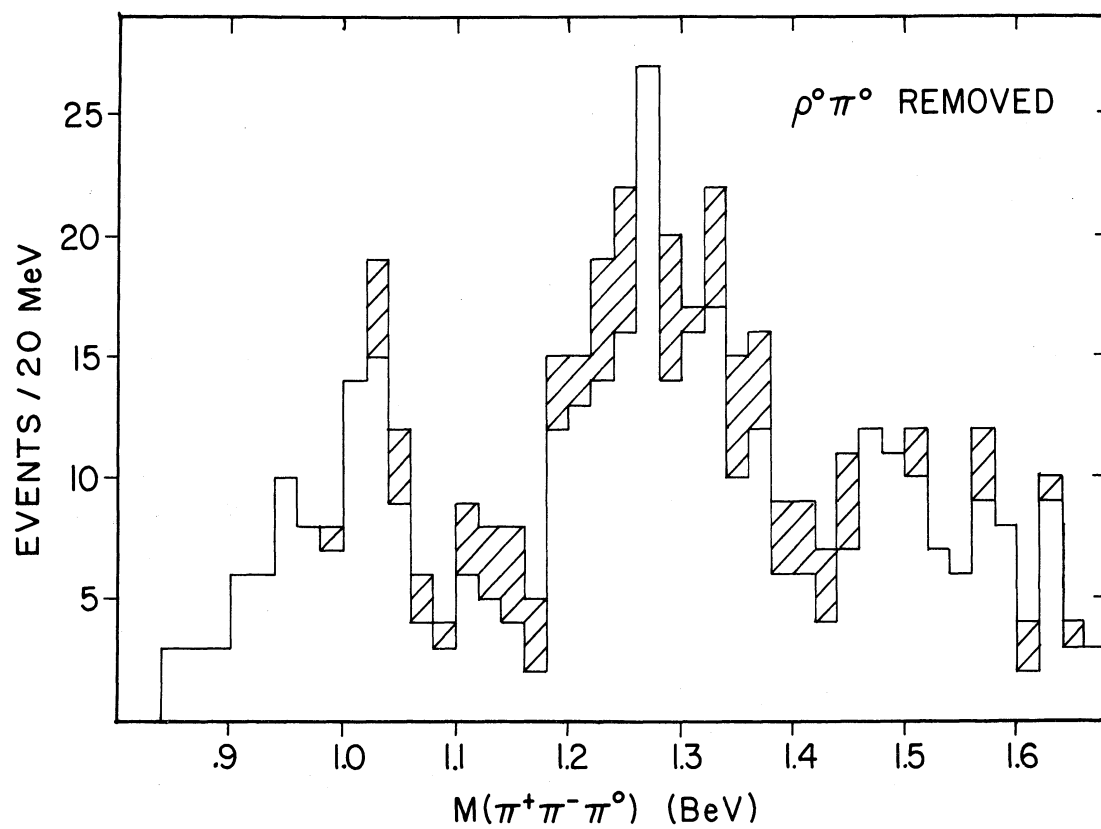


Figure 42. The $(\rho\pi)^0$ mass spectrum of Figure 39 with all ρ^0 events removed. The shaded events are both ρ^+ and ρ^- events.

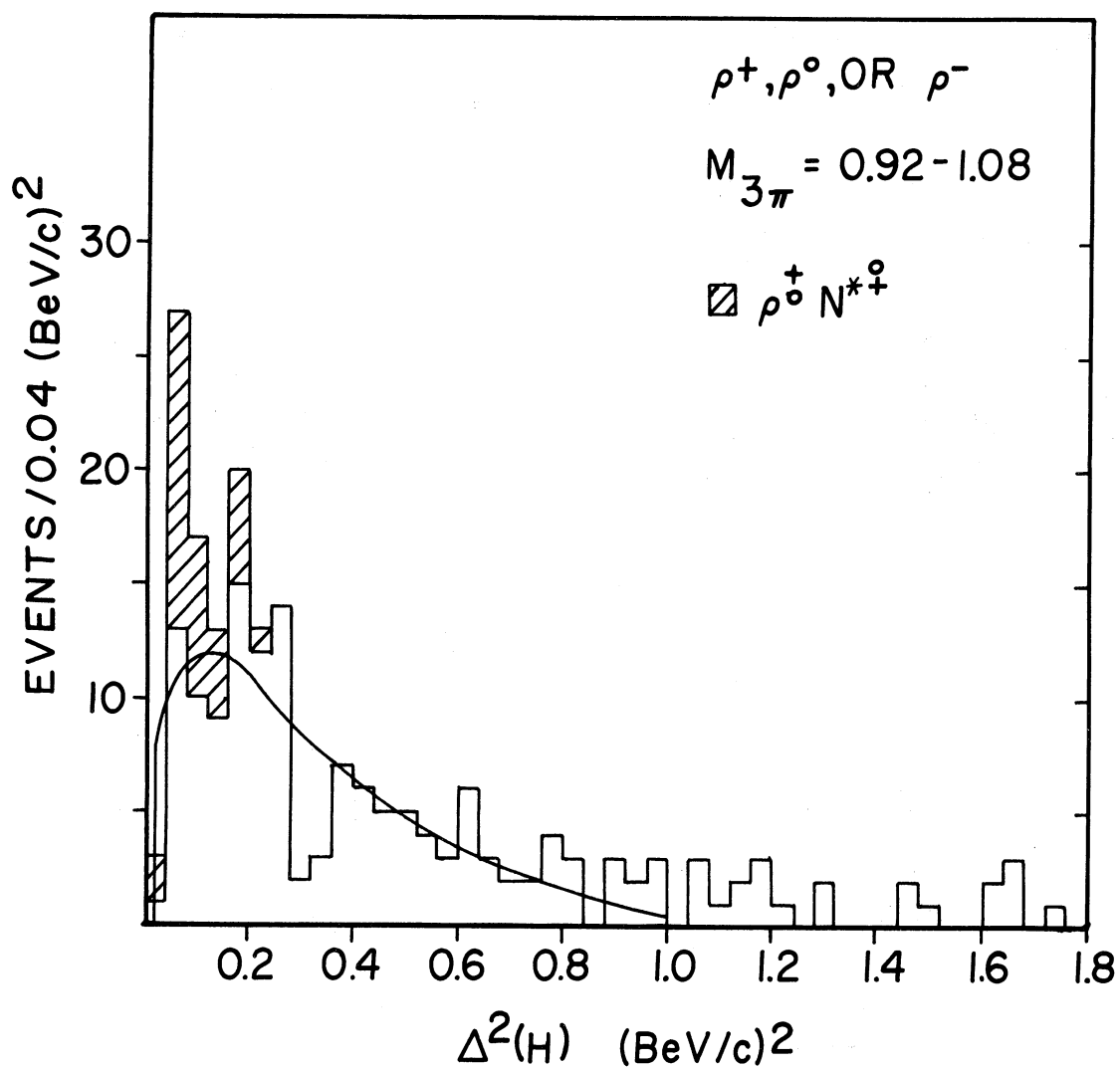


Figure 43. Four-momentum transfer squared to the H meson. The shaded events show the contribution from the $\rho^+ N^{*0}(1238)$ and $\rho^0 N^{*+}(1238)$ final states provided $\Delta^2(\rho) < 0.2$ (BeV/c)² in each case. The smooth curve is from the absorption model.

The scattergram in Fig. 44 shows $x = M(3\pi)$ and $y = \Delta^2(\rho)$. We have plotted $\Delta^2(\rho^+)$ if the event has a dipion mass in the ρ^+ band; if not, we plot $\Delta^2(\rho^-)$ if it falls in the ρ^- band; otherwise we plot $\Delta^2(\rho^0)$ if it falls in the ρ^0 band. Only one point is plotted for each event. We wish to point out from this plot, and a similar one by Chen,⁴⁸ that kinematics at $\rho\pi$ threshold restricts $\Delta^2(\rho)$ to small values. It is straightforward to show in the rest frame of the three pions that $\Delta^2(\rho)$ is completely specified by $M(3\pi)$, $M(\rho)$, $\Delta^2(3\pi)$, and θ , the angle between the ρ and the beam pion. Specifically, from the usual definition of $\Delta^2(\rho)$.

$$\begin{aligned}\Delta^2(\rho) &= 2E(\text{beam}) \cdot E(\rho) - 2P(\text{beam}) \cdot P(\rho) \cdot \cos\theta \\ &\quad - M(\text{beam})^2 - M(\rho)^2.\end{aligned}$$

From $M(3\pi)$ and conservation of energy and momentum in the decay, it is easy to eliminate $E(\rho)$ and $P(\rho)$. In the same way $E(\text{beam})$ can be replaced by using energy and momentum conservation and $\Delta^2(3\pi)$. The resulting relations for $E(\text{beam})$ and $P(\text{beam})$ which are substituted into the equation for $\Delta^2(\rho)$ are

$$\begin{aligned}E(\text{beam}) &= \frac{M(\text{beam})^2 + \Delta^2(3\pi) + M(3\pi)^2}{2M(3\pi)}, \text{ and} \\ P(\text{beam}) &= (E(\text{beam})^2 - M(\text{beam})^2)^{\frac{1}{2}}.\end{aligned}$$

After calculation it can be seen that if $\Delta^2(3\pi)$ is limited to small values, then so is $\Delta^2(\rho)$. The smooth curve shown in Fig. 44 is the highest value of $\Delta^2(\rho)$ that can be reached ($\cos\theta = -1$) for $\Delta^2(3\pi) < 0.6 \text{ (BeV/c)}^2$.

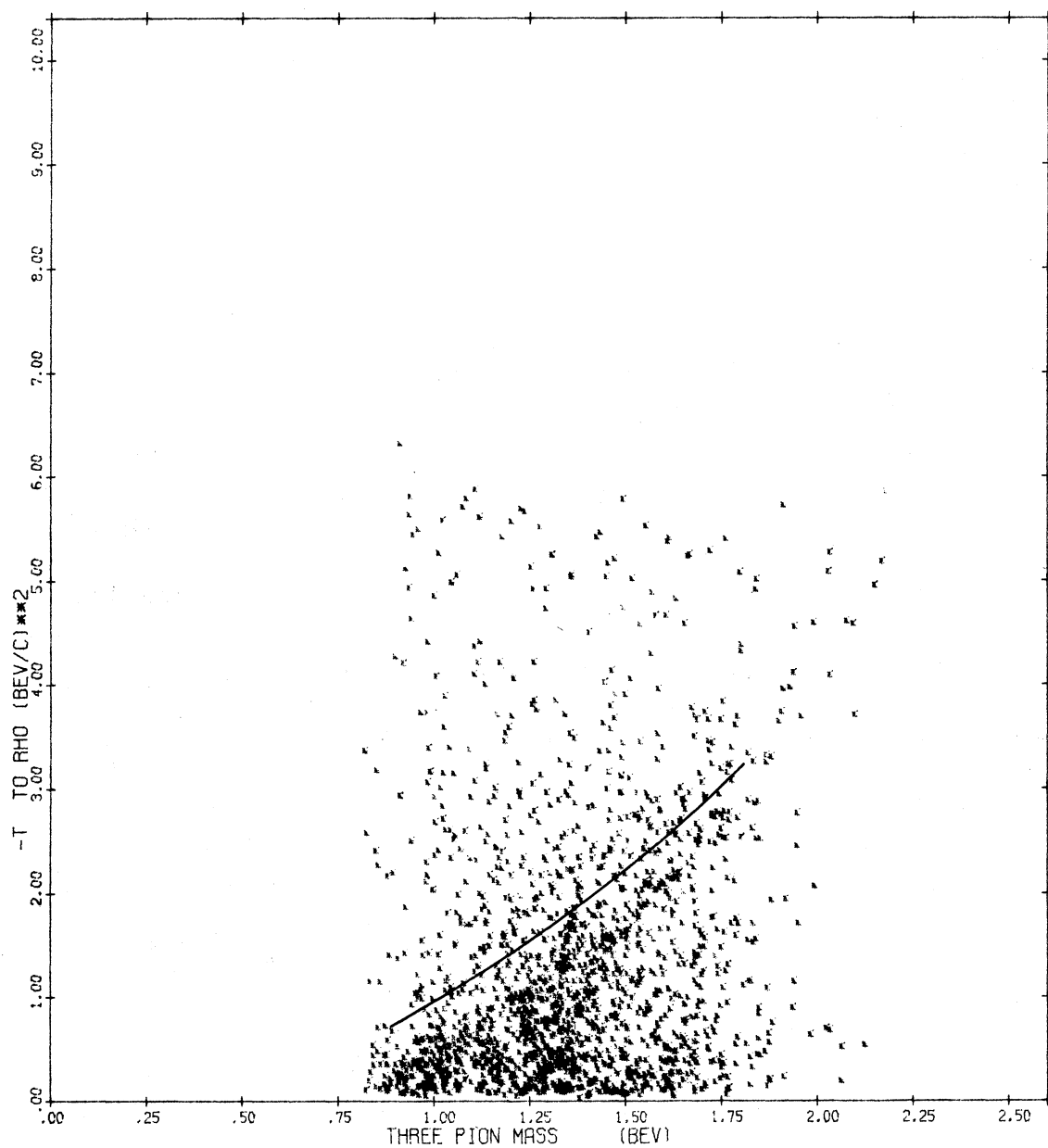


Figure 44. Scattergram of $\Lambda^2(\rho^+)$, $\Lambda^2(\rho^-)$, or $\Lambda^2(\rho^0)$ (one point for each event) against $M(3\pi)$ for all events with ρ^+ , ρ^- , or ρ^0 .

This "abnormally" low $\Delta^2(\rho)$ behavior has previously been taken as evidence⁹⁰ for a diffraction dissociation process contributing to events in the region of the A_1 . It is important to note with regard to both A_1 and H production that low $\Delta^2(\rho)$ will result from any peripheral production mechanism.

C.4 Spin-Parity Test

In order to test various J^P assignments for the H, we have plotted the distributions of the three polar angles θ_n , θ_m , θ_b . The angles θ_n and θ_b are measured in the H rest frame and are defined as the angle between the beam and the H decay plane normal, and that between the beam and the bachelor pion (i.e., the one that doesn't make a ρ), respectively. The angle θ_m is measured in the ρ rest frame between the beam and one of the pions from the ρ . We have counted the double ρ events as 1/2 event each in the appropriate distribution. If the three $\cos\theta$ distributions are not all flat, this rules out $J^P = 0^+$ immediately. ($J^P = 0^+$ is also ruled out by spin-parity conservation.)

In order to test for other J^P , we have used a method very similar to one proposed by Berman and Jacob.⁹¹ In principle, we determine the alignment of the H-meson spin from the distribution of the decay plane normal,⁹¹ $\cos\theta_n$, in Fig. 45 (a). A fit to this distribution gives the diagonal elements of the spin density matrix, ρ_{mm} . When the ρ_{mm} are known, the $\cos\theta_b$ and $\cos\theta_m$ distributions (Figs. 45 (b,c)) can be predicted and tested for compatibility with a given J^P assignment. This

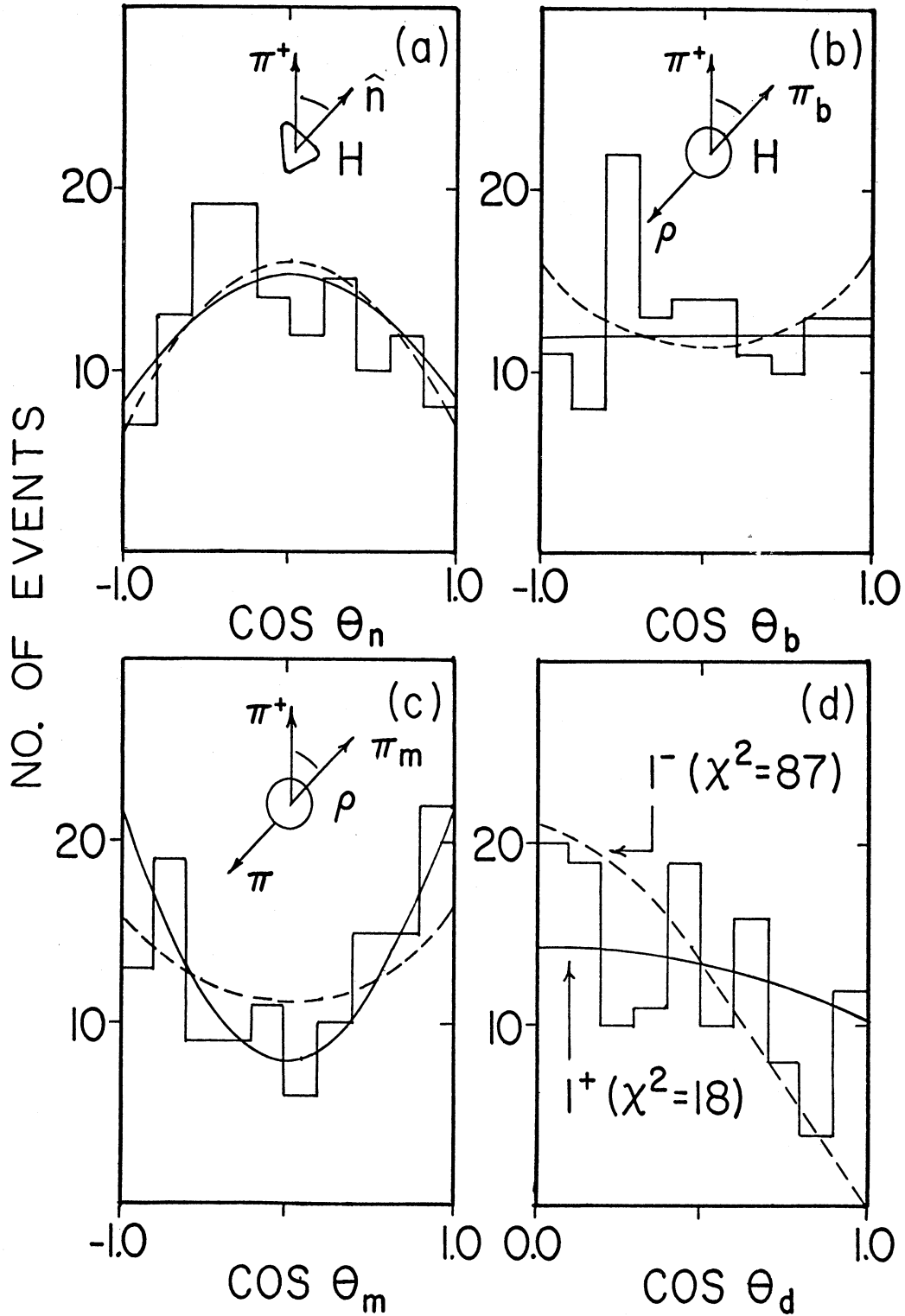


Figure 45. Angular distributions in the H-meson region (0.92 - 1.08 BeV/c^2). Shown are the cosines of the angles between the beam pion and (a) the decay plane normal, (b) the pion from the decay of the H-meson, and (c) a pion from the decay of the ρ meson. The Dalitz plot variable is shown in (d). The solid (dashed) curves assume the H-meson has $J^P = 1^+(1^-)$.

method fails, of course, if the $\cos\theta_n$ distribution is flat. Then the H meson would be completely without polarization; the diagonal elements of the H density matrix would have the value $\rho_{mm} = 1/(2J + 1)$; and $\cos\theta_b$ and $\cos\theta_m$ distribution would also be flat regardless of the spin of the H.

The predicted distribution for the $J^P = 1^+$ case is, with $x = \cos\theta$,

$$\frac{dW}{d \cos\theta_n} = 3/4 \left[\left(\frac{1 - \rho_{00}}{2} \right) (1 + x^2) + \rho_{00}(1 - x^2) \right]$$

$$\frac{dW}{d \cos\theta_b} = 1/2$$

$$\frac{dW}{d \cos\theta_m} = 3/2 \left[\left(\frac{1 - \rho_{00}}{2} \right) (1 - x^2) + \rho_{00}x^2 \right]$$

and for $J^P = 1^-$

$$\frac{dW}{d \cos\theta_n} = 3/2 \left[\left(\frac{1 - \rho_{00}}{2} \right) (1 - x^2) + \rho_{00} x^2 \right]$$

$$\frac{dW}{d \cos\theta_b} = 3/4 \left[\left(\frac{1 - \rho_{00}}{2} \right) (1 + x^2) + \rho_{00}(1 - x^2) \right]$$

$$\frac{dW}{d \cos\theta_m} = \frac{dW}{d \cos\theta_b} .$$

These non-relativistic equations should be valid since the velocity of the ρ in the H rest frame is $\approx .3$ c. We have also neglected d-wave decay for the 1^+ case since it presumably would be small because of this small velocity and the centrifugal barrier effects.

For spin-parity 2^+ , the $\cos\theta_n$ and $\cos\theta_b$ distributions should be identical and will have x^4 terms. The $\cos\theta_m$ distribution only requires terms up to x^2 . Two parameters, ρ_{00} and ρ_{22} , are needed to describe the decay. For $J^P = 2^-$, the $\cos\theta_m$ and $\cos\theta_b$ distributions should be identical and only require terms up to x^2 . Two parameters, ρ_{00} and ρ_{22} , describe these angular distributions and we assume no f-wave in the decay. The $\cos\theta_n$ distribution has an x^4 term and an additional parameter R_0 .⁹¹ The explicit formulas and further discussion of the method are given in Appendix L.

In practice, we have made simultaneous least squares fits to the three distributions for each of the above mentioned J^P assignments, using the appropriate number of parameters in each case.

The results are shown in Figs. 45 (a,b,c) for 1^+ and 1^- and in Figs. 46 (a,b,c) for 2^+ and 2^- . The fitted values of the parameters and the χ^2 values are given in Table VIII. Examination of Table VIII indicates there is no clear choice for J^P . Considering that our H peak may contain more than 50% background, we may not be able to come to a definite conclusion about J^P . The appearance of the curves on our data in Figs. 45 (a,b,c,d) does however favor the 1^+ assignment. The arguments against the other choices can be summarized as follows:

(1) If we say that the $\cos\theta_b$ and $\cos\theta_m$ distributions are not compatible with being identical, then this rules out 1^- and 2^- (and, of course, 0^-). The χ^2 probability for their being at least this non-identical is 10%.

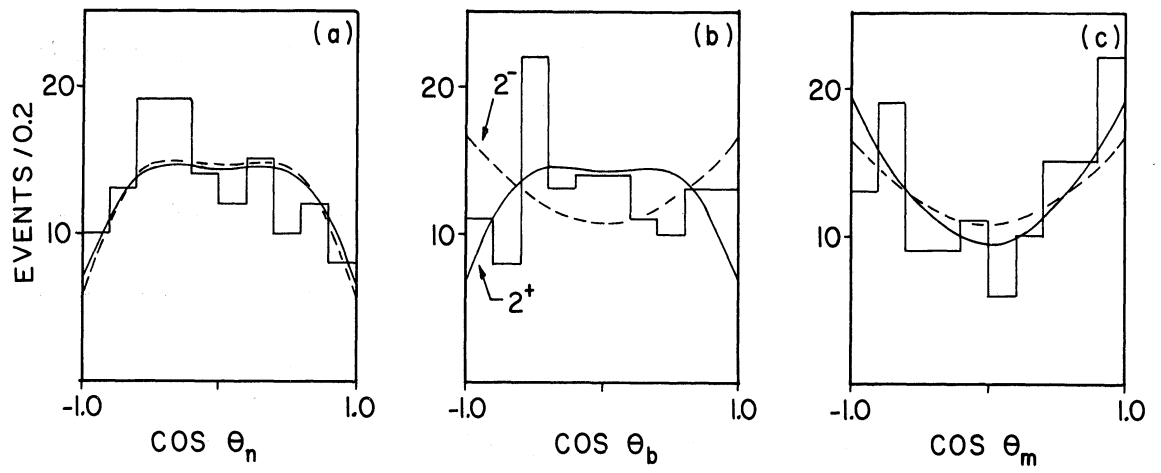


Figure 46. Angular distributions for $\cos \theta_n$, and $\cos \theta_b$, and $\cos \theta_m$ showing the simultaneously fitted curves which assume the H meson has $J^P = 2^+$ (solid) or 2^- (dashed).

(2) If we say that the $\cos\theta_d$ distribution (Fig. 2(d)) is not compatible with vanishing at $\cos\theta_d = 1$, then this rules out 1^- and 2^+ . The description of θ_d is given below.

TABLE VIII
RESULTS OF FITTING THE $\cos\theta_n$, $\cos\theta_m$, AND $\cos\theta_d$
DISTRIBUTIONS FOR VARIOUS J^P ASSIGNMENTS

J^P	ρ_{00}	ρ_{22}	$\chi^2(\text{Deg})$	Prob.
0^-	---	---	37 (27)	0.10
1^+	$0.57 \pm .06$	---	22 (26)	0.70
1^-	$0.17 \pm .05$	---	29 (26)	0.30
2^+	$0.11 \pm .04$	$0.36 \pm .04$	23 (25)	0.55
$2^- (R_0 = 0)$	$0.00 \pm .20$	$0.06 \pm .05$	28 (24)	0.25

An independent test for J^P can be made by examining the Dalitz plot of the 3π system. We have chosen as orthogonal Dalitz plot variables $m^2(\pi\pi)$ and $\cos\theta_d$, where θ_d is the angle between the dipion line and bachelor pion in the dipion rest frame. We have made a six-way fold of the data by ordering the kinetic energies of the three pions in the H rest frame. The bachelor pion is then identified as having the smallest kinetic energy, and the direction of the dipion line is identified by the pion of intermediate kinetic energy. Because of this folding, $\cos\theta_d$ does not run through its full range for all values of $m^2(\pi\pi)$. The projection of the data on the $\cos\theta_d$ axis is shown in Fig. 45(d). The curve labeled 1^+ was calculated by building a ρ enhancement into a Dalitz plot density appropriate for a $1^+(I=0)$ decay,⁸⁹ and then making an average

over the 3π mass, weighted according to our observed mass distribution. It gives a reasonable fit to the data. The 1^- curve is typical of the series $1^-, 2^+, \dots$ which gives a vanishing density at $\cos\theta_d = 1$ (edge of the Dalitz plot). The 12 events in the last bin cause curves of this nature to fit very poorly, although the addition of a flat background would obviously improve the fit.

The projection of the data on the $m^2(\pi\pi)$ axis also gives reasonable agreement with the 1^+ assignment.

The three $\cos\theta_b$ distributions (one for each ρ), which are summed (with a weight of one-half for double ρ events) to give Fig. 45 (b), are shown in Figs. 47 (a,b,c). The shaded events are the $\rho^0 N^{*0}$. It can be seen that the ρN^* subtraction is very important if $\cos\theta_b$ is to be used as part of the spin test.

The three $\cos\theta_m$ distributions are shown in Figs. 47 (d,e,f) but here have been calculated in the rest frame of the H meson. Again the $\rho^0 N^{*0}$ events are shaded. The fact that the sum of these distributions is similar to Fig. 45 (c) is a consequence of the non-relativistic momenta of the ρ mesons. Although statistics are very limited, it is surprising that the ρ^0 events have more events with $\cos\theta_m > 0$ than with $\cos\theta_m < 0$ just as observed in ρ^0 production by pion exchange. (Any contribution of $\eta^* \rightarrow \rho^0 \gamma$ will have added a flat background to H events since the η^* has $J = 0$). The $\cos^2\theta_m$ shape of the ρ^- angular distribution is strong evidence for decay from a resonant state since the ρ^- cannot be produced by pion exchange in this channel.

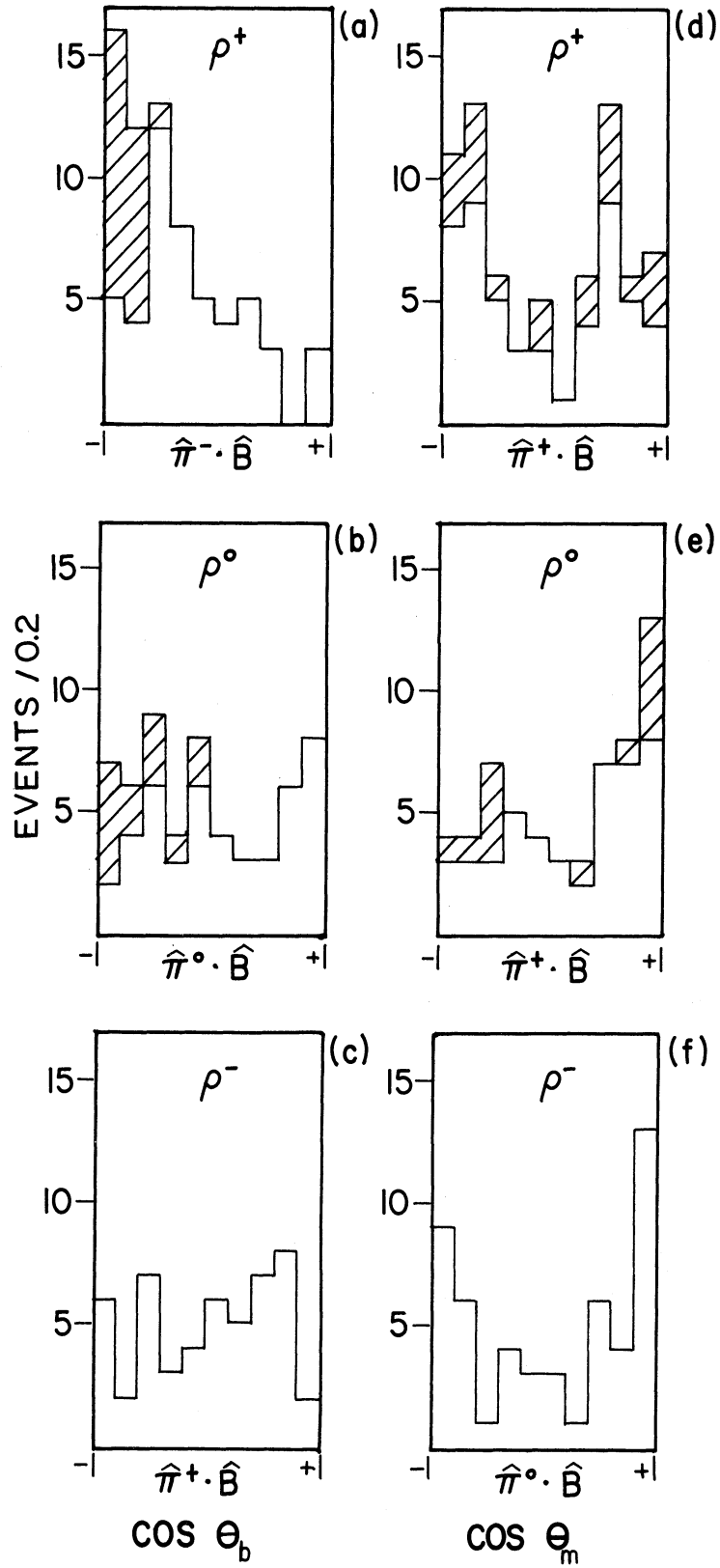


Figure 47. The distributions of $\cos \theta_b$ and $\cos \theta_m$, both calculated in the H-meson rest frame. Figs. (a,d); (b,e); and (c,f) show the events in the ρ^+ ; ρ^0 ; and ρ^- bands separately. The ρN^* contribution is shaded.

C.5 Density Matrix Elements

We will now assume that the H meson is a resonant state of $J^P 1^+$. As pointed out to us by Jackson and Donahue,^{92,89} the entire density matrices of the H and ρ mesons should be the same to order β^2 . The coordinate system we use has been discussed in connection with Fig. 35 (a). Using the angular distributions of Figs. 48(a-d), we have determined the density matrix of the H from the decay plane normal in the H rest frame and the density matrix of the ρ from the decay pion in the ρ rest frame. The fitted curves are shown in Figs. 48 (a-d); the resulting density matrix elements are given in Table IX; and the density matrix elements are plotted with the predictions of the absorption model in Fig. 49. The points are plotted at the median value of $\Delta^2(H)$ used in the determination (events with $\Delta^2 < 0.85 \text{ (BeV/c)}^2$ were used).

TABLE IX

DENSITY MATRIX ELEMENTS FOR THE H MESON AND BACKGROUND EVENTS

		ρ_{00}	χ^2 prob.	ρ_{1-1}	χ^2 prob.	$\text{Re } \rho_{10}$
H	normal	0.65 ± 0.11	70%	-0.41 ± 0.10	2%	-0.06 ± 0.10
	ρ -pion	0.55 ± 0.06	50%	-0.08 ± 0.06	4%	-0.10 ± 0.05
Back-ground	normal	0.58 ± 0.12	20%	-0.22 ± 0.12	20%	-0.01 ± 0.10
	ρ -pion	0.36 ± 0.07	95%	$+0.01 \pm 0.07$	50%	-0.02 ± 0.06

The expressions for $\cos\theta_n$ and $\cos\theta_m$ were previously given in the J^P discussion of the H meson. The Φ_n and Φ_m distributions are given by^{91,92}

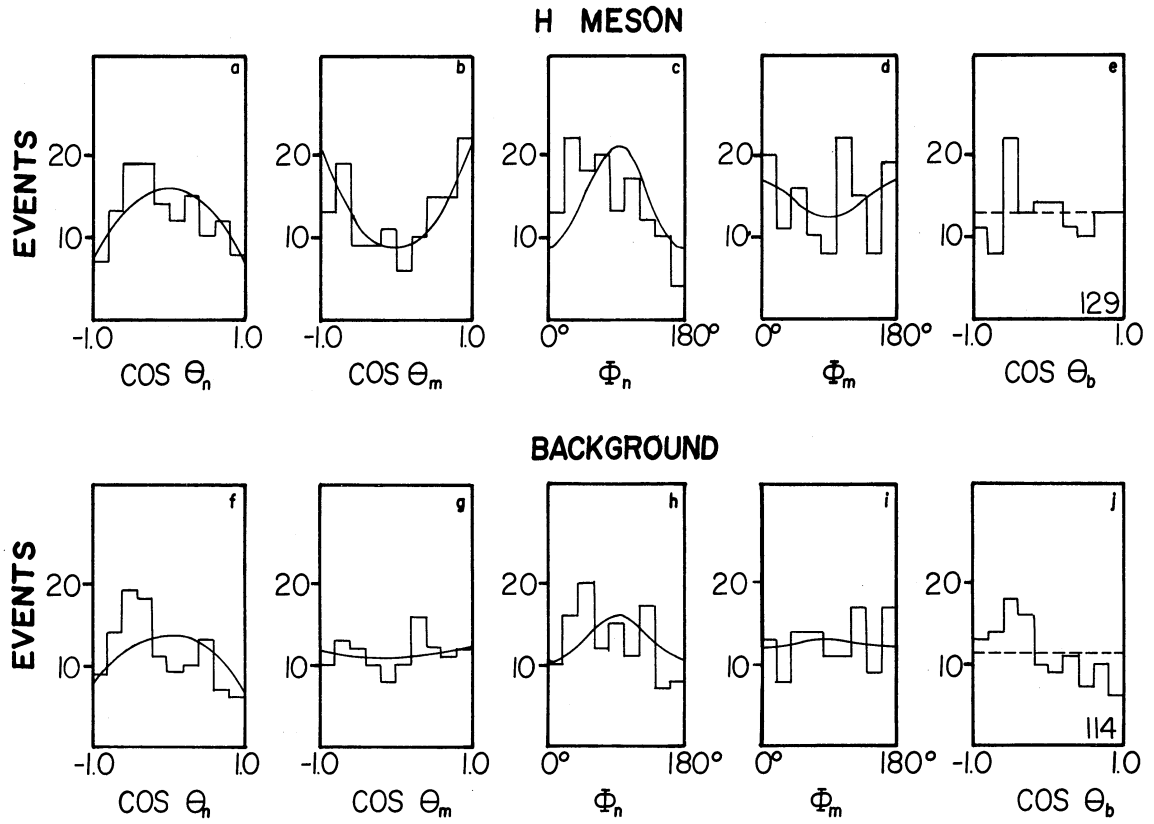


Figure 48. Angular distributions for $\cos \theta_n$, $\cos \theta_m$, Φ_n , Φ_m , and $\cos \theta_b$ for events in the H region, $M(3\pi) = 0.92 - 1.08$ BeV, and for events in the region between the H^0 and A_2^0 peaks, $M(3\pi) = 1.04 - 1.2$ BeV.

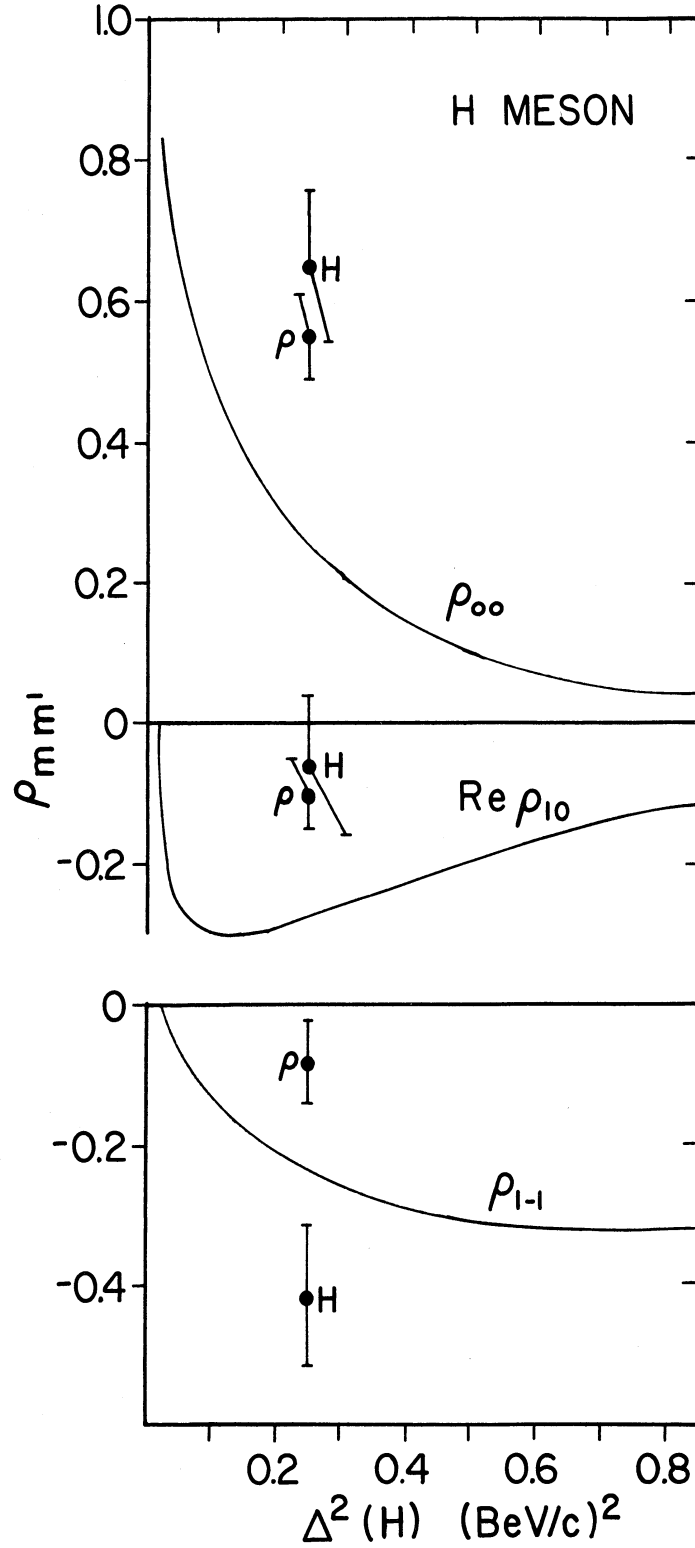


Figure 49. A comparison of the experimental density matrix elements with the values predicted by the absorption model. The points (H) are from the decay plane normal in the H rest frame, and (ρ) from the married pion in the ρ rest frame. The points are shown at the median value of momentum transfer squared.

$$\frac{dW}{d\Phi_n} = \frac{1}{2\pi} (1 - \rho_{1-1} \cos 2\Phi_n) , \text{ and}$$

$$\frac{dW}{d\Phi_m} = \frac{1}{2\pi} (1 - 2\rho_{1-1} \cos 2\Phi_m) .$$

The values for Rep_{10} are obtained by an averaging method which uses the expressions,^{91,92}

$$\text{Rep}_{10}(n) = + \frac{5}{2\sqrt{2}} \langle \sin 2\theta_n \cos \Phi_n \rangle , \text{ and}$$

$$\text{Rep}_{10}(m) = - \frac{5}{4\sqrt{2}} \langle \sin 2\theta_m \cos \Phi_m \rangle .$$

Although our small statistics and large backgrounds complicate the density matrix determination, the results are interesting. (It is encouraging that the events we have studied just above the H mass with $M(3\pi) = 1.04\text{--}1.20$ BeV have similar but less pronounced structures than the H events do. These "background" events are shown in Figs. 48 (f-j), and the results of fitting are shown in Table IX. Two triple ρ -meson events are included in Fig. 48 (f) and Fig. 48 (h) which are not included in Figs. 48 (g,i,j).) Our results show that the density matrix elements for the ρ and the H mesons are indeed very similar, and they are in poor agreement with the predictions of the absorption model (Fig. 49).⁸⁹ We observe more alignment ($\bar{\rho}_{00} = 0.6$) than predicted by the model ($\bar{\rho}_{00} = 0.3$). It is interesting to note that the absorption model predicts (for a wide range of values of G_T/G_V)⁸⁹ that the shape of the $\cos\theta_n$ plot should change, from the convex shape (shown) to a concave shape, on either side of $\Delta^2(H) = 0.2 \text{ BeV}/c^2$.

The values of ρ_{1-1} are in rather poor agreement with each other, and $|\rho_{1-1}|$ determined from Φ_n is too large compared to the value of ρ_{00} from $\cos\theta_n$. The general requirement for a $J=1$ state is (see Property 10, Appendix K)

$$|\rho_{1-1}| \leq \frac{1 - \rho_{00}}{2} = 0.18 \pm 0.05 ,$$

while our value is

$$|\rho_{1-1}| = 0.41 \pm 0.10 .$$

This and the low χ^2 probability for the Φ_n fit cause us to favor a smaller value of $|\rho_{1-1}|$ (for example, the one determined from Φ_m) as the correct value for the H meson.

D. $\pi^+ d \rightarrow A_2^0 pp$

The three-pion mass spectrum in Fig. 50 shows an enhancement at about 1300 MeV which we interpret as the $A_2^0(1300)$ meson. Further analysis of the data shows its subsequent decay into $\rho^\pm \pi^\pm$. The properties of the A_2^0 appear to be consistent with those expected for the neutral member of the A_2 triplet, the charged members of which have been observed^{66,93-97} in the reactions $\pi^\pm p \rightarrow A_2^\pm p$. The branching ratios of the A_2^0 indicate an $I = 1$ state which strongly prefers $\rho\pi$ (as opposed to direct 3π) decay. The Dalitz plot density favors a spin-parity assignment of 2^+ . Some of these results have been published previously.⁹⁸

To study the production mechanism we examine the four-momentum trans-

fer squared distribution $\Delta^2(A_2^0)$ and compare the production cross section with data for A_2^- . We also compare the density matrix elements with the predictions of the absorption model and also with very recent results from $A_2^- \rightarrow K^- K^0$.⁹⁹ We discuss the decay properties first.

D.1 Three-pion and $\rho\pi$ Mass Spectra

When we began the study of the peak near 1300 MeV in Fig. 50, previous studies^{100,73,101} had been unable to demonstrate that the peak was substantially due to $A_2^0 \rightarrow \rho^+ \pi^-$. Our own study of data from the first half of the film was also unable to detect the $\rho\pi$ decay.¹⁰² We presumed that the peak was a new $I = 0$ resonance decaying directly to three pions and proceeded to study Dalitz plots of the type shown in Fig. 51. There is no obvious concentration of events in the ρ bands even though we have taken a small mass interval of $M(3\pi) = 1.2 - 1.4$ BeV and a cut of $\Delta^2(3\pi) < 0.85 \text{ (BeV/c)}^2$ and removed $\rho^0 N^{*+}(1238)$ events. (The radial distribution of this plot with only the $M(3\pi)$ cut is shown in Fig. 31 (d).)

Because all three ρ bands overlap in the center of the plot, and the radial distribution shows a large excess in the center, we temporarily considered that some interference effect might be causing the enhancement. Fortunately, our theoretical advisors did not encourage this point of view.⁴³ (A. Rosenfeld has recently presented a detailed argument also discouraging this view.⁵¹) We then began to search for $\rho\pi$ decay in other ways. The method we present in the following discussion shows conclusively that events in the peak are decaying primarily to $\rho^+ \pi^-$ and $\rho^- \pi^+$.

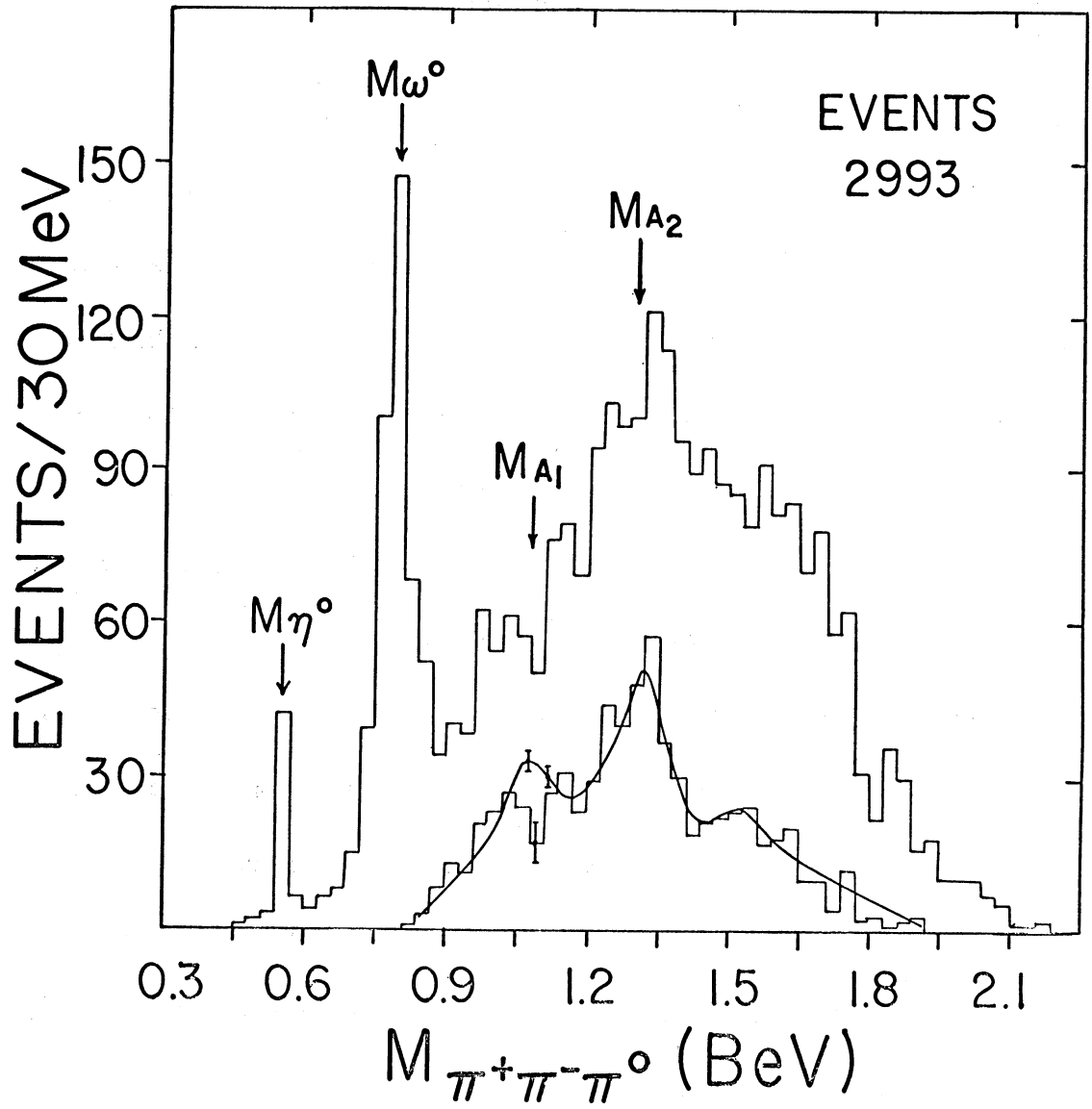


Figure 50. Effective mass of $\pi^+\pi^-\pi^0$ for all events from $\pi^+d \rightarrow \pi^+\pi^-\pi^0 p p$. The subsample of our events with ρ^+ or ρ^- and $\Delta^2(3\pi) < 0.85 \text{ (BeV/c)}^2$ is shown with a smooth curve taken from the $\pi^\pm p \rightarrow \rho^0 \pi^\pm p$ data in Fig. 40.

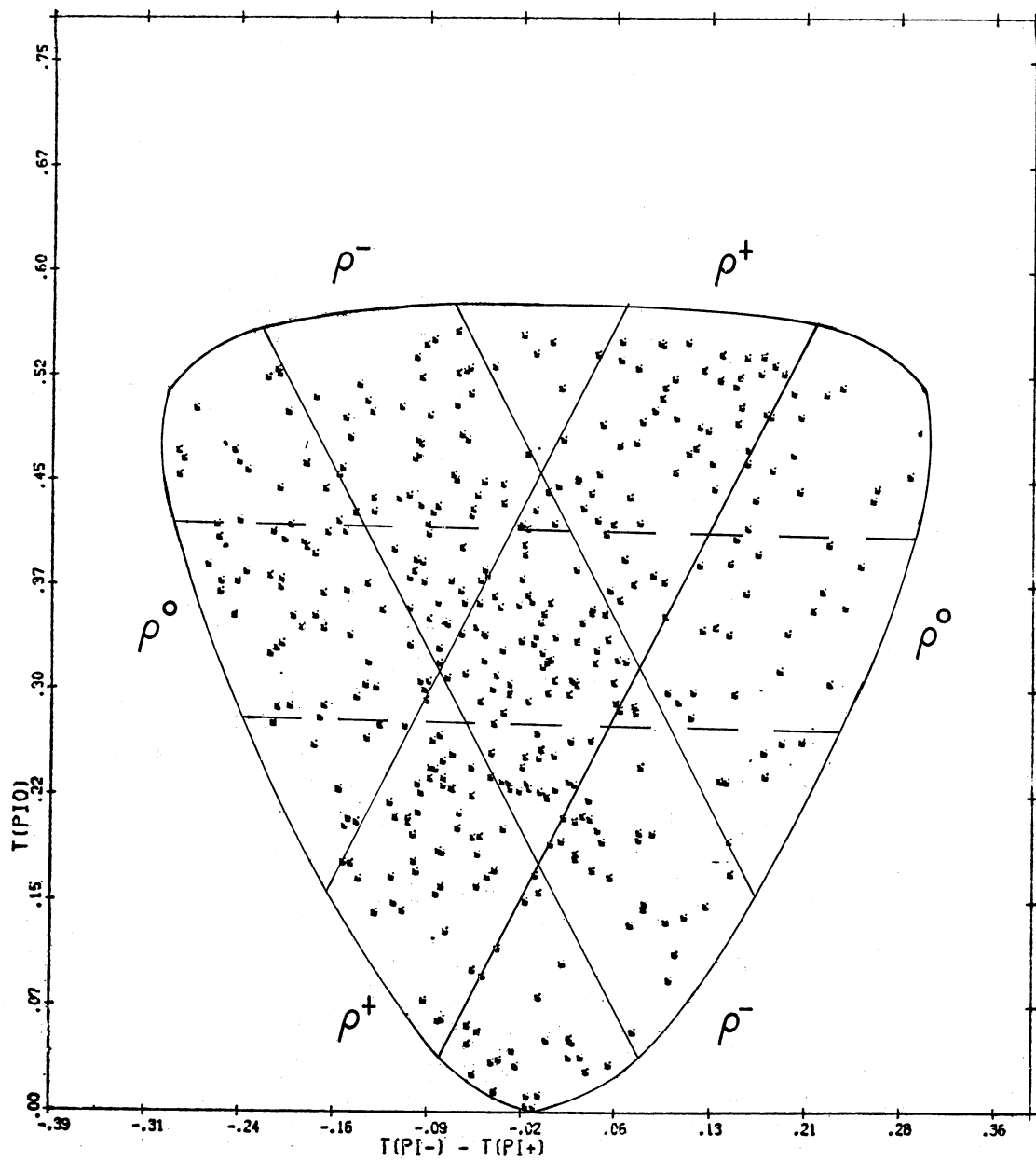


Figure 51. Dalitz plot for A_2 events with $M(3\pi) = 1.2 - 1.4$ BeV and $\Delta^2(3\pi) < 0.85$ (BeV/c) 2 . The axes are proportional to the kinetic energies of the pions as labeled.

The three-pion mass spectrum has been broken into eight parts to search for decays into $\rho^+\pi^-$, $\rho^0\pi^0$, $\rho^-\pi^+$, and 3π without ρ . Plotted in Figs. 52 (a,b,c) are the $\pi^+\pi^-\pi^0$ invariant mass distributions for those events having one and only one $\pi\pi$ invariant mass in the ρ region. Plotted in Figs. 52 (d,e,f) are those events with exactly two $\pi\pi$ mass combinations in the ρ region. Fig. 52 (g) contains events with three simultaneous combinations in the ρ region. The three-pion mass spectrum for the 1288 events with no $\pi\pi$ mass combination in a ρ region is shown in Fig. 53. It is smooth except for the η^0 and ω^0 peaks.

In order to estimate the distortion of the three-pion mass spectrum caused by this eight-way cut in the data, a three-pion phase space background estimate was made and plotted on the histograms. To obtain the curves, we calculated the expected density of points on a symmetrized Dalitz plot⁶² at a particular three-pion mass by dividing the number of events predicted from the unnormalized phase space curve of Fig. 21 by the total area of the plot. The curves in Fig. 52 are then calculated assuming this density is constant over the entire plot for a given three-pion mass. The positions of the ρ bands on the symmetrized Dalitz plot at $M(3\pi) = 1.0$ BeV and at 1.3 BeV are shown in Figs. 52 (h,i). The normalization for the resulting curves has been chosen from the non- ρ events at $M(3\pi) = 1.7$ BeV (Fig. 53). This procedure also gives the overall three-pion phase space normalization shown in Fig. 21 (solid curve). The fit of all these curves to the data is considerably improved if a peripheral correction is made to phase space as was done in Fig. 21 (dashed curve).

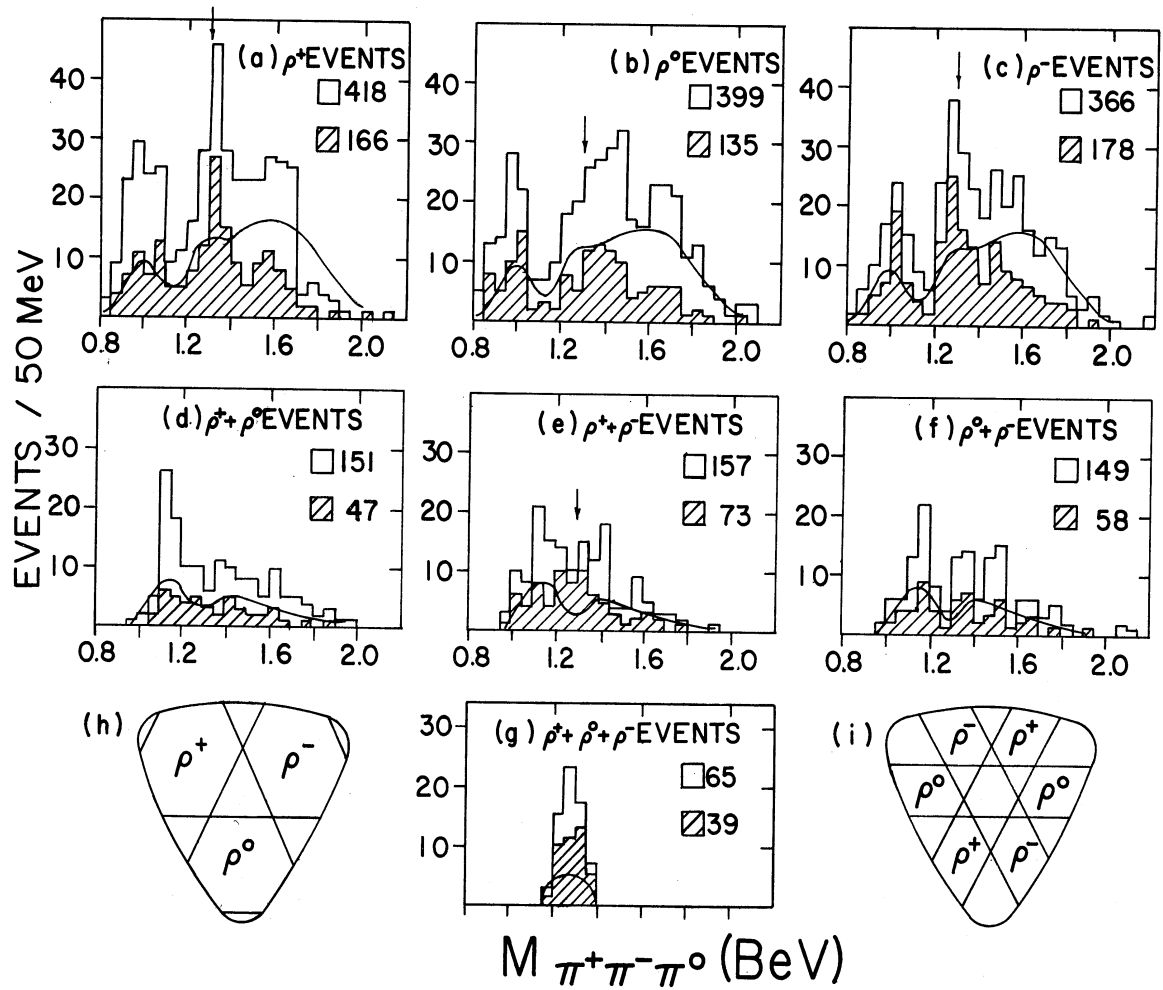


Figure 52. Effective mass of the $\pi^+\pi^-\pi^0$ system for events with (a) only ρ^+ , (b) only ρ^0 , (c) only ρ^- , (d) ρ^+ and ρ^0 , (e) ρ^+ and ρ^- , (f) ρ^0 and ρ^- , and (g) ρ^+ and ρ^0 and ρ^- . The solid curve shows the number of three-pion phase space events lying in each ρ band. The locations of the ρ bands are shown on the Dalitz plot (h) at $M(3\pi) = 1.0$ BeV and (i) at $M(3\pi) = 1.3$ BeV. The shaded events are explained in the text.

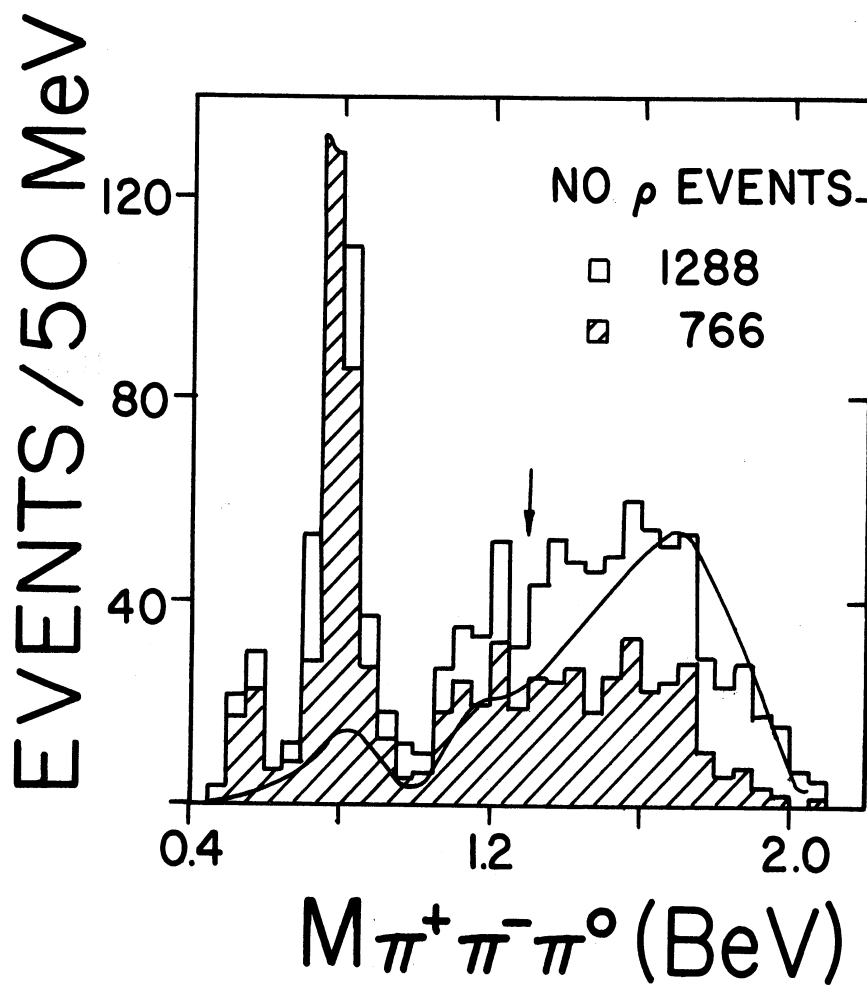


Figure 53. Effective mass of the $\pi^+\pi^-\pi^0$ system for events without ρ^+ , ρ^0 , or ρ^- . The shaded events have $A^2(3\pi) < 0.85 (\text{BeV}/c)^2$. The arrow is at 1.3 BeV.

D.2 Branching Ratios of the A_2^0

An isotopic spin determination can be made by examining the $\rho\pi$ decay of this resonance. A neutral meson state of definite isospin, $I = 0(1 \text{ or } 2)$ which decays (with \vec{I} conservation) into $\rho\pi$, should decay with the ratios $\rho^+\pi^- : \rho^0\pi^0 : \rho^-\pi^+$ of $1:1:1(1:0:1 \text{ or } 1:4:1)$. We note that Figs. 52 (a,b,c) show a narrow peak at $M_{\rho\pi} \approx 1.3 \text{ BeV}$ in the ρ^+ and ρ^- plots. A much broader and somewhat shifted peak appears in the ρ^0 plot. The shaded events of Fig. 52 result from an attempt to remove background events. The shaded events are those which remain after the removal of non-peripheral events with $\Delta^2(3\pi) > 0.85 (\text{BeV}/c)^2$, plus peripheral events with $\rho^+N^{*0}(1238)$ and $\rho^0N^{*+}(1238)$. The ρN^* events are removed only if $\Delta^2(\rho)$ is less than $0.6 (\text{BeV}/c)^2$ (see Figs. 26 (d',e')). To obtain a quantitative estimate of the decay branching ratios, all shaded events in Figs. 52 (a,b,c) are counted between $1.2 - 1.4 \text{ BeV}$. A subtraction of 24 background events is made from the number of events in each of the three intervals. An additional subtraction of 14 events is made from the single ρ^- events since these also lie in the N^{*++} region (Fig. 26(f')). This is necessary because we are assuming identical backgrounds and similar ρN^* events were previously removed from the ρ^+ and ρ^0 events. This gives for the branching ratios

$$\rho^+\pi^- : \rho^0\pi^0 : \rho^-\pi^+ = (1.3 \pm 0.4) : (0.5 \pm 0.3) : 1 .$$

The errors include an uncertainty of 5 events in the background subtraction. The results slightly favor an $I = 1$ state assignment. Because

the observed position (1310 ± 10 MeV) and width* (100 ± 15 MeV) of this state and the $I = 1$ assignment agree with those found for the A_2^\pm , we conclude that the peak at 1.3 BeV is the A_2^0 .

In the non- ρ events (Fig. 53) no peak above the general background at the A_2 mass is observed. The subsample of non- ρ events with $\Delta^2(3\pi) \leq 0.85$ (BeV/c)² still shows no evidence for A_2^0 . We obtain the following upper limit for the branching ratio

$$(A_2^0 \rightarrow 3\pi)/(A_2^0 \rightarrow \rho^+\pi^- \text{ or } \rho^-\pi^+) \leq 0.17.$$

Since there are essentially no events above background, we use for the numerator the square root of the events with $\Delta^2(3\pi) \leq 0.85$ (BeV/c)² in the A_2 region (1.2 - 1.4 BeV) and outside the ρ^+ or ρ^- bands, multiplied by 2.1. This is the factor (estimated from phase space) that would be used to obtain the total number of $A_2^0 \rightarrow 3\pi$ from a (hypothetical) peak observed in those events outside the ρ^+ or ρ^- bands. The denominator is taken as the number of A_2^0 events above the curve in Fig. 54 (a).

D.3 Spin-Parity of the A_2^0

A spin test for the A_2^0 can be made from the Dalitz plot density within the ρ^+ and ρ^- bands. No knowledge of the production mechanism is needed for this test. We have used the theoretical equations of Frazer, Fulco, and Halpern⁶⁴ which are based on a simplest matrix ele-

*This width measurement is preferred over the value we previously reported (110 ± 45) because of our improved phase space and resolution estimates.

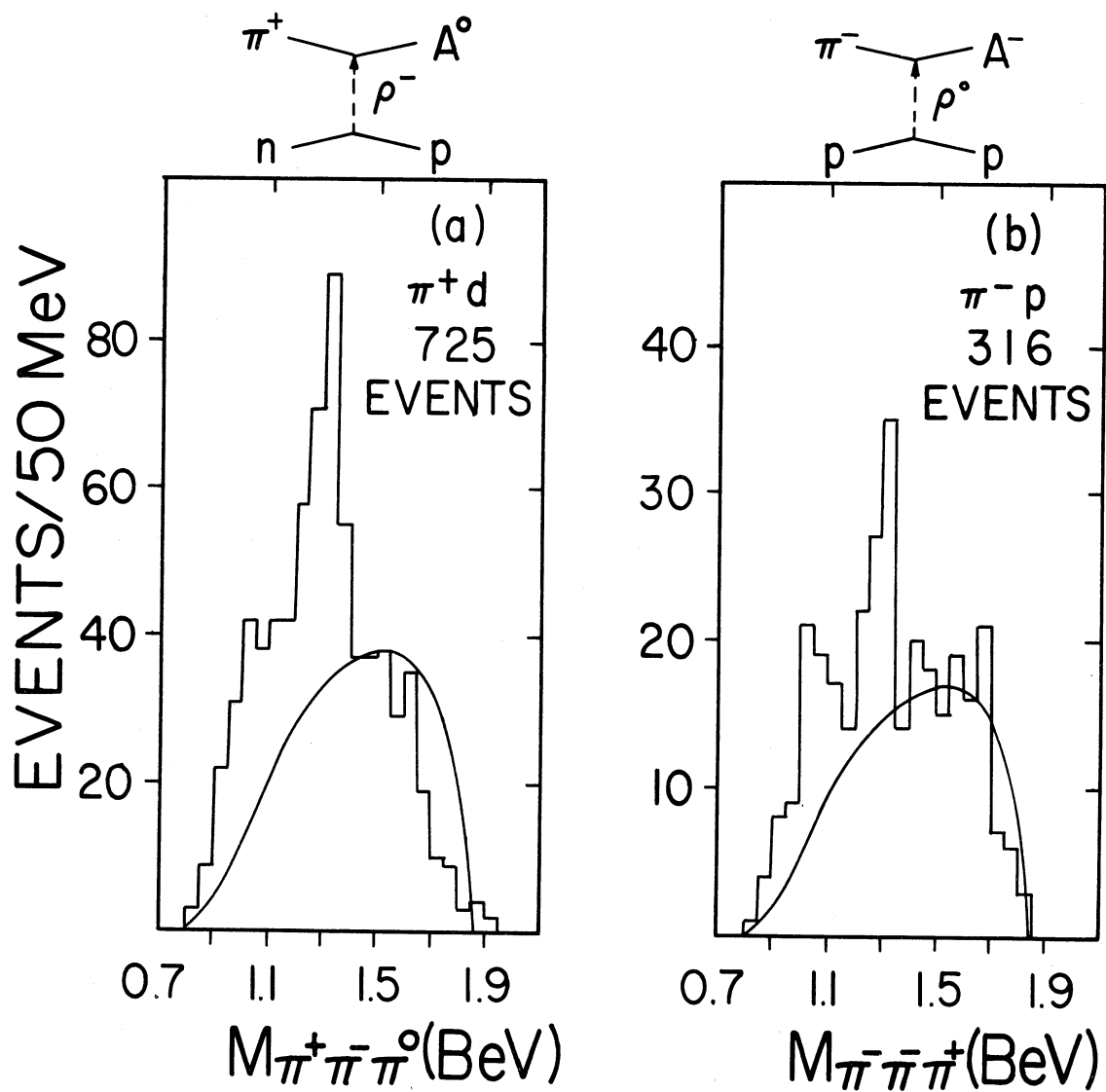


Figure 54. (a) Mass of $\pi^+\pi^-\pi^0$ for events with $\Delta^2(3\pi) < 0.85 (\text{BeV}/c)^2$ and ρ^+ or ρ^- . (b) Mass of $\pi^-\pi^-\pi^+$ from the π^-p data at 3.65 BeV/c of Ref. 46 for events with $\Delta^2(3\pi) < 0.85$ and ρ_1^0 or ρ_2^0 . The curve is the phase space estimate for $\pi n \rightarrow \rho\pi n$ normalized at $M(3\pi) = 1.5 \text{ BeV}$.

ment approach.¹⁰³ The ρ^+ or ρ^- half width (Γ' of Ref. 8) is taken to be 0.150 BeV^2 . This corresponds to a full width in mass of 200 MeV, which includes an experimental $\pi^\pm \pi^0$ resolution of 60 MeV. Except for experimental parameters of this type, the predictions for the A_2^0 (see Fig. 55) are exactly the same as for the A_2^\pm . The interference terms also shown in Fig. 55 between ρ^+ and ρ^- are the same as those between ρ_1^0 and ρ_2^0 in the $\pi^\pm p$ data. Previous Dalitz plot spin-parity tests with $\pi^\pm p$ data² have resulted in possible assignments of $J^P = 1^+$ s-wave, 2^- , or 2^+ . If the A_2 decays to $K\bar{K}$ as observed by Chung et al.,⁹⁵ then the choice is limited to $J^P = 2^+, 4^+, \dots$. This decay mode is now very firmly established.⁹⁹

Figure 56(a) shows $M^2(\pi^-\pi^0)$ for A_2^0 events with $\rho^+(650\text{-}850 \text{ MeV})$. One might expect the background for these events to be similar to $\pi^\pm p$ data since the ρ^+ in our $\pi^+ n$ experiment, like the ρ^0 in $\pi^\pm p$, can be produced through pion exchange. Figure 56 (b) shows $M^2(\pi^+\pi^0)$ for our events with ρ^- , which cannot be produced in pion exchange. A comparison of these distributions with $\pi^\pm p$ data shows in fact that Fig. 56(a) does have a shape similar to $\pi^\pm p$ data while Fig. 56 (b) has fewer events in the low $M^2(\pi\pi)$ region. The events having $\rho^+ N^*0$ or $\rho^0 N^{*+}$ with $\Delta^2(\rho) \leq 0.6 (\text{BeV}/c)^2$ are shaded. They are distributed approximately according to phase space in Fig. 56 (a) but can lie only in the ρ overlap regions of Fig. 56 (b). Figure 56 (c) is the sum of (a) and (b) excluding the shaded events. As required for the theoretical curves, events with both ρ^+ and ρ^- are included twice in this plot but both of them do not fall, in general, at the same mass values.

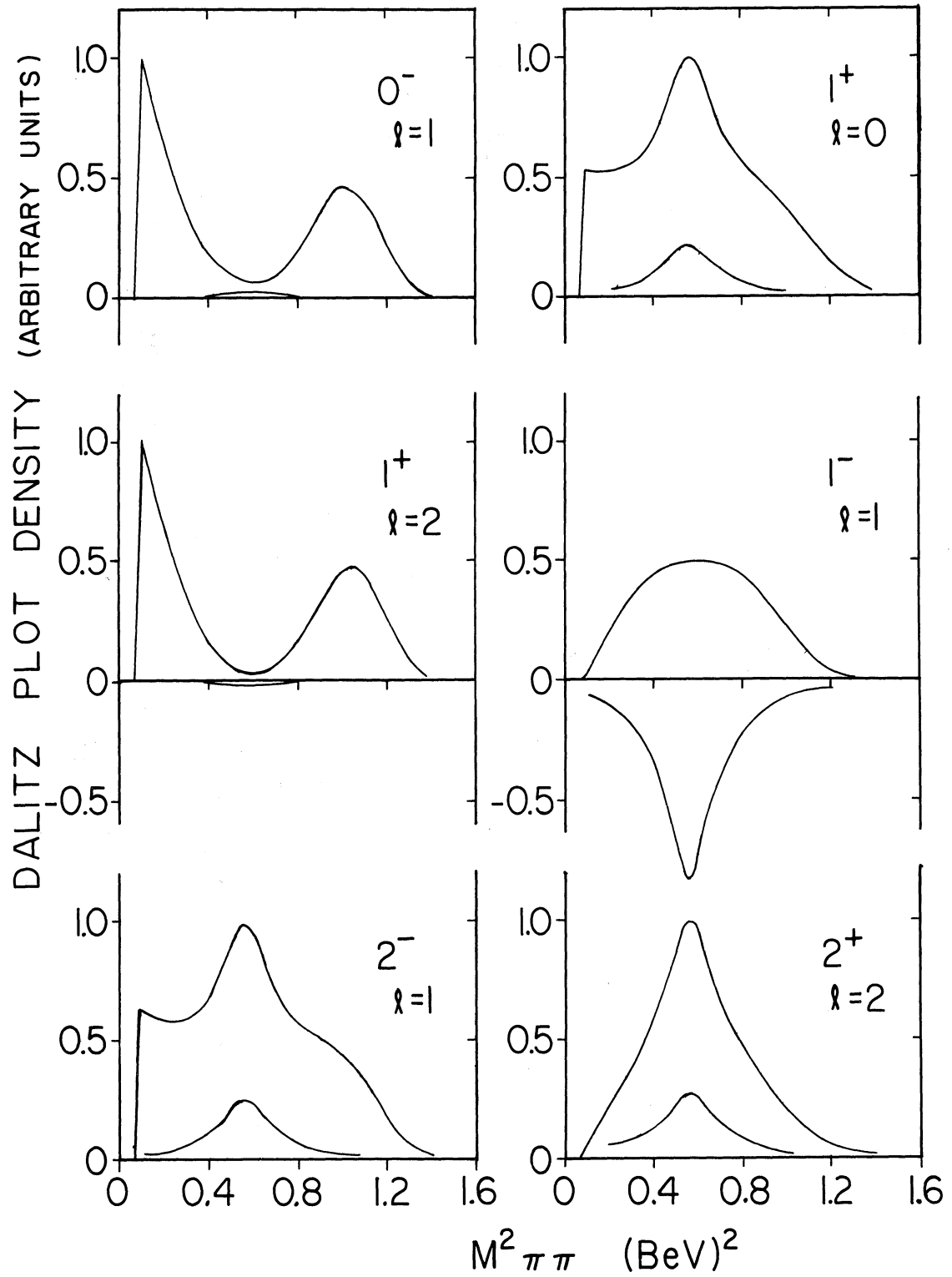


Figure 55. Predicted densities on the mass squared Dalitz plot (in the ρ bands) for various J^P and orbital angular momentum values " l ". The contribution of interference between $A_2^0 \rightarrow \rho^+\pi^-$ and $A_2^0 \rightarrow \rho^-\pi^+$ is shown below and to the same scale as each density profile.

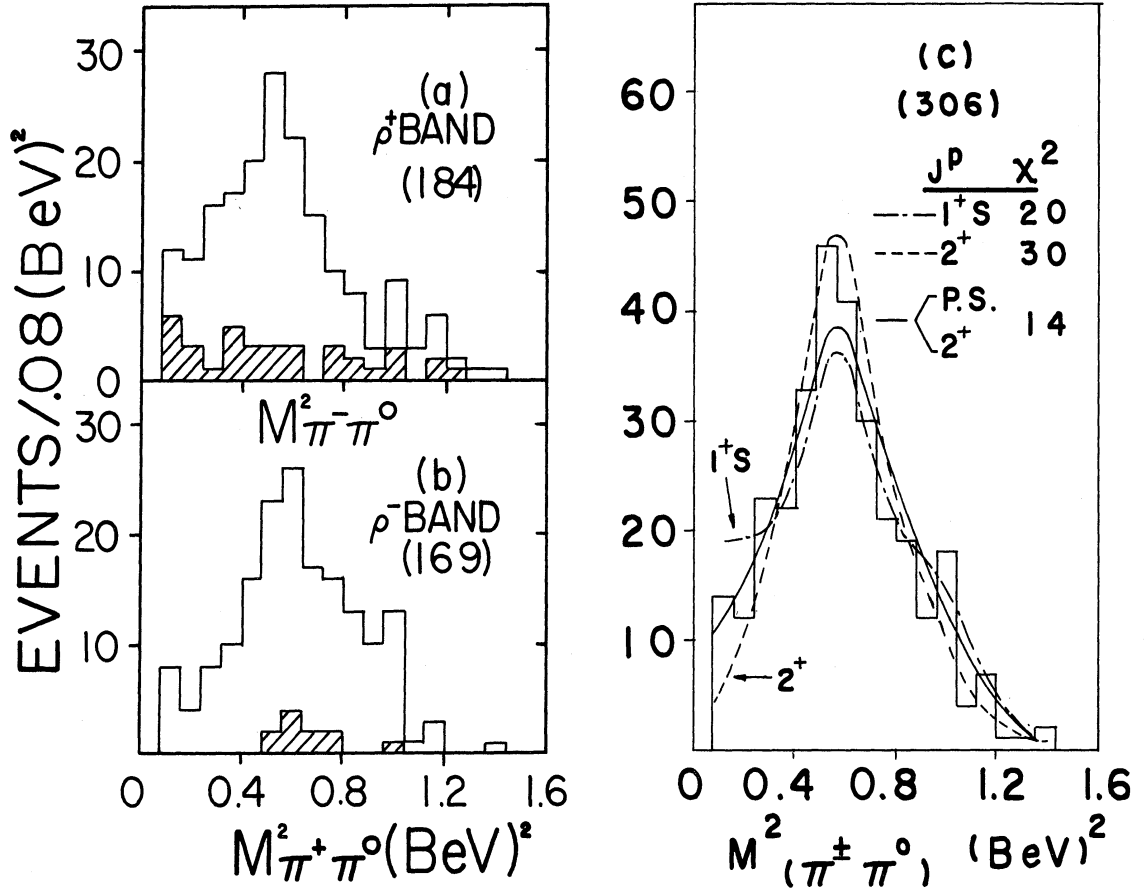


Figure 56. (a), (b) Mass squared distributions for events in the ρ bands with $1.2 < M(3\pi) < 1.4$ BeV and $\Delta^2(3\pi) < 0.85$ (BeV/c)². (c) Sum of events in (a) and (b) less the shaded events as explained in the text. Theoretical curves are for $J^P = 1^+$ s-wave and 2^+ both without background, and 2^+ with 37% background distributed according to phase space.

Three of the theoretical curves are shown in Fig. 56 (c). If we do not take into account the presence of background, the three best assignments, with (J^P , χ^2 probability) are: (2^+ , 0.01), (1^+ s-wave, 0.25), and (2^- , 0.02). From the 3π mass plots for these events, the background level is estimated to be 37%. With the addition of this background distributed according to phase space, the above J^P assignments become: (2^+ , 0.55), (1^+ s-wave, 0.02), and (2^- , 0.002) for 16 degrees of freedom. Thus with the assumptions of our experimental parameters, and the distribution of background according to phase space, our data definitely favor the 2^+ assignment over all other J^P with $J \leq 2$. It is interesting that for $J^P = 1^+$ s-wave and 2^- , the minimum values of χ^2 are reached with 0% background, but for 2^+ the χ^2 is minimized at 32% background.

D.4 A_2^0 Production Mechanism

Assuming that we are observing the A_2^0 , a test of ρ exchange (diagrammed above Fig. 54) as a production mechanism can be made. The cross section for $\pi^+n \rightarrow A_2^0 p$ at a given energy should be twice that for $\pi^-p \rightarrow A_2^- p$, based on the ratio of the isospin vector addition coefficients at the npp and ppp vertices. An additional factor of two for the observed ratio of A_2^0/A_2^- results from the fact that both $\rho^+\pi^-$ and $\rho^-\pi^+$ decays are observed in this experiment, whereas only $A^- \rightarrow \rho^0\pi^-$ (and not $A^- \rightarrow \rho^-\pi^0$) is normally observed in π^-p experiments.

In Fig. 54 a comparison of this experiment is made with our data from $\pi^-p \rightarrow \pi_1^-\pi_2^-\pi^+p$ also at 3.65 BeV/c.⁴⁶ In each set of data, $\Delta^2(3\pi) \leq 0.85 (\text{BeV}/c)^2$ is required. Additionally in π^+d , Fig. 54 (a), ρ^+ or ρ^-

is required, and in π^-p , Fig. 54 (b), ρ_1^0 or ρ_2^0 is required. The solid curve is a $\rho\pi$ phase space corrected for the Δ^2 limitation, but not for Fermi momentum, and normalized at $M(3\pi) = 1.5$ BeV. The sample size for the π^-p data is $2.1 \pm 0.2 \mu\text{b}/\text{event}$. For the π^+d data the corresponding number is $1.2 \pm 0.1 \mu\text{b}/\text{event}$. Using the events above the curve in Fig. 54, we obtain

$$R_2 = \sigma(A_2^0)/\sigma(A_2^-)_{\text{observed}} = \frac{170 \pm 30\mu\text{b}}{90 \pm 30\mu\text{b}} = 1.9 \pm 0.6 *$$

which is more than three standard deviations below 4.0, as predicted by the simple argument above. We will show later that ρN^* production is also one half the value predicted from pion exchange and π^-p data.

The observed value of R_2 could be understood if roughly half of the A_2^- were produced by f^0 exchange. Contributions from η^0 exchange should be small in A_2^\pm production since the observed rate of decay⁵⁸ into $\eta^0\pi^\pm$ (which is energetically favored over the dominant $\rho\pi$ mode) is small. Neutral meson exchange, of course, can not contribute to A_2^0 production in $\pi^+n \rightarrow A_2^0p$ since a charged meson must be exchanged.

Independent evidence for f^0 exchange may be found by comparing

- a) the $\Delta^2(A_2^0)$ and $\Delta^2(A_2^\pm)$ distributions, or
- b) the density matrix elements (particularly ρ_{22}) for A_2^\pm and A_2^0 , or by observing either of

*The 0.6 error includes a 9% uncertainty in normalization for $\sigma(A_2^0)$ and 10% and 14% uncertainties in the normalization of the two phase space curves, but no error for uncertainty in the shape of the background. The shapes should be identical (kinematically) in the two channels in the mass region being studied.

c) the reactions $\pi^\pm d \rightarrow A_2^\pm d$.

All of these tests are hampered by background events present with the A_2 .

D.5 Aside on A_1^0 Production

Although we have no evidence for A_1^0 production, we can set an upper limit for its production by counting all events above the curve in Fig. 54 (a). We compare it with the A_1^- production shown in Fig. 54 (b). The cross section ratio in the A_1 region, $M(3\pi) = 1.0-1.2$ BeV, is

$$R_1 = \frac{\sigma(A_1^0)}{\sigma(A_1^-)}_{\text{observed}} \leq \frac{100 \pm 20\mu\text{b}}{90 \pm 20\mu\text{b}} = 1.1 \pm 0.3 .$$

The fact that the ratio R_2/R_1 is 1.7 ± 0.3 rather than 1.0 seems to indicate a fundamental difference in the production mechanism for the events in the A_1 and A_2 regions. If the Deck effect^{84,90} is present in A_1 production, one would expect a diminished value for R_1 due to the requirement of charge exchange at the nucleon vertex. It should be noted that the normalization uncertainties included in R_2 and R_1 cancel in the calculation of R_2/R_1 . Also note that a subtraction of H-meson events from the A_1^0 region would increase R_2/R_1 and strengthen our conclusion.

D.6 Momentum Transfer Distributions

The distribution of $\Delta^2(A_2^0)$ is shown in Fig. 57. The $\rho N^*(1238)$ events with $\Delta^2(\rho) < 0.6 (\text{BeV}/c)^2$ have been shaded. The subtraction is not as important here as it was for the H meson. The fitted curve shown is exponential with $A = 2.9 \pm 0.3 (\text{BeV}/c)^{-2}$. This value of A is smaller than the values of A found in processes attributed to pion exchange (we

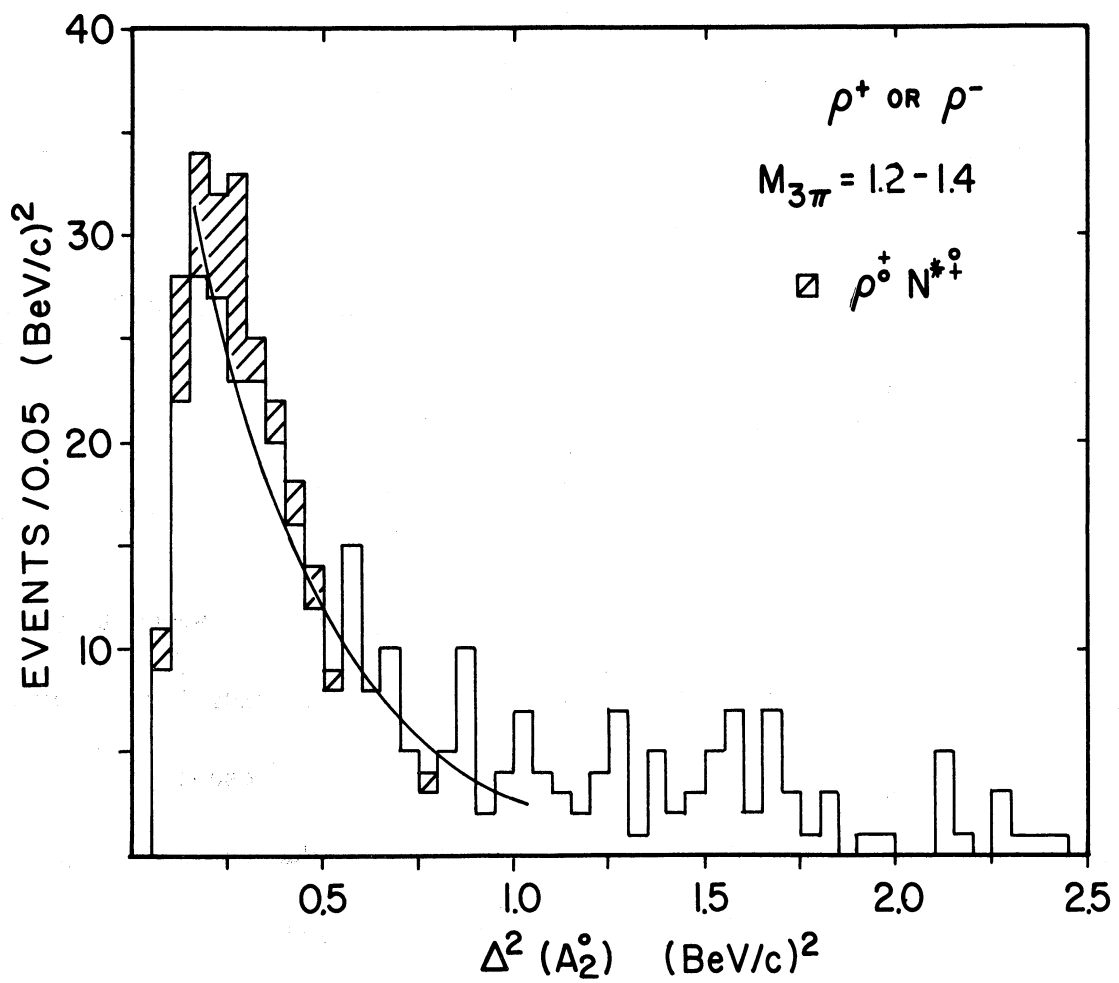


Figure 57. Distribution of $\Delta^2(3\pi)$ for A_2^0 events. The contribution of ρN^* events is shaded.

observe $A(\rho^0) = 5.5 \text{ (BeV/c)}^{-2}$ as discussed in Section E). This can be taken as evidence that a heavy meson such as the ρ meson is being exchanged. A variety of predicted differential cross sections for A_2 production based on the absorption model can be found in a recent paper on 2^+ mesons.¹⁰⁴

The $\Delta^2(\rho)$ distribution in the region of the A_2^0 can be seen in Fig. 44. We note that it is in disagreement with a similar distribution obtained by Shen.⁴⁸ His result, from events of the type $\pi^\pm p \rightarrow \rho^0 \pi^\pm p$, shows $\Delta^2(\rho^0)$ has two humps, one near $\Delta^2 = 0$ and one above $\Delta^2 = 1.0 \text{ (BeV/c)}^2$. We have no evidence for this behavior with the A_2^0 , nor do we have it in our $\pi^- p \rightarrow A_2^- p$ events.^{46,105} An understanding of this difference is very important since it would indicate differences in the polarization of the A_2 mesons produced in these experiments.

D.7 Density Matrix Elements

The determination of the density matrix is very important for understanding A_2 production. If the A_2 meson is produced by ρ -meson exchange, then the diagonal elements of the density matrix will be $\rho_{00} = \rho_{22} = 0$, and $\rho_{11} = 0.5$ just as for ω^0 production. Calculations¹⁰⁶ show that absorption tends to "depolarize" the A_2 , causing the elements to approach the random production values of $\rho_{mm} = 0.2$. Unsubtracted isotropic backgrounds would also have this effect.

Very few results have been presented on the density matrix elements of the A_2 ; however, there are results for $A_2^- \rightarrow \rho^0 \pi^-$ at 2.75 BeV/c⁹⁶

and $A_2^- \rightarrow K^0 K^-$ at 2.9 - 3.3 BeV/c.⁹⁹ Alitti, et al.,⁹⁶ have presented the decay plane normal distribution for events with $M(\rho^0 \pi^-) = 1.24 - 1.36$ BeV and $\Delta^2(A_2^-) < 0.8$ (BeV/c)². The data is further restricted to be outside the interference region, i.e., outside the region where the ρ bands overlap on the Dalitz plot (Fig. 51). The cosine of the decay plane normal relative to the beam direction in the A_2^- rest frame is shown in Fig. 58 for the 2.75 BeV/c data. The predicted distributions for ρ exchange (solid) and η exchange (dashed) without absorption are also shown. This data is consistent with the ρ -exchange prediction.

Hess⁹⁹ has determined the entire real part of the density matrix from $A_2^- \rightarrow K^0 K^-$ where the direction of a K meson in the A_2^- rest frame is the spin analyzer. There is only a single decay mode here, and, therefore, there is no self-interference region. His coordinate system differs from ours by a 180° rotation about the beam (z axis). We present his results in Table X with his results altered to fit our coordinate system as explained in the Table. These results are also shown in Fig. 59 with the predictions of the absorption model for 3.65 BeV/c. We are deeply indebted to W. Fischer for making the absorption calculations for us.¹⁰⁶ An excellent theoretical review of the absorption model and 2^+ mesons has been presented by Høgaasen, et al.¹⁰⁴ The parameters used in the calculation are $G_T/G_V = 3.7$, $\gamma_1 = \gamma_2 = 0.038$, and $C_1 = C_2 = 1.0$.

In determining ρ_{mm} , for our A_2^0 , we perform a least squares fit to the following distributions (with $x = \cos\theta$ and $\rho_{11} = (1 - 2\rho_{22} - \rho_{00})/2$):

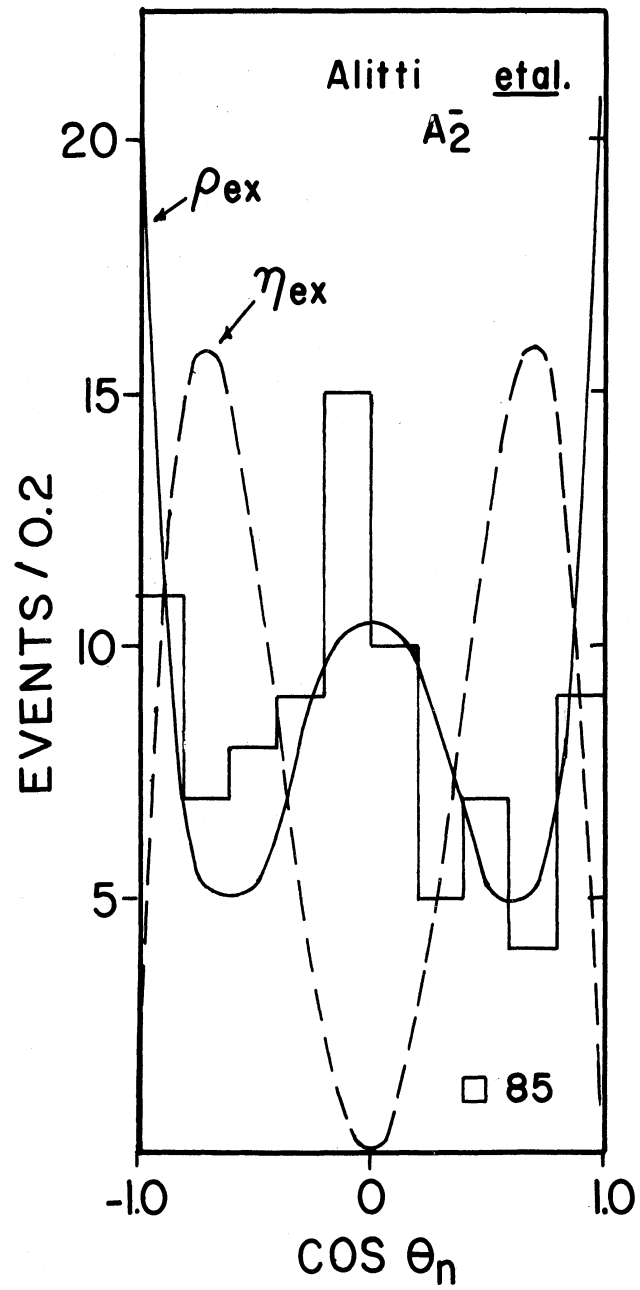


Figure 58. Distribution of the decay plane normal for A_2^- production at 2.75 BeV/c. The curves show the predictions for ρ^0 and η^0 exchange without absorption.

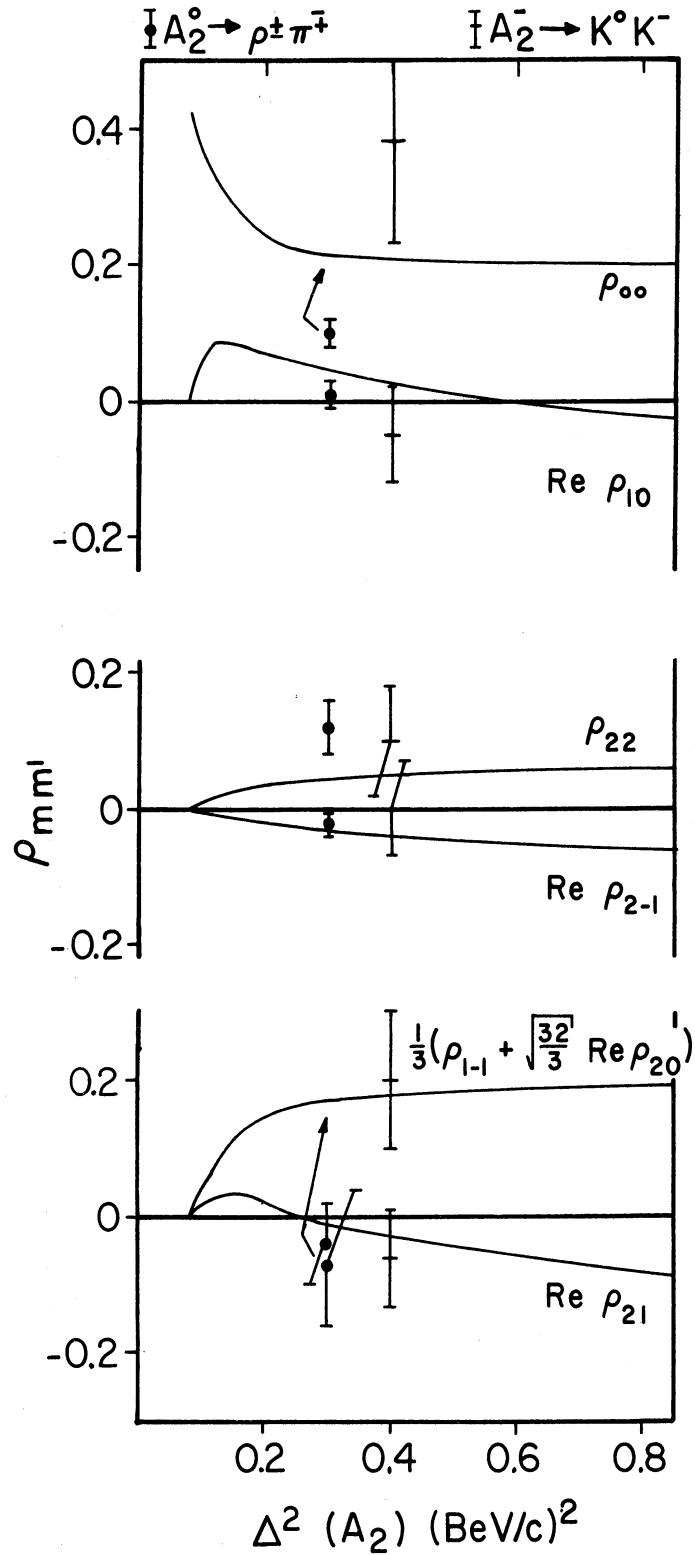


Figure 59. Predicted values of the density matrix for the A_2 based on ρ exchange with absorption. The results for $A_2^0 \rightarrow \rho^\pm \pi^\mp$ (this experiment) and $A_2^- \rightarrow K^0 K^-$ are compared with the predicted values. Arrows show the curve being compared in ambiguous cases.

TABLE X

DENSITY MATRIX ELEMENTS FOR $A_2^- \rightarrow K^0 K^-$ AND $A_2^0 \rightarrow p^- \pi^+$

(We have multiplied Rep_{10} , Rep_{21} , and Rep_{2-1} in the A_2^- data (of Hess) by -1 to correct for the difference in the coordinate systems used in the experimental determinations.)

Mass Interval (BeV)	1.267 - 1.367	1.2 - 1.4	1.2 - 1.4	1.4 - 1.6
Event Class	$A_2^- \rightarrow K^0 K^-$	$A_2^0 \rightarrow p^- \pi^+$ (not both)	$A_2^0 \rightarrow p^- \pi^+$ (all)	Above A_2^0 (not both)
ρ_{00}	$0.38 \pm .15$	$0.10 \pm .02$	$0.12 \pm .02$	$0.00 \pm .03$
ρ_{22}	$0.10 \pm .08$	$0.12 \pm .04$	$0.16 \pm .03$	$0.10 \pm .05$
$\chi^2_{\text{prob.}}$	----	1/2%	5%	1%
$\left(\rho_{1-1} + \sqrt{32/3} \cdot \text{Rep}_{20} \right)$	$+0.6 \pm .3$	$-0.2 \pm .3$	$+0.3 \pm .3$	$+0.0 \pm .4$
ρ_{2-2}	$-0.04 \pm .09$	$-0.02 \pm .08$	$+0.00 \pm .06$	$+0.0 \pm .1$
$\chi^2_{\text{prob.}}$	---	90%	40%	70%
Rep_{10}	$-0.05 \pm .07$	$+0.01 \pm .02$	$+0.01 \pm .02$	$+0.01 \pm .03$
Rep_{21}	$-0.06 \pm .07$	$-0.04 \pm .06$	$-0.01 \pm .05$	$+0.14 \pm .08$
Rep_{2-1}	$0.00 \pm .07$	$-0.02 \pm .02$	$-0.01 \pm .02$	$-0.01 \pm .03$

$$\frac{dW}{d \cos \theta_n} = \frac{dW}{d \cos \theta_p} = \frac{5}{4} \left[\rho_{22}(1 - x^4) + \rho_{11}(4x^4 - 3x^2 + 1) - 3\rho_{00}(x^2 - x^4) \right],$$

$$\frac{dW}{d \Phi_n} = \frac{1}{2\pi} \left[1 - \frac{4}{3} \rho_{2-2} \cos^4 \Phi_n - \frac{1}{3} \left(\rho_{1-1} + \sqrt{\frac{32}{3}} \text{Rep}_{20} \right) \cos^2 \Phi_n \right],$$

and use an averaging method to obtain

$$\text{Rep}_{10} = \frac{21}{40} \sqrt{\frac{3}{2}} \langle \sin^4 \theta_n \cos \Phi_n \rangle,$$

$$\text{Re}\rho_{21} = -\frac{7}{4} \langle \sin 2\theta_n \cos \Phi_n \rangle ,$$

$$\text{Re}\rho_{2-1} = -\frac{21}{32} \langle \sin 2\theta_n \cos 3\Phi_n \rangle .$$

The results are given in Table X and Fig. 59. We use the bachelor pion (the pion not from the decay of the ρ meson) just as we did for the H analysis and make a simultaneous fit to the decay plane normal and the bachelor pion distributions. For $J^P = 2^+$ the two distributions must be identical for any production mechanism. This has been pointed out by Høgaasen, et al.¹⁰⁴

Our data is shown in Fig. 60. The coordinate system has been defined in Fig. 35 (a). We have limited $\Delta^2(A_2^0) < 0.85 \text{ (BeV/c)}^2$ and require $\rho^+\pi^-$ or $\rho^-\pi^+$ in these plots. Figures 60 (a-f) are in the A_2 region with $M(3\pi) = 1.2 - 1.4 \text{ BeV}$. Figures 60(g-i) are from a control region above the A_2 with $M(3\pi) = 1.4 - 1.6$. The last six figures, Figs. 60 (d-i), show only non-interfering events; i.e., single ρ events are plotted. The shaded events are the subsample with ρ^+N^{*0} or ρ^0N^{*+} .

We note a number of properties of these distributions. The $\cos\theta_n$ and $\cos\theta_b$ distributions do not seem to be identical as indicated by the low χ^2 probabilities of the fitted curves. The $\cos\theta_b$ distributions all look like the $\cos\theta_n$ distribution presented by Alitti, et al.⁹⁶ Of the values of J^P tested on the A_2 Dalitz plot, only the 2^+ value can have the $\cos\theta^4$ powers which we see in the $\cos\theta_b$ distributions. A fit to the $\cos\theta_n$ distribution alone gives $\rho_{00} = 0$, $\rho_{22} = 0.35$. The large

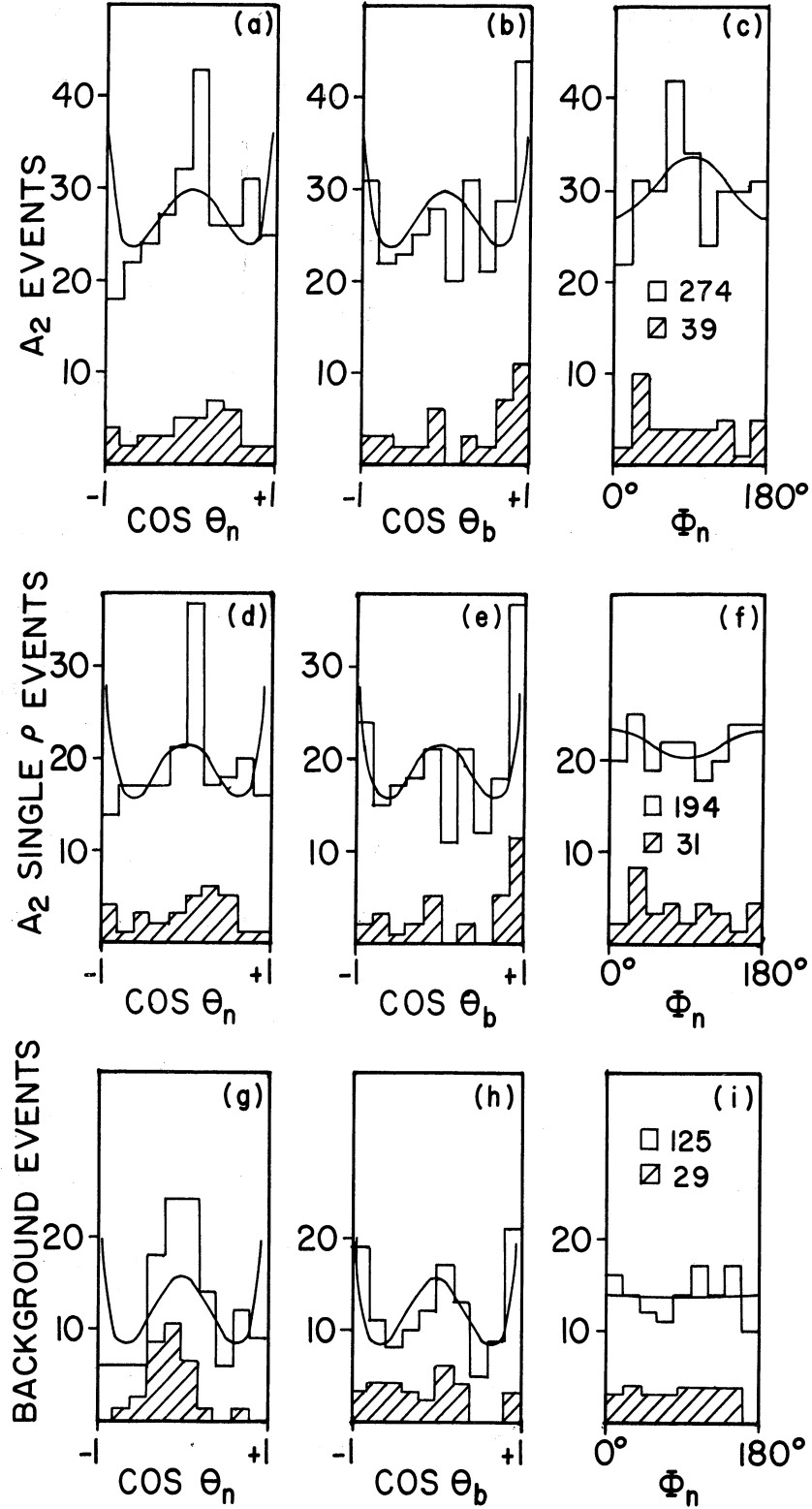


Figure 60. Angular distributions of the decay plane normal for the A_2^0 and for the bachelor pion. (a - i) have $\Lambda^2(3\pi) < 0.85$ (BeV/c) 2 and ρ^+ or ρ^- , (a - f) have $M(3\pi) = 1.2 - 1.4$ BeV, (j - i) have $M(3\pi) = 1.4 - 1.6$ BeV, and (d - i) are for single ρ events only.

value of ρ_{22} would be realistic only if a spin two particle were being exchanged in the production process. A (preliminary) large value of ρ_{22} has also been observed in A_2^0 production at 3.25 BeV/c,¹⁰⁷ so the problem is not peculiar to this experiment.

In an attempt to learn more about the differences in $\cos\theta_n$ and $\cos\theta_p$, we have cut the A_2^0 data into two parts, a central part with $M(3\pi) = 1.26-1.36$ BeV and an edge part with $M(3\pi) = 1.2-1.26$ or $1.36-1.4$ BeV (see Fig. 61). The central sample should be richer in A_2^0 events than the outside. Background effects should be contained equally in the two samples. Figures 61 (c-f) are single ρ events only. There is very little difference in the single ρ distributions; however, there is possibly more structure in the edge sample. This suggests that the observed structure could be coming from background events. The parameters for the fitted curves are (ρ_{00} , ρ_{22} , χ^2 prob.) for

Figs. 61 (a,b)	$(0.16 \pm 0.02, 0.16 \pm 0.05, 30\%)$
Figs. 61 (c,d)	$(0.14 \pm 0.02, 0.12 \pm 0.06, 15\%)$ and
Figs. 61 (e,f)	$(0.02 \pm 0.02, 0.12 \pm 0.07, 25\%)$.

Detailed studies of the $\rho^0\pi^+$ and $\rho^-\pi^-$ events in and out of the A_2 regions should shed further light on this problem. Examining the present wide range of values of ρ_{11} for the A_2 and A_2^0 , we conclude that the values are consistent either with the modified or unmodified ρ -exchange predictions.

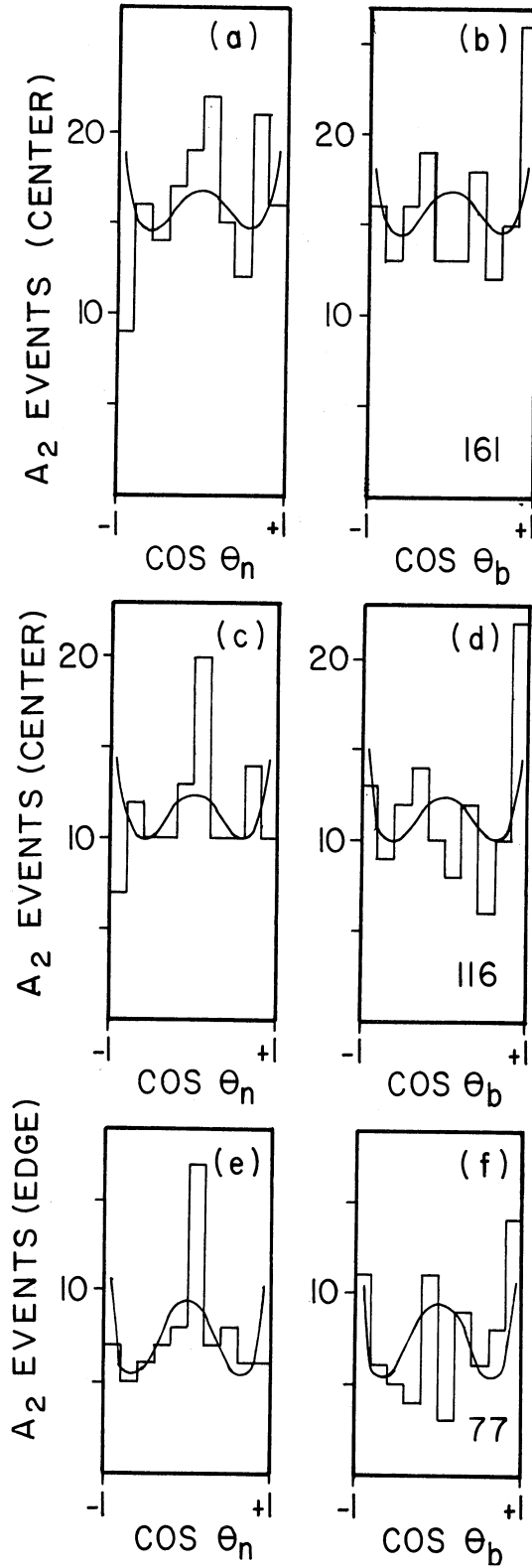


Figure 61. Decay plane normal and bachelor pion distributions for (a - d) the center of the A_2^0 , $M(3\pi) = 1.26 - 1.36$ BeV, and (e - f) edge, $M(3\pi) = 1.2 - 1.26$ and $1.36 - 1.4$ BeV. Single ρ is required in (c - f). (a - f) all have $\Lambda^2(3\pi) < 0.85$ (BeV/c)².

E. $\pi^+ d \rightarrow \rho \pi p p$

The ρ mesons have been well studied in the reactions

$$\pi^\pm p \rightarrow \rho^\pm p$$

$$\pi^- p \rightarrow \rho^0 n$$

$$\pi^\pm p \rightarrow \rho^0 \pi^\pm p \quad .$$

In each of these reactions, only one charge state of the ρ can be observed. In the reaction $\pi^+ d \rightarrow \pi^+ \pi^- \pi^0 p p$, all three charge states are observed

$$\pi^+ n \rightarrow \rho^+ \pi^- p$$

$$\rightarrow \rho^0 \pi^0 p$$

$$\rightarrow \rho^- \pi^+ p \quad .$$

Comparisons of ρ production in these three charge states with identical experimental treatment can provide information on production mechanisms.

E.1 Cross Sections, Masses, and Widths

The mass plots of the dipion systems are shown in Figs. 26 (a,b,c).

Counting the events above the phase space curves with $M(2\pi) = 600 - 900$

MeV gives

$$400 \rho^+ \text{ events} \quad \text{or} \quad \sigma(\rho^+) = 480 \pm 70 \mu\text{b}$$

$$330 \rho^0 \text{ events} \quad \text{or} \quad \sigma(\rho^0) = 400 \pm 60 \mu\text{b}$$

$$300 \rho^- \text{ events} \quad \text{or} \quad \sigma(\rho^-) = 360 \pm 50 \mu\text{b}$$

A fit of an s-wave Breit-Wigner form plus phase space to the data of Fig. 26 (a) gives

$$M(\rho^+) = 771 \pm 11 \text{ MeV} \quad \text{and} \quad \Gamma(\rho^+) = 230 \pm 45 \text{ MeV} .$$

Our (corrected) average resolution of $M(\pi^+\pi^0)$ and $M(\pi^-\pi^0)$ is $40 \pm 7 \text{ MeV}$. For $M(\pi^+\pi^-)$ the resolution is $15 \pm 5 \text{ MeV}$. A linear subtraction of the $\pi^+\pi^0$ resolution gives a corrected full width of

$$\Gamma(\rho^+) = 190 \pm 45 \text{ MeV} .$$

The world average values of ρ mass and width are $765 \pm 4 \text{ MeV}$ and $124 \pm 12 \text{ MeV}$.⁵⁸ The mass agreement is excellent, but our width is greater than the comparison value. Attempts to fit the ρ^0 and ρ^- data in an identical way have not been successful. This is primarily due to deviations of the data from the phase space estimate at low values of $M(\pi\pi)$. Superposition of Figs. 26 (b and c) on Fig. 26 (a) shows that the central values and widths of the ρ^0 and ρ^- peaks are comparable to those we quote for the ρ^+ .

E.2 Pion Exchange

In Figs. 26 (d',e',f') are shown $\Delta^2(\rho)$ distributions for events simultaneously in the ρ and $N^*(1238)$ bands. These bands are defined to be $M(2\pi) = 650 - 850 \text{ MeV}$ and $M(p\pi) = 1140 - 1340 \text{ MeV}$. Exponential fits to these $\Delta^2(\rho)$ distributions between 0.1 and 0.45 (BeV/c)^2 gives

$$A(\rho^+) = 5.6 \pm 1.2$$

$$A(\rho^0) = 5.4 \pm 1.2$$

$$A(\rho^-) = -2.7 \pm 1.8 \text{ (BeV/c)}^2 .$$

Since the production of ρ^- requires the exchange of two units of charge, a single pion cannot be exchanged in its production. This may explain the much lower value of $A(\rho^-)$. The large and equal values of $A(\rho^+)$ and $A(\rho^0)$ are expected for ρ production by pion exchange.

Another quantitative test of pion exchange may be made by comparing hydrogen data at 3.65 BeV/c⁴⁶

$$\pi^- p \rightarrow \rho^0 N^{*0} \quad (0, 0)$$

$$\rho^0 \rightarrow \pi^+ \pi_1^- \text{ or } \pi^+ \pi_2^-$$

$$N^{*0} \rightarrow p \pi_2^- \text{ or } p \pi_1^-$$

with deuterium data at 3.65 BeV/c

$$\pi^+ n \rightarrow \rho^+ N^{*0} \quad (+, 0), \text{ and}$$

$$\pi^+ n \rightarrow \rho^0 N^{*+} \quad (0, +) .$$

Clebsch-Gordan coefficients for pion exchange predict that the ratios of observed events will be

$$(0, 0) : (+, 0) : (0, +) = 1 : 2 : 2 .$$

We observe the cross sections

$$(0, 0) : (+, 0) : (0, +) = 197 \pm 30 : 182 \pm 20 : 180 \pm 20 \text{ } \mu\text{b}$$

$$= 1 : 1 : 1 .$$

In both experiments we have counted all events with $M(2\pi) = 650-850$ MeV as ρ , $M(p\pi) = 1140-1340$ MeV as N^* , and further required $\Delta^2(\rho) < 1.0$ $(\text{BeV}/c)^2$. This selection gives 96 (0, 0) events with 2 overlap events, and 155 (+, 0) and 153 (0, +) events with 6 overlap events. The sample sizes are $2.1 \pm 0.2 \mu\text{b}/\text{event}$ for the π^-p data and 1.2 ± 0.1 for the π^+d data. The small amount of experimental overlap (actually in momentum space) suggests that self-interference between the ρN^* pairs can be neglected.

We therefore seek possible experimental reasons for the discrepancy. A comparison of $\Delta^2(\rho)$ for these two reactions is made in Fig. 62. There is no evidence for any differences in backgrounds for these two samples. The chief contaminating reaction for π^-p is

$$\pi^-p \rightarrow \pi^-\pi^-N^{*++}$$

A careful study by W. Moebis⁴⁶ of the overlap of this reaction with $\rho^0 N^{*0}$ indicated that the 96 $\rho^0 N^{*0}$ events should be reduced to 80 events.

While there are very likely backgrounds also present in the one-constraint π^+d data, there is no dominating reaction which can be unambiguously removed. (Note that η^0 and ω^0 production do not contribute to any extent when the ρ requirement is made.) Inspection of the ρ^+ and ρ^0 peaks in our overall data indicates that the ρ^+ and ρ^0 bands contain 60-70% background. In the ρ^0 band of the π^-p data, the background level is about 50%. It therefore seems unreasonable to reduce the (0,0)

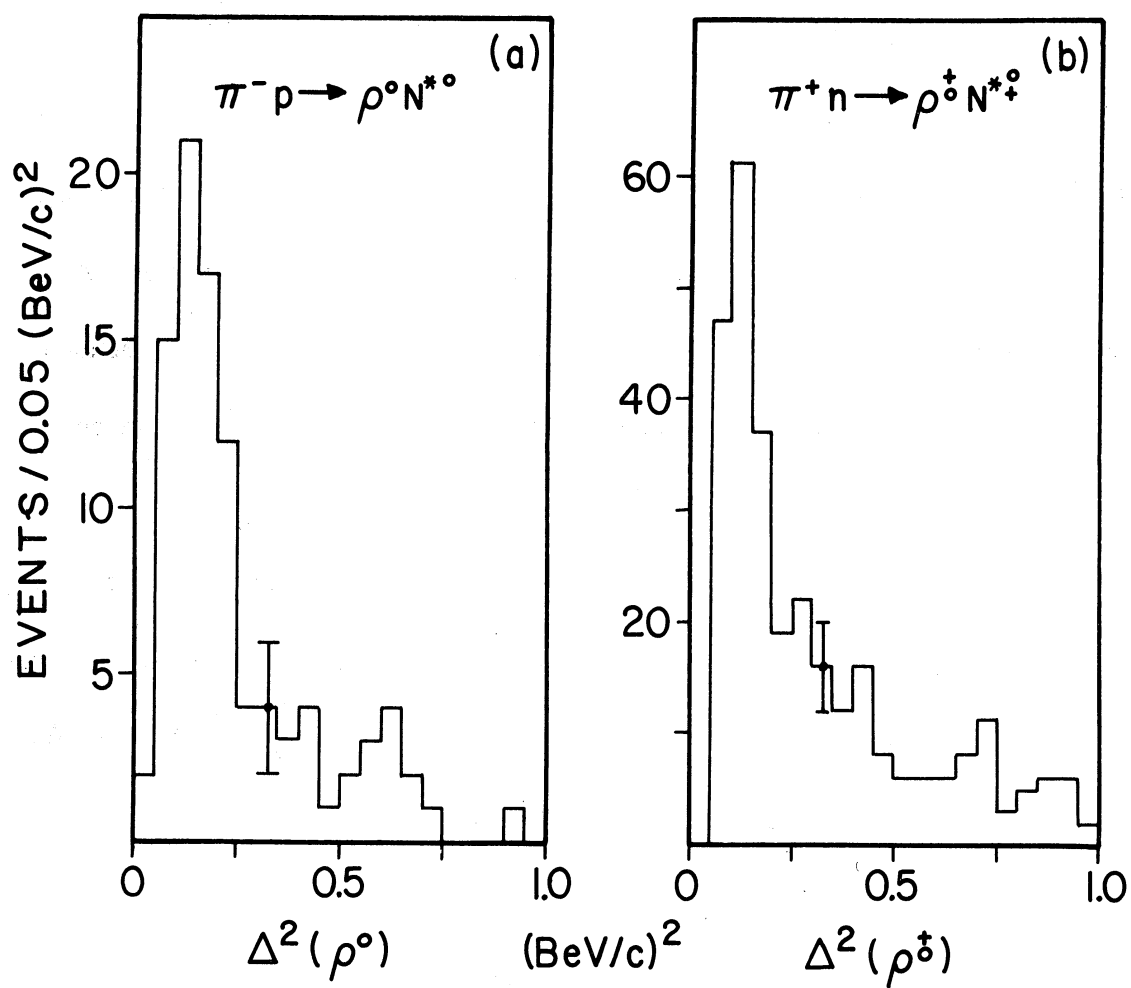


Figure 62. (a) $\Delta^2(\rho^0)$ for the reaction $\pi^- p \rightarrow \rho^0 N^{*0}$ at 3.65 BeV/c and (b) $\Delta^2(\rho^+ \text{ or } \rho^0)$ for the reactions $\pi^+ d \rightarrow (\rho^+ N^{*0} \text{ or } \rho^0 N^{*+}) p_s$ at 3.65 BeV/c.

cross section without a similar or greater reduction of the (+, 0) and (0, +) cross sections.

As we pointed out in Chapter IV, our πp_s mass spectrum is about the same as our πp spectrum. An investigation of the $\pi\pi$ scattering angle for the ρ 's from low πp and low πp_s masses shows very little difference. It is possible that some of the events with high πp mass are really $N^*(1238)$ if the πp_s mass value is accepted.

To estimate an upper limit for N^{*+0} production we have plotted for each event the lower of the πp and πp_s masses. The results are 190 (+, 0) and 178 (0, +) events. Ignoring a subtraction for overlap, our upper limit becomes

$$\begin{aligned} (0, 0) : (+, 0) : (0, +) &= 197 \pm 30 : 228 \pm 30 : 214 \pm 30 \text{ } \mu\text{b} \\ &= 1 : (1.2 \pm 0.2) : (1.1 \pm 0.2) \end{aligned}$$

Our deuterium production is still about one half of what was expected. We note that this is the same result found in our comparison of A_2^- and A_2^0 . We also note that it is not clear that the argument should work in practice since the experimental ratio $(\pi^- p \rightarrow \rho^- p) : (\pi^- p \rightarrow \rho^0 n)$ does not always equal the expected value of 2,³⁰ even though the result is obtained in a single experiment. It is possible that our result could be understood if interference effects were properly taken into account.

E.3 Nucleon Exchange

A pion exchange interpretation may be made of the forward production angular distributions of the ρ 's shown in Figs. 63 (a,b,c). These

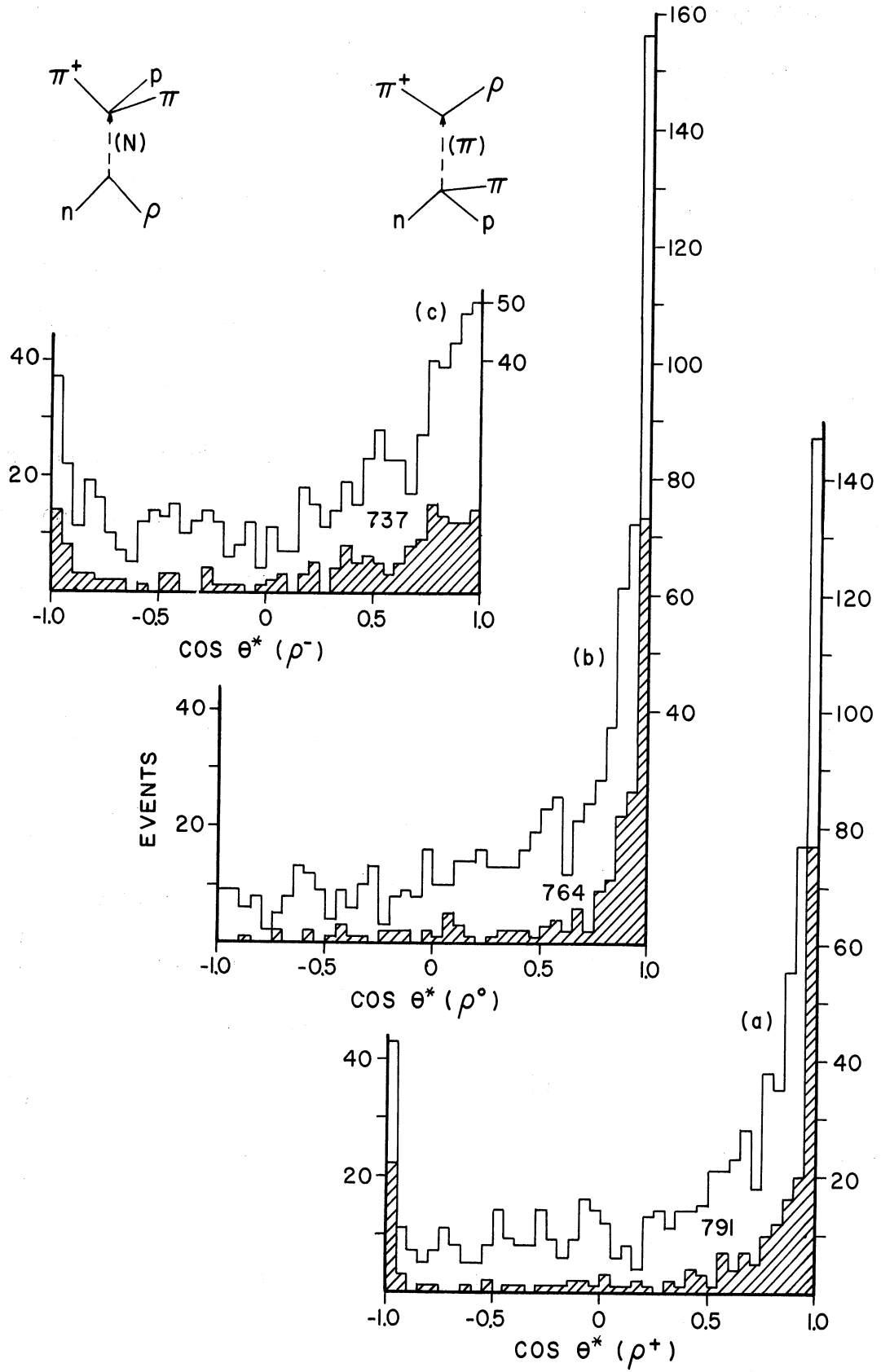


Figure 63. Center of mass production angular distribution for (a) ρ^+ , (b) ρ^0 , and (c) ρ^- events. Shaded events fall simultaneously in the ρ and $N^*(1238)$ bands.

angles are calculated in the center of mass of all the outgoing particles except the spectator. The shaded events are limited to $\rho N^*(1238)$ events.

It is interesting to predict the backward peaking of the shaded events assuming nucleon or $N^*(1238)$ exchange as a model, and assuming the $\pi\pi$ and $p\pi$ systems are in definite states with the quantum numbers of the ρ and $N^*(1238)$ resonances respectively. We use Clebsch-Gordan coefficients and neglect interference.

For N^* exchange the events in the backward shaded peaks should be in the ratio

$$N^{*0}\rho^+ : N^{*+}\rho^0 : N^{*++}\rho^- = 1 : \frac{16}{9} : 1 ,$$

and for nucleon exchange they should be in the ratio

$$N^{*0}\rho^+ : N^{*+}\rho^0 : N^{*++}\rho^- = 0 : \frac{1}{9} : 1 .$$

Neither of these predictions fits the data, nor does any incoherent sum of the two.

This is not a surprise because an examination of the backward events in the ρ^+ bands shows a strong asymmetry which would indicate interfering rather than definite quantum states. The angle between the beam and the charged pion in the ρ rest frame is more often less than 90° (47 events) than greater than 90° (12 events). The neutral particle is, in fact, generally moving in the backward hemisphere in the lab, relative to the beam. We note also that the high momentum transfer nature of the events makes it difficult to identify the faster proton by bubble density. For this

reason these events could possibly be of the type

$$\pi^+ d \rightarrow \pi^+ \pi^+ \pi^- pn .$$

Spectator neutrons can go backward in the lab. A check of the reasons why these events did not fit the (pn) reaction shows that nearly all of them have an unfitted missing mass more than three standard deviations below the neutron mass as expected for good (π^0) events. The ambiguous (π^0)-(pn) events show similar $\cos\theta^*(\rho)$ distributions, with the number of backward $pN^*(1238)$ events roughly equal to those in the good (π^0) events.* This suggests that the backward peaks are from good (π^0) events, but we have not ruled out the possibility that the neutron mass spectrum has a large tail which is not correctly treated by the fitting program .

We also have not ruled out the possibility that these events are really

$$\pi^+ d \rightarrow \pi^+ \pi^- pp ,$$

but we have been unable to suggest a mechanism for producing a fake neutral which is predominately backward in the lab.

E.4 Pion-Pion Scattering Angles

In Fig. 64 the $\pi\pi$ scattering angle in the ρ^+ , ρ^0 , and ρ^- rest frames

* For cross section purposes the numbers of events shown in the backward peaks should be doubled and multiplied by $1.1 \pm 0.10 \mu\text{b/event}$.

are given. The result shown in Figs. 64 (a,c,e) is for all events and in Figs. 64 (b,d,f) for only the $\rho N^*(1238)$ events. Additionally $\Delta^2(\rho) < 1.0 \text{ (BeV/c)}^2$ has been required for all six figures. The alignment ($\cos^2 \theta$ distribution) of the spin of the ρ^+ and ρ^0 mesons is to be expected for a pion exchange process.³⁰ The asymmetry of the decay of the ρ^0 is also as one would expect from π^+p experiments.^{30,46,48}

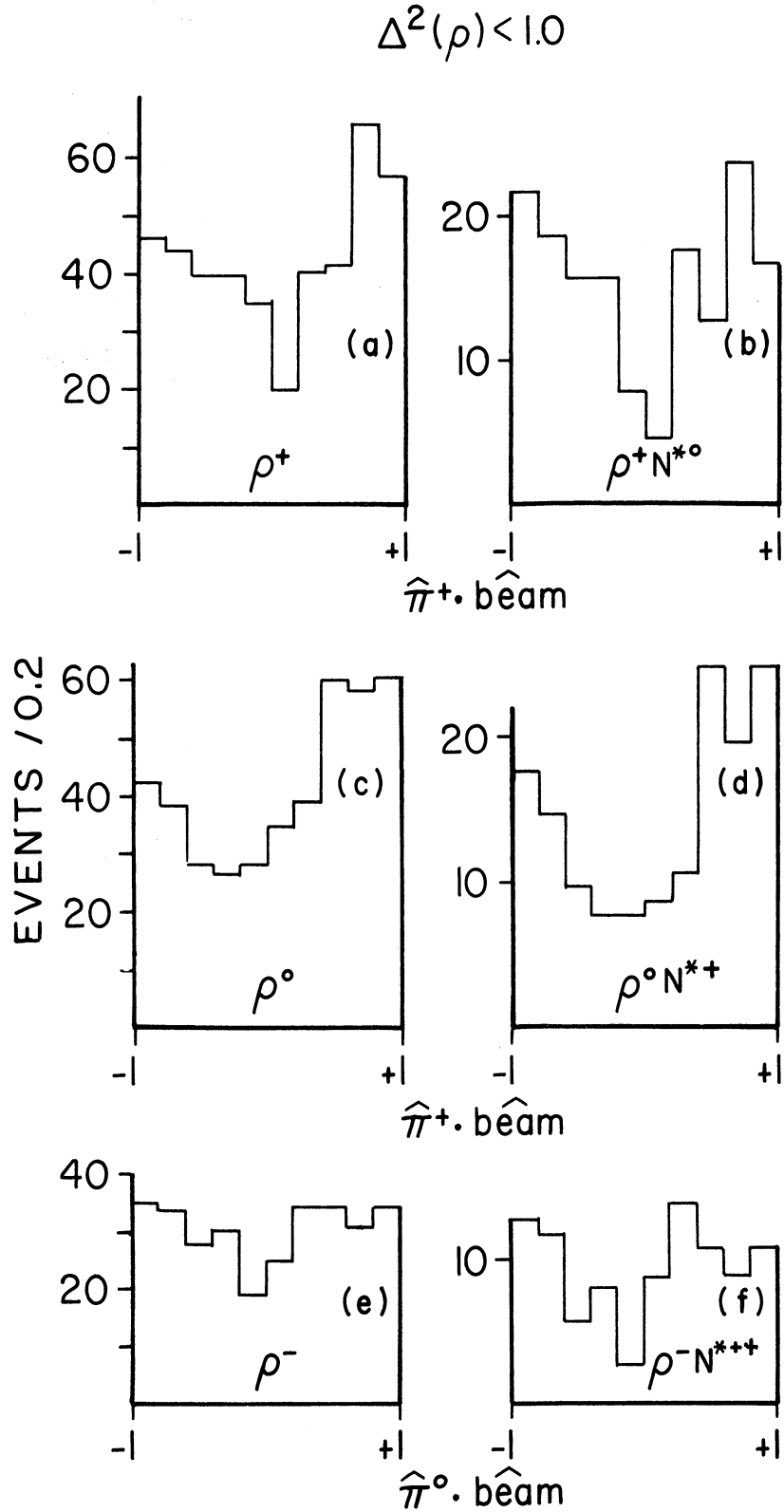


Figure 64. Angle between the beam pion and the pion from the decay of the ρ as seen in the ρ rest frame. We show in (a, c, e) all events with $\Delta^2(\rho) < 1.0 \text{ (BeV/c)}^2$ and in (b, d, f) these events with the further requirement of $N^*(1238)$.

CHAPTER VI

THREE-PRONG EVENTS

When the neutron in the deuteron is struck by the beam pion, its loosely bound proton remains virtually at rest in the bubble chamber. When such a proton has a laboratory momentum less than 60 MeV/c, it travels less than 0.4 mm in the bubble chamber and usually cannot be observed at all. This causes events to appear to have an odd number of tracks rather than the even number which is required by charge conservation. These "odd prongs" are potentially very useful since they are a clean sample of π^+n collisions with a nearly constant center of mass energy. In addition the identification of the missing track as a proton is unique since, if the missing track were a π^+ or a K^+ , it would decay and the decay products would be observed.

A. FITTING ODD-PRONG EVENTS

The odd-prong events have the disadvantage that the two angles of the missing proton track are entirely unknown, and only an upper limit can be placed on the unseen momentum. With a kinematic program like GRIND which is based on momentum, dip, and theta, this loss in two angular constraints reduces the (pp) reaction from four to two constraints, and makes the normally one-constraint (π^0) reaction unfittable. A program based on x, y, and z components of momentum, however, has no such loss of constraint since the average value of

each momentum component is known to be zero with an error of about 60 MeV/c. One would expect that errors in missing momentum of this magnitude could be tolerated. This is because in this experiment events thought to have no missing neutral have a missing momentum distribution in the beam direction with a half width at half maximum of 200 MeV/c.

In this experiment it was decided to process enough three-prong events to obtain an absolute cross section and to check the cross section prediction based on the Hulthen wave function in the (pp), (π^0), ($m^0\pi^0$), and (pn) reactions. Three possible ways of fitting the (pp) reaction were studied.

(a) The first method set the initial momentum of the spectator to 64 ± 64 MeV/c and left the angles unmeasured. This two-constraint fit worked well and was used to obtain the fitted variables for the mass plot to be discussed later.

(b) The second method left the proton entirely unmeasured and performed a one-constraint fit to a missing proton for the (pp) reaction. This resulted in many false fits which had an unreasonably high spectator proton momentum; however, the fitted momentum of the proton was not inherently biased toward 64 MeV/c or 0 MeV/c as it was in the previous or following methods. We found that 22% of the events which fit with method (a) failed to fit with method (d) even though there is one less constraint. Nearly all of the 22% failed because the correction terms needed to conserve energy and momentum were not getting smaller in succeeding steps of the fit.

(c) The third method fixed the proton momentum and angles at zero by setting initial values and errors at zero. This method did not work well for the four-constraint (pp) reaction. It is, however, the only one of the three methods which can be used to detect the one-constraint reactions (π^0) and (pn). The one-constraint fits to the π^0 and neutron appeared to be satisfactory.

The great difference in sensitivity between one-constraint and four-constraint reactions can be seen in a test we made on GRIND in which the measured spectator momentum in a sample of events was lowered by 10% (an average of 12 MeV/c) and the events were refitted. The average difference in probability (the altered momentum probability minus the original probability) was $-21 \pm 9\%$ for four-constraint fits, and $-2 \pm 3\%$ for one-constraint fits. It can be seen from these differences that in contrast to the four-constraint fits, the one-constraint fits are not sensitive to a 10% change in spectator momentum even though this change is large relative to the average spectator momentum measurement error which is 3.8%.

To summarize, fitting method (a) (spectator proton angles free) was used to fit the (pp) reaction in odd-prong events, and method (c) (spectator proton momentum fixed) was used for fitting the (π^0) and (pn) reactions. Method (b) (spectator momentum and angles free) was used to obtain an unbiased but fitted spectator proton momentum distribution.

B. THREE-PRONG EVENT CROSS SECTIONS

From film having a useful beam path length of $2.47 \pm 0.17 \times 10^6$ cm, 823 three-prong events (event type 03) were found in a double scan. All events were counted as three-prong events if two scanners agreed that the spectator was not measurable. A spectator was defined to be measurable if its apparent length (in the two views of the chamber which were scanned) was at least 0.7 mm (scaled to chamber dimensions). Such a rule cannot be applied rigidly, and we found that $7 \pm 2\%$ of the 823 events were judged to have a measurable spectator proton when reexamined by a measurer with a higher magnification. These events were not measured as odd-prong events but are counted in the total odd-prong cross section. To obtain the three-prong total cross section of 8.9 ± 0.8 mb, the constants given in Table XIV of Appendix H were used except for the path length as given above, the 03 interaction loss ($3 \pm 2\%$) and the 03 measuring loss (0%).

Table XI shows the numbers of events classified by bubble density and χ^2 in each π^+n channel. Ambiguous events have been apportioned using our experience with even-prong events. The errors shown are the result of an orthogonal combination of an 8% uncertainty in normalization with the percentage error determined from the uncertainty in the corrected numbers of events. The error in the corrected number of events is the combination of the statistical and the identification uncertainty.

TABLE XI

THREE-PRONG CROSS SECTIONS

Reaction	Events	Events Corrected	$\sigma(03)$ mb
1. $\pi^+ n \rightarrow \pi^+ \pi^- p$	91	111 ± 15	1.6 ± 0.3
2. $\pi^+ \pi^- p \pi^0$	157	165 ± 15	2.3 ± 0.4
3. $\pi^+ \pi^- p(\pi\pi^0)$	122	111 ± 10	1.6 ± 0.2
4. $\pi^+ \pi^+ \pi^- n$	87	124 ± 15	1.7 ± 0.3
5. $\pi^+ \pi^+ \pi^- n(\pi\pi^0)$	95	108 ± 15	1.5 ± 0.3
Strange Particle (K^+)	10	10 ± 7	0.14 ± 0.10
Ambiguous (2. - 4.)	44	---	
Ambiguous (3. - 5.)	23	---	
Total	629	629	8.8 ± 0.8

C. MASS SPECTRA

In Fig. 65 (a) the $\pi^+ \pi^-$ invariant mass is shown for the $\pi^+ \pi^- p$, three-prong final state. The ρ^0 and f^0 resonances can be seen.

In Fig. 65 (b) the $\pi^+ \pi^- \pi^0$ invariant mass is shown for the $\pi^+ \pi^- \pi^0 p$ final state. A clear ω^0 peak can be seen. A comparative study of the ω^0 peak in odd- and even-prong events at 1.7 BeV/c^{3,32} has found that the width of the ω^0 peak increases from 35 MeV in even-prong events to 55 MeV in odd-prong events due to the uncertainty in the spectator momentum. Assuming that this error (Γ_{spec}) contributes to the final width (Γ_{03}) according to $\Gamma_{03}^2 = \Gamma_{04}^2 + \Gamma_{\text{spec}}^2$, we obtain $\Gamma_{\text{spec}} = 42$ MeV. If instead Γ_{spec} adds linearly, then $\Gamma_{\text{spec}} = 20$ MeV. In either case, as the beam energy increases in a given bubble chamber, Γ_{04} should increase and Γ_{spec} remain constant. Thus the ratio Γ_{03}/Γ_{04} approaches one, and

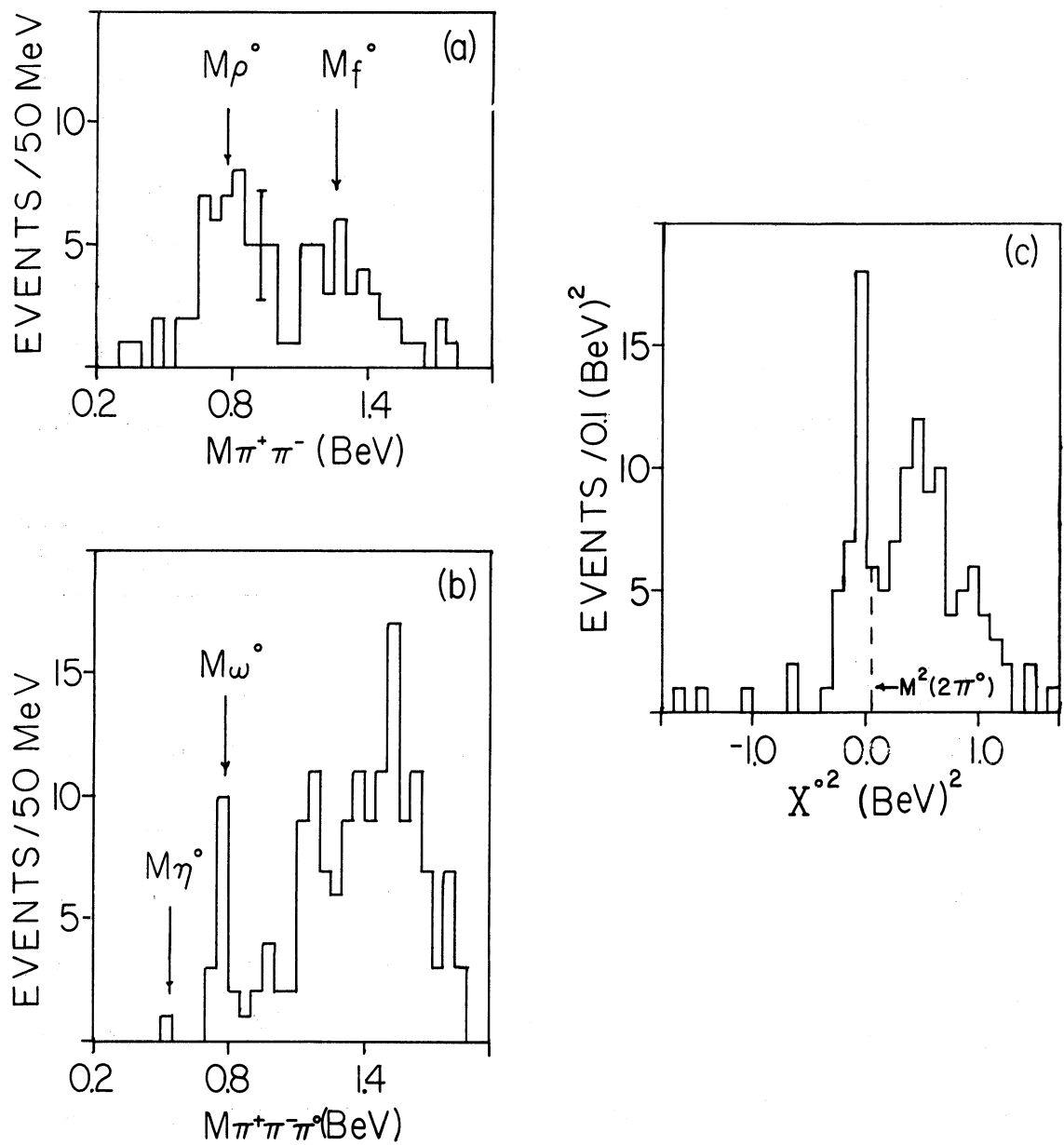


Figure 65. Invariant mass of (a) the $\pi^+\pi^-$ system for $\pi^+\pi^-p$ events, (b) the $\pi^+\pi^-\pi^0$ system for $\pi^+\pi^-\pi^0p$ events and (c) the missing mass squared for $\pi^+\pi^-(\pi^0)p$ events.

the odd-prong events become more and more useful for searches for resonance peaks at high energies.

In Fig. 65 (c) is plotted the missing mass squared for the $\pi^+\pi^-X^0p$ final state. The percentage of these events having an $X^0 < 2 M_{\pi^0}$ is $30 \pm 5\%$. In the even-prong events $20 \pm 1\%$ of this "no fit" channel have $X^0 < 2M_{\pi^0}$. This is one piece of evidence that the fitting procedure is less reliable for odd- than even-prong events.

Another indication of fitting difficulty is found in the 157 events identified as (π^0) events. Of these events 24/157 (16%) failed the (pp) hypothesis for a reason other than χ^2 being too large.* Nine of these 24 events had a missing momentum (unfitted) less than 200 MeV/c. However, since the total number of these events with a missing momentum less than 200 MeV/c (13 in 157, or 8.3%) is consistent with the number found in even-prong events ($7.7 \pm 0.5\%$), we conclude that for cross section purposes these are correctly identified as (π^0) events.

In Table XII we compare the three-prong cross sections with π^-p bubble chamber data (see Table II). In calculating the $\sigma(03)/\sigma(\pi^-p)$ ratio, we assume an error of 10% in each π^-p channel cross section. The results in each channel are consistent with the average result that the cross section for a given odd-prong channel in deuterium is $62 \pm 7\%$

*The most reliable failure reason is χ^2 . The missing mass test cannot discriminate between zero missing mass and the π^0 mass in this experiment. In even-prong (π^0) events 21/3000 were separated from the (pp) reaction by missing mass, 5/3000 had a convergence problem, and the remainder were separated by χ^2 probability being less than 2% from the (pp) reaction hypothesis.

of the charge symmetric π^-p cross section. By comparing our three-prong and four-prong cross sections in deuterium, we find that the three-prong cross section is $65 \pm 2\%$ of the total deuterium cross section. The small error is achieved by using the uncorrected 370 odd-prong events (5.2 ± 0.5 mb) in which one proton was found by bubble density or by fitting. We compare this to 7051 four-prong events (2.75 ± 0.16 mb) with nearly identical selection criteria. We will compare this result below to the value estimated from the Hulthen wave function.

TABLE XII
COMPARISON OF THREE-PRONG AND π^-p CROSS SECTIONS

Reaction	$\sigma(\pi^-p)$ mb	$\sigma(03)$ mb	$\sigma(03)/\sigma(\pi^-p)$
$\pi^+n \rightarrow \pi^+\pi^-p$	3.2	1.6	0.5 ± 0.1
$\pi^+\pi^-\pi^0$	6.2	2.3	0.6 ± 0.1
$\pi^+\pi^-\pi(0\pi^0)$		1.6	
$\pi^+\pi^+\pi^-n$	1.9	1.7	0.9 ± 0.2
$\pi^+\pi^+\pi^-\pi^0$	2.0	1.5	0.5 ± 0.1
$\pi^+\pi^+\pi^-\pi(0\pi^0)$	0.7		
Total	14.0	8.7	0.62 ± 0.07

D. MOMENTUM OF THE MISSING SPECTATOR

We have asserted that the momentum of the spectator proton can be ignored in the fit to a missing π^0 since it is small compared to typical measuring errors. It is therefore an open question whether or not we have enough resolution to make a one-constraint fit to the missing spec-

tator proton and obtain its momentum distribution. We show in Fig. 66 that the average fitted momentum of the spectator (shaded) is smaller than the average measuring error (dashed). The dashed histogram shows the missing momentum for four-prong events identified as $\pi^+ d \rightarrow \pi^+ \pi^- p p_s$. Since there is no missing neutral particle, the momentum difference between the beam and the four outgoing charged tracks is just measurement error. We note that two distributions peak at the same value of momentum.

In Fig. 67 we show the fitted momenta of the missing spectators for $\pi^+ \pi^- p$ events. These events have been selected by fitting method (a). This time they are added to the observed spectator distribution for $\pi^+ \pi^- \pi^0 p p_s$ events. The horizontal error bars show the average error in fitted momentum for the events in the adjacent bins. It is probable that the spectator distribution has been distorted by the large measurement uncertainties. The relative normalization of the 03 and 04 events in Fig. 67 is based on the ratio $03/(03 + 04) = 65 \pm 2\%$.

In the past it has been standard practice² to use the Hulthen prediction with $\beta = 7\alpha$ (dashed curve of Fig. 67) to estimate the missing odd-prong cross section when it has not been measured. Kraemer, et al.,² used such a curve normalized at 150-200 MeV/c and estimated the odd-prong contribution to their cross section to be $69 \pm 6\%$. This cannot be compared directly with our result since their estimated spectator range cutoff was 2 mm while ours is 0.7 mm. They did not make an independent measurement of the odd-prong cross section. Using the dashed curve shown in Fig. 67, we estimate the 03 loss, and using our known number

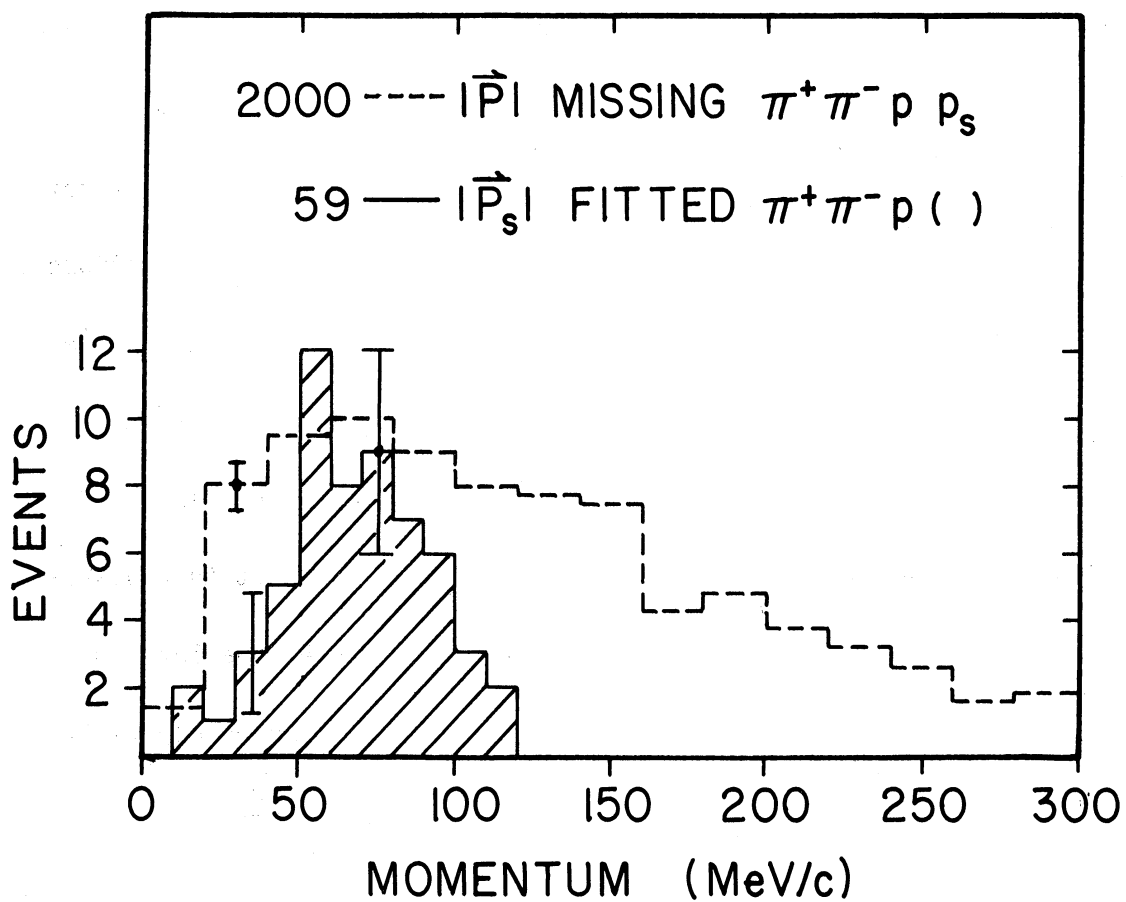


Figure 66. Comparison of the missing momentum (dashed) for events identified as $\pi^+\pi^-pp_s$ and the fitted missing spectator momentum for 59 three-prong events identified as $\pi^+\pi^-p$.

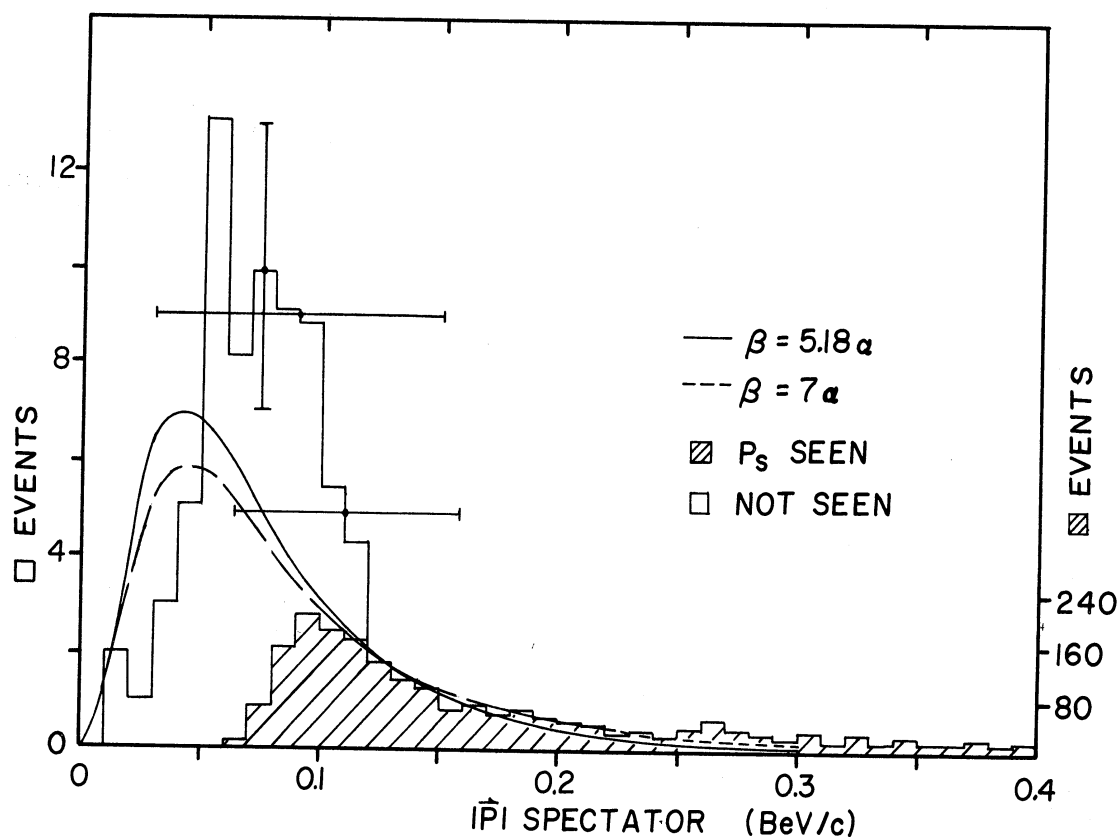


Figure 67. Fitted missing spectator momentum distribution for $59 \pi^+ \pi^- p$ events. These are added to the observed spectator momentum distribution (shaded) for $\pi^+ \pi^- 0 p p_s$ events. The smooth curves are predictions from the Hulthén wave function. The horizontal error bars show average uncertainties in the fitted momentum of the missing spectator.

of 04 events, we get $03/(03 + 04) = 52 \pm 4\%$. This disagrees with our observed value of $65 \pm 2\%$. Some variation of this number is expected from experiment to experiment due to variations in the treatment of short and long range tracks; however, we would expect our Hulthen prediction to agree with our observed $03/(03 + 04)$ ratio since agreement was found in a low energy K^+d experiment.²⁸

The chief problem at our energy is how to normalize the Hulthen curve. If we took the events with missing spectator momenta greater than 100 MeV/c seriously, we would raise the Hulthen curve and improve our agreement.

Although we do not have confidence in the odd-prong momentum spectrum, the even-prong momentum spectrum is well measured, and we can use the angle made by the spectator relative to the film plane (dip angle λ) to estimate the fraction of spectators lost at each value of spectator momentum. Our average uncertainty of $\cos \lambda$ for events with $-45^\circ < \lambda < +45^\circ$ and $|\vec{P}_s| = 100-125$ MeV/c is less than ± 0.1 . (We have approximated $\overline{d\cos\lambda} = \overline{\sin\lambda \, d\lambda}$ by $\overline{d\cos\lambda} \leq \sin\lambda_{\max} \overline{d\lambda} = 0.7 \overline{d\lambda}$.)

Because the spectator should be approximately isotropic about any fixed axis in the lab, a plot of $\cos\lambda$ should be flat. Scan losses will appear as depleted areas near $\cos\lambda = \pm 1$. This can clearly be seen in Figs. 68 (a-d). The lines shown indicate scan losses of 38%, 29%, 12% and 8% respectively. The 38% loss estimate is probably too low for Fig. 68 (a) since the theoretical scan bias based on an 0.7 mm range cut-off extends to $\cos\lambda = 0$, and the scan is probably biased even in the center

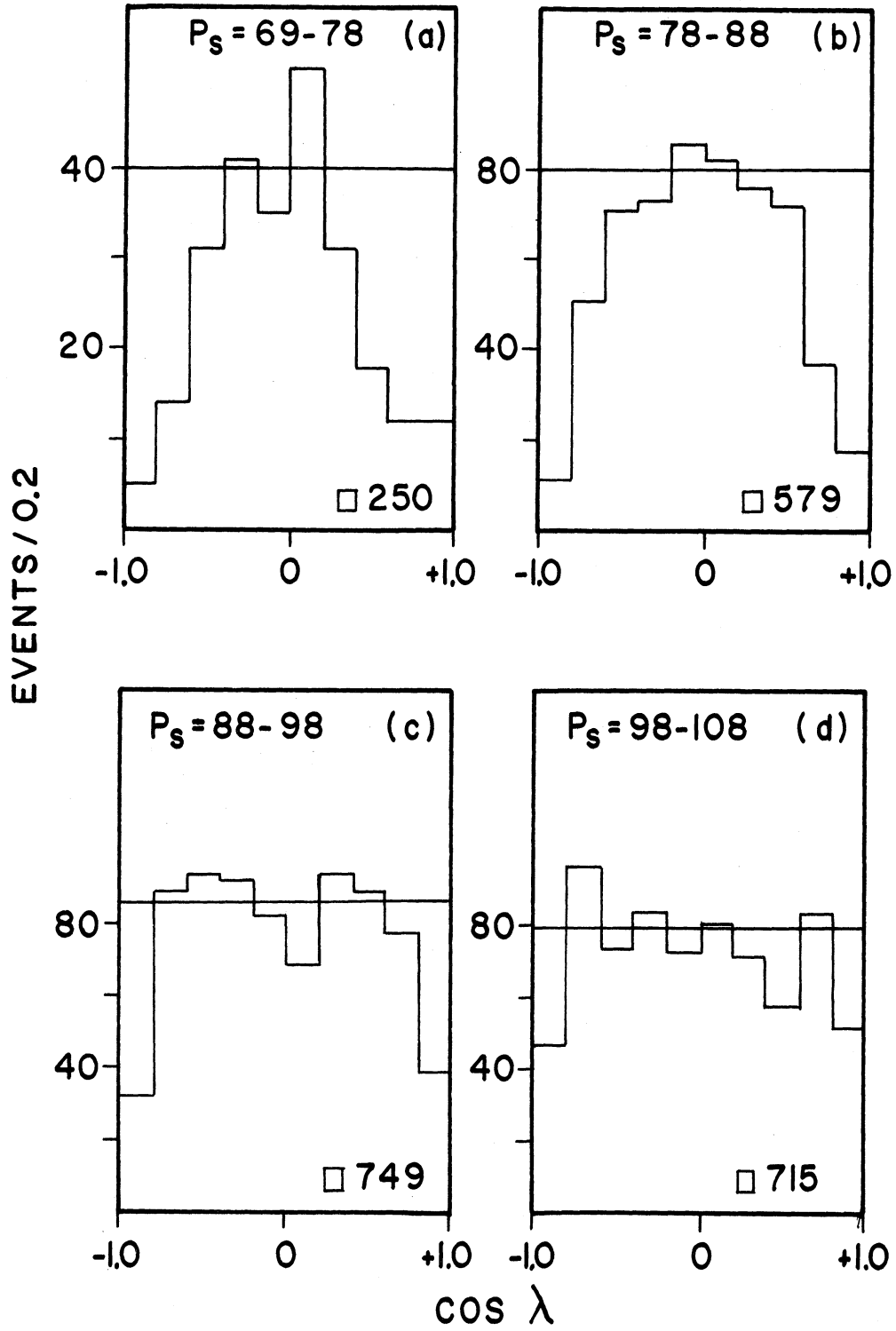


Figure 68. Dip angular distributions for spectators with momenta in the intervals (a) 59 - 78, (b) 78 - 88, (c) 88 - 98, and (d) 98 - 108 MeV/c. The spectators are taken from $X^0_{pp_S}$, $\pi^+\pi^-pp_S$, $\pi^+\pi^-\pi^0pp_S$, and $\pi^+\pi^-(m\pi^0)pp_S$ channels.

of the plot. To gain statistics for these plots we have used the spectators from the X^0_{pp} , $\pi^+\pi^-pp$, $\pi^+\pi^-\pi^0_{pp}$, and $\pi^+\pi^-X^0_{pp}$ channels. If we make a plot from only the (π^0) events with $|\vec{P}_S| = 98-127 \text{ MeV}/c$, the loss is 6%. If our assumption of little or no scan loss of spectators in the film plane is correct, then we conclude that the Hulthen curve is at most 6% under normalized. We observe more odd-prong events than the curve predicts.

CHAPTER VII

SUMMARY OF RESULTS AND CONCLUSIONS

In Chapter II we discussed effects associated with the deuteron target: spectator proton momentum and angular distribution, Glauber screening and Pauli exclusion. The cross sections in deuterium were found to be roughly equal to charge symmetric hydrogen data. An empirical study of the number of high momentum spectator protons was made in two- and four-prong two proton channels. Although the channels have different numbers of high momentum spectators initially, they all appear the same if this number is plotted as a function of Δ^2 (mesons). A dependence of this number on mass (mesons) was found, but this again is the same in the channels investigated. We do not know of any theoretical predictions or other similar studies of these effects.

In Chapter III we discussed the contamination of this channel by events with $2\pi^0$'s and showed that there was no evidence for contamination by $\pi^+\pi^+\pi^-\pi^0$ events even in the high momentum proton events. We showed that the missing mass squared and χ^2 probability distributions were consistent with a 20% overestimate of measuring error. Using a missing mass method and resolution functions, the ambiguous events between $\pi^+\pi^-\pi^0$ pp and $\pi^+\pi^+\pi^-\pi^0$ pn were found to be 75% of the (pn) type.

The η^0 , ω^0 , H^0 , and A_2^0 mesons were studied in detail. The η^0 production cross section in deuterium was found to be comparable to a measurement in hydrogen. The masses of the well-known mesons (η^0 , ω^0 ,

A_2 , and ρ^+) are all in excellent agreement with accepted values.

In fitting the ω^0 , we found that it was well described by a Breit-Wigner form as was the missing mass spectrum of the π^0 . We have for this reason subtracted resolution widths linearly from observed resonance widths rather than quadratically. The resulting widths of the ω^0 and ρ^+ are in fair agreement but are still wider than the accepted widths.

The density matrix for the ω^0 was measured and found in agreement with either production by ρ exchange modified by absorption, or production by ρ exchange plus B-meson exchange in the Regge model. The Dalitz plot density was found to be in excellent agreement with the simplest matrix element prediction provided only events from the center of the ω^0 mass region were used. We attributed this effect to measuring error.

Further evidence for the H meson was found in this experiment. The $\rho\pi$ decay modes were consistent with $I = 0$. A simultaneous fitting of the decay plane normal, the bachelor pion, and the married pion angular distributions favored an assignment of $J^P = 1^+$. Assuming $J^P = 1^+$, we compared the density matrix with the absorption model prediction based on ρ exchange and found ρ_{00} to be larger than predicted. If the success of the model in predicting the ω^0 is not an accident, this may be evidence that the H meson is not produced by ρ exchange. The consequences of other diagrams (such as double pion exchange) should be explored.

The $\rho\pi$ decay of the A_2^0 was found to be consistent with $I = 1$. A spin test was made for the Dalitz plot density, and $J^P = 2^+$ was favored. An attempt was made to determine the A_2^0 density matrix by simultaneously

fitting the decay plane normal and the bachelor pion distributions. The distributions, which should be identical, were found to be different. It is possible that the structure is associated with background rather than A_2^0 events. Further studies of the A_2^+ and $\rho^-\pi^-$ systems are needed to clarify this situation. The A_2^0 production cross section was found to be equal to the A_2^- production cross section in hydrogen at our energy. This is in disagreement with a predicted ratio of two to one which ignores interference effects.

Production of ρ^+ , ρ^0 , and ρ^- mesons was observed. The ρ^+ and ρ^0 events are more peripheral than the ρ^- events as expected from a pion exchange production mechanism. Evidence was presented for the two-body final states ρ^+N^{*0} and ρ^0N^{*+} . The production cross section for each of these states equals the $\pi^-p \rightarrow \rho^0N^{*0}$ cross section at our energy. This is in disagreement with a predicted ratio of two to one which ignores interference effects.

A few three-prong events were studied primarily for cross section purposes. We discussed the fitting problems associated with the missing spectator and showed some of the mass distributions and the missing spectator momentum distribution. We found our three-prong cross section was greater than our estimate from the Hulthen wave function.

The total cross section for $\pi^+d \rightarrow \pi^+\pi^-\pi^0pp$ was found to be

$$3.44 \pm 0.31 \text{ mb} .$$

This consists of

$$\rho^+ = 0.48 \pm 0.07$$

$$\rho^0 = 0.40 \pm 0.06$$

$$\rho^- = 0.36 \pm 0.05$$

$$\eta^0 = 0.05 \pm 0.01$$

$$\omega^0 = 0.46 \pm 0.05$$

$$N^{*++}(1238) = \underline{0.25 \pm 0.04}$$

$$\text{Total resonant} \quad 2.00 \pm 0.18 \text{ mb} .$$

Contributing to ρ production are the processes

$$\rho^0 N^{*+}(1238) = 0.18 \pm 0.02$$

$$\rho^+ N^{*0}(1238) = 0.18 \pm 0.02$$

$$H^0 = 0.08 \pm 0.02$$

$$A_2^0 = 0.17 \pm 0.03 \text{ mb} .$$

We see that the difference in the total resonant cross section and the total cross section is 1.44 ± 0.13 mb or 42% of the channel. These events are essentially unstudied. Whether they contain interesting physics, or follow phase space in every detail, we leave for future studies.

APPENDIX A

EXPOSURE DETAILS

The film analyzed in this experiment was exposed at the Brookhaven National Laboratory 20-inch bubble chamber. An initial exposure of 82,500 pictures was made in September and November 1963. An additional exposure was made in two parts: 46,000 pictures in September 1964, and 128,000 pictures in November and December 1964. This made a total of 256,500 frames.

The chamber was filled with liquid deuterium. Its temperature was maintained within the range 30.7 to 31.1°K throughout the exposure. The expansion stroke was adjusted to give a gauge pressure drop from 77 lbs/in.² to 5.3 lbs/in.² in the liquid. These temperature and pressure variables were chosen to give approximately 10 bubbles per centimeter along the beam tracks in the chamber. The chamber lights were flashed 150 μ seconds after the arrival of the beam, thus taking the picture while the bubbles were still of small apparent diameter, \approx 0.015 cm in the chamber.

During the first two portions of the exposure when the chamber was at optimum temperature, it tended to overfill with deuterium. This distorted the pressure stroke and caused the bubbles to disappear. Heating the chamber restored the pressure stroke but also raised the temperature. This temperature rise caused the bubbles to become too dense. Cooling caused a repetition of this cycle and another loss of

bubbles. This unfortunate instability which is peculiar to deuterium, reduced the number of frames of scanable quality by 10%, 16%, and 0% in the three portions of the exposure. During the second portion the chamber crews discovered that bleeding the excess deuterium from the chamber without altering the temperature gave the desired stable operation. The procedure of cutting and developing a test strip of film from every 1600 frames further reduced the number of usable frames by 1 to 2%.

Incident on the chamber were π^+ mesons created in small metallic targets placed in the internal proton beam of the Brookhaven Alternating Gradient Synchrotron (AGS). Both aluminum and stainless steel were used as targets. Bending and focusing magnet currents were set to select all particles leaving the target at 3.7 BeV/c nominal momentum. Pions were separated from the protons in the beam by two mass separating stages. The final bending magnet and the "pitching" magnet were set to center the beam horizontally and vertically in the bubble chamber.

A paddle-shaped scintillation counter was placed in the beam after the final mass and momentum resolving slit. The count on each pulse was registered electronically, and the signal to fire the chamber lights was generated only if the count fell between a lower and an upper limit. For example, during the third portion of the exposure, the limits were set to give more than 8 and less than 30 tracks in the chamber. The actual limits were set at ≈ 20 to ≈ 50 . These numbers were greater than 8 and 30 because the counter's large size and position

close to the final mass slit caused it to detect particles not "aimed" at the chamber.

Assuming that the intensity and position of the internal proton beam were set to produce 35 counts in the detector on the average, the actual number of counts recorded should have been distributed according to Poisson statistics with a standard deviation of $\sqrt{35}$. With limits of 20 and 50 (± 2.5 standard deviations) an acceptable count should thus have been registered on ≈ 99 of every 100 beam pulses.

In practice the ratio of pictures taken to the number of beam pulses rarely exceeded 80% - 90% during any 1500 picture interval (≈ 1.5 hours). This indicates that the major picture taking loss was not statistical but was caused by variations in the internal proton beam of the AGS. The AGS variations were partially compensated for manually with a correcting magnet which swept the beam vertically in front of a slit located after the first bending magnet. The average number of beam tracks per picture in the three exposure intervals were $\approx 7^*$, 13.7 and $\approx 22^*$.

The inside dimensions of the chamber were 10 in. x 10 in. x 20 in. The beam entered and left the 10 in. x 10 in. faces. The front and rear windows formed opposite 10 in. x 20 in. faces. Four separate cameras viewed the chamber from the corners of a 9-inch square, 35 inches from the liquid side of the front window of the chamber. Each camera view was recorded on 35 mm film. The total length of film exposed was 4

* These numbers have been inferred from the events observed rather than by track counting.

views x (3 in./frame)/view x 2.6×10^5 frames or 49 miles. A more complete description of the chamber and beam has been given by Rau, et al.¹⁰⁸

APPENDIX B

SCAN DETAILS

Camera views 1 and 2 of the chamber were scanned for events satisfying the following criteria:

- 1) the beam track which interacts be parallel to the other beam tracks,
- 2) the vertex lie within a chosen fiducial area on view 1,
- 3) the number of beam tracks crossing the bottom of the fiducial area be less than 25, 30, and 40 in the first, second, and third exposure regions,
- 4) outgoing tracks with secondary scatters have a measurable length of at least 2.1 cm,
- 5) short stopping tracks be ≥ 0.07 cm in length, and
- 6) the bubbles be sufficiently visible for bubble counting.

The given lengths are projected lengths and are scaled to chamber dimensions. The corrections to the cross sections which these rules make necessary are discussed in Appendix H.

The scanning was performed on standard projection-type scanning machines with the emulsion coated side of the screen, rather than the glass side, near the scanner.

This permitted us to place curvature templates directly on the projected image, thus making momentum-ionization estimates more accurate. The magnifications of the machines (defined as screen length/ chamber

length) ranged from 1.0 to 1.45 for the four machines used.

Because the chief reason for the exposure was to study reactions with two protons in the final state, scanning personnel were instructed to eliminate events which did not have two protons as follows:

- A. In the entire exposure, all events with one stopping proton were recorded in the scan, but in exposure interval III, events shown by positive identification not to have two protons were not measured.
- B. The curvature templates were used for positive identification of pions on any track whose momentum was less than 900 MeV/c in exposure interval III.
- C. In exposure intervals I and III, events without a stopping proton were also included if two protons could be identified by ionization. This limited the faster proton on such events to $\lesssim 1.7$ BeV/c.

Scanners recorded the following information on one line of the scan sheets for an acceptable event: frame number, event number (if there was more than one event in the frame of a given topology), length of stopping proton, number of positive and negative tracks, and number of V's, gamma ray conversions, or Dalitz pairs. Spaces were provided for measurement dates and pertinent comments.

In exposure intervals I and II the film was scanned twice, sheets were compared, and disagreements were listed by scanning personnel. Experienced scanners resolved disagreements and the corrected sheets

from the first scan were used as measuring lists.

In exposure interval III, only 72% of the 128,000 frames were double scanned. From these scan sheets a card was punched for each event. The cards from each scan were compared using a computer program, and a disagreement sheet was printed. After the disagreement scan, the cards were corrected and the events to be measured were selected and printed by the computer using another program (by J. Oh).

A check of the scan efficiency was made for four different topologies in the first exposure interval using the double scan and disagreement scan results. For one-prong events (the spectator proton is not seen) 17% were missed; for two-prong events (with one very fast track and one stopping track) 15% were missed; for two-prong events (with one stopping track and the other track with momentum less than 1.7 BeV/c) 12% were missed; and finally 7% of all three- and four-prong events were missed in a single scan.

The miss rates were calculated from the formula

$$\text{miss rate} = \bar{M}/(N-\bar{M}),$$

where N is the total number of events to be measured, and \bar{M} is one half the sum of the events missed by scanner 1 and scanner 2. It can be shown that this expression accounts correctly for the events both scanners missed assuming that the events in the given category are equally easy to miss. This assumption is approximately correct for the three- and four-prong events which are the primary concern of this study. The per-

centage of events missed by both scanners was estimated by squaring the single scan miss rate and is thus $\approx 1/2\%$ for three- and four-prong events.

APPENDIX C

EVENT MEASUREMENT

The events were measured on two types of measuring machines. Two machines used a Moire-fringe pattern produced by pairs of gratings ruled with 100,000 lines per inch for measurement of distances on the film. This gave a least count of $1/10,000$ inch. The third machine used an accurately ground screw coupled to an encoder with a least count of $1/8000$ inch for distance measurement.

The film was projected onto a screen with a magnification of ≈ 2.8 over chamber size on each of the machines. The chamber to film demagnification was 10. Points on the tracks to be measured were moved under a fixed cross hair on the inside of the screen. The operator then initiated the electronic storage of the x-y coordinates of the point and the automatic punching of the stored information on cards.

The projection machines were constructed at the University of Michigan. The electronic and encoding equipment was obtained from the Datex Corporation.

Three film views were used for measurement. The measurer determined which pair of views were to be measured for a given track. Six to ten points were measured on non-stopping tracks. The measuring rate is approximately 10 two-prong events, or 5 four-prong events, or 3 six-prong events per hour on one machine.

Because the least count of the screw machine was larger than that of the grating machines, and because it was difficult to assess directly the smoothness and linearity of the screws to one ten thousandth of an inch, there was some concern about the quality of the events measured on the screw machine. To answer this question, several indirect tests were made on the screw machine to compare its accuracy with that of the grating machines. A summary of the results is given in Table XIII. Several poorer screws were rejected before these results were obtained.

TABLE XIII

RESULTS OF MEASURING MACHINE TESTS
(rms distance in units of 10^{-4} in.)

	A	B	C	D	Bubble Diameter
screw	2.2	1.2	1.1	10.4	~ 6.0
grating	1.2	.9	.9	8.5	~ 6.0

Two hundred points were measured on a photograph of a straight line. A least squares fit was made and the rms deviation of the perpendicular distance of the measured points to the fitted line is shown in column A of Table XIII. Another straight line measurement was made to more closely simulate track measurements. Measurements consisting of eight points were made on the straight line over only one half the width of the film, and the averaged results are shown under column B. The line was placed at 45° to the x axis in both tests.

Columns C and D show results taken from routine measurements of 5 to 10 points each on tracks of momentum ≥ 1.7 BeV/c. C shows the rms deviation of the perpendicular distance from the measured points to the fitted curve projected on an x-y plane parallel to the chamber windows. D is the rms deviation of the fitted and measured z coordinates. These rms values are given in units of 1/10,000 inch on the film and are compared with a bubble diameter of 0.0006 inches as it appears on the film. Noteworthy conclusions are:

- 1) C and D show that measurement errors in the z direction are ≈ 10 times those in the x-y plane.
- 2) B, C, and D show that the ratio of screw to grating machine measurement errors is ≈ 1.25 , which is also the ratio of the least counts.
- 3) B and C show that track measurement errors in the film plane are nearly the same as straight line measurement errors.
- 4) The large screw/grating error ratio in column A may reflect either the greater width of the cross hair on the screw machine or a non-linearity in the screw thread appearing when measurements are made over the full width of the film.
- 5) A more recent study by T. Fisher has shown the uncertainty in measuring the vertex of a strange "V" is $dx = dy = 6 \times 10^{-4}$ in. and $dz = 30 \times 10^{-4}$ in. in film coordinates.

APPENDIX D

GEOMETRIC RECONSTRUCTION

The cards containing the measured coordinates were first checked for all errors not depending on three dimensional reconstruction with a program written locally.¹⁰⁹ Errors not requiring remeasurement were corrected and for all events which passed, new cards were punched in a format acceptable to the TRED reconstruction program.⁴⁶ The program was developed by Brookhaven National Laboratory and is designed to reconstruct events into three dimensions from measurements in two stereo film views. The program determined momentum and angles for each track and estimated the bubble density the track would have if it were an electron, a π or K meson, a proton, or a deuteron.

The version of TRED used for this experiment was obtained from the Carnegie Institute of Technology. It differed from previous versions in that all six of the possible pairs of the four camera views could be used for measurement.

The TRED program made tests on the quality of the reconstruction, such as: "Were the measured points too far from the fitted curve?", "Was a reasonably good view pair used?", and "Did all measured points have reconstructed coordinates lying inside the chamber?" Typical failure rates for events submitted to TRED were 10% for two-prong events, 20% for four-prong events, and 30% for six-prong events.

The input constants specifically for deuterium which were used by the Carnegie group were retained for the Michigan experiment. The deuterium index of refraction used was 1.11, and the density used in momentum-range calculation was 0.0668 g/cm^3 . The density was checked by measuring muons resulting from $\pi\mu e$ decay chains. A sample of 88 events give an average muon momentum of $29.73 \pm 0.06 \text{ MeV/c}$ in good agreement with the value of $29.81 \pm 0.03 \text{ MeV/c}$ calculated from the $\pi\text{-}\mu$ mass difference.⁵⁰

The muon range was observed to be $0.920 \pm 0.006 \text{ cm}$. The standard deviations in average momentum and range were obtained from the experimental spread in values by the usual formula

$$\sigma_{\bar{x}}^2 = \sigma_x^2/n = (\overline{x^2} - \bar{x}^2)/(n-1) .$$

APPENDIX E

BUBBLE DENSITY

After the event was reconstructed, momentum and angles were known for each track, but it was not yet known what particle caused the track. For this reason each event was reexamined on film and the bubble density of each track was compared with the mass dependent estimates from the TRED program. The estimated number of bubbles per centimeter, k , measured along a track of energy E (BeV), momentum P (BeV/c), and mass M (BeV/c²) was calculated from the knowledge that k is approximately proportional to $1/\beta^2 = (E/P)^2 = 1 + (M/P)^2$.*

The constant of proportionality unfortunately varies significantly from picture to picture and thus was determined from beam tracks in the same frame as the event being examined. Since $\beta \approx 1$ for beam tracks, the number of bubbles per centimeter in the beam is itself the desired constant of proportionality.

The bubble density estimates were made at first by physicists and later by selected scanners. The negative tracks were assumed to be pions unless they were in gross disagreement with the TRED estimate for the pion. Positive tracks of momenta less than 1.7 BeV/c were identified as pion or proton.

*The reader is referred to Ref. 110 for a summary of results pertaining to the dependence of k on β .

Protons with momenta greater than 1.7 BeV/c have a bubble density less than 30% higher than that of the pion and therefore cannot be identified reliably even by counting the number of bubbles per centimeter since the statistical and nonstatistical fluctuations in bubble formation can lead to uncertainties of this order. Thus events with fast positive tracks were only identified using energy-momentum conservation. This led to ambiguities in event classification as discussed in Chapter III.

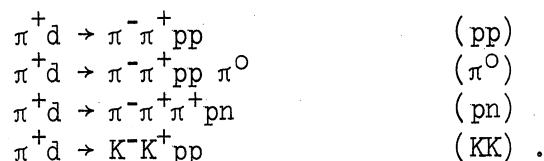
For tracks with momenta ≈ 1.2 BeV/c to 1.7 BeV/c the number of bubbles per centimeter in the track was counted and compared to the count of a beam track. The counting was done with a simple counter constructed by the author. It consisted of an electrically activated counter connected in series to the 110 V power line through a normally open microswitch. The microswitch was closed by a shaft moving inside a ball point pen barrel. Depressing the "pen" on the projected image of a bubble registered one count.

Tracks of momentum less than ≈ 1.2 BeV/c were visually compared with beam tracks rather than counted. The "blackness" of the track was the quantity actually observed and was translated to the quantity k (the number of bubbles per centimeter as estimated by TRED) essentially by the experience of the person making the judgment.

APPENDIX F

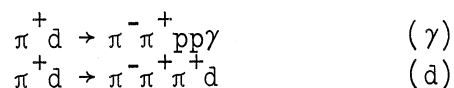
KINEMATIC ANALYSIS

All four-prong events were tested by energy and momentum conservation for compatibility with the following reactions:



In reactions (pp) and (KK), the energy and the three components of momentum may be tested independently. Reactions (π^0) and (pn) each have an unobserved neutral particle, and only the missing mass, $(E(\text{missing})^2 - \vec{P}(\text{missing})^2)^{1/2}$, can be tested for compatibility with the mass of the particle assumed to be missing. These two types of fits are called respectively four-constraint and one-constraint. A hypothesis was rejected if its χ^2 probability was less than 2%.

The two reactions



were included in part of the data analysis. Reaction (γ) was found to be highly ambiguous with reactions (pp) and (π^0), as one would expect, and was dropped. Reaction (d) was begun after Abolins, et al.,¹¹¹ demonstrated that these events existed in detectable numbers in $\pi^- d \rightarrow \pi^- \pi^- \pi^+ d$.

If the probability was acceptable, the measured momenta were adjusted until momentum and energy were conserved. These fitted quantities were then written on magnetic tape for further analysis. The computer program, GRIND, developed at Cern and adapted for Michigan by B. Roe, was used for the kinematic analysis.⁴⁵ The measured quantities used as input were read from the magnetic tape generated by the TRED program.

The events used in this experiment were chosen to have vertices close to the beam entrance point of the chamber so that the outgoing tracks could be well measured. As a consequence, the momentum of the beam track was poorly measured. In GRIND, the measured beam momentum was set at 3.65 BeV/c with an error of 37 MeV/c at the beam entrance point. This value was then lowered for the energy loss to the vertex. In deuterium the beam energy loss is 0.246 MeV/cm. The value 3.65 BeV/c was obtained by an average of fitted beam momenta from four- and six-prong, four-constraint events. A study of the stretch variable^{*} for the beam momentum of the first 400 events of reaction (pp) showed that the 3.65 BeV/c input value was too high by 7 ± 5 MeV/c. This difference was considered negligible and no change was made. Because the momentum bite of the beam was $\approx \pm 1\%$,¹¹² the uncertainty in the beam momentum for each event was set at 37 MeV/c.

^{*}The stretch variable for x is defined as $(x\text{-fitted} - x\text{-unfitted}) / (\sigma(x\text{-unfitted})^2 - \sigma(x\text{-fitted})^2)^{1/2}$. A histogram of stretch variables should have a Gaussian shape, $\sigma=1$, and mean value=0 if the errors of each measurement have been properly assessed. Our stretch variable for (1/P) of the beam had $\sigma \approx 1$ and a mean of $+0.07 \pm 0.05$. The relationship of stretch and momentum was determined by altering the momentum and observing the change in stretch.

Two of the four-constraint reactions, (pp) and (d) , were found experimentally to be strong, i.e., of the events having one of these fits, 97% and 86% respectively had a bubble density consistent with the fit. Because of this strength, bubble density decisions disagreeing with these fits were reexamined. The ratio of bubble density decision errors to total decisions made in the (pp) reaction was $1.0 \pm 0.5\%$. This indicates that the errors made in similar reactions (where the bubble density was not reexamined) are negligible.

The other four-constraint reaction, (KK) , was weak, with only 36% of the fits of low momentum transfer to the deuteron being consistent with bubble density. One reason for this low value is that the K-meson mass is not sufficiently different from the π -meson mass to correctly distinguish the two kinematically at the beam energy of this experiment. A possibly more important reason is the smallness of the (KK) cross section compared to the other reactions.

The one-constraint reactions, (π^0) and (pn) , were also weak with respectively 51% and 28% of each type agreeing with bubble density. These figures underline the importance of the bubble density decision in this experiment.

Of those events which fit the (pp) reaction, 13% also fit the (π^0) reaction with the protons assigned to the same positive tracks. In this case examining bubble density cannot help, and we have assigned all these events to the (pp) reaction. This is based on the relative strengths of the fits of these two reactions, as noted above, and on the results of

detailed studies of this problem made by others.^{30,46,113}

Because the GRIND program was new to the Michigan group, a study of the fitting process was made, using events which had failed to give any fit agreeing with the bubble density decision. Of 100 "no fit" events (all having two observed protons), 31 events were found to have a missing mass squared, MM^2 , less than 0.1 BeV^2 . Upon remeasurement, 16 of these events fit the (pp) reaction and 6 fit the (π^0) reaction. A histogram of the missing mass squared as observed in the first measurement is particularly revealing and is shown in Fig. 69. Events still not fitting are shown as X, new (pp) fits as 4, and new (π^0) fits as 1.

These 31 events have come from a total sample of about 200 (pp) plus (π^0) events. If these 31 events are assumed to have failed at random, either because of fitting problems or because of mistakes made by the measurer, then $85 \pm 15\%$ of these would be expected to fit on the second try. Since our result of 70% agrees with this, we conclude that the events now fitting do not represent a special class of events, and that most of the events failing twice are the natural result of a double coincidence.

Of the 69 events that were remeasured with $MM^2 > 0.1 \text{ BeV}^2$, none fit the (pp) reaction; however 11 fit the (π^0) reaction. This number provides a rough estimate of the single π^0 contamination in events of the type $\pi^+d \rightarrow \pi^+\pi^-pp \pi^0 (m \geq 2)$, i.e., $\sim 6/70$ assuming $1/2 \pm 1/2$ of them are really single π^0 events.

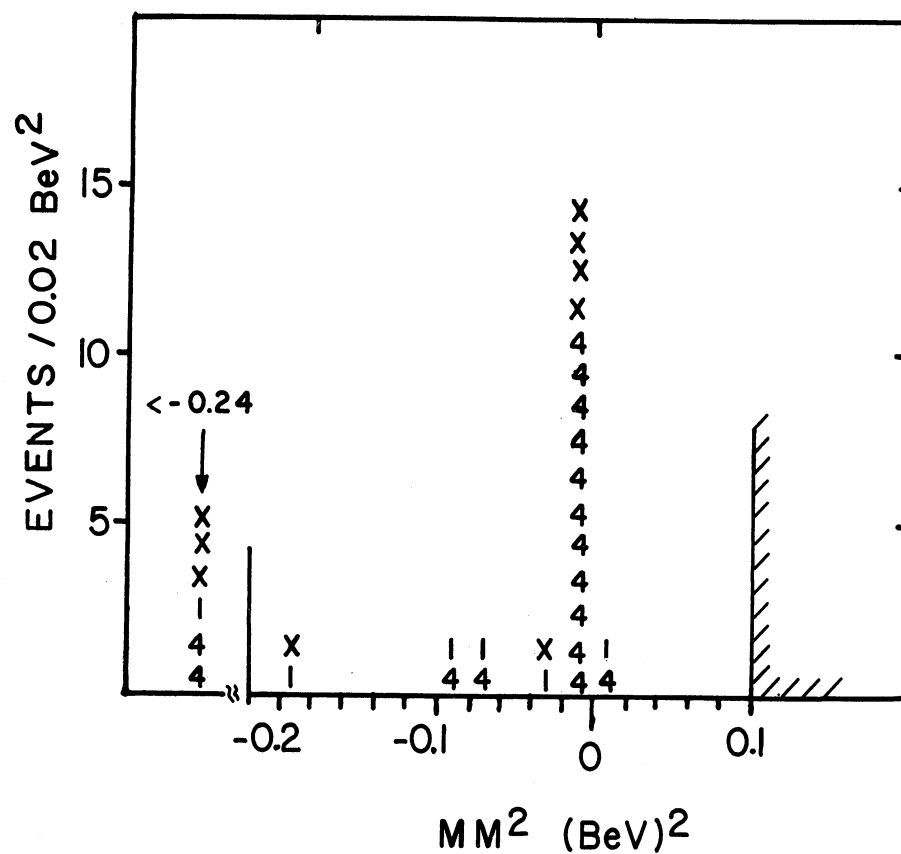


Figure 69. Distribution of missing mass squared for a small sample of "no-fit" events with $MM^2 = 0.1 \text{ BeV}^2$. Upon remeasurement the event fits the (pp) reaction (4), the (π^0) reaction (1), or remained a no-fit (x).

A study was made to find the cause of each failure. The original and new measurements were compared, and the error signal as printed by the GRIND program tabulated. Of the 22 events with $MM^2 < 0.1 \text{ BeV}^2$ fitting on the second try, approximately 6 had a noticeable change in measured parameters. Of the seven common error signals in GRIND other than "probability too small," the signal indicating "too many iterative steps" was found most frequently. Approximately 50% of the original measurements with this error were found to fit when the allowed number of steps was increased to 20 and the momentum and energy conservation was required to be less exactly conserved. No cure other than re-measurement was found in this study for the other error signals.

APPENDIX G

EVENT ANALYSIS

The analysis of the fitted and identified events was completed using two program systems. The first, developed by E. Marquit at Michigan, was most useful in the initial analysis. Cards containing x, y, and z momentum components for each event were obtained from GRIND output tapes or TRED output tapes. These were then analyzed with a program which plotted on paper any desired scattergram.

A second system was used in later stages. It consisted of the FILE program written at Michigan, which used card input to select the good fits from the GRIND tape and write the events on a new tape. The SUMX program⁴⁴ was used for histogramming, etc.

Most of the least squares fitting for this work was done using the program subroutine written by B. Ronne¹¹⁴. It used the same matrix manipulating subroutines as used by the GRIND program for event fitting. A Michigan program written by L. Lovell and W. Gibbs was also used.

APPENDIX H

CROSS SECTION DETERMINATION

In this section the details of the absolute cross section calculation are presented. Because we did not attempt to measure all interactions seen in the chamber (recall that there are nearly twice as many as when the chamber is filled with hydrogen), we could not normalize to total cross section measurements from counter experiments. Instead, the normalization was obtained from the scanned path length.

1. DEUTERIUM DENSITY

The experimental range of muons in deuterium in this experiment was 0.920 ± 0.006 cm (see Appendix D). In hydrogen, this range would imply a density of 0.0702 ± 0.0007 g/cc. If the stopping power of an electron bound to a deuteron were the same as an electron bound to a proton, then the deuterium density would be found by multiplying by $(M_d + M_e)/(M_p + M_e)$, giving 0.140 ± 0.001 g/cc. The Illinois bubble chamber group has investigated the problem in more detail and has obtained values ranging from 0.137 to 0.142 g/cc.¹¹⁵ These values are used in estimating our uncertainty in the density as $\pm 2\%$. Dividing by $M_d + M_e$ gives the deuteron (or neutron) density as 4.19×10^{22} /cc.

2. DEUTERIUM PURITY

The assay of the chamber deuterium dated August 11, 1964, showed the liquid to be 98.9% D₂, 0.48% HD, and 0.42% O₂. Thus the deuteron

content was 99.1%. No corrections were made for this small lack of purity.

3. TOTAL PATH LENGTH

The second exposure interval was chosen for the cross section normalization. The frame interval was from 250,078 to 296,147 or 46,069 frames. Of these 1.7% had been cut away due to tests at the accelerator, and 15.8% more were rejected as too poor in quality to scan. This left 37,996 frames which were scanned.

The scan rules retained an event only if its vertex lay in a rectangular area superimposed on view 1. The fiducial volume so defined was visualized by drawing lines from the center of camera lens 1 through the corners of this rectangle. These lines formed a pyramid with a rectangular cross section. The volume of the pyramid between the two windows of the chamber was the fiducial volume. The images of the fiducial marks on the front and back windows were measured with a ruler to construct the pyramid in space. As a check, the distance of camera lens 1 above the chamber, as calculated by this rough method, was found to be only 2% less than the known value of 89 cm. A straight track passing through this pyramid at a constant depth, z , in centimeters below the front glass-liquid interface, parallel to the long side of the rectangular cross section, traversed a length $L = 0.2140 z + 19.25$ cm.*

About two thirds of our beam was located between $z = 12.5$ cm and 15.5 cm. A weighted average gave $\bar{L} = 22.0$ cm. The corrections for

* This was further checked by plotting the x , z coordinates of the vertices of a large sample of events. The x direction is along the beam.

track curvature, non-constant depth, and non-parallel alignment with the sides of the rectangle, were found to be negligible in the calculation of \bar{L} .

The number of tracks per frame was counted in every tenth frame on every fourth roll. Every eighth roll was counted first, then the alternate rolls. This was done to check against changes in judgment and errors in calculation, and to see if enough tracks were counted. The two counts were within $\pm 0.6\%$ of the average which indicated that a sufficiently large sample had been counted.

The numbers of tracks in four different categories were obtained as follows (see Fig. 70):

- a) the number of tracks crossing the entire fiducial area from 1 to 3 (13.2/frame),
- b) the number of tracks entering late on side 4 of the fiducial area (0.92/frame),
- c) the number of tracks leaving early on side 2 of the fiducial area (0.046/frame), and
- d) the number of "faint" beam tracks (0.71/frame).

A weighted average path length for item b) gave $\bar{L}' = 10.4$ cm. The track distribution of item b) was found to be approximately uniformly spread along the edge of the fiducial.* Item c) can be neglected. Item d)

*Since the width of the beam was approximately the width of the fiducial area, this uniform distribution shows that the beam was badly centered in the fiducial area in film segment II. The inequality of items b) and c) shows this also. The fiducial region was determined from the beam in the first exposure interval and was held fixed for the rest of the experiment.

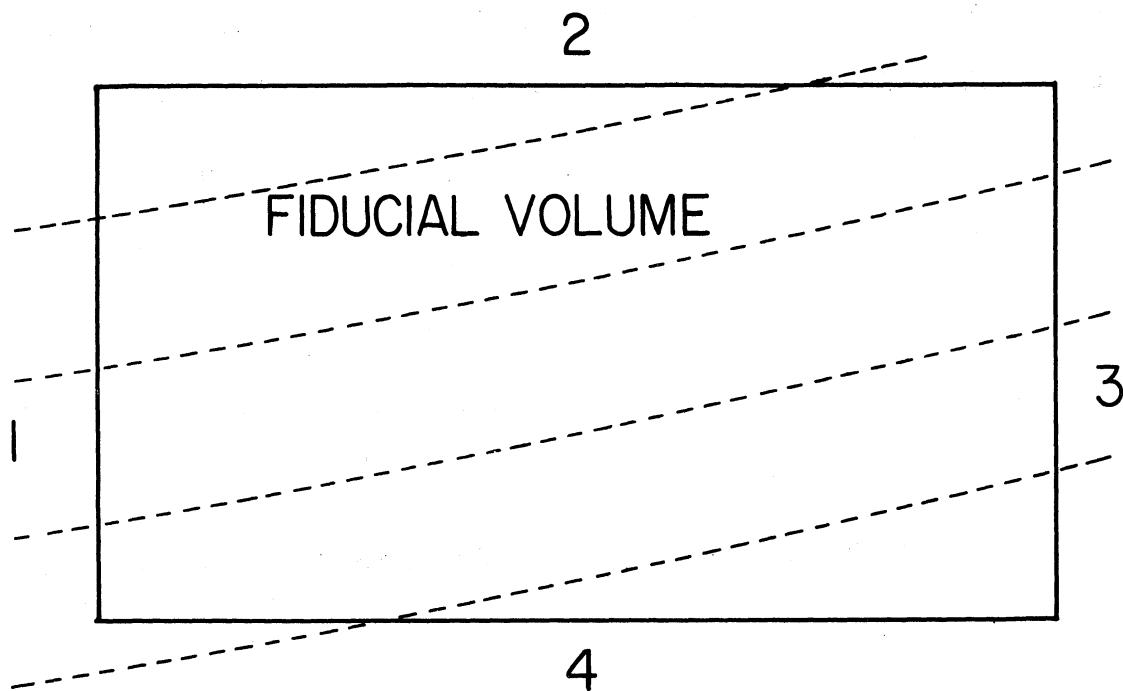


Figure 70. Sketch of the fiducial region used to select measurable events. The sides of the rectangle are numbered 1, 2, 3, 4.

was tabulated since scanners were told to disregard events whose tracks were all distinctly fainter than the average beam track. A portion of the above beam tracks were recounted by the author. This recount agreed with the original count to 3%, and, in the opinion of the author, none of the tracks counted in item d) would have produced events which the scanners would have recorded or measured. Therefore the path length per frame is

$$\bar{L} = (13.2 \times 22.0) + (0.92 \times 10.4) = 300.0 \text{ cm/frame.}$$

The total length is then

$$L = 3.80 \times 10^4 \text{ frames} \times 300 \text{ cm/frame} = 1.14 \times 10^7 \text{ cm.}$$

The error in L is taken as 4%, with roughly equal contributions coming from the track count and the faint track judgment.

4. BEAM CONTAMINATION

The chief contaminants in a positive pion beam are protons and muons. The beam tuning curves made during the run showed no proton peak when the beam was swept past the final mass slit. We thus estimate that the proton contamination was negligible.

No direct experimental determination of the muon contamination at the 20-in. chamber is known to the author. Some efforts have been made in πp collisions to estimate the number of muons in the beam from the known total cross sections.¹¹⁶ In the Michigan $\pi^- p$ experiment a value of $3 \pm 2\%$ was used. The partial cross sections were in good agreement

with values from other bubble chamber experiments.⁴⁶

The following calculation is presented to give insight into the source of the contamination and to make the figure we use ($5 \pm 3\%$) at least plausible. We consider N_0 pions leaving the target with such a direction and momentum that they are destined to enter the bubble chamber. After traveling a distance, d , the fraction having decayed is $1 - e^{-d/\bar{d}}$, where $\bar{d} = \gamma c \tau = 652$ feet is the mean decay length for 3.65 BeV/c pions. Thus 32% of the pions decay before reaching the final mass slit which is 250 feet from the target. The momentum spectrum of the resulting muons is flat, lying between 2.10 and 3.65 BeV/c. All lie within 0.63° of the original pion direction. Because the momentum resolution of the beam is $\approx \pm 1\%$, it is estimated (with a safety factor of two) that only those muons with a momentum within 2% of the beam will be transmitted by the final mass slit. This assumes that the ≈ 450 MeV energy loss and the multiple scattering in the lead defining the mass slit is sufficient to remove muons from the beam. The rms multiple scattering angle is such that a ray of muons would be fanned into a cone with a one foot rms radius at the chamber if there were no intervening magnets. The 2% in momentum corresponds to a transmission of 5% of the total number of muons. Thus $0.05 \times 0.32 \times N_0$ muons and $0.68 N_0$ pions are transmitted by the final mass slit.

Another 4.6% of the pions decay in the remaining 30 feet to the chamber. It is estimated that $\frac{1}{2} \pm \frac{1}{2}$ of these muons (those with momentum < 2.8 BeV/c) are swept to the rear of the chamber by the final

bending magnet and are observed by the scanners as non-parallel beam tracks. This gives the final composition of the beam as $0.65 N_0$ pions and $0.03 \pm 0.02 N_0$ muons. The contamination at the chamber is thus $5 \pm 3\%$.

5. BEAM ABSORPTION

The total π^+d cross section at 3.65 BeV/c is 57.0 ± 0.1 mb.³⁴ Since the total path length was based on the number of tracks entering the fiducial volume, it must be reduced by half the amount lost in traveling the entire length of the fiducial volume. Using the deuteron density, ρ , the reduction is given by $\frac{1}{2} \sigma \rho L = 2.6 \pm 0.1\%$.

6. INTERACTING TRACKS

Scanners were instructed to ignore events with tracks having visible interactions within 2.1 cm of the vertex. Of the events observed, $5.2 \pm 1.5\%$ had an identifiable proton scatter within this distance, and $2 \pm 1\%$ had a track (which was thought to be a pion) scatter. These values were obtained in a small sample of the film by having events with interaction specifically so recorded. The proton value is an average over events having one or two visible protons with the double proton events 1.3 times as frequent as single proton events. The non-proton value was evaluated for four-prong events and should be proportional to the number of outgoing non-proton tracks.

7. SCAN EFFICIENCY

The four-prong single scan loss as estimated from the double scan was 7%. This implies that both scanners missed $(7\%)^2$ or 0.5% of the total

number of events on the film. In the film from the third exposure interval, 28% of the frames were only single scanned, so that the average scan loss for this film portion was 3%.

These values were checked by taking good events from the final sample and reexamining their scan history. The average efficiency for these selected events was not different from the above value which was obtained as an average for all three- and four-prong events observed.

8. EVENTS NOT MEASURED

A comparison of some of the original "to be measured" lists and the final lists of events passing the geometry program showed 8% of the original events in the second exposure interval were not yet measured. This 8% is composed of 3.5% which were fatally noted by a measurer or a physicist as "not measurable," "no event," etc. The other 4.5% failed in pre-geometry or geometry programs after two measurements. As a check on our bookkeeping of the events, the 4.5% is in good agreement with the 5% that would be calculated from our known pre-geometry failure rate (0.07) and our geometry failure rates (0.15 and 0.18) for the first measurement and the remeasurement.

It is believed that the events failing twice should be apportioned to the various fit classes in the same ratio as those events that passed. The reasons for this are that the failure rate for the remeasurement was only slightly higher than for the initial measurement and that the numbers of the remeasured events falling in each fit class were the same as those from the first measurement.

Taking the above factors into account gives the expression for the cross section per event in the second exposure interval

$$\sigma/\text{event} = [\rho_1 L_3 F_4 F_5 F_6 F_7 F_8]^{-1},$$

where the subscripts refer to the sections in which the correction factors are discussed and F_i stands for 1 minus the factor i listed in Table XIV. The errors of the factors are also shown in Table XIV. The orthogonal combination of these errors gives an overall uncertainty of 6%.

TABLE XIV
FACTORS USED IN EVALUATING THE CROSS SECTION

<u>Section</u>	<u>Factor</u>	<u>Value</u>	<u>% Error</u>
1	Density, deuterons/cc	$4.19 \pm 0.08 \times 10^{22}$	2%
3	Track Length, cm	$1.14 \pm 0.04 \times 10^7$	4%
4	Beam Contamination, %	5 ± 3	--
5	Beam Absorption, %	2.6 ± 0.1	--
6	Interaction Loss, %	7.3 ± 2.5	--
7	Scan Loss, %	0.5 ± 0.3	--
8	Not Measured, %	8 ± 2	--
	$\sigma/\text{event}, \mu\text{b}$	2.66 ± 0.16	6%

The σ/event in Table XIV is for film segment II. We normalize to the total film sample by using the ratios of two-proton events (with no relative scan bias) found in film segments I, II, and III. The ratios

are

$$I:II:III = 0.88 \pm 0.04 : 1 : 5.00 \pm 0.17 .$$

This implies that the cross section per event in the whole film is $(6.9 \pm 0.2)^{-1}$ times the cross section per event in part II. The four-prong cross section is thus

$$\sigma_{04}/\text{event} = 0.39 \pm 0.03 \text{ } \mu\text{b}/\text{event} .$$

To predict free nucleon cross sections, we need to correct this for the three-prong events not included in this study. The cross section for the 7051 (pp), (π^0) , and $(m\pi^0)$ four-prong events is $7051 \times 0.39 = 2.75 \pm 0.16 \text{ mb}$. The cross section for 370 three-prong events (event class 03) with nearly identical selection criteria (see Table XI) is $5.2 \pm 0.5 \text{ mb}$. Multiplying the ratio $(03 + 04)/04 = 2.89 \pm 0.17$ times σ_{04}/event , gives

$$\sigma_{\text{tot}}/\text{event} = 1.13 \pm 0.08 \text{ } \mu\text{b}/\text{event} .$$

Further corrections must be made to the individual channels before total cross sections can be quoted. Some of these are discussed in Chapter III. In particular, corrections have been made for: 1) scanning bias against fast protons by comparing results from the three exposure intervals which were scanned under different rules; 2) ambiguities in fitting by using probabilities, unfitted missing mass, and relative numbers observed; and 3) the false fitting of two neutrals to single neutral channels by

missing mass and phase space estimates. These are summarized in Table XV.

TABLE XV
CHANNEL CROSS SECTION CORRECTIONS

	pp	π^0	$m\pi^0$
1. Fast proton called π in scan	$0.01 \pm .01$	$0.02 \pm .01$	---
2. $(m\pi^0)$ events in (π^0) events	---	$-.12 \pm .04$	$0.20 \pm .06$
3. (π^0) events in $(\pi^0$ -pn) ambig.	---	$0.04 \pm .03$	---
4. $ \vec{P} $ spectator $> .25$ BeV/c not scanned	$0.01 \pm .01$	$0.02 \pm .01$	$0.02 \pm .01$
5. $MM^2 < 2 \pi^0$ events in no fits	$0.12 \pm .05$	$0.04 \pm .02$	$0.03 \pm .02$
6. High Δ^2 loss when $ \vec{P} $ spectator $> .25$	$0.01 \pm .01$	$0.02 \pm .01$	---
7. High Δ^2 loss $ \vec{P} $ proton > 1.7 BeV/c	---	---	$0.30 \pm .13$
Sum of Correction Terms	$+0.15 \pm .05$	$+0.02 \pm .06$	$+0.55 \pm .15$
Events	1983	2993	1646
$\sigma_{\text{tot}}(\text{mb})$ corrected	$2.58 \pm .21$	$3.44 \pm .31$	$2.88 \pm .35$

We have assumed here that the three- to four-prong ratio is the same for the three channels. There is some experimental evidence supporting this (see Chapter VI). However, since the percentages of spectator

protons above 250 MeV/c is channel dependent, this may not be the case. If, instead, we assume the spectator excess is accompanied by an equal loss of three-prong events, then our (pp) cross section result would increase by 3%, the (π^0) cross section would remain the same, and the ($\pi\pi^0$) cross section would decrease by 2%.

The 1646 events of the "no-fit" channel $\pi^+\pi^-X^0pp$, ($\pi\pi^0$), do not include events with $MM < M(2\pi^0)$. Furthermore, a rough estimate based on $2\pi^0$ and $3\pi^0$ phase spaces indicates that 300 of the 1646 events are really $\pi^+\pi^-\pi^0\pi^0\pi^0pp$.

To estimate resonance cross sections, which are mostly low Δ^2 , the only applicable corrections are 4 and 5 (provided only events above backgrounds are used). This gives for the (π^0) reaction

$$1.20 \pm 0.10 \text{ } \mu\text{b/event (above background)}$$

If background events are included, then correction 2 also applies to give

$$1.60 \pm 0.09 \text{ } \mu\text{b/event (all events)}$$

Corrections 1, 3, 6, and 7 apply only to high Δ^2 events which are 1/6 of the (π^0) channel. Thus, when examining (π^0) events with $\Delta^2 > (1.9 \pm 0.3) (\text{BeV/c})^2$, the appropriate factors are

$$1.74 \pm 0.26 \text{ } \mu\text{b/event (above background)}$$

$$1.60 \pm 0.24 \text{ } \mu\text{b/event (all events)}$$

The average value is

$$1.15 \pm 0.10 \text{ } \mu\text{b/event}$$

APPENDIX I

TOTAL DEUTERIUM CROSS SECTION DETERMINATION

In order to test the values used in Appendix H for the deuteron density, track length, beam contamination, and beam absorption, a scan was made for all interactions occurring on a total of 455 frames of good quality film. The total cross section obtained from this scan was

$$\sigma(\pi^+ d) = 62 \pm 6 \text{ mb}$$

which is in good agreement with the counter result of 57.0 ± 0.1 mb of Baker, et al.³⁴ This agreement indicates that our cross section determination is correct within the estimated errors.

Our total cross section is based on a path length of 7.9×10^4 cm, $96 \pm 3\%$ single scan efficiency, and 0% interaction loss and measuring loss. The value of 0% is correct since all events were recorded regardless of interacting tracks and no attempt was made to measure them. The other factors used are the same as in Table XIV of Appendix H.

We present in Table XVI a breakdown of our total cross section by topology. Cross sections for background events encountered in this experiment can be inferred from this table. The 01 and 03 prong events were processed in only 3% of the film and, therefore, represent 18 mb of background. The 02 events of interest (the ppX^0 reaction) amounted to 0.5 mb or 1/40 of the topology, and the 04 prong events of interest [reactions (pp), (π^0), ($m \pi^0$), and (pn)] totaled 3.5 mb or 1/4 of the

TABLE XVI

CROSS SECTION BY TOPOLOGY

Topology	Events	
01	28	9.1 ± 1.9
02	64	20.0 ± 2.8
03	29	9.4 ± 2.0
04	47	14.7 ± 2.3
05	4	1.2 ± 0.6
06	7	2.2 ± 0.7
Strange V	3	0.9 ± 0.5
Total	182	62 ± 6

topology. Our scan rules, of course, were designed to reduce these backgrounds before the measuring stage of our analysis.

The 01 + 02 cross section of 29.1 ± 3.4 mb compares favorably with a prediction from bubble chamber data of 30.6 mb taken from π^+p and π^-p data (see Table II). The 03 + 04 prong cross section of 24.1 ± 2.9 mb also agrees with the $\pi^+p + \pi^-p$ estimate of 25.0 mb. We can neglect any correction for the cross section defect in deuterium since it is only $2.6 \pm 0.5\%$ of the total π^+d cross section at our energy.*

*At our energy the sum of the cross section for π^+p and π^+n (as inferred from π^-p by charge symmetry) measured by Baker, et al., is 58.52 ± 0.24 mb showing a defect of 1.5 ± 0.3 mb or $2.6 \pm 0.5\%$ of the total π^+d cross section.

APPENDIX J

THE LUBATTI-ROSENFELD CORRECTION TO PHASE SPACE

Lubatti and Rosenfeld suggested a simple correction⁵¹ that should be applied to phase space to reflect nature's preference for producing mesons at low values of Δ^2 to the target. The statistical model, of course, predicts that all kinematically allowed values of Δ^2 are equally preferable. We present our version of their suggestion as follows.

Suppose that a statistical phase space predicts that Δn_0 events fall in a mass interval, Δm , by

$$\begin{aligned}\Delta n_0 &= \int_{\Delta^2_{\min}}^{\Delta^2_{\max}} \frac{dn}{dm} d\Delta^2(\Delta m) \\ &= \frac{dn}{dm} \int d\Delta^2 \Delta m \\ &= \frac{dn}{dm} (\Delta^2_{\max} - \Delta^2_{\min}) \Delta m .\end{aligned}$$

If an exponential drop in Δ^2 is placed in the above, rather than a constant Δ^2 distribution, then

$$\begin{aligned}\Delta n &= \int \frac{dn}{dm} e^{-A\Delta^2} d\Delta^2 \Delta m \\ &= \frac{dn}{dm} \Delta m \frac{(e^{-A\Delta^2_{\min}} - e^{-A\Delta^2_{\max}})}{A} \\ \Delta n &= \frac{\Delta n_0}{A} \frac{e^{-A\Delta^2_{\min}} - e^{-A\Delta^2_{\max}}}{\Delta^2_{\max} - \Delta^2_{\min}} \\ &= \frac{\Delta n_0}{\text{const.}} \times C .\end{aligned}$$

The factor C above times the statistical phase space, Δn_0 , gives the corrected phase space.

We show in Fig. 71 the correction factor for a stationary neutron and for a neutron with Fermi momentum (variable center of mass energy). To correct our phase space we have approximated the correct average (over the center of mass energy), $\overline{C\Delta n_0}$, by $\bar{C} \cdot \overline{\Delta n_0}$. In computing \bar{C} , the average runs only over kinematically allowed center of mass energies. The curves can be seen to be the same to about 1.8 BeV. Figure 71 shows the correction with no Δ^2 cut imposed on the data and the correction if only those events with $\Delta^2(3\pi) < 0.85 \text{ (BeV/c)}^2$ are selected. We determine the appropriate value of A in Fig. 24.

The insertion of $e^{-A\Delta^2}$ as the correction is by no means obvious. It implies that the statistical phase space gives the correct prediction at $\Delta^2 = 0$ ($\cos \theta^* > 1$). One might also guess that the correction should be $e^{-A(\Delta^2 - \Delta_{\min}^2)}$ which implies that the phase space prediction holds at $\cos \theta^* = 1$ for all mass values. Finally as Rosenfeld suggested,⁵¹ one might simply multiply Δn_0 by $e^{-A\Delta_{\min}^2}$. This correction has the virtue that it forces phase space to look like the peripheralized predictions of Deck.⁸⁴

Further studies of this type of correction should be made. If a simple correction could be found which works for many channels at many energies, it would make easier the estimating of resonance positions, widths, and cross sections when they appear with large backgrounds. At the very least, the present suggestions have the virtue that they provide

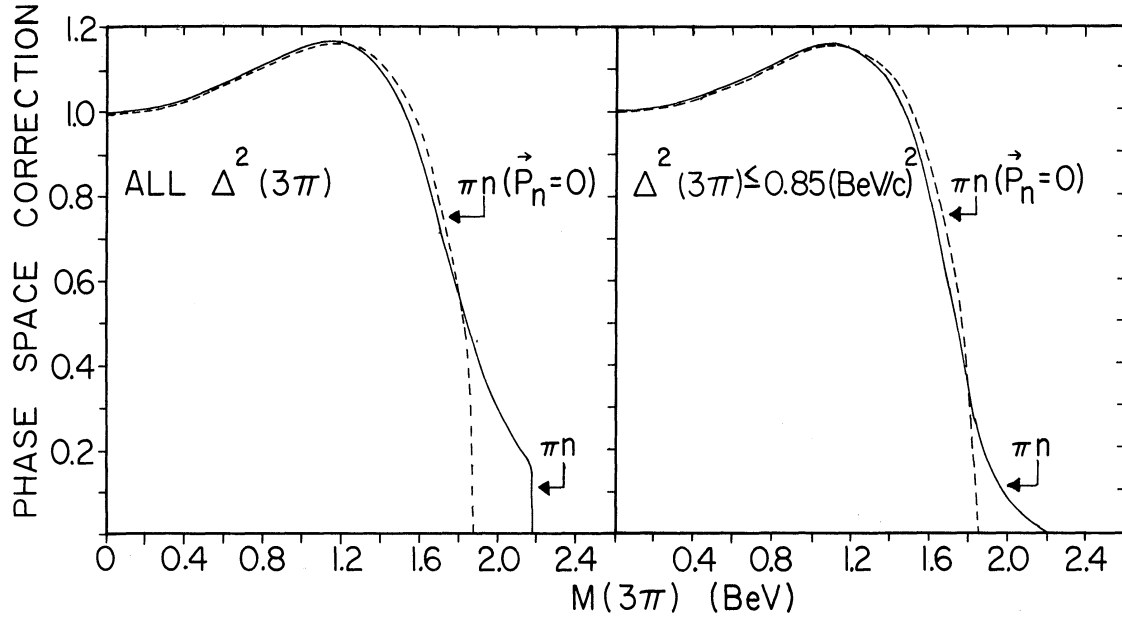


Figure 71. The phase space correction factor for events with all Δ^2 or with an experimentally imposed limit of $0.85 (\text{BeV}/c)^2$. The dashed curves are for a stationary target, while the solid curves have taken into account the variable center of mass energy caused by the Fermi motion of the target neutron.

a meaningful way to correct the phase space estimate for Δ^2 cuts in the data.

APPENDIX K

NOTES ON THE DENSITY MATRIX

In much of this work we discuss the decay properties of resonant states in terms of the density matrix. We review here ten properties of the density matrix^{117,118,119} which are needed to appreciate the physical meaning of the numbers (elements) of the density matrix. We also discuss the limits placed on these numbers by the general theory of the density matrix.

A state of spin J can be fully specified by a $(2J + 1)$ by $(2J + 1)$ matrix of possibly complex numbers. For $J=1$ it takes the form

$$\rho = \begin{pmatrix} \rho_{11} & \rho_{10} & \rho_{1-1} \\ \rho_{01} & \rho_{00} & \rho_{0-1} \\ \rho_{-11} & \rho_{-10} & \rho_{-1-1} \end{pmatrix}$$

If the state is a "pure state," then by definition the state may be described by expanding it in terms of basis vectors (e.g., spherical harmonics, etc.),

$$\psi^J = \sum_{m=-J}^{m=+J} a_m \psi_m^J.$$

The density matrix elements for such a state are defined as $\rho_{mm'} = a_m a_{m'}^*$. Knowledge of the a_m thus completely determines the density matrix and vice versa. A $J=1$ pure state requires three complex numbers (a_m) which, with the usual normalization condition, means that five real numbers can

describe the state.

From the above definition of ρ it can be seen that ρ is hermetian ($\rho^\dagger = \rho$). A general $(2J + 1) \times (2J + 1)$ complex matrix can have $2 \times (2J + 1)^2$ independent real numbers. The hermetian nature of ρ means that only half of these are needed (i.e., $(2J + 1)^2$), and also that the diagonal elements are real. Furthermore, the diagonal elements sum to 1 by the normalization condition ($\sum_m a_m a_m^* = \text{Tr} \rho = 1$). Thus we need for the case $J=1$, $(2J + 1)^2 - 1 = 8$ numbers to specify ρ in general. It is only for the pure $J=1$ state that five numbers are sufficient. The extra three numbers are necessary to fully describe a statistical mixture of pure states, which is the more general case.

The general definition is then

$$\rho_{mm'} \equiv \frac{a_m a_{m'}^*}{\sum_i p_i} = \frac{\sum_i p_i a_m^i a_{m'}^{i*}}{\sum_i p_i}$$

where the p_i are factors which weight the various pure states. From this definition the previously mentioned properties directly follow:

1. $\rho^\dagger = \rho$ (the diagonal elements are real).
2. $\text{Tr} \rho = 1$.

Other properties are:

3. The values of the elements on the diagonal must all lie between zero and one ($0 \leq \rho_{mm} \leq 1$). This is because these elements are sums of positive numbers ($|a_m|^2$) which are normalized to be 1, at most, by $\text{Tr} \rho = 1$. If any diagonal element is 1, then all other elements are zero and the density matrix

describes a completely aligned pure state. In general the value of ρ_{mm} tells what fraction of the sample has a spin component m in the z direction.

4. If the basis vectors are transformed by a unitary operator U , the density matrix transforms as an operator, i.e.,

$$\rho' = U \rho U^{-1}.$$

5. The random state density matrix is given by $\frac{1}{2J+1} (I)$ where I is the unit matrix. This is seen by noting that the only matrix which is invariant under all rotations ($\rho = D \rho D^{-1}$) is a multiple of the unit matrix (Schur's Lemma¹²⁰).
6. $\text{Tr} \rho^2 \leq 1$. This is seen in the following steps. A unitary transformation of ρ^2 leaves the trace unchanged. We apply that one which will diagonalize ρ to give

$$\text{Tr} \rho = \lambda_1 + \lambda_2 + \dots = 1.$$

Then

$$\text{Tr} \rho^2 = \lambda_1^2 + \lambda_2^2 + \dots \leq (\lambda_1 + \lambda_2 + \dots)^2 = 1.$$

The inequality holds since the λ_i are positive by Property 3.

For a pure state, $\text{Tr} \rho^2 = 1$. For a random state, $\text{Tr} \rho^2 = \frac{1}{2J+1}$.

7. For a spin one density matrix, $2 \text{Tr} \rho^3 - 3 \text{Tr} \rho^2 + 1 \geq 0$. The proof which is similar to that for Property 6, may be found in Ref. 77.

8. The expectation value of the operator matrix, Q , with elements

$$Q_{m'm} = \int \psi_m^* Q \psi_m dV, \text{ is found by}$$

$$\langle Q \rangle = \text{Tr}(\rho Q).$$

Since the expectation value for any operator may be calculated once the density matrix elements are known, it is asserted that the density matrix contains all the physically meaningful information about the spin state.

9. Parity conservation provides additional relations between pairs of $\rho_{mm'}$. We now specialize the discussion to the production of a particle with spin. The beam and target are assumed to be unpolarized. If the production plane normal is along \hat{z} , the spin quantization direction, the reaction must be invariant under the combined operation $D_z(\pi) \times P$. (P is the parity operation.) Then¹¹⁸

$$\rho' = D_z(\pi) \rho D_z^{-1}(\pi) = \rho$$

implies that $\rho_{mm'} = (-1)^{m-m'} \rho_{mm'}$ using the properties of $D_z(\theta)$. If \hat{y} is the normal, then

$$\rho' = D_y(\pi) \rho D_y^{-1}(\pi)$$

implies that $\rho_{mm'} = (-1)^{m-m'} \rho_{-m-m'}$.

We now apply the parity property to show the form ρ takes in a particular coordinate system. Following Gottfried and Jackson,⁷⁴ we take

the z axis along the beam, the y axis along the production plane normal, and $\hat{x} = \hat{y} \times \hat{z}$. Property 9, in addition to Properties 1 and 2, reduces the spin one density matrix from 8 real parameters to 4 of the form

$$\begin{pmatrix} \rho_{11} & \rho_{10} & \rho_{1-1} \\ \rho_{10}^* (1-2\rho_{11}) & -\rho_{10}^* & \\ \rho_{1-1} & -\rho_{10} & \rho_{11} \end{pmatrix}$$

where ρ_{11} and ρ_{1-1} are real and ρ_{10} is complex.

Similarly the spin two density matrix is reduced from 24 parameters to 12 parameters by Property 9 to the form

$$\begin{pmatrix} \rho_{22} & \rho_{21} & \rho_{20} & \rho_{2-1} & \rho_{2-2} \\ \rho_{21}^* & \rho_{11} & \rho_{10} & \rho_{1-1} & -\rho_{2-1}^* \\ \rho_{20}^* & \rho_{10} & (1-2\rho_{22}-2\rho_{11}) & -\rho_{10}^* & \rho_{20}^* \\ \rho_{2-1}^* & \rho_{1-1} & -\rho_{10} & \rho_{11} & -\rho_{21}^* \\ \rho_{2-2} & -\rho_{2-1} & \rho_{20} & -\rho_{21} & \rho_{22} \end{pmatrix}$$

where ρ_{22} , ρ_{11} , ρ_{2-2} , and ρ_{1-1} are real and the rest are complex.

From our experimental angular distributions for spin one particles, we are able to determine three of the four numbers (all but $\text{Im}\rho_{10}$). For spin two particles we can determine six numbers and the sum, $\rho_{1-1} + \text{const. Re}\rho_{20}^*$. Again the imaginary parameters of the density matrix do not affect the decay angular distributions.

* $\text{Re}\rho_{20}$ and ρ_{1-1} may be determined separately if the θ variable is not averaged over (see Ref. 99).

Parity conservation requires $\langle J_z \rangle = \langle J_x \rangle = 0$ with our choice of axes. By explicitly calculating $\langle J_z \rangle$, for example, from the general form of ρ , we see

$$\langle J_z \rangle = \text{Tr} \rho J_z = \hbar (\rho_{11} - \rho_{-1-1}) .$$

Thus it can be seen that our special form of the density matrix gives the correct result since in it we have required $\rho_{-1-1} = \rho_{11}$. Calculating $\langle J_y \rangle$ as above for spin one gives:

$$\langle J_y \rangle = \frac{i\hbar}{\sqrt{2}} (\rho_{10} - \rho_{01} + \rho_{0-1} - \rho_{-10}) = -\sqrt{8} \hbar \text{Im } \rho_{10} .$$

Conservation of parity does not require $\langle J_y \rangle$ to be zero. Since $\text{Im} \rho_{10}$ does not appear in the formula for the decay angular distribution, we cannot determine this element and thus do not know $\langle J_y \rangle$.

Minnaert⁷⁷ and, independently, Dalitz have shown that Property 7,

$$2 \text{Tr } \rho^3 - 3 \text{Tr } \rho^2 + 1 \geq 0 ,$$

may be used to place an upper limit on the magnitude of $\text{Im} \rho_{10}$. It turns out that this property places narrower limits on $\text{Im} \rho_{10}$ than does Property 6, $\text{Tr} \rho^2 \leq 1$. Minnaert has applied these inequalities to "multipole parameters," t_L^M , which are particular linear combinations of density matrix elements (see Table XVII). The multipole parameters are convenient to work with since they

- a) are invariant under rotations of the coordinate system, and
- b) are expressible as expectation values of angular momentum

operators and thus have an immediate (but perhaps not intuitive) physical interpretation.

In Table XVII we express the multipole parameters in terms of density matrix elements in two coordinate systems.* The unprimed system is that of Gottfried and Jackson, with the x and z axes in the production plane. The primed system has the x' and y' axes in the production plane. The two are related by $(x, y, z) \rightarrow (y', z', x')$. If a further rotation is made about the production plane normal in either coordinate system, the expressions for t_0^0 , t_1^0 , t_2^0 , and $|t_2^2|^2$ will not change. Since only these moments appear in the inequalities,⁷⁷ our results (6' and 7' below) are valid for any coordinate systems that designate the production plane normal as the y axis.

TABLE XVII

MULTIPOLE MOMENTS EXPRESSED AS A FUNCTION OF DENSITY MATRIX ELEMENTS
(The unprimed (primed) coordinate system has the y(z') axis along the
the production plane normal)

t_0^0	$(2\rho_{11} - \rho_{00})$	$(\rho_{11}' + \rho_{00}' + \rho_{-1-1}')$
t_1^0	$-2 \operatorname{Im} \rho_{10}$	$\frac{1}{\sqrt{2}} (\rho_{11}' - \rho_{-1-1}')$
t_2^0	$\frac{1}{\sqrt{40}} (3\rho_{00} - 6\rho_{1-1} - 1)$	$\frac{1}{\sqrt{10}} (\rho_{11}' - 2\rho_{00}' - \rho_{-1-1}')$
t_2^{+2}	$\sqrt{\frac{3}{80}} (1 - 3\rho_{00} - 2\rho_{1-1} - \frac{8}{\sqrt{2}} i \operatorname{Re} \rho_{10})$	$\sqrt{3/5} \rho_{1-1}'$
t_2^{-2}	t_2^{+2*}	$\sqrt{3/5} \rho_{1-1}'^*$

*The author is indebted to R. Bogenrief for assistance with these calculations.

The calculation of $t_L^M(\rho')$ in Table XVII has been made from the definition of the multipole moments in the primed system:¹²¹

$$t_0^0 = \frac{1}{2} \langle J^2 \rangle = 1$$

$$t_1^0 = \frac{1}{\sqrt{2}} \langle J_z' \rangle$$

$$t_2^0 = \frac{1}{\sqrt{10}} \langle 3 J_z'^2 - J^2 \rangle$$

$$t_2^{\pm 2} = \frac{3}{\sqrt{20}} \langle (J_{x'} \pm iJ_{y'})^2 \rangle.$$

The angular momentum operators in the expectation values are to be used without factors of \hbar so that the t_L^M are dimensionless. The definitions in the Gottfried and Jackson coordinate system are the same but with the replacements $(y', z', x') \rightarrow (x, y, z)$. The moments $t_1^{\pm 1}$ and $t_2^{\pm 1}$ are zero by parity conservation. From a measurement of t_1^0 , t_2^0 , and the real and imaginary parts of $t_2^{\pm 2}$, the density matrix elements can all be constructed. This implies that the multipole moments also contain all of the physical information of the spin state.

To apply the inequalities to the density matrix elements, we have taken the expressions for $t_L^M(\rho)$ from Table XVII and substituted these in Minnaert's conditions on the t_L^M . (The same results can be directly obtained by calculating $\text{Tr} \rho^2$ and $\text{Tr} \rho^3$ explicitly from the "parity conserving" form of ρ .) Therefore the result from $\text{Tr} \rho^2 \leq 1$ is

$$6 \dots 4|\rho_{10}|^2 + 2\rho_{1-1}^2 + \frac{1}{6} (1-3\rho_{00})^2 \leq 2/3,$$

and from Property 7 is

$$7'. \quad 12|\rho_{10}|^2 + 3\rho_{00}(\rho_{00} + 2\rho_{1-1} - 1) \leq 0.$$

Before using Property 7' to set a limit on $|\text{Im}\rho_{10}|$ from the measured values of $\text{Re}\rho_{10}$, ρ_{00} , and ρ_{1-1} , one should be sure that

$$t_2^0 = \frac{1}{\sqrt{40}} (3\rho_{00} - 6\rho_{1-1} - 1) \leq \frac{1}{\sqrt{10}}.$$

(This must hold since the insertion of the trace condition into $t_2^0(\rho')$ gives $t_2^0 = \frac{1}{\sqrt{10}} (1 - 3\rho_{00}') \leq \frac{1}{\sqrt{10}}$, and $t_2^0(\rho') = t_2^0(\rho)$.)

When the upper limit to $|\text{Im}\rho_{10}|$ has been calculated, one can set limits on the "degree of polarization," $\delta (0 \leq \delta \leq 1)$, which is defined by⁷⁷

$$\delta^2 = (2J)^{-1} [(2J + 1) \text{Tr}\rho^2 - 1].$$

For $J=1$ this becomes

$$\delta^2 = 6|\rho_{10}|^2 + 3\rho_{1-1}^2 + \frac{1}{4} (1 - 3\rho_{00})^2.$$

One can see from this expression that only for the random state value of $\rho_{00} = 1/3$ can δ be zero.

The final property we present is

$$10. \quad |\rho_{1-1}| \leq \rho_{11} \quad (\text{recall that } \rho_{11} = \frac{1-\rho_{00}}{2} \text{ for } J=1)$$

which holds only in the Gottfried and Jackson coordinate system. This condition on $|\rho_{1-1}|$ provides an interesting aside on the Treiman-Yang test for pion exchange. Traditionally, the $\cos^2\theta$ distribution of the π - π scattering angle and the lack of structure in the Treiman-Yang

angle have been presented as independent pieces of evidence for the exchange of a spinless particle in ρ -meson production.^{30,46} A $\cos^2\theta$ distribution implies $\rho_{00} = 1$. (The relevant equations have been given for the ω^0 decay plane normal in Chapter V, Section B.) Using this value in Property 10 shows ρ_{1-1} must then be zero. Because $\rho_{1-1} = 0$ causes the Treiman-Yang angle distribution to be flat, we see that the lack of structure follows directly from the strong alignment of the ρ meson ($\rho_{00} = 1$) and does not offer an additional test of pion exchange.

To prove the condition, we use the definition of ρ_{1-1} for the n^{th} pure state

$$\rho_{1-1}^n = a_1^n a_{-1}^{n*}.$$

Now, taking the magnitude of ρ_{1-1}^n and specifying the coordinate system by using the consequence of parity conservation, $|a_1|^2 = |a_{-1}|^2$, gives

$$|\rho_{1-1}^n| = \sqrt{|a_1^n|^2 |a_{-1}^n|^2} = \sqrt{|a_1^n|^4} = |a_1^n|^2 = \rho_{11}^n.$$

Averaging over all of the states in the sample gives the desired result

$$|\rho_{1-1}| \equiv |\overline{\rho_{1-1}^n}| \leq \overline{|\rho_{1-1}^n|} = \overline{\rho_{11}^n} \equiv \rho_{11}.$$

We discuss now how the predicted values of the density matrix elements depend on the assumed production process. For example, in the production (in a pion initiated reaction) of any meson of spin J by one-pion exchange, the only non-zero element is $\rho_{00} = 1$. This is because the orbital angular momentum has zero z component, and the maximum z component of the produced particle will, therefore, be just that of the

exchanged particle. Thus in the production of A_2 (assuming $J = 2$) by ρ exchange ($J = 1$), only the 3×3 submatrix $-1 \leq m, m' \leq +1$ would be non-zero. The Regge pole model (at least in ω^0 production⁷⁹) makes the same prediction as meson exchange. The absorption model of Jackson and others, however, modifies the meson exchange predictions. In all three models the imaginary terms are expected to be zero.¹⁰⁴ These models are discussed in more detail elsewhere in the text. The reader is also referred to the work of Dennery and Krzywicki.¹²²

APPENDIX L

ANGULAR DISTRIBUTIONS FOR THE H MESON

We discuss here the derivation of the angular distributions used in the spin-parity analysis of the H meson. The explicit formulas used for 1^+ and 1^- have been given in Chapter V, Section C.4. We present the formulas for 2^+ and 2^- here. The following explanation of the method is by J. Vander Velde.

The distribution for $\cos \theta_n$ has been taken from Ref. 91. The distributions for $\cos \theta_b$ and $\cos \theta_m$ were derived using standard non-relativistic techniques. We illustrate this calculation for 1^- :

$$\frac{dW}{d(\cos \theta_b)} = \sum_{\rho \text{ spin}} \{ \rho_{11} |A_1^1|^2 + \rho_{00} |A_1^0|^2 + \rho_{-1-1} |A_1^{-1}|^2 \}$$

The ρ 's here are the diagonal elements of the H meson's density matrix and the A's are its spin amplitudes. To describe the decay $H(1^-) \rightarrow \rho(1^-) + \pi(0^-)$ in p-wave we can decompose the A's as follows:

$$A_1^1 = \frac{1}{\sqrt{2}} (Y_1^1 (\cos \theta_b) \chi_1^0 - Y_1^0 (\cos \theta_b) \chi_1^1)$$

etc.

The χ 's are the ρ -meson spin functions. When we sum over ρ -meson spin, we then get

$$\frac{dW}{d(\cos \theta_b)} = 2\rho_{11} (|Y_1^1|^2 + |Y_1^0|^2) + \rho_{00} (|Y_1^1|^2 + |Y_1^{-1}|^2)$$

where we have used the fact that $\rho_{-1-1} = \rho_{11}$ and $|Y_1^1| = |Y_1^{-1}|$. We can also use $\text{Tr}(\rho) = 1$ to eliminate ρ_{11} . This gives

$$\frac{dW}{d(\cos \theta_b)} = 3/4 \left[\left(\frac{1-\rho_{00}}{2} \right) (1 + \cos^2 \theta_b) + \rho_{00}(1 - \cos^2 \theta_b) \right].$$

To get the $\cos \theta_m$ distribution, instead of summing over ρ spin, we integrate over $\cos \theta_b$ and then replace the ρ -spin functions χ_1^m by the corresponding Y_1^m spherical harmonics which describe the two-pion decay of the ρ .

For 2^+ the result is (with $x = \cos \theta$)

$$\begin{aligned} \frac{dW}{d(\cos \theta_b)} &= \frac{5}{4} \left[\rho_{22}(1 - x^4) + \left(\frac{1 - \rho_{00} - 2\rho_{22}}{2} \right) (1 - 3x^2 - 4x^4) \right. \\ &\quad \left. + 3\rho_{00}(1 - x^2)x^2 \right] \\ \frac{dW}{d(\cos \theta_m)} &= \frac{3}{2} \left[\rho_{22} \left(\frac{1 + 3x^2}{3} \right) + \left(\frac{1 - \rho_{00} - 2\rho_{22}}{2} \right) \left(\frac{5 - 3x^2}{6} \right) \right. \\ &\quad \left. + \rho_{00} \left(\frac{1 - x^2}{2} \right) \right]. \end{aligned}$$

For 2^- p-wave the result is

$$\begin{aligned} \frac{dW}{d(\cos \theta_b)} &= \frac{3}{2} \left[\rho_{22}(1 - x^2) + \left(\frac{1 - \rho_{00} - 2\rho_{22}}{2} \right) \left(\frac{1 + x^2}{2} \right) \right. \\ &\quad \left. + \rho_{00} \left(\frac{1 + 3x^2}{6} \right) \right] \end{aligned}$$

$$\frac{dW}{d(\cos \theta_m)} = \frac{dW}{d(\cos \theta_n)}.$$

REFERENCES

1. C. Baltay, P. Frazini, J. Kim, L. Kirsch, D. Zanello, J. Lee-Franzini, R. Loveless, J. McFadyen, and H. Yarger, Phys. Rev. Letters 16, 1224 (1966).
2. R. Kraemer, L. Madansky, M. Meer, M. Nussbaum, A. Pevsner, C. Richardson, R. Strand, R. Zdanis, T. Fields, S. Orenstein, and T. Toohig, Phys. Rev. 136, B496 (1964).
3. T. Bacon, W. Fickinger, D. Hill, H. Hopkins, D. Robinson, and E. Salant, Proceedings of the Athens Conference on Resonant Particles, Edited by B. Munir (Ohio University, Athens, Ohio, 1965).
4. U. Kruse, G. Ascoli, M. Firebaugh, E. Goldwasser, R. Hanft, D. Richardson, R. Sard, and G. Thiel, Bull. Am. Phys. Soc. 9, 431 (1964).
5. N. Gelfand, G. Lütjens, M. Nussbaum, J. Steinberger, H. Cohn, W. Bugg, and G. Condo, Phys. Rev. Letters 12, 567 (1964).
6. G. Benson, L. Lovell, E. Marquit, B. Roe, D. Sinclair, J. Vander Velde, and K. Weaver, Phys. Rev. Letters 12, 600 (1964).
7. A. Forino, et al., Saclay-Orsay-Bologna Collaboration, Phys. Letters 11, 347 (1964).
8. Bari-Bologna-Firenze-Orsay Collaboration, submitted to the XIII International Conference on High Energy Physics (Berkeley, California, 1966).
9. F. Bruyant, M. Goldberg, G. Vegni, H. Winzeler, P. Fleury, J. Huc, R. Lestienne, G. de Rosny, and R. Vanderhagen, Phys. Letters 12, 278 (1964).
10. J. M. Blatt and V. F. Weisskopf, Theoretical Nuclear Physics (John Wiley and Sons, New York, 1952).
11. L. Hulthén and M. Sugawara, Handbuch der Physik (Springer-Verlag, Berlin, 1957), Vol. 39, p. 1.
12. V. Stenger, W. Slater, D. Stock, H. Ticho, G. Goldhaber, and S. Goldhaber, Phys. Rev. 134, B1111 (1964).
13. V. Franco and R. Glauber, Phys. Rev. 142, 1195 (1966).

REFERENCES (Continued)

14. E. Salpeter, quoted by R. Gluckstern and H. Bethe, Phys. Rev. 81, 761 (1951).
15. M. Moravcsik, Nucl. Phys. 1, 113 (1958).
16. L. Landau and Ya. Smorodinsky, Lectures on Nuclear Theory (Plenum Press, Inc., New York, 1959).
17. M. Perl, L. Jones, and C. Ting, Phys. Rev. 132, 2152 (1963).
18. B. Chen (private communication, 1965).
19. D. Carmony (private communication, 1965).
20. J. Joseph and H. Pilkuhn, CERN Report No. 8591/TH. 414 (unpublished, 1964).
21. R. Heinz, A Study of the Reaction $p + p \rightarrow d + \pi^+$ from 1 to 2.8 BeV, dissertation (University of Michigan Technical Report 03106-18-T, 1964).
22. G. Chew and F. Low, Phys. Rev. 113, 1640 (1959).
23. R. Carlson, Rev. Mod. Phys. 37, 531 (1965).
24. I. Butterworth, J. Brown, G. Goldhaber, S. Goldhaber, A. Hirata, J. Kadyk, B. Schwarzschild, and G. Trilling, Phys. Rev. Letters 15, 734 (1965).
25. S. Drell and J. Trefil, Phys. Rev. Letters 16, 552 (1966); 16, 832 (E).
26. K. Nishijima, Fundamental Particles (W. A. Benjamin, Inc., New York, 1963).
27. A. Bilas, Phys. Letters 19, 604 (1965).
28. W. Chinowsky, G. Goldhaber, S. Goldhaber, W. Lee, T. O'Halloran, T. Stubbs, W. Slater, D. Stork, and H. Ticho, Proceedings of the 1960 Annual International Conference on High Energy Physics at Rochester (Interscience Publishers, Inc., New York, 1960), p. 451.
29. D. Robinson, E. Salant, A. Engler, H. Fisk, C. Meltzer, and J. Westgard, Phys. Rev. 139, B1420 (1965).

REFERENCES (Continued)

30. Y. Lee, Investigation of Di-Pion Resonances in 3.7 BeV/c π^- p Collisions, dissertation (University of Michigan Technical Report 04938-1-T, 1964).
31. E. Marquit, G. Benson, L. Lovell, B. Roe, D. Sinclair, J. Vander Velde, and C. Weaver, Bull. Am. Phys. Soc. 9, 410 (1964).
32. D. K. Robinson (private communication, 1966).
33. R. Glauber, Phys. Rev. 100, 242 (1955).
34. W. Baker, E. Jenkins, T. Kycia, R. Phillips, A. Read, K. Riley, and H. Ruderman, Proceedings of the Siena International Conference on Elementary Particles (Società Italiana Di Fisica, 1963).
35. C. Wilkin, Phys. Rev. Letters 17, 561 (1966).
36. E. Abers, H. Burkhardt, V. Teplitz, and C. Wilkin, Phys. Letters 21, 339 (1966).
37. A. Sitenko, J. Exptl. Theoret. Phys. (U.S.S.R.) 36, 1419 (1959); English translation, Soviet Phys. JETP 36, 1008 (1959).
38. E. Coleman, Proton-Deuteron Elastic Scattering at High Momentum Transfers, dissertation (University of Michigan Technical Report 03106-25-T, 1966); E. Coleman (private communication, 1966).
39. R. Phillips and W. Rarita, Phys. Rev. 139, B1336 (1965); 143, 1390 (E). We use Solution 1.
40. R. Phillips and W. Rarita, Phys. Rev. Letters 15, 807 (1965). We use Solution 0 (a).
41. A. V. Stirling, P. Sonderegger, J. Kirz, P. Falk-Vairant, O. Guisan, C. Bruneton, P. Borgeaud, M. Yvert, J. P. Guillaud, C. Caverzasio, and B. Amblard, Phys. Rev. Letters 14, 763 (1965).
42. O. Guisan, et al., Phys. Rev. Letters 18, 200 (1965).
43. M. Ross (private communication, 1965).
44. L. Champomier, Lawrence Radiation Laboratory Report UCRL 11222 (1963).
45. R. Böck, CERN Report 61-29 (1961).

REFERENCES (Continued)

46. W. Moebs, Four- and Five-Particle Production in 3.7 BeV/c π^- p Collisions, dissertation (University of Michigan Technical Report C00-1112-3, 1965).
47. G. Breit and P. Wigner, Phys. Rev. 49, 519 (1936).
48. B. Shen, Resonance Production in Pion-Proton Interactions at 3.65 BeV/c and 3.7 BeV/c, dissertation (University of California, Lawrence Radiation Laboratory Report UCRL-16170, 1965).
49. H. Lubatti, H. Bingham, W. Fretter, W. Michael, and K. Moriyasu, Bull. Am. Phys. Soc. 10, 701 (1965).
50. A. Rosenfeld, A. Barbaro-Galtieri, W. Barkas, P. Bastien, J. Kirz, and M. Roos, Rev. Mod. Phys. 37, 633 (1965).
51. A. Rosenfeld, "Mesons," Lawrence Radiation Laboratory Report No. UCRL-16462 (1965).
52. C. Coffin, N. Dikmen, L. Ettlinger, D. Meyer, A. Saulys, K. Terwilliger, and D. Williams, Phys. Rev. Letters 17, 458 (1966).
53. S. Kormanyos, A. Krisch, J. O'Fallon, K. Ruddick, and L. Ratner, Phys. Rev. Letters 16, 709 (1966).
54. V. Barger and D. Cline, Phys. Rev. Letters 16, 913 (1966); 1135 (E).
55. A. Pevsner, R. Kraemer, M. Nussbaum, C. Richardson, P. Schlein, R. Strand, T. Toohig, M. Block, A. Engler, R. Gessaroli, and C. Meltzer, Phys. Rev. Letters 7, 421 (1961).
56. R. Grossman, L. Price, and F. Crawford, Phys. Rev. 146, 993 (1966).
57. A. Cnops, et al., Phys. Letters 22, 546 (1966).
58. A. Rosenfeld, A. Barbaro-Galtieri, W. Barkas, P. Bastien, J. Kirz, and M. Roos, Lawrence Radiation Laboratory Report No. UCRL-8030, Part I (1965); corrected (1966).
59. V. Peterson (University of Hawaii, private communication quoted in Ref. 40).
60. R. Phillips and W. Rarita, Phys. Letters 19, 598 (1965).
61. F. Bulos, et al., Phys. Rev. Letters 13, 486 (1964).

REFERENCES (Continued)

62. G. Källén, Elementary Particle Physics (Addison-Wesley Publishing Company, Inc., Reading, Massachusetts, 1964).
63. B. Maglic, L. Alvarez, A. Rosenfeld, and M. Stevenson, Phys. Rev. Letters 1, 178 (1961).
64. W. Frazer, J. Fulco, and F. Halpern, Phys. Rev. 136, B1207 (1964).
65. G. Benson, L. Lovell, E. Marquit, B. Roe, D. Sinclair, and J. Vander Velde, Bull. Am. Phys. Soc. 10, 502 (1965).
66. T. Ferbel, Phys. Letters 21, 111 (1966).
67. S. Chung, M. Neveu-René, O. Dahl, J. Kirz, D. Miller, and Z. Guiragossian, Phys. Rev. Letters 16, 481 (1966); 16, 635 (E) (1966).
68. C. Baltay, et al. (submitted to XIII International Conference on High Energy Physics, Berkeley, California, 1966, to be published).
69. M. Barmawi, Phys. Rev. 142, 1088 (1966).
70. J. D. Jackson (private communication, 1965).
71. J. D. Jackson, Rev. Mod. Phys. 37, 484 (1965).
72. J. D. Jackson, J. Donahue, K. Gottfried, R. Keyser, and B. Svensson, Phys. Rev. 139, B428 (1965).
73. H. Cohn, W. Bugg, and G. Condo, Phys. Letters 15, 344 (1965).
74. K. Gottfried and J. D. Jackson, Nuovo Cimento 33, 309 (1964).
75. S. Berman and M. Jacob, Phys. Rev. 139, B1023 (1965).
76. J. D. Jackson, Nuovo Cimento 34, 1644 (1964).
77. P. Minnaert, Phys. Rev. Letters 16, 672 (1966); 16 1030 (E).
78. J. Alitti, J. Baton, W. Fickinger, M. Neveu-René, A. Romano, and R. Gessaroli, Phys. Letters 21, 345 (1966).
79. M. Barmawi, Phys. Rev. Letters 16, 595 (1966).
80. R. Warnock, Conference on Elementary Particles, Annual Summer Institute for Theoretical Physics, Boulder, Colorado, 1966 (to be published).

REFERENCES (Continued)

81. S. Flatté, D. Huwe, J. Murray, J. Button-Shafer, F. Solmitz, M. Stevenson, and C. Wohl, Phys. Rev. 145, 1050 (1966).
82. Aachen-Berlin-Birmingham-Bonn-Hamburg-London (I.C.)-Munich Collaboration, Phys. Letters 11, 167 (1964).
83. G. Benson, E. Marquit, B. Roe, D. Sinclair, and J. Vander Velde, submitted to the XIII International Conference on High Energy Physics (Berkeley, California, 1966).
84. R. Deck, Phys. Rev. Letters 13, 169 (1964).
85. M. Month, Phys. Letters 18, 357 (1965).
86. A compilation of $\rho^0 \pi^\pm$ mass distributions from $\pi^\pm p$ experiments with beam momenta 3.2 - 4.0 BeV/c has been presented by G. Goldhaber, UCRL Report No. 11971 (1965). We have added to this our own data from $\pi^- p$ at 3.65 BeV/c.
87. C. T. Murphy, et al. (to be published).
88. G. London, R. Rau, N. Samios, S. Yamamoto, M. Goldberg, S. Lichtman, M. Primer, and J. Leitner, Phys. Rev. 143, B1034 (1966).
89. J. D. Jackson and J. Donahue (private communication, 1966).
90. B. Chen, G. Goldhaber, S. Goldhaber, and J. Kadyk, Phys. Rev. Letters 15, 731 (1965).
91. S. Berman and M. Jacob, Phys. Rev. 139, B1023 (1965).
92. J. D. Jackson (private communication, 1966).
93. L. Seidlitz, O. Dahl, and D. Miller, Phys. Rev. Letters 15, 217 (1965).
94. R. Lander, M. Abolins, D. Carmony, T. Hendricks, N. Xuong, and P. Yager, Phys. Rev. Letters 13, 346a (1964).
95. S-U. Chung, O. Dahl, L. Hardy, R. Hess, G. Kalbfleisch, J. Kirz, D. Miller, and G. Smith, Phys. Rev. Letters 12, 621 (1964).
96. J. Alitti, et al. (Saclay-Bologna), Phys. Letters 15, 69 (1965).

REFERENCES (Continued)

97. V. Barnes, W. Fowler, K. Lai, S. Orenstein, D. Radojićić, and M. Webster, Phys. Rev. Letters 16, 41 (1966).
98. G. Benson, L. Lovell, E. Marquit, B. Roe, D. Sinclair, and J. Vander Velde, Phys. Rev. Letters 16, 1177 (1966).
99. R. Hess, Production of $K\bar{K}$ Pairs in $\pi^- p$ Interactions, dissertation (University of California, Lawrence Radiation Laboratory Report UCRL-16832, 1966).
100. A. Forino, et al. (Saclay, Orsay, Bologna), Phys. Letters 11, 347 (1964).
101. A. Forino, et al. (Bologna, Bari, Firenze, Orsay, Saclay), Phys. Letters 19, 68 (1965).
102. L. Lovell, G. Benson, E. Marquit, B. Roe, D. Sinclair, and J. Vander Velde, Bull. Am. Phys. Soc. 10, 502 (1965).
103. C. Zemach, Phys. Rev. 133, B1201 (1964).
104. H. Högaasen, J. Högaasen, R. Keyser, and B. Svensson, Nuovo Cimento 42, 323 (1966).
105. We wish to thank W. Moebs for permitting us to use his $\pi^- p$ data.
106. W. Fischer (private communication, 1966).
107. W. Bugg (private communication, 1966).
108. R. Rau, N. Samios, S. Yamamoto, M. Goldberg, S. Lichtman, M. Primer, and J. Leitner, Phys. Rev. 143, 1034 (1966).
109. J. Vander Velde (University of Michigan Bubble Chamber Research Notes HI-1 and HI-3, 1963).
110. B. Sechi-Zorn and G. T. Zorn, Nuovo Cimento Supplemento 26, 197 (1962).
111. M. Abolins, D. Carmony, R. Lander, and Hg.-h. Xuong, Phys. Rev. Letters 15, 125 (1965).
112. J. Sanford (Brookhaven National Laboratory Report JRS-1, 1962).
113. M. Perl, Y. Lee, and E. Marquit, Phys. Rev. 138, B707 (1965).

REFERENCES (Concluded)

- 114. B. Ronne, Proceedings of the 1964 Easter School for Physicists, Vol. I, p.87(CERN Report 64-13, 1964).
- 115. R. D. Sard (private communication, 1964).
- 116. J. Sanford (private communication, 1965).
- 117. R. H. Dicke and J. P. Wittke, Introduction to Quantum Mechanics (Addison-Wesley Publishing Company, Inc., Reading, Massachusetts, 1960).
- 118. W. Koch, Proceedings of the Easter School for Physicists, Vol. II (CERN Report 64-13, 1964).
- 119. W.S.C. Williams, An Introduction to Elementary Particles (Academic Press, Inc., New York, 1961).
- 120. S. S. Schweber, An Introduction to Relativistic Quantum Field Theory (Harper and Row Publishers, Inc., New York, 1961).
- 121. N. Byers and S. Fenster, Phys. Rev. Letters 11, 52 (1963).
- 122. P. Dennerly and A. Krzywicki, Phys. Rev. 136, B839 (1964).

ACKNOWLEDGMENTS

I am deeply indebted to the following people, all of whom contributed to the success of this experiment:

the staff of Brookhaven National Laboratory for making the accelerator and bubble chamber available to us,

the members of The University of Michigan Bubble Chamber group, under the leadership of Dr. Daniel Sinclair, for supporting this study,

Dr. Byron Roe for advice and for serving as chairman of my doctoral committee,

Dr. John Vander Velde for many discussions, assistance with the experiment, and for serving on my doctoral committee,

Drs. F. Haddock, O. Overseth, and M. Ross for serving as doctoral committee members,

Dr. E. Marquit and L. Lovell for collaboration throughout this experiment, and for lending me many useful programs,

the 37 scanners and measurers who processed the events, particularly D. Moebs, V. French, M. Rauer, M. Brueckner, and J. Oh,

our programming and technical staff, particularly B. Bell, A. Loceff, and J. Allen,

my graduate student colleagues: C. Arnold, M. Church, T. Fisher, F. Hess, H. Hsiung, B. Meyers, and C. K. Weaver for assistance in a variety of jobs,

W. Beusch, W. Bugg, D. Carmony, B. Chen, E. Coleman, J. Donahue, W. Fischer, V. Hagopian, R. Hess, J. D. Jackson, J. Kirz, U. Kruse, W. Moebs, D. Richardson, D. Robinson, R. Sard, and P. Yamin for private communication of unpublished results and for helpful discussions,

C. Coffin, G. Goldhaber, R. Heinz, G. Kane, C. Meltzer, C. T. Murphy, M. Ross, J. Sanford, and P. K. Williams for helpful discussions,

ACKNOWLEDGMENTS (Concluded)

the Detroit Evening News Association, and the American people (through the U. S. Atomic Energy Commission) for generous financial support,

The University of Michigan Computing Center for computing time,

J. Besancon for drafting most of the figures in this report, and

my wife, Lee, for typing the first copy of this report from a very rough draft.

UNIVERSITY OF MICHIGAN



3 9015 02229 3230